CORA Cork Open Research Archive
Cartlann Taighde Oscailte Chorcaí

Title	Advanced micro-photoluminescence spectroscopy of pyramidal site-controlled quantum dots as spin-photon interfaces
Authors	Mattana, Francesco
Publication date	2025
Original Citation	Mattana, F. 2025. Advanced micro-photoluminescence spectroscopy of pyramidal site-controlled quantum dots as spin-photon interfaces. PhD Thesis, University College Cork.
Type of publication	Doctoral thesis
Rights	© 2025, Francesco Mattana. - https://creativecommons.org/publicdomain/zero/1.0/
Download date	2026-11-07 10:13:25
Item downloaded from	https://hdl.handle.net/10468/18406



UCC
University College Cork, Ireland
Coláiste na hOllscoile Corcaigh

Advanced micro-photoluminescence spectroscopy of pyramidal site-controlled quantum dots as spin-photon interfaces

By

Francesco Mattana

A THESIS SUBMITTED TO
THE NATIONAL UNIVERSITY OF IRELAND, CORK
FOR THE DEGREE OF

DOCTOR OF PHILOSOPHY



Epitaxy and Physics of Nanostructures Group
Tyndall National Institute
Department of Physics, University College Cork
Republic of Ireland

Head of the Department: Professor Paul Callanan

Supervisor: Dr. Gediminas Juška

March 2025

Contents

Abstract **vii**

Acknowledgment **ix**

Publications & Presentations **xi**

1 Background **1**
1.1 Quantum Computing . . . 2
1.1.1 Circuit model . . . 3
1.1.2 Cluster State . . . 7
1.1.3 Decoherence . . . 10
1.2 Quantum Dots . . . 12
1.2.1 Excitonic Complexes . . . 14
1.2.1.1 Heavy/Light Holes and Selection Rules . . . 16
1.2.1.2 Symmetry and Point Groups . . . 17
1.2.1.3 Neutral Excitons . . . 18
1.2.1.4 Charged Excitons . . . 22
1.2.2 Decoherence . . . 23
1.2.3 Entanglement . . . 25
1.3 Conclusions . . . 28
References . . . 31

2 Pyramidal Site-Controlled Quantum Dots and Experimental Techniques **37**
2.1 Substrate Preparation . . . 38
2.2 Metal-Organic Vapour Phase Epitaxy Growth . . . 39
2.3 Sample Post-Processing . . . 41
2.3.1 Polishing and Solid Immersion Lens . . . 41

2.3.2 Back-Etching . . . 42
2.3.3 Cleaving . . . 43
2.3.4 Sample Mapping . . . 43
2.3.4.1 Direct Laser Writing . . . 44
2.3.4.2 Lithographic Photomask . . . 45
2.4 Micro-Photoluminescence . . . 46
2.4.1 Cryostat . . . 46
2.4.2 Quantum Dot Excitation . . . 48
2.4.2.1 Imaging . . . 48
2.4.2.2 Above-band Excitation . . . 48
2.4.2.3 Laser Pulse Shaping . . . 49
2.4.2.4 Beam Path . . . 50
2.4.2.5 Polarization . . . 50
2.4.3 Polarization and Time-Resolved measurements . . . 56
2.4.3.1 Correlation, $g^{(2)}(\tau)$ . . . 57
2.4.4 Cluster State Generation and Characterization Setup . . . 60
2.5 Conclusions . . . 61
References . . . 62

3 Quantum Dot Excitation Schemes 65
3.1 Above-band Excitation . . . 66
3.2 Resonant and Quasi-Resonant Excitation . . . 67
3.2.1 Two-Level System . . . 68
3.2.1.1 Phonons . . . 71
3.2.1.2 Simulations and Experiment . . . 73
3.2.2 Three-Level System . . . 79
3.2.2.1 XX - X Cascade . . . 79
3.2.2.2 X_{11}^{+} to X_{20}^{+} relaxation . . . 86
3.3 Dichromatic Excitation . . . 89
3.3.1 Red-and-Blue Detuned . . . 89
3.3.2 SUPER . . . 92
3.4 Conclusions . . . 95
References . . . 98

4 Energetic Structure of GaAs Quantum Dots 101
4.1 Neutral Excitons . . . 102
4.2 Positive Trions . . . 114
4.3 Negative Trions . . . 123
4.4 Conclusions . . . 125
References . . . 127

5 Hole Spin Initialization and Control **129**
5.1 Hole Initialization at $\vec{B} = 0T$ . . . 130
5.1.1 Phonon Assisted Excitation . . . 130
5.1.2 Excited State Resonant Excitation . . . 132
5.2 Hole Precession in Weak Magnetic Field . . . 138
5.3 Cluster State Generation . . . 144
5.4 Conclusions . . . 146
References . . . 148

6 Summary and Perspectives **149**
6.1 Summary . . . 149
6.2 Perspectives . . . 149
References . . . 152

Declaration

This is to certify that the work I am submitting is my own and has not been submitted for another degree, either at University College Cork or elsewhere. All external references and sources are clearly acknowledged and identified within the contents. I have read and understood the regulations of University College Cork concerning plagiarism and intellectual property.

Francesco Mattana
September 16, 2025

Abstract

Semiconductor quantum dots (QDs) are low dimensional system, typically a few nanometers in size, characterized by discrete energy levels and strong light - matter interaction. Due to their optoelectronics properties they have emerged as a promising candidate for qubit system and platform for quantum computing, cryptography and information processing. Quantum dots are capable of single and polarization-entangled photon emission and can be easily integrated into photonics circuits. The strong light - matter interaction that characterizes quantum dots system allows optical control of electron and hole spins states of individual quantum dots, thus enabling quantum gate operations or implementation of different quantum computing protocols.

One of these protocols relies on cluster state, highly entangled quantum states. Processing of such states, through measurements of single qubits, allows implementation of quantum computing. This protocol is deemed less demanding than a *classic* quantum gates approach, which requires multi-qubit input gates.

However, environment noise for single charge carrier is still a limiting factor for any quantum information protocol, because loss of coherence in quantum systems limits the number of operations executable on a qubit. Recently, $GaAs$ quantum dots produced by droplet etching epitaxy are currently state of the art in terms of low-noise environments for single charge carriers.

In this work, we studied $GaAs$ quantum dots fabricated by a different technique, metalorganic vapour-phase epitaxy (MOVPE) growth on (111)B oriented GaAs substrates pre-patterned by micrometre-scale tetrahedron recesses. This method enables much higher degree of QD engineering flexibility and site-control of the growth process.

In Chap.1, we introduce the concept of quantum computing and give an overview of a specific implementation, the so called one-way quantum computer, using a specific class of entangled states, cluster states, as main resource for computation. We will also describe quantum dots, their properties and how they can be used as single and entangled photon emitters.

In Chap.2, we will describe the fabrication steps for producing and processing a particular family of quantum dots, pyramidal site-controlled quantum dots, in order to make them useable for characterization and measurements. We will also describe the instruments, custom built setups and procedures to optically characterize the quantum dots.

In Chap.3, we investigate several excitation and initialization schemes for quantum dots. Quantum systems with two or three energy levels are simulated under a variety of optical excitation schemes. These simulation will define a range of suitable parameters of the optical pulses, compatible the resources available in our laboratory. Several experimental examples of these excitation scheme will also be provided.

In Chap.4, we carry out an in-depth study of the energetic structure of $GaAs$ quantum dots. Using a variety of spectroscopic techniques, such as polarization and time resolved micro-photoluminescence, we investigate the optical recombination of several quantum dots to associate to each transition line an excitonic state. Optical selection rules of our quantum dots have also been investigated, uncovering light-hole-like excited states and deviations from the expected group theory calculations.

In Chap.5, we demonstrate quantum dot initialization by a hole with a well defined spin state, one of the requirements for the physical implementation of quantum computation. As a step towards cluster state generation, we demonstrate periodic precession of the spin state in a weak magnetic field. We also attempt cluster state generation, but low quantum dot brightness and fast loss of coherence of the spin state will prove to be very limiting.

Acknowledgment

I would like to express my gratitude first of all to my supervisor, Gediminas. For what has been a great opportunity of personal and professional development, for teaching me so much in the lab and allowing me to pursue my interests.

I'm grateful also to Emanuele, for all the interesting talks about the physics and for always be available to help to solve issues that arose during the PhD.

I am deeply grateful to both of them (especially for having a lot of patience in the last year during the writing process!).

A big thank you to Iman, for being a friend all these years and for helping me countless times since the first week that I arrived in Ireland. Thanks for all the endless chats about everything, they are greatly missed!

Thanks to Armando, John, Luca, Nicola and Salam, for the fun of having worked with you and the many beers shared together!

A big thank you to Diego and Sheshank, for allowing me to turn the flat into a trattoria so many times!

And another big thank to all the other people that made the years I spent in Ireland an unforgettable experience; Aashi, Alida, David, Gabriele, Mario, Martina, Paolo, Simone, Soumitro, Swati... I'm sure I forgot somebody, but it is 1am so I will be forgiven!

Ultimo, ma non per importanza, un grazie dal profondo del cuore a babbo, mamma e Luisa per avermi supportato fino ad oggi in ogni modo possibile.

Procurad'e moderare,
barones, sa tirannia,
chi si no, pro vida mia
torrades a pe' in terra!
Declarada est già sa gherra
contra de sa prepotenzia:
e incomintza' sa passenzia
in su populu a mancare!

Mirade ch'est'atzendende
contra de ois su fogu,
mirade chi no e' giogu,
chi sa cosa andat 'e veras;
mirade chi sas aeras
minettana temporale;
zente cussizzada male,
iscultade sa oghe mia

No apprettedas s 'isprone
A su poveru ronzinu,
Si no in mesu caminu
S'arrempellat appuradu;
Mizzi chi est lanzu e cansadu
E non 'nde podet piusu;
Finalmente a fundu in susu
S'imbastu 'nd hat a bettare

Su pobulu chi in profundu
Letargu fit sepultadu
Finalmente despertadu
S'abbizzat ch 'est in cadena,
Ch'istat suffrende sa pena
De s'indolenzia antiga:
Feudu, legge inimiga
A bona filosofia!

Publications & Presentations

Publications

- G. Juška, I. Ranjbar Jahromi, **F. Mattana**, S. Varo, V. Dimastrodonato, and E. Pelucchi; *Biexciton initialization by two-photon excitation in site-controlled quantum dots: The complexity of the antibinding state case.* Appl. Phys. Lett. 28 September 2020; 117 (13): 134001. DOI: 10.1063/5.0011383

- Provided simulations of anti-binding biexciton studies and phonon assisted excitation with QuTiP (Quantum Toolbox in Python) library and participated in routine data collection and analysis

- I. Ranjbar Jahromi, G. Juška, S. Varo, F. Basso Basset, F. Salusti, R. Trotta, A. Gocalinska, **F. Mattana**, and E. Pelucchi; *Optical properties and symmetry optimization of spectrally (excitonically) uniform site-controlled GaAs pyramidal quantum dots.* Appl. Phys. Lett. 15 February 2021; 118 (7): 073103. DOI: 10.1063/5.0030296

- Participated in routine data collection and analysis

- G. Juška, S. Varo, N. Maraviglia, J. O'Hara, S. Medina, L. Colavecchi, **F. Mattana**, A. Trapala, M. Schmidt, and E. Pelucchi; *Self-aligned pillar arrays embedding site-controlled single quantum dots for enhanced non-classical light emission.* Adv. Photonics Res.. 2025, 0, e202500116. DOI: 10.1002/adpr.202500116

- Participated in routine data collection and analysis, built lithography setup with off the self components and writing of software for operations, studied QDs photoluminescence polarization distortions from optical elements of the setup

Conference Proceedings

- **F. Mattana**, I. R. Jahromi, G. Ronco, M. Rota, F. B. Basset, R. Trotta, E. Pelucchi, and G. Juška, *GaAs Site-controlled Pyramidal Quantum Dots as Spin Qubit Sources for a Photonic Cluster State Construction: the Role of Light-hole-like Excited States.* in CLEO 2023, Technical Digest Series (Optica Publishing Group, 2023), paper FF3G.2 DOI: CLEO_FS-2023-FF3G.2

- Data collection and analysis of core topics presented in the conference

List of Oral Presentations (presenting author)

- **F. Mattana**, I. Ranjbar Jahromi, G. Ronco, M. Rota, F. Basso Basset, R. Trotta, E. Pelucchi, and G. Juška, *GaAs Site-controlled Pyramidal Quantum Dots as Spin Qubit Sources for a Photonic Cluster State Construction: the Role of Light-hole-like Excited States.* Photonics Ireland 2023

- **F. Mattana**, I. Ranjbar Jahromi, G. Ronco, M. Rota, F. Basso Basset, R. Trotta, E. Pelucchi, and G. Juška, *GaAs Site-controlled Pyramidal Quantum Dots as Spin Qubit Sources for a Photonic Cluster State Construction: the Role of Light-hole-like Excited States.* CLEO/Europe-EQEC 2023

- Data collection and analysis of hole coherence properties in GaAs QDs in Superlatice, built various setups for time-resolved spectroscopy, such as delay lines for Ramsey Interferometry measurements, setup for cluster states generation and characterization

- **F. Mattana**, I. Ranjbar Jahromi, S. Varo, J. O'Hara, G. Ronco, M. Rota, F. Basso Basset, R. Trotta, E. Pelucchi, and G. Juška, *Towards the experimental realisation of a photonic cluster state with site-controlled GaAs QDs.* Quantum Festival at UCD 2022

- **F. Mattana**, I. Ranjbar Jahromi, S. Varo, J. O'Hara, G. Ronco, M. Rota, F. Basso Basset, R. Trotta, E. Pelucchi, and G. Juška, *Towards the experimental realisation of a photonic cluster state with site-controlled GaAs QDs.* Photon 2022

- **F. Mattana**, I. Ranjbar Jahromi, S. Varo, J. O'Hara, G. Ronco, M. Rota, F. Basso Basset, R. Trotta, E. Pelucchi, and G. Juška, *Towards the experimental realisation of a photonic cluster state with site-controlled GaAs QDs.* Quantum Dot Day 2022

- **F. Mattana**, I. Ranjbar Jahromi, S. Varo, J. O'Hara, A. Gocalinska, E. Pelucchi, and G. Juška, *Towards the experimental realisation of a photonic cluster state with pyramidal site-controlled GaAs quantum dots.* European Quantum Technologies Conference 2021

- **F. Mattana**, I. Ranjbar Jahromi, S. Varo, J. O'Hara, A. Gocalinska, E. Pelucchi, and G. Juška, *Towards the experimental realisation of a photonic cluster state with pyramidal site-controlled GaAs quantum dots.* Photonics Ireland 2021

- Collected and analysed data for studies of energy structure of GaAs QDs in Superlattice with a variety of spectroscopic techniques, such as polarization and time resolved micro-photoluminescence at cryogenic temperatures, studied in depth polarization properties of optical elements of setup

List of Oral Presentations (contributing author)

- G. Juška (invited talk), **F. Mattana**, I. Ranjbar Jahromi, L. Colavecchi, S. Varo, J. O'Hara, N. Maraviglia, G. Ronco, M. Rota, F. Basso Basset, R. Trotta, and E. Pelucchi, *Recent developments of site-controlled pyramidal quantum dots as spin and photon qubit sources.* 8th International workshop. Engineering of Quantum Emitter properties, Paderborn, Germany, 06 - 07 December 2023.

- G. Juška (invited talk), **F. Mattana**, I. Ranjbar Jahromi, G. Ronco, M. Rota, F. Basso Basset, R. Trotta, and E. Pelucchi, *Resonant excitation study of GaAs site-controlled pyramidal quantum dots as spin qubit sources.* 8th International workshop. Engineering of Quantum Emitter properties, Stuttgart, Germany, 15 - 16 December 2022.

- E. Pelucchi (invited talk), G. Juška, S. Varo, I. Ranjbar Jahromi, **F. Mattana**, and A. Gocalinska, *InGaAs and GaAs site-controlled pyramidal quantum dots.* SemiconNano, 8th International Workshop Epitaxial Growth and Fundamental Properties of Semiconductor Nanostructures, Milano (Italy) - 30 August - 3 September

- E. Pelucchi (plenary talk), S. Varo, I. Ranjbar Jahromi, **F. Mattana**, A. Gocalinska, and G. Juška, *Engineering site-controlled QDs for quantum technologies on (111)B GaAs substrates.* VII International Conference on Information Technologies and Nanotechnologies (ITNT-2021) 20 - 24 September

- I. Ranjbar Jahromi, G. Juška, S. Varo, A. Gocalinska, **F. Mattana**, and E. Pelucchi, *GaAs Pyramidal Quantum Dots: A Spectrally Uniform Source of Single Photons and Entangled Photon Pairs.* Photon 2022, 30 August - 2 September 2022, IOP, East Midlands Conference Centre, Nottingham, UK

- G. Juška, **F. Mattana** , I. Ranjbar Jahromi, and E. Pelucchi, *Engineering flexibility of site controlled Pyramidal quantum dots as sources of photonic and spin quantum bits.* NanoTR-17, 27 - 29 August 2023, Izmir, Turkey

- Same contributions as above

List of Posters (presenting author)

- **F. Mattana**, I. Ranjbar Jahromi, S. Varo, E. Pelucchi, and G. Juška, *In Depth Study of Pyramidal GaAs Quantum Dots Optical Transitions.* EQEP 2023

- **F. Mattana**, L. Colavecchi, I. Ranjbar Jahromi, E. Pelucchi, and G. Juška1, *Coupling novel GaAs site-controlled QDs.* Summer School on 'Quantum technology from fundamental science to real world applications' 2023

- Data collection and analysis of core topics presented in the posters

List of Posters (contributing author)

- L. Colavecchi, **F. Mattana**, I. Ranjbar Jahromi, G. Juška, and E. Pelucchi, *Coupling novel GaAs site-controlled QDs.* Photonics Ireland Conference 2023, 04 - 06 September 2023, Limerick, Ireland.

- L. Colavecchi, **F. Mattana**, I. Ranjbar Jahromi, G. Juška, and E. Pelucchi, *Coupling novel GaAs site-controlled QDs.* 15^{th} edition, IQIS2023 Italian Quantum Information Science, 18 - 22 September 2023 Trieste Italy.

- E. Pelucchi, G. Juška, **F. Mattana**, and L. Colavecchi, *Coupling novel GaAs site-controlled QDs.* 9th international workshop on 'Engineering of Quantum Emitter Properties' (EQEP), Paderborn, Germany 2023, 7 - 8 December.

- Data collection and analysis of PL of novel GaAs site-controlled coupled QDs

- I. Ranjbar Jahromi, G. Juska, S. Varo, A. Gocalinska, **F. Mattana**, and E. Pelucchi, *Spectral Uniformity and Symmetry of a New Generation of GaAs Site-Controlled Pyramidal Quantum Dots.* QD2020, December 7, 2020.

- I. Ranjbar Jahromi, G. Juska, **F. Mattana**, S. Varo, A. Gocalinska and E. Pelucchi, *GaAs site-controlled Pyramidal quantum dots: enhancing dot reproducibility and controllability (hence scalability) for on-demand single and entangled photon emission.* EQTC 2021, Dublin (Virtual), 29 November - 02 December 2021

- G. Juška, **F. Mattana**, I. Ranjbar Jahromi, G. Ronco, M. Rota, F. Basso Basset, R. Trotta, and E. Pelucchi, *GaAs Site-controlled Pyramidal Quantum Dots as Spin Qubit Sources for a Photonic Cluster State Construction.* 15^{th} edition, IQIS2023 Italian Quantum Information Science, 18 - 22 September 2023 Trieste Italy

- G. Juška, **F. Mattana**, I. Ranjbar Jahromi, G. Ronco, M. Rota, F. Basso Basset, R. Trotta, and E. Pelucchi, *GaAs Site-controlled Pyramidal Quantum Dots as Spin Qubit Sources for a Photonic Cluster State Construction.*

Quantum technology from fundamental science to real world applications, 2 - 7 October 2023 - Summer school at Ettore Majorana Foundation in Erice, Sicily

Chapter 1

Background

Quantum phenomena, with no classical counterpart, can be exploited to overcome the scalability limitations of classical computing and telecommunications [1].

Some specific tasks, such as large prime number factorization [2], simulation of molecules dynamics or other optimization problems [3], can be theoretically sped up and solved in sub-exponential time by using algorithms that employ quantum superposition.

Also telecommunications can be made more secure, by avoiding man-in-the-middle attacks, if quantum cryptography is used [4]. Encrypted keys can be exchange securely using protocols which exploit the impossibility of cloning quantum states and the collapse of an entangled state after a measurement.

The requirements of a quantum system to become a platform to implement quantum computing and communication are codified by the so-called DiVincenzo criteria [5]. This set of 7 conditions are:

1. A scalable physical system with well characterized qubits
2. The ability to initialize the state of the qubits to a simple fiducial state, such as $|000...\rangle$
3. Long relevant decoherence times, much longer than the gate operation time
4. A universal set of quantum gates
5. A qubit-specific measurement capability
6. The ability to interconvert stationary and flying qubits
7. The ability to faithfully transmit flying qubits between specified locations

This thesis will focus on the 2nd, 3rd and 6th criteria for a particular family of semiconductor devices, Pyramidal Site-Controlled Quantum Dots. From Chap.2 to Chap.5 we will describe their structure and characterize their spectrum to evaluate if they are a suitable candidate platform to develop quantum computation and, eventually, the limitations that will need to be overcome. Specifically, we want to evaluate if the quantum dots used are able to generate cluster states, a particular family of entangled states that can be used for quantum computing through the one-way quantum computer protocol [6]. We will show that our fabrication and processing methods enable production of quantum emitters with a very well defined location on a substrate and with reproducible features. These features could lead to a scalable platform.

The following chapter will give an overview of the principles of quantum computing, its applications and, in a general way, implementations using different paradigms.

The second part of the chapter will go into the details of the optical properties of quantum dots, how they can be used in quantum computing and communication and their limitations for said applications.

1.1 Quantum Computing

In 1982 Feynman pointed out the exponential growth of resources required to simulate complex systems on classical computer, like dynamics of molecules, climate on a microscale, or full description of a quantum system [1]. He suggested then the idea that, to describe the evolution of quantum system, other quantum systems could be used as a platform for calculation, in that way the required resources would scale proportionally to the complexity of the system that we wish to simulate.

Three years later Deutsch formalized the theoretical working principles of a quantum computer [7], but it was (and still is) not fully intelligible how many and how much computational tasks would benefit, in terms of speed and required resources, from being run on a quantum computer rather than on a classical one [8].

In the years that followed Feynman's idea, the advantage of quantum computers over classical ones has been proved for several tasks [9] [3] [2]. The most notable one is probably Shor algorithm for factorization of numbers [2], as it has been shown that this task, on a quantum computer, can be carried out in polynomial time rather than sub-exponential time. As of now there is no algorithm to factorize numbers in polynomial time with classical computers, but there is also no mathematical proof that such algorithm does not exist. This decrease in computation time with Shor algorithm is then of great relevance for cryptographic

applications, as the widely implemented RSA scheme generates a public encryption key by multiplying two large prime numbers. So far, the security of the algorithm does not reside in the impossibility of finding such prime numbers, but in the time taken to do it with classical computers.

It has also been proved that quantum states can be helpful in transmitting information safely. A weak point of specific encryption protocols involving an exchange of keys is that they are not safe against eavesdropping; if someone intercepts a set of keys shared with a classical communication channel the two original parties involved in the communication have no way of knowing that and now the third element can decode the encrypted messages.

A quantum state can't be measured without perturbing the original state, and thus an arbitrary state can't be cloned with a single measurement [10]. While it will not be possible to stop the eavesdropping, using quantum states it will be possible for two parties to be notified that such action happened, and exchange then a new set of encryption keys.

Secure exchange can happen with attenuated pulsed lasers, but the fact that the photon statistics is poissonian implies that some pulse may have 0 photons and some other more than 1. This increases the risk that the eavesdropper can have more information on the key without the original sender and receiver noticing. For this reason real single photon emitters are of great interest of this kind of applications.

The use of quantum mechanics to exchange safely encryption keys is known as quantum key distribution, QKD, and several protocols have already been proposed [4] [11] [12].

1.1.1 Circuit model

In quantum computation, the 0 and 1 bits of a classical computer, are replaced by so called qubits. Qubits are quantum states of a two-level system, $|0\rangle$ and $|1\rangle$, and can be represented by a wavefunction $|\phi\rangle = c_0 |0\rangle + c_1 |1\rangle$, with normalization condition $c_0 c_0^* + c_1 c_1^* = 1$.

The qubit can be then in a superposition of the orthogonal states $|0\rangle$ and $|1\rangle$, instead of being just in either state 0 or 1.

The coefficients c_0 and c_1 of the qubit can be converted into angular coordinates and the state can be then visualized on a Bloch Sphere, a sphere of unitary radius. An the north and south pole of the sphere there are the states $|0\rangle$ and $|1\rangle$, on the equator superposition states with even probabilities for $|0\rangle$ and $|1\rangle$, in particular $|\pm\rangle = \frac{1}{\sqrt{2}}(|0\rangle \pm |1\rangle)$ are on the x axis and $|\pm i\rangle = \frac{1}{\sqrt{2}}(|0\rangle \pm i\,|1\rangle)$ on the y axis, see Fig.1.1. Due to the normalization requirement all the pure states are mapped onto the surface of the sphere and correspond to superposition states. Statistical mixture states are instead mapped to the inside of the sphere.

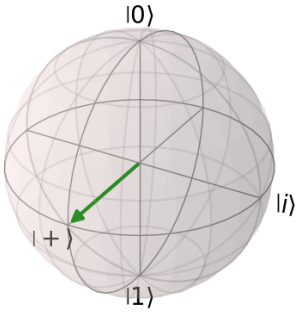


Figure 1.1: Bloch Sphere with a $|+\rangle$ state on it

Several quantum systems have been proposed as qubits candidates, Tab.1.1 taken from [8] lists a few of them.

Quantum system	Physical property	$\|0\rangle$	$\|1\rangle$
Photon	Linear polarization	Horizontal	Vertical
Photon	Circular polarization	Left	Right
Nucleus	Spin	Up	Down
Electron	Spin	Up	Down
Two-level atom	Excitation state	Ground state	Excited state
Josephson junction	Electric charge	N Cooper pairs	N + 1 Cooper pairs
Superconducting loop	Magnetic flux	Up	Down

Table 1.1: Proposed quantum systems to realize qubits. Taken from [8]

By coupling the qubits among each other we can generate so called quantum registers of wavefunction $\phi = c_{000...0}\,|000...0\rangle + c_{000...1}\,|000...1\rangle + ... + c_{011...1}\,|011...1\rangle + c_{111...1}\,|111...1\rangle$. It is clear that to represent such state by its amplitude values c in a classical memory we need to store 2^N complex numbers, which grows exponentially with the increase of the register size.

The register can then be manipulated by using so called quantum gates. These operations on the qubits can be represented by unitary matrices, $MM^\dagger = I$. Quantum gates can take one or more qubit as input, some of them have classical equivalents like the NOT and (N)AND, others are purely quantum mechanical.

Examples of single qubit gates are the Z gate, that leaves $|0\rangle$ states unchanged and flips the phase of $|1\rangle$ states, or the Hadamard gate, that changes basis states into their superpositions.

Important two qubit gates are the Controlled-NOT gate, C-NOT, and Controlled-Z, CZ. One input of these gates is called the control qubit and the other the target, C-NOT and CZ leave the control qubit unchanged and operate on the target state. The CNOT send $|0\rangle$ to $|1\rangle$ and $|1\rangle$ to $|0\rangle$, only if the control input is $|1\rangle$. The CZ swaps the sign of state $|1\rangle$, if the control is $|1\rangle$.

The matrix representations of the above mentioned gates are:

$$
\begin{aligned}
Z \cdot |\psi\rangle &= \begin{pmatrix} 1 & 0 \\ 0 & -1 \end{pmatrix} \begin{pmatrix} c_0 \\ c_1 \end{pmatrix} = \begin{pmatrix} c_0 \\ -c_1 \end{pmatrix} \\
H \cdot |\psi\rangle &= \begin{pmatrix} 1 & 1 \\ 1 & -1 \end{pmatrix} \begin{pmatrix} c_0 \\ c_1 \end{pmatrix} = \frac{1}{\sqrt{2}} \begin{pmatrix} c_0 + c_1 \\ c_0 - c_1 \end{pmatrix} \\
CNOT \cdot |\psi\rangle &= \begin{pmatrix} 1 & 0 & 0 & 0 \\ 0 & 1 & 0 & 0 \\ 0 & 0 & 0 & 1 \\ 0 & 0 & 1 & 0 \end{pmatrix} \begin{pmatrix} c_{00} \\ c_{01} \\ c_{10} \\ c_{11} \end{pmatrix} = \begin{pmatrix} c_{00} \\ c_{01} \\ c_{11} \\ c_{10} \end{pmatrix} \\
CZ \cdot |\psi\rangle &= \begin{pmatrix} 1 & 0 & 0 & 0 \\ 0 & 1 & 0 & 0 \\ 0 & 0 & 1 & 0 \\ 0 & 0 & 0 & -1 \end{pmatrix} \begin{pmatrix} c_{00} \\ c_{01} \\ c_{10} \\ c_{11} \end{pmatrix} = \begin{pmatrix} c_{00} \\ c_{01} \\ c_{10} \\ -c_{11} \end{pmatrix}
\end{aligned}
\tag{1.1}
$$

Graphically qubits are represented by horizontal wires and quantum gates by icons placed along these wires. Below we have the representation of some quantum gates, a Hadamard gate is applied to the first three qubits, CZ operation is applied between the 1st and 2nd and a CNOT between 3rd and 4th:

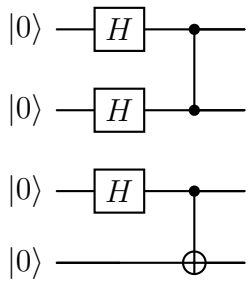


Figure 1.2: Graphical representation of quantum gate operating on qubits.

In classical computation, all the operations can be decomposed in a series of NAND gate operation, the same concept applies to quantum computers: a set of all single qubit rotation gates and CNOT gate constitute an universal set for quantum computation [13].

The measurement of a quantum circuit output is also a complicated task, the act measuring a quantum state *collapses* randomly the wavefunction $|\psi\rangle$ into the bases states $|0\rangle$ or $|1\rangle$ with probability c_0^2 or c_1^2. Complete reconstruction of a wavefunction cannot be done with a single measurement in a single base, but must be done with repeated measurements of several states on different bases. This process is known as quantum tomography [14].

A particular class of multiparticle states are the entangled states. They have attracted the attention of the scientific community since Einstein, Podolsky and Rosen described their counter-intuitive properties in 1935 [15].

The total wavefunction of an entangled state can't be factorized in the product of single particle wavefunctions. A typical example of two particle entangled states are the so called Bell states or EPR pairs:

$$\begin{aligned} |\Phi^{\pm}\rangle &= \frac{1}{\sqrt{2}}\left(|0_A 0_B\rangle \pm |1_A 1_B\rangle\right) \\ |\Psi^{\pm}\rangle &= \frac{1}{\sqrt{2}}\left(|0_A 1_B\rangle \pm |0_A 1_B\rangle\right) \end{aligned} \tag{1.2}$$

$|0_{A/B}\rangle$ and $|1_{A/B}\rangle$ are two orthogonal quantum states of systems A and B.

A generic quantum state given by the tensor product of states from system A and B can be written as:

$$\begin{aligned} |\psi_{AB}\rangle &= |\psi_A\rangle \otimes |\psi_B\rangle = \\ &= c_{0A}c_{0B}\,|0_A 0_B\rangle + c_{0A}c_{1B}\,|0_A 1_B\rangle + c_{1A}c_{0B}\,|1_A 0_B\rangle + c_{1A}c_{1B}\,|1_A 1_B\rangle \end{aligned} \tag{1.3}$$

It is easy to see that no combination of values for c_{0A}, c_{0B}, c_{1A} and c_{1B} can give the states in Eq.1.2. A consequence of this impossibility to factorize the entangled states is that, if we measure the state of the system A, we collapse the wavefunction of the multiparticle state and know immediately the state of B. The Bell state Φ^+ can be generated with quantum gates by having two $|0\rangle$ qubits, applying the Hadamard gate to the control qubit and then a CNOT gate.

Another important class entangled states are GHZ states [16]:

$$|GHZ\rangle = \frac{|0\rangle^{\otimes M} + |1\rangle^{\otimes M}}{\sqrt{2}} \tag{1.4}$$

where M is the number of qubits, so for $M = 3$ the GHZ state is $\frac{|000\rangle+|111\rangle}{\sqrt{2}}$. Detecting just one qubit in the GHZ will give us information on the state of all the others.

These properties make entangled states ideal for QKD application [11] [12] and quantum teleportation [17].

Entangled states can be generated by exploiting non linear properties of a quantum system. Early studies of entanglement were done on photon pairs generated by atomic cascades from calcium. The atoms were excited from the ground state $4s^2\,{}^1S_0$ to $4p^2\,{}^1S_0$ by using spontaneous decay from an excited state [18] or with a two photon process [19]. Initial and final state both have angular momentum $J = 0$, the electron can't relax to the ground directly but has to go through the emission of two photons, $4p^2\,{}^1S_0 \rightarrow 4s4p\,{}^1P_1$ and $4s4p\,{}^1P_1 \rightarrow 4s^2\,{}^1S_0$. The photons are entangled due to conservation of the angular momentum.

Nowadays atomic sources have been replaced for entangled photon pair emission, for example, by a family of crystals with second order non linearity χ^2, like β-barium borate, BBO [20]. The crystal is pumped with powerful laser at frequency w_0. A type-II spontaneous parametric down-conversion process converts this photon into two of frequencies ω_1 and ω_2 and orthogonal polarization. Conservation of energy and momentum requires that $\omega_0 = \omega_1 + \omega_2$ and $\vec{k}_0 = \vec{k}_1 + \vec{k}_2$, where $\vec{k}$ are the wavevectors of the photons. These conditions are called phase-matching conditions and if $\omega_1 = \omega_2$ the photons are degenerate. Dispersion and birefringence from the BBO crystal cause the down-converted photons to be emitted along two cones of orthogonal polarization with two intersection points. At those points the photons are entangled, if we detect horizontal (vertical) polarized photon at the first intersection we know that a vertical (horizontal) polarized photon will be at the second intersection.

In general, the so-called DiVincenzo Criteria [5] establish the minimum requirements to implement quantum computing and communication on a selected platform.

Among the requirements to achieve full quantum communication there is the capability to share quantum states from place to place through so called *flying* qubits. Photons are suited for this task due to their low interaction among each others, to the knowledge already built on classical communication channels, like fiber optics, and to the possibility of manipulating individual photons with benchtop optics or integrated photonics circuits.

Particularly promising are also platform based on semiconductor materials. These materials allow to directly convert quantum states in matter, spins, to flying qubits, photons, thus having the advantage of both worlds: long stability of spins and fast generation rates from solid state physics and low interaction from photons. Some semiconductor based systems offer also the possibility to optically or electronically trigger the production of single and entangled photons, thus proving to be a very versatile platform. Semiconductor material are also very flexible in alloy composition and tuning of the bandgap and can be integrated on complex, but small footprint, devices with several fabrication techniques.

1.1.2 Cluster State

Cluster states are a particular class of entangled states. These states are generated in an ensemble of qubits placed at sites a on a d-dimensional lattice that interact via the Hamiltonian [21]:

$$H_{int} = \hbar g\left(t\right) \sum_{a,a'} f\left(a - a'\right) \frac{1 + \sigma_z^{(a)}}{2} \frac{1 - \sigma_z^{(a')}}{2} \tag{1.5}$$

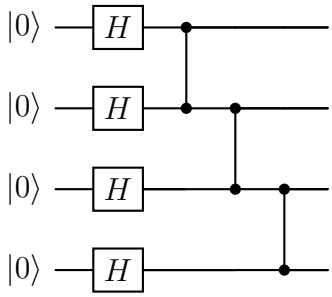


Figure 1.3: A 1-dimensional 4 qubit cluster state

where σ_z is the Pauli matrix operator. The indices of the sum, a and a', run over all the occupied lattices sites, $g(t)$ and $f(a-a')$ determine the interaction strength, which can be also time dependent because of g.

Briegel and Raussendorf focused their studies in 2000 [21] on 1-dimensional cluster states where the interaction is limited to neighbouring qubits, $f(a-a') = \delta_{a+1,a'}$ and $g(t) = const.$ If at time $t = 0$ the qubits are all prepared in the state $\frac{1}{\sqrt{2}}(|0\rangle + |1\rangle)$ the obtained cluster state can be written as:

$$|\phi_N\rangle = \frac{1}{2^{N/2}} \bigotimes_{a=1}^{N} \left(|0\rangle_a \sigma_z^{(a+1)} + |1\rangle_a\right) \tag{1.6}$$

with the convention that $\sigma_z^{(N+1)} = \mathbb{1}$. In the circuit model of quantum computation, this is equivalent to: 1) set the qubits to state $|0\rangle$, 2) apply a Hadamard gate to all of them, 3) apply a CZ gate to neighbouring qubits. Since the CZ gates commute with each other the order in which this gate is applied to the qubit is not relevant [22].

For $N = 2$, according to Eq.1.6 we get:

$$\begin{aligned} |\phi_2\rangle &= \frac{1}{2}\left(|0_1\rangle \sigma_z^{(2)} + |1_1\rangle\right)(|0_2\rangle + |1_2\rangle) = \\ &= \frac{1}{2}\left[|0_1\rangle (|0_2\rangle - |1_2\rangle) + |1_1\rangle (|0_2\rangle + |1_2\rangle)\right] \end{aligned} \tag{1.7}$$

A local unitary transformation, specifically a change of base, can be applied to state 1.7, $\frac{1}{\sqrt{2}}(|0_2\rangle \pm |1_2\rangle) = |\pm_2\rangle$, and then by renaming the new basis states, $|-_2\rangle = |0_2\rangle$ and $|+_2\rangle = |1_2\rangle$, one of the Bell pairs is obtained.

Analogously, for $N = 3$ we can apply local unitary transformations and change the labeling of some qubit to obtain a GHZ state.

$N = 4$ generates an entangled state which is not equivalent to a 4 qubit GHZ state:

$$|\phi_4\rangle = \frac{1}{4}(|0000\rangle + |0011\rangle + |1100\rangle - |1111\rangle) \tag{1.8}$$

One property of a cluster states with $N > 3$ is that is harder to destroy the entanglement of the cluster state compared to a GHZ state with the same number of qubits. A single qubit measurement, loss or depolarization will collapse the GHZ state and entanglement will be lost. Under the same circumstances in a cluster state the leftover state will still be entangled, as it still cannot be expressed as a product state, thus making the cluster state more robust against noise.

In later publications [6] [23] Raussendorf, Browne and Briegel theorized a new approach to quantum computation, the so called one-way quantum computer. In their implementation the main resource of computation is the cluster state itself. The operation that we want to execute is encoded on the cluster state and then the result read using single qubit measurements. The scheme is called one-way quantum computer because once the computation is done the entanglement of the state is destroyed.

In the same publication they showed that it is possible to make a single qubit general rotation and Hadamard gate with a 5 qubit 1-dimensional cluster state and a CNOT gate with a 15 qubit 2-dimensional cluster state.

For the Hadamard gate the procedure to follow is:

1. Prepare all qubit, except the first, in the $|+\rangle$ state.
2. Entangle the neighbouring qubit with the CZ operation.
3. Measure the expectation value of the operators σ_x^1 and $\sigma_x^{2,3,4}$, where σ_x is the Pauli matrix operator.

For the CNOT gate the procedure is

1. Prepare all qubit, except first and ninth, in the $|+\rangle$ state.
2. Entangle the neighbouring qubit with the CZ operation.
3. Measure the expectation value of $\sigma_x^{1,9,10,11,13,14}$ and $\sigma_y^{2,3,4,5,6,8,12}$

Because these operations constitute an universal set of gates, it is then possible to implement full quantum computation on a 2-dimensional cluster state.

The complexity of quantum computation is then moved from the operation of multi qubits gates, in the quantum circuit model, to the preparation of this highly entangled state and the execution of single qubit operations. The latter operations are usually much easier to implement. Moreover, the cluster state is less affected by noise and loss of qubits, because the state does not lose fully its entanglement properties under these conditions.

Browne and Rudolph introduced a scheme to generate 2-dimensional cluster states with just entangled photons and linear optics elements [24]. They showed

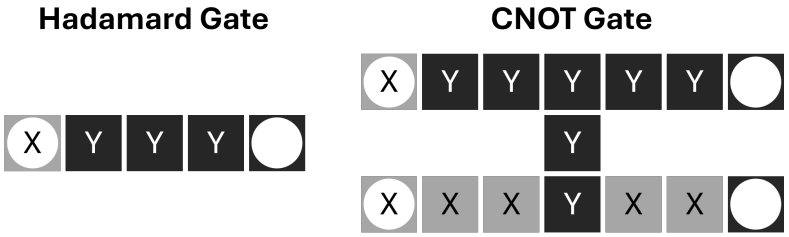


Figure 1.4: Realization of Hadamard and CNOT gates with cluster states.

that with the use of a Type-I fusion gate, see Fig.1.5 (left), 2 1-dimensional cluster states of length n and m can be joined together to obtain a string of entangled photons of length $n + m - 1$. With Type-II fusion gates, see Fig.1.5 (right), 2 1-dimensional cluster can be join to make a 2-dimensional cluster state, which is needed to achieve full quantum computation.

The process is non deterministic due to the need of post-selection by using the detectors at the output of the polarizing beam splitters.

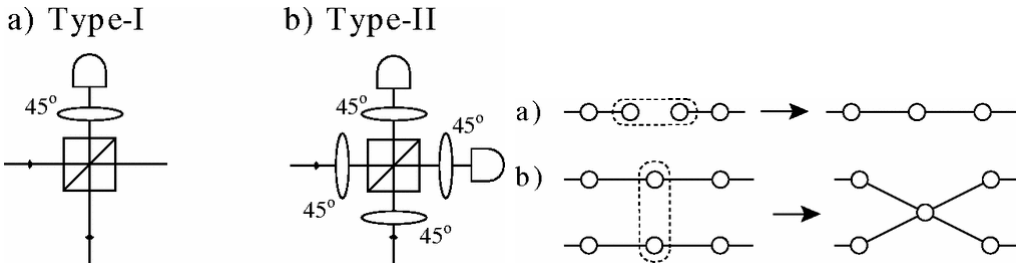


Figure 1.5: (Left) Type-I and Type-II fusion gates (Right) fusion operations between two 1-dimensional cluster states. Taken from [24]

Later in this chapter, protocols to produce deterministically cluster states using quantum dots will be reported.

Experimentally generation of 1-dimensional cluster states has been demonstrated with SPDC [25] [26], up to 12 qubits with ^{87}Rb atoms in an optical cavity [27] and with quantum dots [28] [29].

1.1.3 Decoherence

Qubits don't stay in the same state forever, they couple and interact with the surrounding environment, this interaction shows itself in the form of random noise in the wavefunction of the dot. This process is known as decoherence.

Typically three values are used to describe this loss of coherence; T_1, T_2 and T_2^*. The relation between the three time scales is:

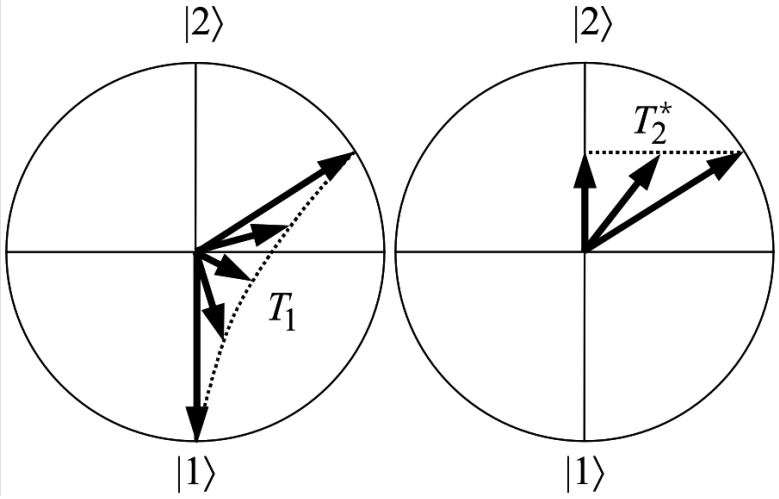


Figure 1.6: Decoherence processes visualized on a Bloch Sphere. Left, a longitudinal relaxation process. Right, a pure dephasing process. Picture adapted from [8]

$$\frac{1}{T_2} = \frac{1}{2T_1} + \frac{1}{T_2^*} \tag{1.9}$$

T_1 is the time scale of so called longitudinal relaxation process, this process involves the exchange of energy between the quantum state and environment and typically is associated with decay processes. The decay can be radiative, with emission of a photon, or non radiative, through, for example, the exchange of phonons with the surrounding environment.

T_2^* is called pure dephasing time, and describes processes in which the interaction with the environment happens through energy and population conserving processes. This can happen in scattering processes, like interaction with lattice through phonons, electric and/or magnetic fields. The interaction changes the phase of the qubit wavefunction, causing loss of coherence, but not changing the expectation value of the state population.

$\frac{1}{T_2}$ is called total dephasing rate, describes transverse relaxation process, and from Eq.1.9 we can see that it is determined by T_1 (T_2^*) for $T_2^* \gg T_1$ ($T_2^* \ll T_1$).

The different decoherence processes can be visualized on a Bloch sphere, see Fig.1.6. A pure dephasing process conserves the expectation value of the population, which is given by projecting a state on the surface of the Bloch sphere onto the vertical axis. A decay process will be visualized by a change in the projection along the vertical axis, for example passing from any state on the surface to the south pole, which corresponds to the ground state of the system.

It is worth noting, as pointed out in [8], that a decay process will also cause loss of coherence in the transverse direction, for this reason the total transverse

relaxation time depends on both the longitudinal and pure dephasing.

In the circuit model of quantum computation, gate operations have to be much faster than decoherence time. A typical upper bound for the number of operations is given by $N_{op} = T_2/T_{op}$, where T_{op} is the time taken to execute an operation.

There are several ways to limit the loss of coherence of quantum states and thus increase the decoherence time. It is known, for example that the spin scattering mechanics that are dominant in bulk III - V semiconductors are suppressed in low dimensionality structures like QD, thus increasing the spin lifetimes for quantum computing applications. Another approach is to cool down the sample to cryogenic temperatures to reduce the interaction of the QD with the phonon bath of the surrounding environment.

Population decays, both radiative and non radiative, also introduce jitter in the emission of photons, thus reducing indistinguishability, one of the key requirements for interferometric applications.

As for classical computer, error-correcting algorithms have also been developed for quantum computing to mitigate the unwanted effects of decoherence processes [30]. These algorithms usually involve the use of several extra qubits, known as ancilla, whose states are compared to the quantum register we wish to preserve. The constant supply of extra qubits in a known state is another reason why full control of a qubit and generation of entangled states are key requirements for quantum computation.

1.2 Quantum Dots

In the previous section we have discussed the requirement of qubits to implement any type of quantum computing. In general, any quantum system that meets the DiVincenzo Criteria [5] could be a suitable platform for generating a qubit, and in Tab.1.1 we have listed a few of them.

We have also discussed how single atoms could be used as qubits and to generate entangled photons through their radiative cascades. While atomic systems highlight the essential physics, practical realizations of quantum technologies often require solid-state platforms that can be engineered and scaled. In this context, semiconductor quantum dots, sometimes referred to as artificial atoms, emerge as a particularly promising candidate, offering both qubit functionality and the ability to generate entangled photons and host spin qubits.

If a semiconductor is sandwiched by another with an higher bandgap a discontinuity is generated at edges of the valence and conduction bands at the interface of the two materials.

If the lower bandgap semiconductor is thin enough then a quantum structure is produced and quantum confinement of the charge carriers along the $\hat{z}$ direction

is achieved, this is known as quantum well. If the carrier confinement is in two or three dimension then a quantum wire or quantum dot are produced.

The more a structure is confined the more discrete its energy levels available to the charge carriers become, due to a lower density of states available to them [8]. For this reason QDs, which have the strongest confinement, are characterized by discrete energy transition and are knows as artificial atoms.

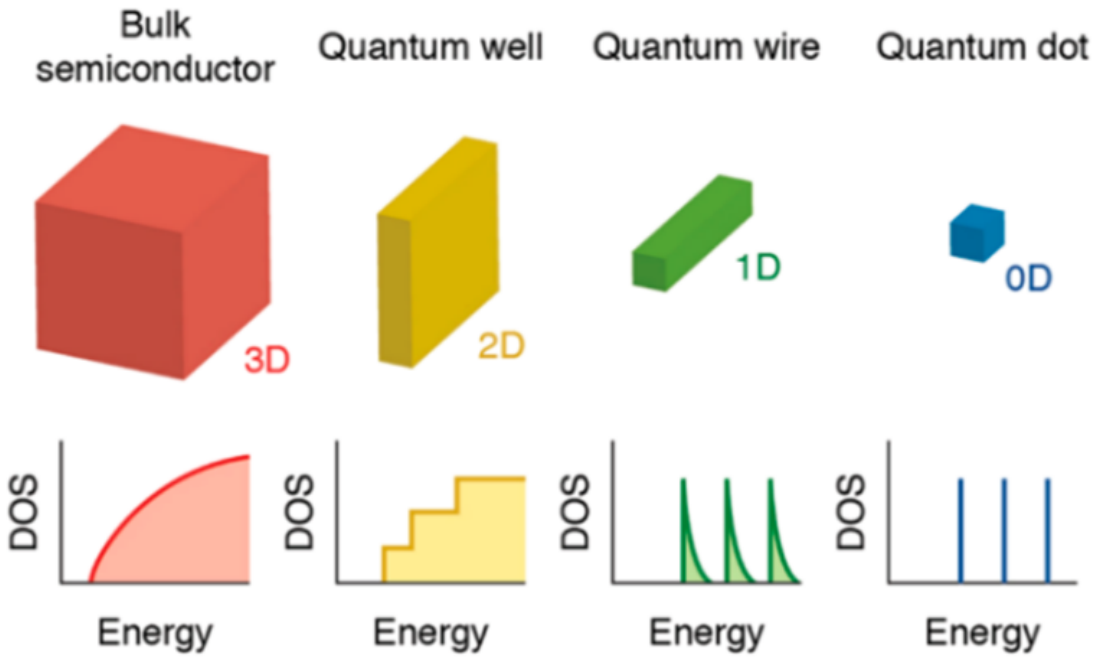


Figure 1.7: Confinement and density of states for different semiconductor structures. Taken from [31]

The most commonly used method to produce QDs for quantum optics applications is a self-assembled growth process. Epitaxy is the process that takes place when a material A is deposited (grown) on the surface of a single crystal B, called substrate.

Material A can be deposited by direct thermal evaporation of the material, in Molecular Beam Epitaxy (MBE), or it can be carried by (organic) gases and then decomposed on the surface of the substrate, in Metal Organic Vapour Phase Epitaxy (MOVPE).

Epitaxial growth of QDs generally happens through Stranski-Krastanov (SK) or droplet epitaxy methods [32].

The SK growth exploits the deformations introduced by lattice constant mismatch of two materials. For example, a thin layer of $In_xGa_{1-x}As$, known as wetting layer, is deposited on a (100) oriented $GaAs$ substrate, the lattice mismatch

will introduce strain in the wetting layer and, after reaching a critical thickness, 3D islands are formed on top of a the wetting layer to minimize the strain. A thick capping layer is then deposited on top to confine and protect the QDs.

Droplet epitaxy allows growth of QDs without the need of wetting layer. A material from group III, such as Al, Ga or In, is deposited on the substrate at a temperature above its melting point. The material forms nanometer sized droplets due to surface tension and then is exposed to a flux of material from group V, such as As, to recrystallize.

QDs formation with the processes described above is random in location and size of the QD, so post selection on QD with the desired properties has to be carried out, unless the growth process is induced in preferred sites [33] [34].

The work done during the PhD has been focused on the study of III-V QD of $GaAs$ with $Al_xGa_{1-x}As$ barriers and $In_xGa_{1-x}As$ with $GaAs$ barriers. These QD are all grown inside pyramidal recesses pre-patterned on (111)B oriented $GaAs$ wafer, more details on their fabrication process will be presented in the following chapter Chap.2.

1.2.1 Excitonic Complexes

Charge carriers in QDs can be generated by supplying energy to the sample, for example by an external electric current [35] or by pumping the sample optically with a laser. Depending on the energy of the laser compared to the QD bandgap we can have different excitation regimes, above-band, quasi-resonant and resonant excitation. In depth description of these excitation methods will be given in Chap.3.

The strong confinement and strong Coulomb interaction, due to low volume, generates bound states of electrons and holes in a QD. These states are known as excitonic states, the recombination of an electron - hole pair causes the emission of a single photon from the QD. The selection rules regulating this process and properties of the photon will be discussed later in the chapter.

The QDs are characterized by discrete energy levels and electrons and holes populate these levels according to the Pauli Exclusion Principle, which means that at most two carriers of opposing spin can populate a single level. The number of levels available to holes (electrons) in the valence (conduction) band depends on the depth of the confinement and material properties. The QDs studied in this thesis will be schematized as having one electron level available in the conduction band and two hole levels in the valance band.

If the number of bound electrons and holes of an excitonic state is the same then we have so-called neutral excitons: exciton and biexciton, for example.

If the number of bound electrons and holes of an excitonic state is not the same then we have so-called charged excitons: positive and negative trion and charged

biexciton, for example.

All the possible combinations using the three levels configuration described above are illustrated in Fig.1.8.

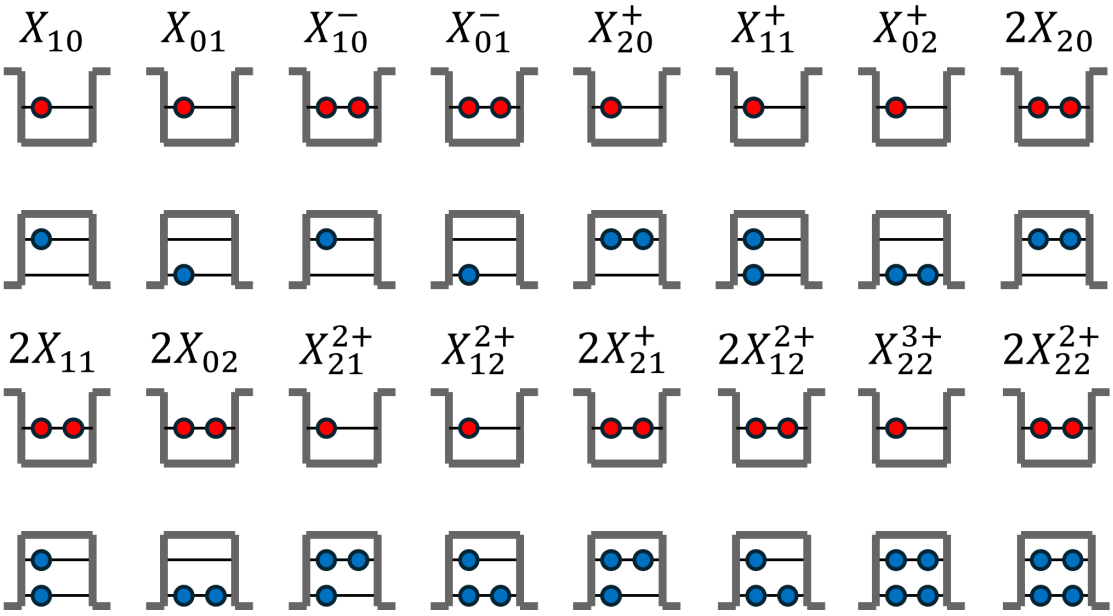


Figure 1.8: Possible charge configuration in a QD described by one electron level in the conduction band and two hole levels in the valance band.

From the diagram in Fig.1.8 we can see how the same number of charge carriers can be organized in the energy levels in different configurations, leading to several excitons and trions. To avoid confusion and unambiguously identify the excitonic state, the notation from [36] will be used to describe the optical decay of the state.

The states are identified by an X, for excitons and trions, or 2X, for biexcitons and charged biexcitons. An empty superscript will indicate a neutral complex, a n+ (n-) superscript indicates the number of excess holes (electrons). Two subscripts will indicate how many holes will populate the first and second levels in the valance band, there won't be any confusion with electrons because we assume that they only have one available level in the conduction band. A bar above the first or second subscript number will indicate the energy level of the recombining hole.

For example, a positive trion with one hole in the first energy level and one hole in the second is X_{11}^{+}, if the hole in the first (second) level recombines with the electron it will be indicated by $X_{\bar{1}1}^{+}$ ($X_{1\bar{1}}^{+}$).

Identification of a spectral line in the QD spectrum corresponds to the identification of the electron - hole pair that recombined from these different charge configurations.

1.2.1.1 Heavy/Light Holes and Selection Rules

Conduction band is characterized by a s-like symmetry. Electrons in the conduction band have a total angular momentum $J = \frac{1}{2}$ and secondary total angular momentum quantum number $J_{e,z} = \pm\frac{1}{2}$, this can be written using the Luttinger – Kohn notation as:

$$\begin{aligned} |\frac{1}{2};+\frac{1}{2}\rangle &= |S\uparrow\rangle \\ |\frac{1}{2};-\frac{1}{2}\rangle &= |S\downarrow\rangle \end{aligned} \tag{1.10}$$

Valence band has p-like symmetry. Heavy holes are characterized by $J = \frac{3}{2}$ and $J_{hh,z} = \pm\frac{3}{2}$ with X and Y orbitals. Light holes on the other hand are characterized by $J = \frac{3}{2}$ and $J_{lh,z} = \pm\frac{1}{2}$ with X, Y and Z orbitals. Using the Luttinger – Kohn notation we can write for heavy and light holes holes:

$$\begin{aligned} |\frac{3}{2};+\frac{3}{2}\rangle &= -\frac{1}{\sqrt{2}}\,|(X+iY)\Uparrow\rangle \\ |\frac{3}{2};-\frac{3}{2}\rangle &= \frac{1}{\sqrt{2}}\,|(X-iY)\Downarrow\rangle \\ |\frac{3}{2};+\frac{1}{2}\rangle &= -\frac{1}{\sqrt{6}}\,[|(X+iY)\Downarrow\rangle + 2\,|Z\Uparrow\rangle] \\ |\frac{3}{2};-\frac{1}{2}\rangle &= \frac{1}{\sqrt{6}}\,[|(X-iY)\Uparrow\rangle - 2\,|Z\Downarrow\rangle] \end{aligned} \tag{1.11}$$

Throughout this thesis we will also identify single spins of electrons with narrow arrows, $|\uparrow\rangle$ and $|\downarrow\rangle$, and holes with thick arrows, $|\Uparrow\rangle$ and $|\Downarrow\rangle$.

In bulk *GaAs* heavy and light hole band are degenerate, but, once the material is strained or quantum confined, the degeneracy is lifted and two bands split [37]. Usually the ground state of a QD exhibits heavy hole characteristics, but if the QD is strained, has reduced symmetry or interface and alloy disorder, then the ground level won't be purely heavy hole and some degree of heavy and light hole band mixing will be introduced [38]. It has also been shown experimentally that the light hole band can be promoted to ground state by straining a QD using a piezoelectric device [39].

Due to conservation of angular momentum, optical recombination between electron and heavy hole can happen only between anti-parallel spins with emission of circularly polarized photons, $\sigma^{\pm}$, if electron and heavy hole have parallel spins then the state is said to be dark.

Light holes can recombine not only with emission of $\sigma^{\pm}$ photons, between parallel spins [39], but also of π photons, linearly polarized along the $\hat{z}$ direction, when the spins are antiparallel. Because the light hole band has a Z orbital com-

ponent and dipole other than the X and Y it will emit linearly polarized light perpendicularly to the $\hat{z}$ axis, referred as growth direction, of the QD.

The selection rules for excitation and emission are illustrated in in Fig.1.9.

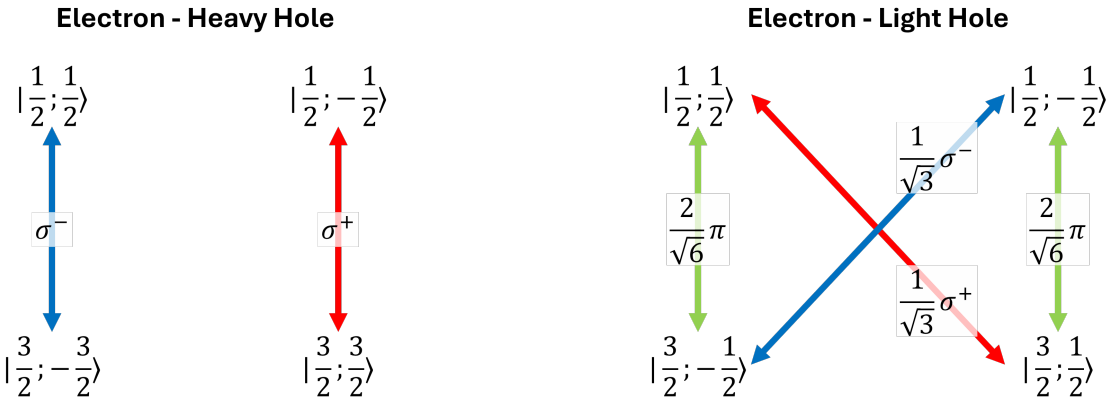


Figure 1.9: Selection rules for electron - hole recombination from different bands.

1.2.1.2 Symmetry and Point Groups

The multiplet states of a QD correspond to different spin configuration of the charges in the available energy levels. The degeneracies (or lack thereof) of these multiplet states is determined by the symmetry of the QD. The emission pattern, known as photoluminesce, PL, of the QD can therefore be a tool to probe the symmetry of its morphology and electronic band structure.

The following section reports the results of several theoretical studies of different symmetries and how they affect the polarization properties of the emission pattern of a QD [36] [40] [41] [42] [43].

Typical point group associated with QD symmetries are D_{2d}, D_{3h}, C_{3v}, C_{2v}. The symmetry operations for the above mentioned groups are [44]:

- Group D_{2d} has 2 vertical dihedral-reflection planes, 2-fold vertical rotation axis and a 2 2-fold rotation axis perpendicular to the vertical rotation axis
- Group D_{3h} has a horizontal reflection plane, 3-fold vertical rotation axis and 3 2-fold rotation axis perpendicular to vertical rotation axis
- Group C_{2v} has a 2-fold vertical rotation axis and 2 vertical mirror plane containing the vertical rotation axis
- Group C_{3v} has a 3-fold vertical rotation axis and 3 vertical mirror plane containing the vertical rotation axis

Point group C_{2v} is of particular interest because it describes the symmetry properties of QD grown in the SK mode on (001) oriented $GaAs$ substrate, which constitute a considerable amount of QD studied in literature.

Pyramidal QD grown (111)B oriented $GaAs$ on the other hand have three symmetry planes, and could belong to groups D_{3h}, C_{3v}. It has been theorized that, because of the additional plane of symmetry compared to (001) QD, they should exhibit better optical properties, like vanishing Fine Structure Splitting [41]. Theoretical calculations also show that, for QD belonging to C_{3v}, there should be no dark states for $X_{\bar{1}0}$, something which has not been observed for pyramidal QDs. This would seem to suggest that either they exhibit some characteristics of higher symmetry groups like D_{3h}, for which dark states are predicted, or the dark states doublet separation is very small and hard to resolve experimentally.

1.2.1.3 Neutral Excitons

The total angular momentum of an exciton X_{10} is given by $M = S_{e,z} + J_{hh,z}$. Therefore, there should be four possible spin configurations:

$$\begin{aligned} |\downarrow\Downarrow\rangle &\rightarrow M = -2 \\ |\uparrow\Downarrow\rangle &\rightarrow M = -1 \\ |\downarrow\Uparrow\rangle &\rightarrow M = +1 \\ |\uparrow\Uparrow\rangle &\rightarrow M = +2 \end{aligned} \tag{1.12}$$

In the absence of exchange interaction between electron and hole, the four $X_{\bar{1}0}$ states should be degenerate. States with $|M| = 2$ (parallel spins) should be dark because electron hole recombination is not permitted by the selection rules of the heavy hole band and only $|M| = 1$ should be visible in the photoluminescence spectrum of a QD, see Fig.1.9.

The exchange interaction is proportional to the integral:

$$E_{exch} \propto \int\int d^3r_1 d^3r_2 \frac{1}{|\vec{r_1}\vec{r_2}|} \Psi_X^* \left(\vec{r_e} = \vec{r_1}, \vec{r_h} = \vec{r_2}\right) \Psi_X \left(\vec{r_e} = \vec{r_2}, \vec{r_h} = \vec{r_1}\right) \tag{1.13}$$

Ψ_X is the exciton wavefunction and $\vec{r_{e/h}}$ the electron and hole coordinates. This integral can be split into two contributions. The first is a short ranged contribution caused by the probability of finding the electron and hole in the same Wigner - Seitz unit cell. The second is long ranged contribution if the two charge carriers are on different unit cells.

For QD characterized by 2-fold in plane symmetry, D_{2d} group, we can use the 4 exciton states as basis of our system and write the Hamiltonian of the exchange

interaction, due to the short ranged contribution, as [40]:

$$H = \begin{pmatrix} +\delta_0 & +\delta_1 & 0 & 0 \\ +\delta_1 & +\delta_0 & 0 & 0 \\ 0 & 0 & -\delta_0 & +\delta_2 \\ 0 & 0 & +\delta_2 & -\delta_0 \end{pmatrix} \tag{1.14}$$

with $\delta_0 = 1.5\,(a_z + 2.25 b_z)$, $\delta_1 = 0.75\,(b_x - b_y)$ and $\delta_2 = 0.75\,(b_x + b_y)$. a_z and $b_{x/y/z}$ are coupling constants and their values depends on the geometry of the QD. The degeneracy between states with $|M| = 1$ and $|M| = 2$ is now lifted by an amount δ_0.

Since the matrix is a block matrix dark and bright X_{10} do not mix. If $b_x = b_y \rightarrow \delta_1 = 0$, this means that the two states with $|M| = 1$ are eigenstates of the system and are degenerate. Under this condition $\delta_2 \neq 0$ and the two dark X_{10} states are mixed, and the other eigenstates of the system are $\frac{1}{\sqrt{2}}\,(|\uparrow\Uparrow\rangle \pm |\downarrow\Downarrow\rangle)$.

If QD symmetry is broken then $b_x \neq b_y \rightarrow \delta_1 \neq 0$, the two bright X_{10} are not eigenstates of the Hamiltonian and mix between each other. The new set of eigenstates is $\frac{1}{\sqrt{2}}\,(|\uparrow\Downarrow\rangle \pm |\downarrow\Uparrow\rangle)$ and $\frac{1}{\sqrt{2}}\,(|\uparrow\Uparrow\rangle \pm |\downarrow\Downarrow\rangle)$. Polarization of the emitted photons from recombination of bright states is linear, H and V, and they are split by δ_1.

The long ranged contribution to the exchange interaction contributes to increase the splitting between dark and bright states. In QD with symmetry lower than D_{2d} it further increases the splitting between the two bright states, without affecting the splitting of dark one. This can be included in Eq.1.14:

$$H = \begin{pmatrix} +\Delta_0 & +\Delta_1 & 0 & 0 \\ +\Delta_1 & +\Delta_0 & 0 & 0 \\ 0 & 0 & -\delta_0 & +\delta_2 \\ 0 & 0 & +\delta_2 & -\delta_0 \end{pmatrix} \tag{1.15}$$

with $\Delta_{0/1} = \delta_{0/1} + \gamma_{0/1}$. γ_0 is the contribution of the long range exchange interaction to the splitting of dark and bright states. The coefficient $\gamma_1 = \gamma_x - \gamma_y$ becomes relevant to the split of bright states only for asymmetric QD because coupling constants $\gamma_{x/y}$ have different values. In general it is assumed that $\gamma_1 \gg \delta_1$ [40]

The split between the mixed bright excitons, $\frac{1}{\sqrt{2}}\,(|\uparrow\Downarrow\rangle \pm |\downarrow\Uparrow\rangle)$ is known as Fine Structure Splitting, FSS for short.

For a QD with very low symmetry, maybe due to strain or non uniform morphology, Eq.1.15 does not describe any more the exchange interaction of the system. There is no distinction between bright and dark states, as they can mix between each other, so they are allowed to optically recombine by selection rules of the system.

Considering that light holes have $J_{lh,z} = \pm\frac{1}{2}$, a similar discussion to the one done so far can be applied to the X_{01} state. The basis is again formed by the:

$$\begin{aligned} |\uparrow\Downarrow\rangle &\rightarrow M = 0 \\ |\downarrow\Uparrow\rangle &\rightarrow M = 0 \\ |\uparrow\Uparrow\rangle &\rightarrow M = +1 \\ |\downarrow\Downarrow\rangle &\rightarrow M = -1 \end{aligned} \tag{1.16}$$

The differences with $X_{\bar{1}0}$ recombination are that now states of parallel spins should be able to recombine via emission of $\sigma^{\pm}$ photons and states with antiparallel spins should emit π photons, linearly polarized along the growth direction.

But these 4 states are not the eigenstates of a system a broken symmetry and electron hole exchange interaction. In that case the eigenstates are $\frac{1}{\sqrt{2}}(|\uparrow\Uparrow\rangle \pm |\downarrow\Downarrow\rangle)$ and $\frac{1}{\sqrt{2}}(|\uparrow\Downarrow\rangle \pm |\downarrow\Uparrow\rangle)$. The first two eigenstates with parallel spin emit then non degenerate linear polarized photons, H and V. Of the last two eigenstates, only the state $\frac{1}{\sqrt{2}}(|\uparrow\Downarrow\rangle + |\downarrow\Uparrow\rangle)$ emits a photon, linearly polarized along the $\hat{z}$ direction, the other is a dark state. Furthermore, the emission from $\frac{1}{\sqrt{2}}(|\uparrow\Downarrow\rangle + |\downarrow\Uparrow\rangle)$, due to electron and hole exchange interaction, will also be non degenerate with the two other bright eigenstates. This recombination pattern is the same for QD belonging to groups C_{3v} and D_{3h} [36]

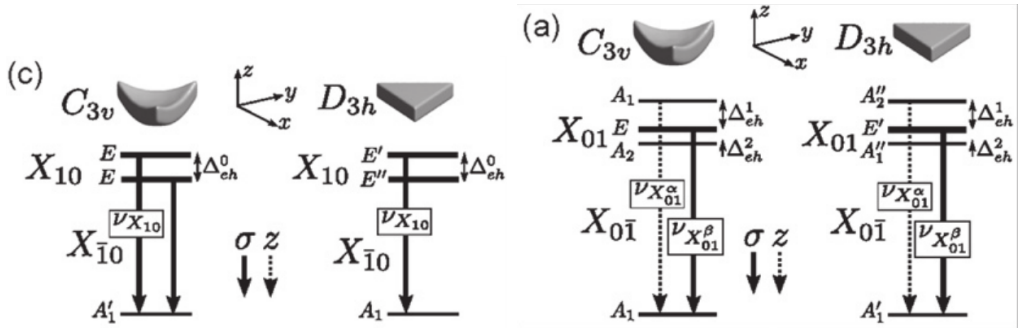


Figure 1.10: Decay of $X_{\bar{1}0}$ and $X_{0\bar{1}}$ with symmetries C_{3v} and D_{3h}. Taken from [36]

The $2X_{\bar{2}0}$ state is composed of two electron and two holes. Because all the charge carriers are in the ground state, there must be two carriers of opposing spin in each energy level, due to Pauli Exclusion Principle, $|\uparrow\downarrow\Uparrow\Downarrow\rangle$. Electrons and holes are in a singlet state and thus no exchange interaction arises between the two types of charge carriers.

Due to Coulomb interaction between the four charge carriers the energy of photons emitted in the $2X_{\bar{2}0} \rightarrow X_{\bar{1}0}$ and $X_{\bar{1}0} \rightarrow 0$ recombinations are different by an amount known as binding energy, $\Delta_B = 2\hbar\omega_X - \hbar\omega_{XX}$, where $\omega_{XX/X}$ is the

frequency of the photon emitted by $2X_{\bar{2}0}/X_{\bar{1}0}$. Binding energy can be negative or positive. In the first case the dot is said to be antibiding and the $2X_{\bar{2}0}$ has higher energy than the $X_{\bar{1}0}$, in the second the dot is binding and the $2X_{\bar{2}0}$ has lower energy than the $X_{\bar{1}0}$.

The $2X_{\bar{2}0}$ recombines to the $X_{\bar{1}0}$, for this reason it is a doublet state with linear polarization with a split equal to the FSS.

If the QD symmetry is further broken to C_{2v} the recombination pattern of $2X_{20}$ is complicated further. Calculations from [36] show that even the $X_{\bar{1}0}$ should show a linearly polarized component along the $\hat{z}$ direction, see Fig.1.11.

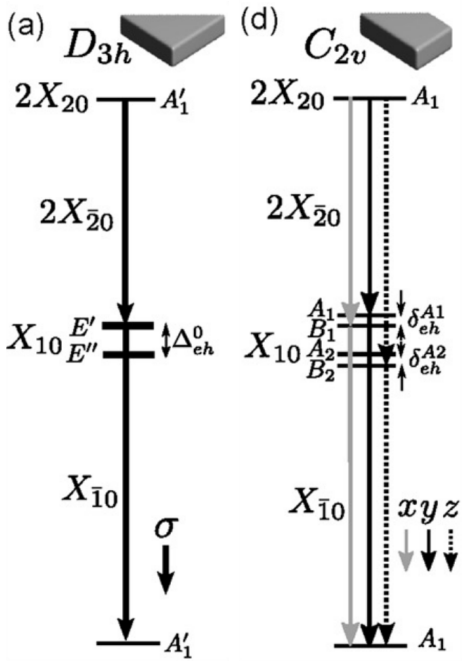


Figure 1.11: Recombination cascade for $2X_{\bar{2}0}$ for D_{3h} and C_{2v} symmetries. Linearly polarized along the $\hat{z}$ direction emission from $X_{\bar{1}0}$ recombination is predicted in C_{2v} symmetry. Taken from [36]

In the QD level scheme that we are considering, see Fig.1.8, only holes can be in excited states.

For this reason the only way that a neutral biexciton can have carrier in the excited states is in the $2X_{11}$ configuration. The electrons fill their only available energy level in a singlet state, therefore electron hole exchange interaction is switched off. On the other hand, hole hole exchange interaction, between the two holes in different levels, splits $2X_{11}$ in two non degenerate transitions. If recombination happens from the light (heavy) hole band then $2X_{1\bar{1}} \rightarrow X_{10}$ ($2X_{\bar{1}1} \rightarrow X_{01}$).

The decay pattern of X_{11} in C_{3v} symmetry is predicted to show up to 16

transitions. Elevating the symmetry of the QD to D_{3h} simplifies the emission pattern by halving the number of transitions [36].

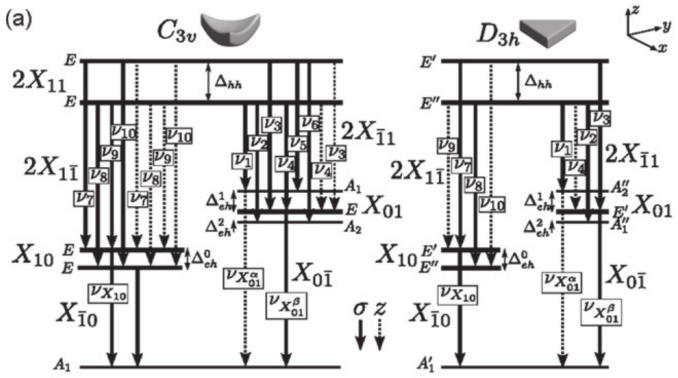


Figure 1.12: Decay of $2X_{\bar{1}1}$ and $2X_{1\bar{1}}$ with symmetries C_{3v} and D_{3h}. Taken from [36]

Breaking the symmetry to C_{2v} will increase the number of possible transitions and split them in linearly polarized, see Fig.1.13.

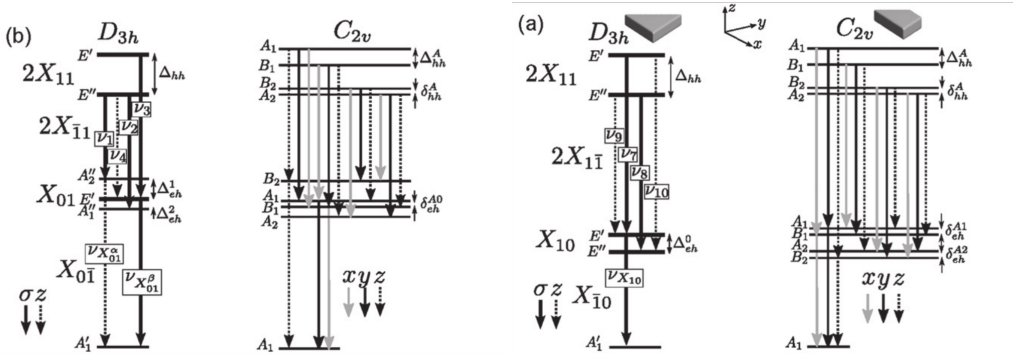


Figure 1.13: Decay of $2X_{\bar{1}1}$ (left side) and $2X_{1\bar{1}}$ (right side) with symmetries D_{3h} and C_{2h}. Taken from [36]

1.2.1.4 Charged Excitons

Positive and negative trions, in their ground states, have two carriers of the same sign in a singlet state, therefore there will be no exchange interaction between the charges of opposing sign. The minority charge, hole for negative or electron for positive trions, can have two spin states and so in the absence of magnetic field the state is doubly degenerate. For QD belonging to C_{2v}, C_{3v}, D_{2d} and D_{3h} groups the strict selection rules shown in Fig.1.9 apply.

The same discussion is valid for a singly charged exciton with the minority carrier in the excited state, for example X^{-}_{01}, and the state can additionally recombine with the emission of a photon linearly polarized along the growth direction.

As for the $2X_{11}$, in the considered QD levels scheme, only positive trions can have the extra majority charge carrier in the excited state, X^{+}_{11}, and it decays to single hole state $X^{+}_{1\bar{1}} \rightarrow lh$ or $X^{+}_{11} \rightarrow hh$. Unlike $2X_{11}$ here the states are further split by the electron hole exchange interaction.

The decay scheme for $X^{+}_{1\bar{1}}$ is the same for C_{3v} and D_{3v}, the spectra is characterized by two circularly polarized transitions and two linearly polarized along the growth direction. These four lines are doubly degenerate due to the possibility of the electron spin to be $\uparrow$ or $\downarrow$. A breaking of the QD symmetry to C_{2v} group would cause the split between the four states to increase each transition line of the spectra to split in three x, y, z polarized transitions, see Fig.1.14.

On the other hand the spectra of $X^{+}_{1\bar{1}}$ passes from 6 bright lines in C_{3v} group to 4 in D_{3h}.

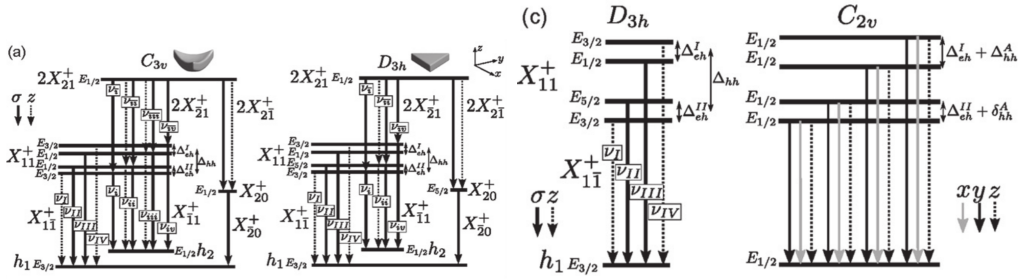


Figure 1.14: Recombination cascade of $2X^{+}_{\bar{2}1}$ (left side) and $2X^{+}_{11}$ (right side) with symmetries C_{3v}, D_{3h} and C_{2h}. Taken from [36]

Therefore the experimental spectra of the $2X_{11}$ and X^{+}_{11} states can be used to probe the actual symmetry of the QD.

1.2.2 Decoherence

The coupling of QDs to the surrounding environment can be beneficial, in the case of the ability to populate the QD with a desired state, or detrimental, loss of coherence of the desired state.

For example, in the previous section we have seen that excitonic states upon recombination emit a photon, if our goal is to store information in the QD using such bound state, the recombination can be seen as a transverse decoherence process due to the spontaneous emission. The timescale of the decoherence is then set by the radiative lifetime. Transverse decoherence of a state can also happen

non radiatively, for example in the case of an excited states that relaxes to ground state through the emission of lattice vibrations, known as phonons.

Charge carrier fluctuations in the QD also lead to noise in the local electric field, which shifts the emission wavelength and linewidth of the transition of the state due to the DC Stark effect. If the goal is to have indistinguishable photons for interferometry applications then this kind noise needs to be limited, for this reason above-band excitation with a CW laser may not be an efficient way to populated the QD, due to the several different bound states that are continuously populated from free charges going to the QD from the other layers of the sample. An excitation pulse with an energy tuned to the desired transition is then a more correct approach.

Another source of noise is the loss of phase of spin states that interact with the random magnetic field generated by the nuclear spins of the material via hyperfine interaction. The nuclear spins are usually randomly aligned, but over short timescales the effective magnetic field can be of a few mT [37], this field is known as Overhauser field.

The interaction of electron spins with nuclear spins is described by the Fermi contact hyperfine interaction:

$$H_{hf}^{e} = \Omega \sum_{j=1}^{N} A_{e}^{j} |\Psi_{e}\left(\vec{R}_{j}\right)|^{2} \vec{I}^{j} \cdot \vec{S} \tag{1.17}$$

Ω is the unit cell volume, A_j^e the coupling coefficient, Ψ_e the electron envelope wavefunction, $\vec{S}$ the electron spin, $\vec{I}$ the nuclear spin and $\vec{R}$ the position vector. The sum runs over all the nuclei, and for QD typically $N \sim 10^5$.

For electrons pure dephasing times, T_2^*, have been estimated to be $\sim 1ns$ [45].

Heavy holes, on the other hand, have no Fermi contact interaction, but interact with the nuclear spins through the dipole - dipole interaction:

$$H_{hf}^{HH} = \Omega \sum_{j=1}^{N} A_{h,z}^{j} |\Psi_{h}\left(\vec{R}_{j}\right)|^{2} I_{z}^{j} S_{z} \tag{1.18}$$

heavy holes are then influenced only by the $\hat{z}$ component of the Overhauser field, the coupling constant is usually smaller than the electron coupling constant [46].

Any mixing between light and heavy hole bands will complicate the spin - nuclei interaction and lead to an Hamiltonian with in plane coupling as well

$$H_{hf}^{h} = \Omega \sum_{j=1}^{N} |\Psi_{h}\left(\vec{R}_{j}\right)|^{2} \vec{A}_{h}^{j} \cdot \vec{I}^{j} \cdot \vec{S}^{j} \tag{1.19}$$

Given the multiple effects taking place in the decoherence dynamics of bound excitonic states, it is difficult to associate a dephasing process only or mostly to electrons or holes, and sometimes fluctuations in the charge noise and electric field have much stronger effect than the hyperfine interaction.

In theory, it is possible to switch off the heavy hole - nuclear spin interaction by applying a counteracting field along the $\hat{z}$ direction [46], but this can happen only for pure heavy hole band with no light hole mixing.

Decoherence times can be increased by using the spin echo technique [47]. The QD is placed in a strong magnetic field, $B_{ext} = 4T$ in the Voigt geometry, that removed the degeneracy from the states $|\uparrow\rangle/|\downarrow\rangle$ and $|\uparrow\downarrow\Uparrow\rangle/|\downarrow\uparrow\Downarrow\rangle$. Dephasing of the precession between the two spin states $|\uparrow\rangle$ and $|\downarrow\rangle$ is increased to μs by applying a series of delayed pulses to the excitation scheme. The first pulse, $\pi/2$, sets the state in a superposition state of $|\uparrow\rangle$ and $|\downarrow\rangle$. The state is then left to freely dephase, at a delay T a second pulse, π, refocuses the state by reversing the depahsing, and then after another delay T the second $\pi/2$ pulse prepares the QD for the readout of the transition $|\downarrow\uparrow\Downarrow\rangle \rightarrow |\uparrow\rangle$.

In [48] the authors study the dephasing dynamics of electron, hole, positive and negative trion and dark exciton from the same QD. Generation of Overhauser field is a avoided, without applying any external field, by pumping the sample with linear polarized light. Under these conditions, the QD spin is not initialized deterministically, like it would happen by exciting with circular polarization, but probabilistically because the desired circular polarized transition is post-selected from the first emitted photon.

1.2.3 Entanglement

As stated in the previous section, entangled photons are a necessary resource for several quantum computing and information tasks. Entangled photons can be generated by QD in the $2X_{\bar{2}0} - X_{\bar{1}0}$ cascade as suggested in [49].

Due to selection rules $2X_{\bar{2}0}$ state can't optically recombine directly to the ground state, its recombination to ground state is a two step process with an intermediate single exciton state. A first electron - hole couple with $M = +1$ ($M = -1$) can recombine and will emit a right (left) circularly polarized photon, L (σ^+). The QD is then left populated by a $X_{\bar{1}0}$ state with $M = -1$ ($M = +1$), and upon recombination the QD will emit a left (right) polarized photon, R (L).

The two photon state is then a maximally entangled Bell pair:

$$\Psi^+ = \frac{1}{\sqrt{2}} \left(|L_{2X_{\bar{2}0}} R_{X_{\bar{1}0}}\rangle + |R_{2X_{\bar{2}0}} L_{X_{\bar{1}0}}\rangle \right) \tag{1.20}$$

The entangled state can be rewritten in linear and diagonal bases by using the

following equivalences:

$$\begin{aligned} |H\rangle &= \frac{1}{\sqrt{2}}\left(|R\rangle + |L\rangle\right) \\ |V\rangle &= \frac{i}{\sqrt{2}}\left(|L\rangle - |R\rangle\right) \\ \Psi^{+} &= \frac{1}{\sqrt{2}}\left(|LR\rangle + |RL\rangle\right) = \frac{1}{\sqrt{2}}\left(|HH\rangle + |VV\rangle\right) \end{aligned} \tag{1.21}$$

$$\begin{aligned} |D\rangle &= \frac{1}{\sqrt{2}}\left(|H\rangle + |V\rangle\right) \\ |A\rangle &= \frac{1}{\sqrt{2}}\left(|H\rangle - |V\rangle\right) \\ \Psi^{+} &= \frac{1}{\sqrt{2}}\left(|LR\rangle + |RL\rangle\right) = \frac{1}{\sqrt{2}}\left(|DD\rangle + |AA\rangle\right) \end{aligned} \tag{1.22}$$

The process described above happens only in perfect symmetrical QD because the two $X_{\bar{1}0}$ state are degenerate and without measuring the polarization of the two photons we can't distinguish which set of electron - hole couples recombined. The absence of FSS is very rare for QDs and implies that great effort needs to be put in post-selection of QDs.

If the degeneracy is lifted because of defects or strain, the two X_{10} states won't have the same energy and they will be separated by the FSS. Thus after the first electron hole couple in the X_{20} state recombines it will emit a linearly polarized state and the QD will be left in entangled state $\frac{1}{\sqrt{2}}\left(|H_{2X_{20}}X_H\rangle + |V_{2X_{20}}X_V\rangle\right)$. The QD is left populated in a superposition of the X_H and X_V, but because the two states are at different energy they will precess and develop a phase difference over time. After a certain time τ the exciton will recombine and emit another photon. The two photon state is then $\frac{1}{\sqrt{2}}\left(|H_{2X_{20}}H_{X_{10}}\rangle + e^{iFSS\tau/\hbar}\,|V_{2X_{20}}V_{X_{10}}\rangle\right)$.

This state is still an entangled state, but τ is a variable delay which depends on the radiative lifetime of the exciton state. Since entanglement is measured not on the single photon pair but over many recombination cycles, the total emission of entangled photon pairs is then given by the integral over all the possible delays between the two photons. The averaged state is then mixed and the entanglement washed out.

The dependence of the phase term on the FSS implies that QD with small, ideally $0\mu eV$, FSS would be good candidates for entangled photons emission. Entangled photons can also be post selected by gating the detection to a fixed delay τ, in this way the other Bell states, Eq.1.2, can be generated as well. This method greatly reduces the intensity of entangled pairs.

Developing QDs with negligible FSS is the preferred approach, and it has been pursued by changing the QD materials, from strained $InGaAs$ to unstrained $GaAs$,

or by compensating the FSS through the use of an in plane magnetic field [50] of electric field [51], or strain applied via a piezoelectric device [52].

Some limitations are still present due to the nature of the cascade. The lifetime of the exciton puts a lower bound on the photon indistinguishability emitted from different recombination cascades and introduces jitter in the generation process of entangled photon pairs [53].

QDs can also be used to generate cluster states according to a proposal by Lindner and Rudolph [54].

The QD is placed in a magnetic field of strength B along the y direction, in plane with the QD.

Let's suppose that the QD is populated by a hole in the super position state $\frac{1}{\sqrt{2}}(|\Uparrow\rangle + |\Downarrow\rangle)$ at time $t = 0s$. We excite the system with a linearly polarized laser pulse, $H = R+L$, tuned to the transition energy of the trion state. Since the states $|\uparrow\Uparrow\Downarrow\rangle$ and $|\downarrow\Uparrow\Downarrow\rangle$ are degenerate the QD will now be populated in a superposition state of the two trion spin configuration, $\frac{1}{\sqrt{2}}(|\uparrow\Uparrow\Downarrow\rangle + |\downarrow\Uparrow\Downarrow\rangle)$.

Electron - hole recombination will result in emission of a circularly polarized photon, the charge carrier - photon state is then a maximally entangled Bell pair, $\frac{1}{\sqrt{2}}(|\Uparrow R_1\rangle + |\Downarrow L_1\rangle)$.

The magnetic field induces spin precession with frequency $\omega_B = g_{e/h}\mu B/\hbar$, for this reason after a time $T = \pi/(2\omega_B)$ the state will evolve into

$$\frac{1}{2}(|\Uparrow + \Downarrow, L_1\rangle + |- \Uparrow + \Downarrow, R_1\rangle) \tag{1.23}$$

By timing the following excitation pulse to the period of spin precession and waiting for the recombination we obtain the state:

$$\frac{1}{2}(|\Uparrow, L_1, L_2\rangle + |\Downarrow, L_1, R_2\rangle - |\Uparrow, R_1, L_2\rangle + |\Downarrow, R_1, R_2\rangle) \tag{1.24}$$

Under the convention $|0\rangle = |L\rangle / |\Uparrow\rangle$, $|1\rangle = |R\rangle / |\Downarrow\rangle$ we can see that this is equivalent to a 3 qubit cluster state.

Repetition of the timed excitation and recombination cycle will generate a string of entangled photons and thus a one-dimensional/linear cluster state. It is interesting to note that the same procedure, but π rotations, will generate GHZ entangled states.

Care must be taken in setting the strength B of the magnetic field, the trion state has a lifetime τ which means that the magnetic field will induce precession of the uncoupled charge carrier as well, due to its non zero spin projection along the magnetic field axis. This unwanted precession will introduce errors on the spin. Stronger fields increase the error probability because the uncoupled charge carrier can precess more during the lifetime of the trion. It has been shown anyway that a value $B \ll 1/\left(g_{e/h}\mu B\tau\right)$ is enough to mitigate the issue [54].

1-dimensional cluster states with QD have been generated by Cogan and Gershoni [28] and Senellart group [29].

In the first paper, the QD has been initialized by tuning a laser to one of the positive trion excited states, in which the electron is in the second energy level. A fast non radiative decay populates the ground trion state, X_{20}^{+}. The non radiative decay needs to be as fast as possible to increase the indistinguishability of the emitted photons, as demonstrated previously by the same group in another paper. The generation rate of entangled photons in $0.5GHz$. Despite the very high rate of generation the procedure is limited by a low extraction efficiency, due to the lack of integration of the QD in a photonic structure needed to boost extraction efficiency.

In the second paper the laser is slightly detuned from the trion transition and the state is populated through phonon assisted excitation. A three photon correlation measurement is used to characterize the entangled state. The first photon emitted by the QD is measured on a circularly polarized base to project the spin to the $\uparrow$ or $\downarrow$, this is done because at time $t = 0s$ the spin is in a statistical mixture of $\uparrow$ and $\downarrow$ and to generate a cluster state it needs to be initialized to a known. The following two photons are measured on a linear or circular base depending on the delay of the third pulse. Initially the delays between the three pulses are set to be the same, $t_{23} = t_{12}$, to generate $\frac{1}{\sqrt{2}}(-i\,|\uparrow, V_2, R_3\rangle + |\downarrow, H_2, L_3\rangle)$. This is a 3 qubit linear cluster state, equivalent to a 3 qubit GHZ state.

1.3 Conclusions

In this chapter we presented the concept of quantum computing and its realisation with the quantum gates or one-way quantum computing approaches. We have introduced the concept of entanglement and several entangled states, Bell pairs, GHZ and cluster states.

We have seen how Bell pairs and GHZ states are ideal for QKD applications, therefore a platform that can generate entangled states on demand by exploiting some non linear property is a very convenient platform to implement quantum computing.

We have highlighted the advantages of the one-way quantum computer approach over the circuit model. The first shifts the complexity from multi-qubit operation to the creation of a complex entangled state, a cluster state, and is more resilient to qubit loss. Bidimensional cluster states are required to be be able to implement general quantum computation. Deterministic linear cluster states are of huge interest for the quantum computing community, even though by themselves they do not allow for general quantum computing, they can be fused with the use of fusion gates to generate probabilistic bidimensional cluster states, see

Fig.1.5.

We have explained decoherence of a qubit state, how it affects quantum computing and how it can be mitigated in certain scenarios.

We have introduced photons and devices based on semiconductors as promising platforms for implementation of quantum computing. Polarization of a photon can be used as qubit and the weak interaction among photons is beneficial to limit the unwanted effects of decoherence. Semiconductor devices let us convert quantum states of spins to quantum states of photons and can be optically or electronically triggered to generate on demand qubit states. The knowledge of fabrication and processing techniques built by the scientific and industrial community over the decades of device development also allows for great flexibility and customizability of such devices.

Later in the chapter we focused on a particular type of semiconductor devices, quantum dots. We presented QDs as single and entangled photon emitters, demonstrated how the optical properties of the QD depend on its geometry and explained the different selection rules for the optical recombination of exciton complexes that can populate QDs. We have also shown how the spectrum of a QD and its polarization properties can be used as a fingerprint of the QD and its symmetry. We have discussed how QDs can be used as Bell pair emitters, by exploiting the non-linear properties of the QD in its $2X_{\bar{2}0} \rightarrow X_{\bar{1}0}$ cascade. We have discussed how the FSS is detrimental to the average entanglement, therefore development of QDs with small FSS is of great interest for the community. We will see in the following chapters how we were able to engineer QDs with small FSS thanks to epitaxial growth processes or to compensate the FSS with external devices.

Lastly we discussed, how according to the Lindner and Rudolph protocol [54], QDs are a suitable platform for the generation of linear cluster states, by exploiting the precession of a single charge carrier in a weak magnetic field and the photon - charge entanglement. As previously mentioned, the ability to generate linear cluster states is of great relevance for quantum computing. Optically or electronically triggering the QD trion emission will allow the researcher to have a stream of entangled photons entangled to the hole left in the QD. Simple one-qubit measurement on the photons will let us manipulate the cluster state. Characterization of cluster states requires high photon throughput from the sample and long coherence times of the hole.

In summary, for quantum computing applications the most relevant photonic resources are high-fidelity, on-demand polarization-entangled photon pairs and, ultimately, linear cluster states that can be fused into two-dimensional cluster states. These photons must be indistinguishable, bright, and coherent to allow scaling in quantum circuits. While QDs naturally provide cascaded emission that can generate Bell pairs, achieving the required quality demands reducing or compensating

the fine-structure splitting. Furthermore, QDs uniquely enable deterministic generation of linear cluster states via the Lindner–Rudolph protocol, provided that long coherence times and high photon extraction are achieved. Thus, although as-grown QDs do not yet meet all the requirements, engineering through epitaxial growth, strain, or external fields can bring them into the regime needed for scalable quantum photonics.

References

[1] R. P. Feynman. "Simulating physics with computers". In: *International Journal of Theoretical Physics* 21 (6 June 1982). DOI: 10.1007/BF02650179.

[2] P.W. Shor. "Algorithms for quantum computation: discrete logarithms and factoring". In: *Proceedings 35th Annual Symposium on Foundations of Computer Science*. 1994, pp. 124–134. DOI: 10.1109/SFCS.1994.365700.

[3] L. K. Grover. "A fast quantum mechanical algorithm for database search". In: *Proceedings of the Twenty-Eighth Annual ACM Symposium on Theory of Computing*. Association for Computing Machinery, 1996, pp. 212–219. DOI: 10.1145/237814.237866.

[4] C. H. Bennett and G. Brassard. "Quantum cryptography: Public key distribution and coin tossing". In: *Theoretical Computer Science* 560 (2014). DOI: https://doi.org/10.1016/j.tcs.2014.05.025.

[5] David P. DiVincenzo. "The Physical Implementation of Quantum Computation". In: *Fortschritte der Physik* 48.9-11 (2000). DOI: https://doi.org/10.1002/1521-3978(200009)48:9/11<771::AID-PROP771>3.0.CO;2-E.

[6] R. Raussendorf, D. E. Browne, and H. J. Briegel. "Measurement-based quantum computation on cluster states". In: *Phys. Rev. A* 68 (2 Aug. 2003). DOI: 10.1103/PhysRevA.68.022312.

[7] D. Deutsch. "Quantum theory, the Church–Turing principle and the universal quantum computer". In: *Proc. R. Soc. Lond. A* 400 (1818 July 1985). DOI: 10.1098/rspa.1985.0070.

[8] M. Fox. "Quantum Optics: An Introduction". In: Oxford University Press, Apr. 2006. ISBN: 9780198566724. DOI: 10.1093/oso/9780198566724.003.0001.

[9] D. Deutsch and R. Jozsa. "Rapid solution of problems by quantum computation". In: *Proc. R. Soc. Lond. A* 439 (1907 Dec. 1992). DOI: 10.1098/rspa.1992.0167.

[10] D. J. Griffiths. *Introduction to Quantum Mechanics*. Pearson Education, 1995. DOI: https://doi.org/10.1017/9781316995433.

[11] A. K. Ekert. "Quantum cryptography based on Bell's theorem". In: *Phys. Rev. Lett.* 67 (6 Aug. 1991). DOI: 10.1103/PhysRevLett.67.661.

[12] C. H. Bennett, G. Brassard, and N. D. Mermin. "Quantum cryptography without Bell's theorem". In: *Phys. Rev. Lett.* 68 (5 Feb. 1992). DOI: 10.1103/PhysRevLett.68.557.

[13] A. Barenco et al. "Elementary gates for quantum computation". In: *Phys. Rev. A* 52 (5 Nov. 1995). DOI: 10.1103/PhysRevA.52.3457.

[14] J.B. Altepeter, E.R. Jeffrey, and P.G. Kwiat. "Photonic State Tomography". In: vol. 52. Academic Press, 2005. DOI: https://doi.org/10.1016/S1049-250X(05)52003-2.

[15] A. Einstein, B. Podolsky, and N. Rosen. "Can Quantum-Mechanical Description of Physical Reality Be Considered Complete?" In: *Phys. Rev.* 47 (10 May 1935). DOI: 10.1103/PhysRev.47.777.

[16] D. M. Greenberger, Mi. A. Horne, and A. Zeilinger. *Going Beyond Bell's Theorem*. 1989. DOI: 10.48550/arXiv.0712.0921.

[17] C. H. Bennett et al. "Teleporting an unknown quantum state via dual classical and Einstein-Podolsky-Rosen channels". In: *Phys. Rev. Lett.* 70 (13 Mar. 1993). DOI: 10.1103/PhysRevLett.70.1895.

[18] C. A. Kocher and E. D. Commins. "Polarization Correlation of Photons Emitted in an Atomic Cascade". In: *Phys. Rev. Lett.* 18 (15 Apr. 1967). DOI: 10.1103/PhysRevLett.18.575.

[19] A. Aspect, P. Grangier, and G. Roger. "Experimental Tests of Realistic Local Theories via Bell's Theorem". In: *Phys. Rev. Lett.* 47 (7 Aug. 1981). DOI: 10.1103/PhysRevLett.47.460.

[20] P. G. Kwiat et al. "New High-Intensity Source of Polarization-Entangled Photon Pairs". In: *Phys. Rev. Lett.* 75 (24 Dec. 1995). DOI: 10.1103/PhysRevLett.75.4337.

[21] H. J. Briegel and R. Raussendorf. "Persistent Entanglement in Arrays of Interacting Particles". In: *Phys. Rev. Lett.* 86 (5 Jan. 2001). DOI: 10.1103/PhysRevLett.86.910.

[22] M. A. Nielsen. "Cluster-state quantum computation". In: *Reports on Mathematical Physics* 57 (Feb. 2006). DOI: 10.1016/s0034-4877(06)80014-5.

[23] Robert Raussendorf and Hans J. Briegel. "A One-Way Quantum Computer". In: *Phys. Rev. Lett.* 86 (22 May 2001). DOI: 10.1103/PhysRevLett.86.5188.

[24] D. E. Browne and T. Rudolph. "Resource-Efficient Linear Optical Quantum Computation". In: *Phys. Rev. Lett.* 95 (1 June 2005). DOI: 10.1103/PhysRevLett.95.010501.

[25] P. Walther et al. "Experimental one-way quantum computing". In: *Nature* 434 (7030 Mar. 2005). DOI: 10.1038/nature03347.

[26] W.-B. Gao et al. "Experimental Realization of a Controlled-NOT Gate with Four-Photon Six-Qubit Cluster States". In: *Phys. Rev. Lett.* 104 (2 Jan. 2010). DOI: 10.1103/PhysRevLett.104.020501.

[27] P. Thomas et al. "Experimental Realization of a Controlled-NOT Gate with Four-Photon Six-Qubit Cluster States". In: *Nature* 608 (7924 Aug. 2022). DOI: 10.1038/s41586-022-04987-5.

[28] D. Cogan et al. "Deterministic generation of indistinguishable photons in a cluster state". In: *Nature Photonics* 17 (4 Apr. 2023). DOI: 10.1038/s41566-022-01152-2.

[29] N. Coste et al. "High-rate entanglement between a semiconductor spin and indistinguishable photons". In: *Nature Photonics* 17 (7 July 2023). DOI: https://doi.org/10.1038/s41566-023-01186-0.

[30] Peter W. Shor. "Scheme for reducing decoherence in quantum computer memory". In: *Phys. Rev. A* 52 (4 Oct. 1995). DOI: 10.1103/PhysRevA.52.R2493.

[31] S. Busatto and C. Donega. "Magic-Size Semiconductor Nanostructures: Where Does the Magic Come from?" In: *ACS Materials Au* 2 (Jan. 2022). DOI: 10.1021/acsmaterialsau.1c00075.

[32] E. Pelucchi. "On the multifaceted journey for the invention of epitaxial quantum dots". In: *Progress in Crystal Growth and Characterization of Materials* 69.2 (2023). DOI: https://doi.org/10.1016/j.pcrysgrow.2023.100603.

[33] K. D. Jöns et al. "Triggered Indistinguishable Single Photons with Narrow Line Widths from Site-Controlled Quantum Dots". In: *Nano Letters* 13.1 (2013). DOI: 10.1021/nl303668z.

[34] D. Dalacu et al. "Directed self-assembly of single quantum dots for telecommunication wavelength optical devices". In: *Laser & Photonics Reviews* 4.2 (2010). DOI: 10.1002/lpor.200810077.

[35] A. J. Bennett et al. "Microcavity single-photon-emitting diode". In: *Applied Physics Letters* 86.18 (Apr. 2005). DOI: 10.1063/1.1921332.

[36] K. F. Karlsson et al. "Spectral signatures of high-symmetry quantum dots and effects of symmetry breaking". In: *New Journal of Physics* 17.10 (Oct. 2015). DOI: 10.1088/1367-2630/17/10/103017.

[37] E. Clarke, E. Harbord, and R. Murray. "Carrier spin dynamics in self-assembled quantum dots". In: *Optical Generation and Control of Quantum Coherence in Semiconductor Nanostructures*. Springer Berlin Heidelberg, 2010. DOI: 10.1007/978-3-642-12491-4_4.

[38] J.-W. Luo, G. Bester, and A. Zunger. "Supercoupling between heavy-hole and light-hole states in nanostructures". In: *Phys. Rev. B* 92 (16 Oct. 2015). DOI: 10.1103/PhysRevB.92.165301.

[39] Y. H. Huo et al. "A light-hole exciton in a quantum dot". In: *Nature Physics* 10.1 (Jan. 2014). DOI: 10.1038/nphys2799.

[40] M. Bayer et al. "Fine structure of neutral and charged excitons in self-assembled In(Ga)As/(Al)GaAs quantum dots". In: *Phys. Rev. B* 65 (19 May 2002). DOI: 10.1103/PhysRevB.65.195315.

[41] K. F. Karlsson et al. "Fine structure of exciton complexes in high-symmetry quantum dots: Effects of symmetry breaking and symmetry elevation". In: *Phys. Rev. B* 81 (16 Apr. 2010). DOI: 10.1103/PhysRevB.81.161307.

[42] R. Singh and G. Bester. "Nanowire Quantum Dots as an Ideal Source of Entangled Photon Pairs". In: *Phys. Rev. Lett.* 103 (6 Aug. 2009). DOI: 10.1103/PhysRevLett.103.063601.

[43] G. Bester and A. Zunger. "Cylindrically shaped zinc-blende semiconductor quantum dots do not have cylindrical symmetry: Atomistic symmetry, atomic relaxation, and piezoelectric effects". In: *Phys. Rev. B* 71 (4 Jan. 2005). DOI: 10.1103/PhysRevB.71.045318.

[44] P. W. Atkins and R. S. Friedman. *Molecular Quantum Mechanics*. OUP Oxford, 2011. ISBN: 9780199541423.

[45] R. J. Warburton. "A Self-assembled Quantum Dot as Single Photon Source and Spin Qubit: Charge Noise and Spin Noise". In: Springer International Publishing, 2017. DOI: 10.1007/978-3-319-56378-7_9.

[46] J. Fischer et al. "Spin decoherence of a heavy hole coupled to nuclear spins in a quantum dot". In: *Phys. Rev. B* 78 (15 Oct. 2008). DOI: 10.1103/PhysRevB.78.155329.

[47] D. Press et al. "Ultrafast optical spin echo in a single quantum dot". In: *Nature Photonics* 4 (6 June 2010). DOI: 10.1038/nphoton.2010.83.

[48] D. Cogan et al. "Depolarization of Electronic Spin Qubits Confined in Semiconductor Quantum Dots". In: *Phys. Rev. X* 8 (4 Dec. 2018). DOI: 10.1103/PhysRevX.8.041050.

[49] O. Benson et al. "Regulated and Entangled Photons from a Single Quantum Dot". In: *Phys. Rev. Lett.* 84 (11 Mar. 2000). DOI: 10.1103/PhysRevLett.84.2513.

[50] R. M. Stevenson et al. "A semiconductor source of triggered entangled photon pairs". In: *Nature* 439 (7073 Jan. 2006). DOI: 10.1038/nature04446.

[51] R. Trotta et al. "Universal Recovery of the Energy-Level Degeneracy of Bright Excitons in InGaAs Quantum Dots without a Structure Symmetry". In: *Phys. Rev. Lett.* 109 (14 Oct. 2012). DOI: 10.1103/PhysRevLett.109.147401.

[52] M. B. Rota et al. "A source of entangled photons based on a cavity-enhanced and strain-tuned GaAs quantum dot". In: *eLight* 4 (1 July 2024). DOI: 10.1186/s43593-024-00072-8.

[53] E. Schöll et al. "Crux of Using the Cascaded Emission of a Three-Level Quantum Ladder System to Generate Indistinguishable Photons". In: *Phys. Rev. Lett.* 125 (23 Dec. 2020). DOI: 10.1103/PhysRevLett.125.233605.

[54] N. H. Lindner and T. Rudolph. "Proposal for Pulsed On-Demand Sources of Photonic Cluster State Strings". In: *Phys. Rev. Lett.* 103 (11 Sept. 2009). DOI: 10.1103/PhysRevLett.103.113602.

Chapter 2

Pyramidal Site-Controlled Quantum Dots and Experimental Techniques

In Chap.1 an overview of quantum computing was given. QDs were introduced as a suitable source of entangled photons to generate cluster states and implement a one-way quantum computer.

In this chapter we will discuss first the fabrication of a particular type of QDs, Pyramidal Site-Controlled Quantum Dots.

Epitaxial growth refers to the process though which a crystalline material is grown on top of a single crystal substrate. The crystalline material can be deposited on the substrate after thermal evaporation, like in Molecular Beam Epitaxy (MBE), or carried by molecules of a gas that decomposes at the surface, like in Metal Organic Vapour Phase Epitaxy (MOVPE).

These processes are carried out at high temperatures of both substrate and deposited material. The diffusion properties of the two crystals, complex dynamics at the surface of the substrate, strain and absorption by defects can be exploited to grow several kinds of structures, like quantum wells, wires and dots, or even complex devices like laser and detectors when epitaxial growth is combined with chemical or mechanical processing.

Several techniques are known in the community to grow semiconductor QDs [1]. This thesis focuses on III - V material QDs grown inside pyramidal recesses of a GaAs substrate. These dots are known as Pyramidal Site-Controlled Quantum Dots.

Using a pre-patterned substrate for the growth process allows the researcher to find the QDs at known locations, unlike Stranski-Krastanov or Droplet Etch QDs which are grown at random locations on the substrate. As detailed later, the MOVPE technique allows for a wide mix, engineering possibilities of materials and structures grown inside the pyramidal recesses with a high yield of uniform QDs

[2].

After describing the details of the growth process we will focus on the several processing steps and techniques to make these dots suitable for optical characterization.

In the last section of the chapter we will describe several experimental setups used for spectroscopic characterization of the QDs.

2.1 Substrate Preparation

These are the steps to prepare the substrate in which the QDs will be fabricated. A pattern of inverted tetrahedrons with a chosen pitch, defined as the tip-to-tip distance, needs to be imprinted on a (111)B oriented GaAs substrate. For this thesis we have worked with samples grown on a $7.5\mu m$ pitched substrate.

1. A $50nm$ thick layer of SiO_2 is sputtered on the wafers.
2. The wafers are coated with a primer layer of Hexamethyldisilazane, HMDS, to promote adhesion of the photoresist.
3. S1805 photoresist is spun over the wafers, soft baked at $115°C$ on a hotplate to remove the excess solvent to avoid sticking to the mask and to harden it to make it more resistant.
4. a chromium mask and Hg-Xe vapour lamp are used to transfer the pattern of triangles to the photoresist, the pattern has a pitch of $7.5\mu m$, $10\mu m$ or $12.5\mu m$ and a tilt of $0.05°$ with the [110] direction to allow cleaving the pyramids at different depths.
5. The photoresist is developed using MF-319.
6. The wafer is cleaned using O_2 plasma.
7. A diluted HF etch transfers the pattern from the photoresist to the SiO_2 layer.
8. The remaining photoresist is washed away with baths of acetone, IPA and water.
9. The pattern transferred to the SiO_2 layer acts like a mask and a Br - Methanol solution is used in a wet etching process to expose the (111)A facets and produce a inverted pyramidal recesses.
10. The SiO_2 layer is removed with another diluted HF etch.

2.2 Metal-Organic Vapour Phase Epitaxy Growth

The growth of QDs is achieved using the Metal-Organic Vapor Phase Epitaxy (MOVPE) technique. The precursors of the QDs materials are carried to the MOVPE machine reactor by using gases like N_2 or H_2.

In order to grow III-V group compound semiconductors, metal-organic compounds are used as precursors for group III semiconductors, which are composed of a metal, typically $In/Al/Ga$, and organic ligands, CH_3, and inorganic precursors compounds for group V semiconductors, AsH_3/PH_3.

The rotation of the sample holder inside the reactor ensures a uniform growth of the epitaxial structures.

The growth of QDs inside the pyramidal recess is a complex process due to the non-planar nature of the the substrate [3].

Two competing phenomena, the anisotropic growth rate on exposed side facets and capillarity effect, produce the so called self limiting profile, which is also known from the growth of V-grooves quantum wires [4].

The first phenomenon, the anisotropic growth rate, happens because of the property of the pyramid sidewall surfaces. These are terminated by Ga atoms, (111)A plane; if the growth conditions are in a certain range, there will be more decomposition of the precursors along the sidewalls than on the base of the pyramid. This will ensure that the base of the pyramid will be kept sharp during the growth process.

The second phenomenon, the capillarity effect, causes the diffusion of adatoms to reduce surface energy by increasing planarity. This will cause the adatoms to accumulate at the bottom of the pyramid, and thus widen the base of the pyramid during the growth process.

When both phenomena are in equilibrium the so called self-limiting profile condition is reached and the size of the (111)B base can be tuned. By controlling the growth conditions QDs of different size can be grown along the (111)B direction.

In this thesis QDs with different epitaxial structures will be studied. Common features of the epitaxial structures of different types of QDs are: an initial thick buffer of $GaAs$ to reduce defects introduced by the sidewall surfaces defects produced during patterning and sample post processing; and a layer of high Al content $Al_xGa_{1-x}As$ is introduced after to protect the QDs stack from the wet-etching process that the samples will go through after the growth is completed. This layer acts like an etch-stop layer and blocks the ammonia from damaging the sample due to the high selectivity between $GaAs$ and $Al_xGa_{1-x}As$.

The $InGaAs$ QDs are confined by $GaAs$ barriers. The QD is interconnected with three lateral quantum wires and three lateral quantum wells that develop during the growth process, respectively, along the edges and parallel to the sidewall surfaces of the pyramidal recess, see Fig.2.1 [5].

The $GaAs$ QDs are confined in $Al_xGa_{1-x}As$ barriers. Since the barrier alloy is a ternary compound, alloy segregation is produced and a vertical quantum wire and three vertical quantum wells appear. These additional structures might increase disorder in the system and thus lower the quality of certain QD properties, for example the FSS [2].

The biggest contribution to the *degradation* of the optical properties of the $GaAs$ in $Al_xGa_{1-x}As$ QD comes from the vertical quantum wire, due to the high surface shared between the two structures and its being an intrinsically disordered alloy.

In general, we observe a reduction of FSS with increasing Al content. $GaAs$ QDs in $AlAs$ barrier are, for example, characterized by the lowest average value of $FSS = 11 \pm 8\mu eV$ [2]. Because $AlAs$ is a binary compound, disorder is absent and the leftover FSS is due to other phenomena.

To reduce the disorder influence while keep the $Al_xGa_{1-x}As$ barriers, a thin superlattice structure, alternating layers of binary compounds $GaAs$ and $AlAs$, can be introduced to sandwich the dot and detach the two structures. This strategy lead to a drastic reduction in average FSS, down to $6 \pm 4\mu eV$ [2].

The typical stack of layer is reported in Fig.2.2

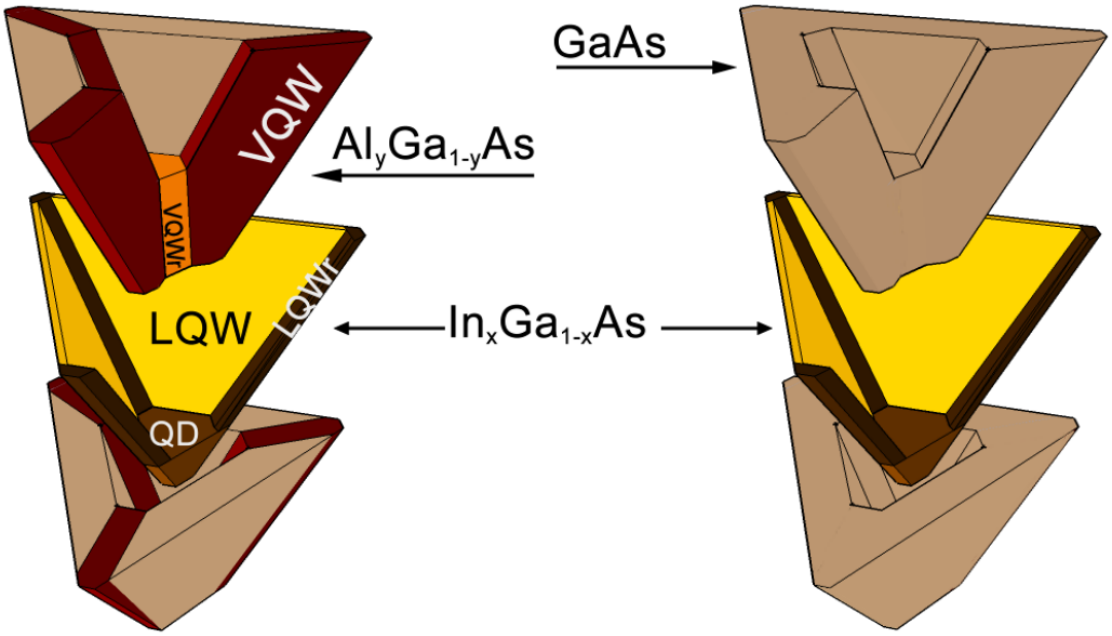


Figure 2.1: Features formed in a pyramidal recess during the QD growth process. VQW/LQW are the Vertical/Lateral Quantum Wells and VQWr/LQWr are the Vertical/Lateral Quantum Wires, these features are formed by Ga segregation in the ternary compound $Al_xGa_{1-x}As$. Image taken from [6]



Figure 2.2: Stacks of material used for the different types of QDs studied in this thesis. In light grey the etch stop layers, in dark green the barriers, in light green superlattice ($GaAs$ QDs) and additional barriers ($InGaAs$ QDs), in yellow the QDs.

2.3 Sample Post-Processing

While it is possible to measure as grown samples, it is not very practical for any useful application because the sidewalls of the pyramids would scatter most of the outgoing light. Characterizing the dots in this way would require very high laser power, which degrades optical properties, and very long acquisition time to gather emission signal.

To improve light collection several light extraction and collection strategies can be realized.

2.3.1 Polishing and Solid Immersion Lens

The goal of the polishing process is to reduce the length of the sides of the base of the pyramid to a few hundred nm. The sample is attached to a glass slide with the base of the pyramids facing up, and mounted in a rotating jig on a polishing pad. A slurry with $80nm$ particulate is poured on the pad, and the removal of material is monitored with the optical microscope. When the pyramids have the desired base the process is stopped.

To improve light collection from the objective a solid immersion lens, SIL, can be placed on the sample. The SIL increases magnification and numerical aperture of the setup compared to a regular lens by filling the object space with a higher refractive index material. We used a Weierstrass SIL made of LaSFN-9, which has a refractive index $n = 1.83$ and is characterized by a truncated sphere shape of radius $r = 0.5mm$ and height $h = (1 + 1/n)r = 0.77mm$.

The SIL should theoretically increase the numerical aperture of the setup by a factor n^2 [7]. In our measurements a $\sim 5x$ increase in collection efficiency has been observed compared to measurements without SIL.

2.3.2 Back-Etching

In the following section the back-etching process is described. This process exposes the tip of the pyramid by removing the excess material on the wafer through mechanical grinding and wet etching.

This processing, see Fig. 2.3, compared to polishing, improves light collection efficiency by 2 orders of magnitude.

1. The sample is cleaved by scribing a small scratch close to the edge with a diamond-tip scriber and gently pressing across the scratch with a pair of tweezers; the same procedure is done to a (100) GaAs substrate that will be used as a carrier.

2. A drop of SU8 is used to bond the carrier and the sample, with the pyramids tip pointing up, and is cured on a hotplate for 2 to 4 minutes at $150°C$.

3. The carrier is attached to a round glass slide with some wax and the planarity is checked with a dial indicator.

4. The glass slide is attached through suction to the rotating jig and placed on the grinding pad.

5. A slurry with $1\mu m$ particulate is added and rate of grinding of excess material is checked every few minutes to avoid removing the quantum dot.

6. When a few tens of μm of excess substrate are left on top of the pyramids, the mechanical grinding process is finished.

7. A solution of $120ml H_2O_2 : 3.8ml NH_3 33\%$ is prepared and mixed in a beaker with a magnetic stirrer at high speed setting.

8. Once the solution is properly mixed, the speed of the stirrer can be lowered and the sample dipped in the solution.

9. After 10 minutes the surface of the sample is checked with an optical microscope and the etching is continued until the pyramids start to be exposed; the process is not uniform and the etching starts to remove material from the sides.

10. Once enough small pyramids start to appear, the etching can be stopped, as excessive etching will not only remove the GaAs from the facets but damage the quantum dots as well.

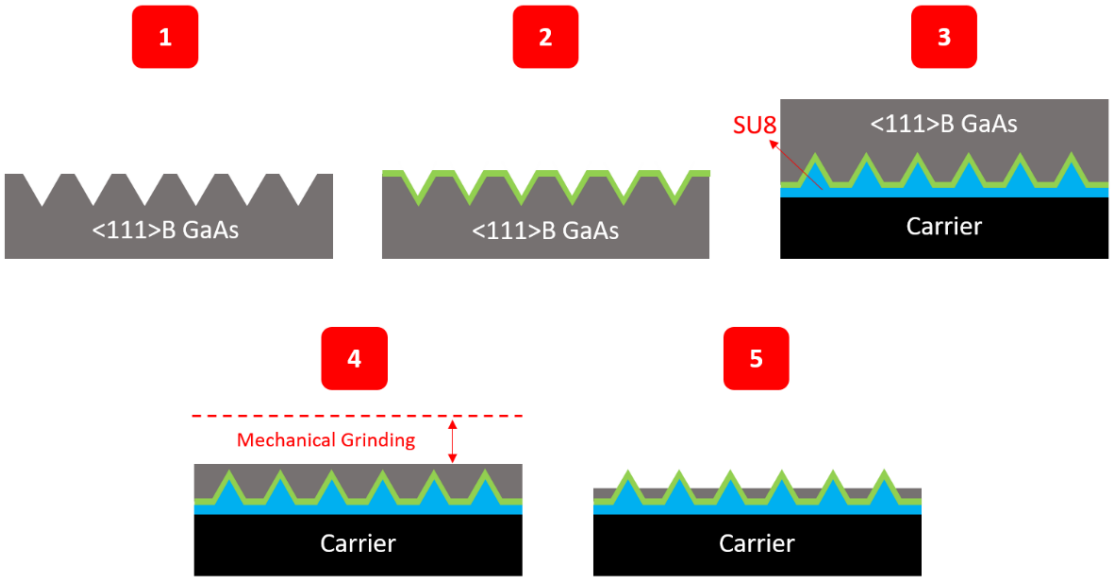


Figure 2.3: Backetch process, image taken from [8]. Steps: 1) Recesses are patterned on a (111)B *GaAs* substrate, 2) the QDs are grown inside the recesses in the MOVPE reactor, 3) as-grown sample is flipped and attached with SU8 to a (100) *GaAs* carrier, 4) excess substrate material is mechanically removed, down to a thickness of $\sim 30\mu m$, 5) the leftover substrate is removed using a chemical back-etching process until the pyramid's tips are exposed.

2.3.3 Cleaving

The sample needs to be cleaved to measure the QDs photoluminescence from excitons composed of holes with a p_z component of the angular momentum, where $\hat{z}$ is the growth direction of the QDs. The surface with the pyramid bases is scratched with a carbide scriber, light pressure is applied across the scratch with some tweezers and this will cause the sample to split in two pieces along the (110). Due to the tilt in the patterning mask, the pyramids will be cleaved at different depths, and some areas of the cleaved edge will still have the dot inside the pyramid, see Fig.2.4.

2.3.4 Sample Mapping

It is often necessary to be able to go back to a specific quantum dot over several measurement sessions, this requires the ability to map the sample surface. Two different lithography techniques have been used for this task, a direct laser writing and a lithographic photomask.

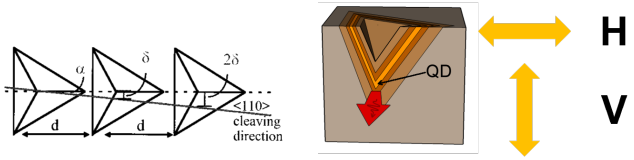


Figure 2.4: Schematic of a cross section of a pyramidal QD. (Left) angle α between the pyramid orientation and cleaving plane (110), highlighting the different distances of the QD from the exposed plane. Image taken from [3] (Right) Emission from the p_z component will be vertically polarized at the spectrometer due to the configuration in which the sample is mounted. Image taken from [9]

2.3.4.1 Direct Laser Writing

Two linear stages model X-LSM-E from Zaber have been mounted in a perpendicular configuration to move the sample in the XY plane. A piezoelectric actuator from Newport controls the distance of a 40x objective from the sample surface along the $\hat{z}$ direction. A $405nm$ laser diode from Thorlabs is routed to the objective, and a red LED with a CMOS camera allows the user of the setup to have imaging on the sample without affecting the photoresist. The focus can be adjusted coarsely by manually turning the actuator screw and then fine tuned with an ESA-C Ultra-Resolution Actuator Controller.

The minimum feature that can be printed with this system is given by the laser spot diameter, $3\mu m$, and not by the minimum step of the XY stages, which is much smaller, $\sim 0.04\mu m$.

A custom software has been written in LabVIEW to control the position of the stages in the XY plane moving the sample and to control a mechanical shutter that blocks the $405nm$ laser diode to write selected shapes on the sample. The shapes can be drawn in software like GIMP or Inkscape and then converted to GCode that can be interpreted by LabVIEW into commands for the stages.

A combination of lift off resist, LOR, and S1805 is spun over the sample. The desired pattern is written on the sample with setup and then developed removing the exposed areas. The LOR is needed to give an undercut to the S1805 and to not allow the deposited metal to be continuous.

A metal, usually gold, is evaporated on the sample and the resist washed away with a solvent leaving only the exposed pattern covered in metal, completing the lift-off process. The high reflectivity of the metal gives an high contrast for imaging purposes.

This approach to lithography allows to easily write custom patterns, not only markers, but also electrical contacts, without the costly investment into a customized mask. Another advantage is that the setup can be used without issues for

a sample with a rough surface, like a backetched sample, because there is no need for the a mask to contact the surface.

Some test results of the procedure can be seen in Fig.2.5. The first picture is a wide view of the area, highlighting the wide range over which the features can be printed, the zoomed in picture highlight the different shapes that can be written and their minimum size.

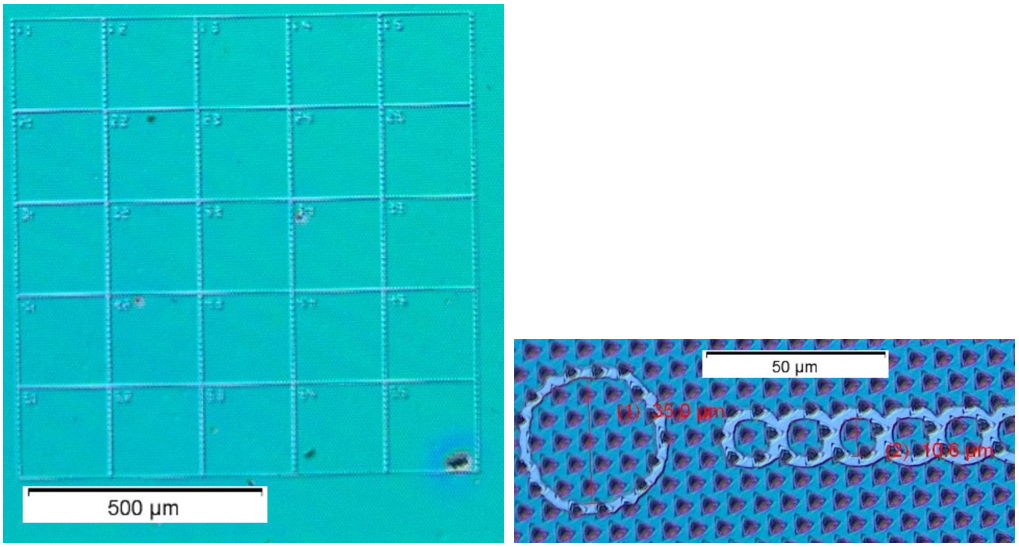


Figure 2.5: Test patterns written with the scratch built lithography setup. The scale bars for reference are (left) $500\mu m$, (right) $50\mu m$.

2.3.4.2 Lithographic Photomask

One of the drawbacks of the direct laser writing is the slowness, as the stages have to scan the desired shape and the shutter has to open and close along the travel. The process requires also additional steps: spinning of two resists, writing (which is a slow process in itself), developing of the resist, metal deposition and removal of excess material.

A much faster process involves the use of a lithographic photomask. A copper stencil is used to cover a glass slide and deposit metal in a matrix of square holes. The glass slide is then used as a mask to expose to UV Light a sample with SU8 spun on top. The SU8 is a negative resist, so the exposed part becomes cross-linked and can't be washed away by the solvent.

This process leaves the sample with a matrix of square holes in the photoresist where the pyramids are accessible for micro-photoluminescence measurements. The cross-linked SU8 is also resistant to common solvents like acetone, so this allows the sample to be cleaned after measurements.

Usually a combination of these square patterns and some defects on the sample surface, used as reference, are enough to get back to the desired dots.

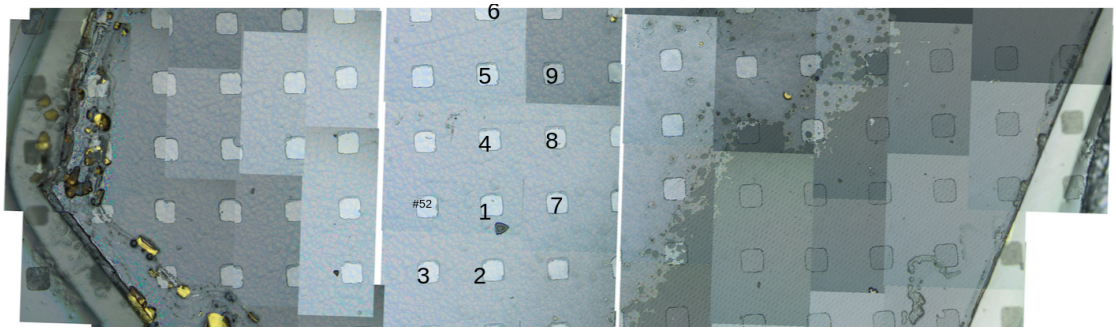


Figure 2.6: Sample mapping with squares identified by a number, each square contains a few hundred dots that can be identified by their distance from the edges.

2.4 Micro-Photoluminescence

After processing, the quantum dots are characterized by the time and polarization resolved microphotoluminescence techniques at cryogenic temperature using the setup described below.

2.4.1 Cryostat

The samples are mounted on a the cold finger of an ArsCryo closed cycle He probe station. Thermal contact between sample and cold finger is ensured by the silver based thermal paste.

Measurements are typically done at 10K to limit noise in the QDs emission due to the thermal distribution of charge carriers.

The temperature can be monitored in three points of the probe station using a Lakeshore module model 336. The module is also capable of controlling the sample temperature by driving two heaters.

A variety of mounting strategies is used depending on the desired measurement.

For cross section measurements, after the sample has been cleaved, it is attached to a copper piece using silver paint and copper tape. The copper stage is then placed inside the cryostat and thermal contact is again ensured using silver paint. The cleaved edge is set to point up, along the $\hat{z}$ axis of the optical setup and coupling directly to an objective.

For measurements involving electric fields, like QDs mounted on a piezoelectric substrate or diode structures, at least two electric contacts are needed. Samples are mounted on a copper round base; a Kapton coated copper wire is stripped of the coating at the end and then is attached to the round base using silver paint, these will form the ground contact. The second contact changes depending on the application.

Monolithic piezoelectric substrates have both square surfaces covered in gold, one is attached to the copper stage and then the sample is placed on top of the other surface. Another enamel coated copper wire can be stripped and bonded on the sample and thus is used as a second contact.

In the case of diodes the whole QDs structure is made so that the stack of layer creates the two contacts, after the wet etching process the second contact is exposed and be accessed using the probes of the probe station, which have a BNC connector to carry electric signal and voltages.

The two contacts exit the probe station through a custom made flange or the BNC connector of the probes.

A Keithley module applies the required voltage and monitors the currents through the samples.

For measurements involving the use of a weak magnetic field, a custom made copper stage has been designed and produced by the Tyndall workshop, see Fig.2.7.

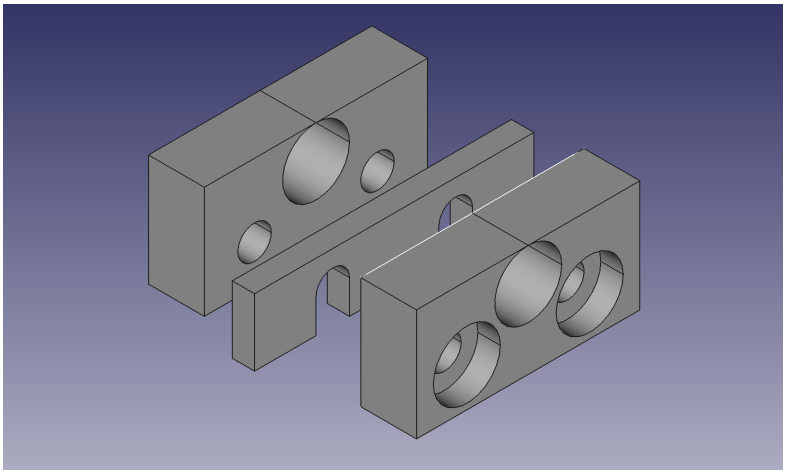


Figure 2.7: 3D model of the custom built magnet holder. The cylindrical magnets, of $3mm$ radius, are inserted in the two round holes at the center of the left and right pieces. The magnets holder are $10mm$ tall, $5mm$ wide and $20mm$ long. The sample, up to $2mm$ in length, is attached in the central part. The whole unit is kept together by M3 bolts.

The stage allows two cylindrical N35 magnets of $6mm$ length and diameter to be mounted and, through the use of copper spacer, the intensity can be regulated by changing the distance of the sample from the dots. The magnetic flux density as high as $|B| = 0.7T$ can be achieved with a $2mm$ spacer and N52 magnets. The magnetic field was measured with a portable Gauss meter probe positioned at the central axis of the magnets. During the typical measurements, N35 magnets were used with a larger spacer to position the QD of interest in the field of $|B|$ $0.3-0.4T$. To minimize possible nonuniformity effects at the lateral borders of the magnets, the QD was placed as close as possible to the central axis. This configuration allows to investigate some quantum dot properties like hole precession. To mount the samples on this stage they have to be mechanically diced beforehand.

The sample and its various holder sit on Attocube stages which allow movement along xyz axis.

Measurements requiring a stronger magnetic field have been conducted in the laboratories of the La Sapienza University in Rome, using an AttoDry system and a 45 deg silver coated mirror to direct the beam on the sample.

2.4.2 Quantum Dot Excitation

The quantum dots are excited with a variety of lasers as discussed below in more details.

2.4.2.1 Imaging

It is often useful to have a live image of the sample surface to look for QDs or recover their position while measuring. To this end an off the shelf red LED is powered by a benchtop power supply, its divergent beam is collimated by a small lens and then sent to the sample surface by placing a $50R : 50T$ non polarizing beam splitter along the beam path. The reflection of the LED light from the sample surface is then sent to a camera using a cold mirror, which reflects visible light and transmits the QD emission, thus allowing to have live video and be able to continue spectroscopy measurements in parallel, see Fig.2.11.

2.4.2.2 Above-band Excitation

A PicoQuant model D-C-635M is the main workhorse for regular characterization of the quantum dots, it is used to excited the samples with above-band excitation. It has a wavelength of $\lambda = 635nm$ and can operate in continuous wave and pulsed mode with a repetition rate from $31.25kHz$ to $80MHz$ and a $FWHM \approx 100ps$, the power output can be adjusted with a built in potentiometer of the PDL-800-D

control unit. CW operation is useful for regular spectra collection, power dependence, fine structure splitting measurements or cascade identification through cross-correlation measurements. Pulse mode is used for collecting lifetimes of several peaks which may not be excited under resonant pumping.

2.4.2.3 Laser Pulse Shaping

For resonant pumping, a Ti:Sapphire 80MHz fs laser output, a Tsunami from SpectraPhysics or a Chameleon from Coherent, is pulse shaped using a double transmission grating *4f* configuration, see Fig.2.8. The fs laser is set roughly to the wavelength range in which the user wants to operate the pulse shaper. The first grating disperses the fs pulse with a $FWHM \approx 100fs$, the dispersed pulse is then focused by a concave mirror and a slit is placed on the focal plane to select only a small wavelength range.

The adjustable slit allows to tune the pulse temporal length, but too small of an aperture will cause diffraction of the beam, so typically a pulse width of $FWHM \approx 10ps$ is used. Another concave mirror focuses the beam on a second grating to recombine to the same spatial mode the dispersed beam.

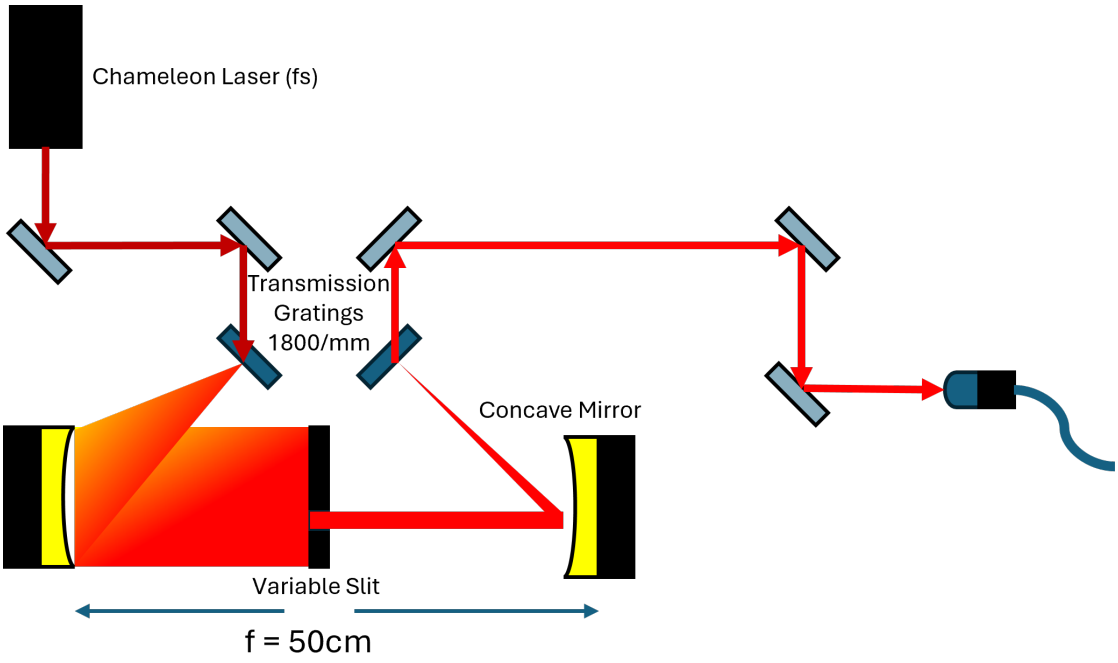


Figure 2.8: 4f Pulse Shaper to convert a fs pulse to ps

The output of the pulse shaper can either be sent to a fiber to excite the sample directly or sent to different setups.

For measurements requiring a variable pulse delay, like a Ramsey fringes measurement, the pulse is split by a $50R : 50T$ beam splitter, the reflection is sent to a retroreflector mounted on a piezo stage that moves along the beam path, the transmission is sent to another retroreflector mounted on a linear stage with a travel range of $60cm$. The retroreflectors are aligned so that the two beams, upon reflection, overlap again and can be sent into a fiber coupler.

For measurements where only one of the two pulses needs to be delayed the piezoelectric actuator is kept still in the same position and only the coarse delay arm is moved.

The output of these setup is coupled to a panda fiber to preserve the linear polarization of the pulses. To improve the beam degree of linear polarization a polarizer is placed in front of the fiber output.

The power of the pulse can be controlled according to Malus Law, Eq.2.1, using a half wave plate (HWP) and polarizing beamsplitter.

$$I = I_0 cos^2(\theta) \tag{2.1}$$

2.4.2.4 Beam Path

The beams, either from the CW/pulsed red laser or ps pulse shaper, are steered to the sample using dielectric or protected silver mirrors. To avoid needless realignment the pulse shaped beam can be introduced along the red beam optical path by using a short pass filter. The filter will transmit the red laser and reflect the pulse shaped beam, by steering the fiber coupler and a mirror the two beams can be overlapped on the sample.

The laser beams and imaging light are reflected from a $10R : 90T$ and sent thought an objective onto the sample surface.

The objective is a 50x Mitutoyo optimized with for near infrared range and has a focal spot with a diameter of $\sim 3\mu m$. It is mounted on a xyz stage to coarsely align its spot on the sample and regulate the focal distance.

To maximize light collection from the sample and since laser power is not a limiting factor, a beam splitter with an high transmittance has been chosen.

2.4.2.5 Polarization

An important property of light waves is the polarization, which specifies the orientation of the electric field oscillations. The plane of polarization of light is the plane located by the direction of propagation of the wave and the electric field vector.

If light propagates along the $\hat{z}$ direction and its electric field vector oscillates only on a single plane, the polarization is said to be linear. In particular, polar-

ization is said to be horizontal (vertical) if the electric field vector is confined to the XZ (XY) plane, and diagonal (antidiagonal) if oscillations happen in a plane ad 45° (135°) with the $\hat{x}$ axis.

If the plane of polarization is not fixed, we typically have elliptically polarized light, which can be described as the superposition of two linearly polarized component with a phase shift. Particular cases of elliptically polarized light are right-handed and left-handed light, $\sigma^{\mp}$, in which the two linear components are perpendicular, have the same magnitude and a $\pm 90°$ phase shift.

During the measurement it is often necessary to send circularly polarized light to the QDs, but this type of polarization is very often distorted by the optical elements due to birifringence or imbalance in the s and p reflection coefficients, where s and p are the components of the polarization perpendicular and parallel to the plane of incidence [10]. Extensive studies have been done to characterize and try to compensate the distortions introduced by the setup.

Polarized, unpolarized and partially polarized light can be described by a set of four values known as Stokes parameters. Depending on the notation they may be written as S_0, S_1, S_2, S_3 or I, Q, U, V or in vector form:

$$\vec{S} = \begin{pmatrix} S_0 \\ S_1 \\ S_2 \\ S_3 \end{pmatrix} = \begin{pmatrix} I \\ Q \\ U \\ V \end{pmatrix} \tag{2.2}$$

$S_0 = I = \langle E_H^2 \rangle + \langle E_V^2 \rangle = \langle E_D^2 \rangle + \langle E_A^2 \rangle = \langle E_R^2 \rangle + \langle E_L^2 \rangle$ represents the intensity of the state, or the sum of the expectation values on H/V, D/A or R/L bases.

$S_1 = Q = \langle E_H^2 \rangle - \langle E_V^2 \rangle$ the amount of linearly polarized light in the H and V base, 1 (-1) represents a purely horizontally (vertically) polarized state.

$S_2 = U = \langle E_D^2 \rangle - \langle E_A^2 \rangle$ the amount of diagonally polarized light in the D and A base, 1 (-1) represents a purely linearly polarized at 45° ($-45°$) state.

$S_3 = V = \langle E_R^2 \rangle - \langle E_L^2 \rangle$ the amount of circularly polarized light in the R and L base, 1 (-1) represents a purely right handed (left handed) circularly polarized state.

$$\begin{aligned}
\vec{S_H} &= \begin{pmatrix} 1 \\ 1 \\ 0 \\ 0 \end{pmatrix} \qquad \vec{S_V} = \begin{pmatrix} 1 \\ -1 \\ 0 \\ 0 \end{pmatrix} \\
\vec{S_D} &= \begin{pmatrix} 1 \\ 0 \\ 1 \\ 0 \end{pmatrix} \qquad \vec{S_A} = \begin{pmatrix} 1 \\ 0 \\ -1 \\ 0 \end{pmatrix} \\
\vec{S_R} &= \begin{pmatrix} 1 \\ 0 \\ 0 \\ 1 \end{pmatrix} \qquad \vec{S_L} = \begin{pmatrix} 1 \\ 0 \\ 0 \\ -1 \end{pmatrix}
\end{aligned} \tag{2.3}$$

In general $I^2 \geq Q^2 + U^2 + V^2$ and $\frac{\sqrt{Q^2+U^2+V^2}}{I}$ is the Degree of Polarization, DOP, that describes the percentages of an electromagnetic wave which is polarized.

We can also defined the degree of linear and circular polarizations as:

$$\begin{aligned}
DOP_{linear} = DOLP &= \frac{\langle E_H^2 \rangle - \langle E_V^2 \rangle}{\langle E_H^2 \rangle + \langle E_V^2 \rangle} \\
DOP_{circular} = DOCP &= \frac{\langle E_R^2 \rangle - \langle E_L^2 \rangle}{\langle E_R^2 \rangle + \langle E_L^2 \rangle}
\end{aligned} \tag{2.4}$$

the degree of linear polarization can be easily measured with a polarizer and HWP, by rotating the HWP and plotting the measured intensity as function of the wave-plate angle we obtain a signal, from whose amplitude and offset we can measure the DOLP.

The classical approach to measure the Stokes vector of light is to use a combination of QWP, HWP and polarizer. A set of 4 measurements is usually required:

$$\begin{aligned}
S_0 &= I(H) + I(V) \\
S_1 &= I(H) - I(V) \\
S_2 &= 2I(D) - S_0 \\
S_3 &= S_0 - 2I(R)
\end{aligned} \tag{2.5}$$

where $I(x)$ is the intensity of light on H, V, D or R basis.

We have implemented an automated measurement of the Stokes vector by using two ELL14 rotators from Thorlabs. Predefined angles, see Tab.2.1, based on the measurement procedure exposed in [11], are set for the HWP and QWP and the intensity is measured with a power meter, applying the equations above gives us the Stokes vector value.

Measurement Base	QWP angle	HWP angle
H	0°	0°
V	0°	45°
D	315°	337.5°
R	0°	22.5°

Table 2.1: Combination of angles used to measure the Stokes vector.

Another approach to measure the Stokes vector is to use only a polarizer and rotating QWP [12]. The intensity of the beam as function of the QWP angle θ is given by:

$$I(\theta) + \frac{1}{2}\left[S_0 + S_1 cos^2(2\theta) + S_2 cos(2\theta)\, sin(2\theta) + S_3 sin(2\theta)\right] \tag{2.6}$$

using the trigonometric half-angle formula this can be rewritten as:

$$I(\theta) + \frac{1}{2}\left[A + B sin(2\theta) + C cos(4\theta) + D sin(4\theta)\right] \tag{2.7}$$

where

$$\begin{aligned} A &= S_0 + \frac{S_1}{2} \\ B &= S_3 \\ C &= \frac{S_1}{2} \\ D &= \frac{S_2}{2} \end{aligned} \tag{2.8}$$

It can be shown that Eq.2.7 is a truncated Fourier series and that at least 8 points are required to determine the coefficients A, B, C and D as:

$$\begin{aligned} A &= \frac{2}{N}\sum_{n=1}^{N} I_n \\ B &= \frac{4}{N}\sum_{n=1}^{N} I_n sin(2\theta_n) \\ C &= \frac{4}{N}\sum_{n=1}^{N} I_n cos(4\theta_n) \\ D &= \frac{4}{N}\sum_{n=1}^{N} I_n sin(4\theta_n) \end{aligned} \tag{2.9}$$

therefore:

$$\begin{aligned} S_0 &= A - C \\ S_1 &= 2C \\ S_2 &= 2D \\ S_3 &= B \end{aligned} \tag{2.10}$$

While this second measurement approach requires more data points to be collected, compared to the projection method which requires only 4 measurements, it involves less optical elements and moving parts, thus performing better in terms of complexity, footprint and cost.

We benchmarked the rotating QWP method by measuring the Stokes vector of the basis states, see Eq.2.3, generated using a $785nm$ laser, polarizer and HWP or QWP. In Fig.2.9 we can see the collected data from $\theta = 0°$ to $\theta = 180°$, and in Tab.2.2 the measured (normalized) Stokes parameters, which are in agreement with the theoretical values.

State	S_0	S_1	S_2	S_3
H	1	1.020	0.007	-0.005
V	1	-0.999	-0.005	0.002
D	1	0.014	0.993	-0.012
A	1	0.040	-1.004	0.036
R	1	-0.007	-0.023	1.001
L	1	0.019	-0.017	-1.001

Table 2.2: Normalized Stokes vector of the polarization basis states, measured with the rotating QWP method.

Using this variety of measurements techniques, it has been found that in general horizontal and vertical polarized light are barely affected by the optics, because the light polarization is aligned with the s or p axis of the optical element. On the other hand diagonal and circular polarized light usually become elliptically polarized when reflected. This effect is more pronounced in optics such as beam splitters with low transmission values.

In our laboratory we had available $50R : 50T$, $30R : 70T$ and $10R : 90T$ non-polarizing beamsplitters, testing their polarization properties, we have found that the best performing beamsplitter was the $10R : 90T$. From Fig Fig.2.10, we can observe the DOLP of a $852nm$, circularly polarized with a QWP (blue reference lines), with a rotating HWP and fixed linear polarizer. The very low DOLP, typical of circularly polarized light, is lost for almost all transmitted and reflected outputs of the beamsplitters, indicating that the laser is now elliptically or only partially polarized.

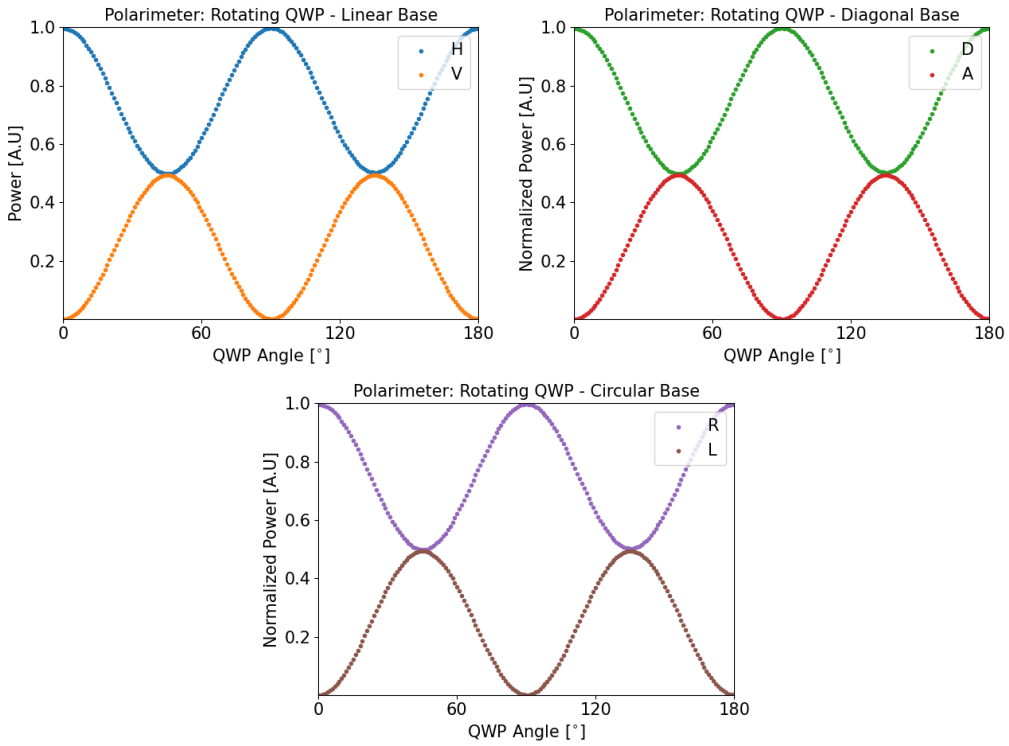


Figure 2.9: Measured intensity as function of the QWP angle for the polarization basis states.

In our experiments we decided to use the BS044 $10R : 90T$ non-polarizing beamsplitter from Thorlabs, to maximize the collected photoluminescence from our sample and minimize the distortions of its polarization properties.

To further reduce distortions of circularly polarized light emitted by the QDs, that may have been induced by mirrors and other optics, when the QD is excited with linearly polarized light, we place a quarter wave plate (QWP) at 45° after the transmission output. This QWP converts circularly polarized light to linear, which is less problematic to deal with.

In some measurements, such as spin injection, a very high degree of circularly polarized light is needed to excite the QD, but the reflection output of the $10R : 90T$ non-polarizing beamsplitter, still shows some distortion of circularly polarized light, see Fig.2.10 (lower right plot, green line). For this reason a QWP will be placed at 45° between the $10R : 90T$ beamsplitter and 50x objective. Light emitted from the QDs will also pass through this QWP and will be converted from circular to linear as if going through a $-45°$ QWP ($R(L) \rightarrow V(H)$). Once converted to linear, there is no distortion of the polarization induced by the other optical elements and no need for the QWP on the transmission output of the

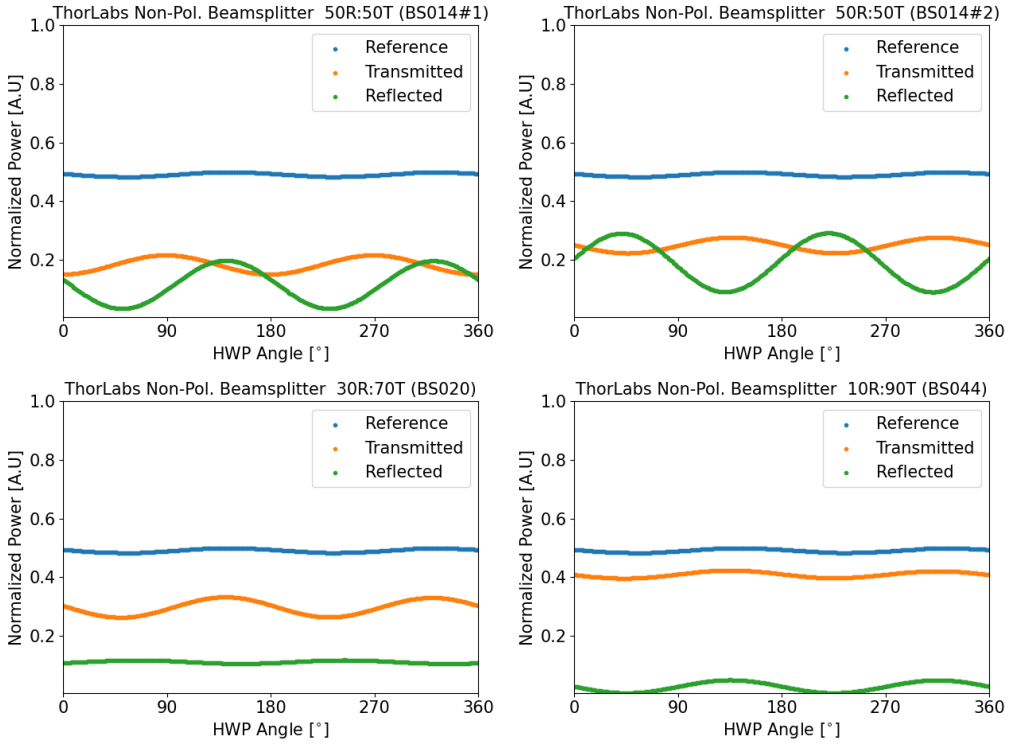


Figure 2.10: Characterization of four beam splitters available in the laboratory, 2 $50R:50T$, $30R:70T$ and $10R:90T$ using circular polarized light as input and a rotating HWP and fixed polarizer as analyser.

non-polarizing beamsplitter

If the QDs need to be excited with linear polarized light, but emit in a circular base (for example trions) then the QWP at 45° can be placed on top of the beamsplitter and thus the laser light going to the sample will be unaffected but the QDs emission will be converted to linear base and further distortions its polarization will be minimized.

2.4.3 Polarization and Time-Resolved measurements

To spectrally analyze the light emitted by the QDs we use a monochromator model FHR1000. The monochromator has 1m focal length and a rotating turret system loaded with a $950gr/mm$ and a $1800gr/mm$ gratings.

To remove unwanted scattered laser light and avoid saturating the detectors a $700nm$ long pass filter (to suppress the $635nm$ laser light) or 3 volume Bragg grating notch filters (to suppress the pulse shaped laser) are placed in front of the lens before the monochromator. The notch filters are placed on 3 mechanical

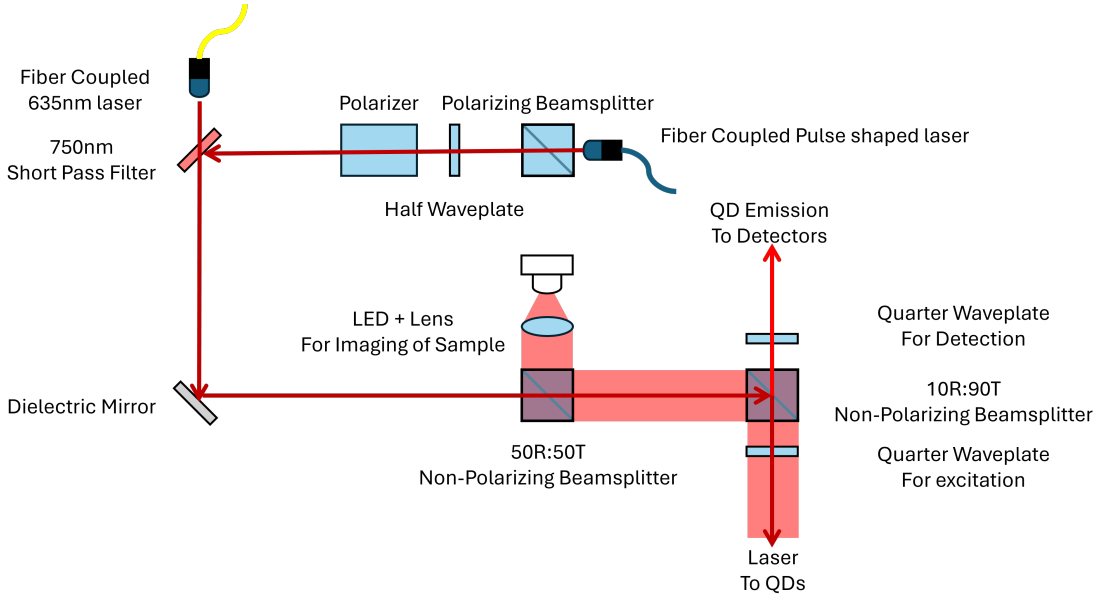


Figure 2.11: Beam path of lasers and imagining system. If the QWP for excitation is inserted, the QWP for detection is removed.

rotator to set remotely their angle with respect to the beam path and to match the laser wavelength.

The light dispersed by the gratings can be analyzed using a Symphony CCD or sent through a folding mirror to a side exit and then to an APD for time resolved measurement.

If there is the need to analyze the polarization of the QDs light then a HWP on mechanical rotator and polarizer can be placed before the lens at the entrance slit of the monochromator.

2.4.3.1 Correlation, $g^{(2)}(\tau)$

Second-order correlation function of light is defined as:

$$g^{(2)}(\tau) = \frac{\langle E^{\dagger}(t) E^{\dagger}(t+\tau) E(t) E(t+\tau)\rangle}{\langle E^{\dagger}(t) E(t)\rangle\langle E^{\dagger}(t+\tau) E(t+\tau)\rangle} = \frac{\langle I(t) I(t+\tau)\rangle}{\langle I(t)\rangle\langle I(t+\tau)\rangle} \tag{2.11}$$

where $E(t)$ is the electric field, $I(t)$ the intensity of the light beam and $\langle ...\rangle$ indicates the time averaging operation.

$g^{(2)}(\tau)$ can be measured with a Hanbury Brown - Twiss (HBT) setup [13]. Light is sent to a $50R:50T$ beamsplitter, the light from the two outputs goes to two photodetectors, typically a Photomultiplier Tube (PMT) or Avalanche Photodiode (APD), and is converted into electronic signals. A timing unit measures the time

difference between the two signals, τ, and a histogram can be built with the number of Start - Stop events from the photodetectors. $g^{(2)}(\tau)$ can then be rewritten as a function of the photon counting events at the two detectors, $n_{1/2}(t)$:

$$g^{(2)}(\tau) = \frac{\langle n_1(t)\, n_2(t+\tau)\rangle}{\langle n_1(t)\rangle\langle n_2(t+\tau)\rangle} \tag{2.12}$$

Expressed this way $g^{(2)}(\tau)$ is the conditional probability of detecting a photon at the first detector at time $t = 0$ and detecting another photon at the second detector at time $t + \tau$.

It can be shown [13] that for sources of classical and coherent light $g^{(2)}(0) \geq 1$ and $g^{(2)}(0) \geq g^{(2)}(\tau)$. In particular a perfectly coherent light source will have $g^{(2)}(\tau) = 1$.

Non-classical light is generally characterized by sub-poissonian photon statistics, by a $g^{(2)}(0) < 1$ and is said to show antibunching.

For a Fock state, an eigenstate of the particle number operator, $|n\rangle$ with $n \geq 1$ it can be shown that [14]:

$$g^{(2)}(0) = 1 - \frac{1}{n} \tag{2.13}$$

In theory any single photon emitters, for which $n = 1$, should be characterized by a $g^{(2)}(0) = 0$ and for any state with $n > 1$ we will have $g^{(2)}(0) \geq 1/2$. Therefore, in the quantum optics community, any state which is characterized by $g^{(2)}(0) \leq 1/2$ is considered a single photon emitter [14].

Individual atoms, molecules and quantum dots are all single-photon emitters. After excitation, for example with a pulsed laser or an electric impulse, these quantum emitters emit a photon. The excitation - single photon emission cycle can be repeated approximately after the radiative lifetime thus leaving time gaps in the photon emission over time.

In our laboratory, PL emission from the QDs is split using a non polarizing $50R : 50T$ beamsplitter and sent to two FHR1000 spectrometers. The gratings of each spectrometer are centered at the interested transitions and the outputs sent through the folding mirror to the side exit. The slit at the exit ensures that only light coming from the transition at the center of the grating is sent to the APD.

The APDs are connected to the input of a Swabian TimeTagger Ultra TCSPC module, which collects the absolute time of arrivals of the photons at the two channels and then post-processes the data building the histogram of coincidences, see Fig.2.12. The histogram of these time differences represents a non normalized $g^2(\tau)$ curve. This measurement can be carried out in a CW and pulsed mode.

If both spectrometers are centered around the same transition then an auto-correlation measurement is taken. If they are centered around different transition lines then a cross-correlation is taken.

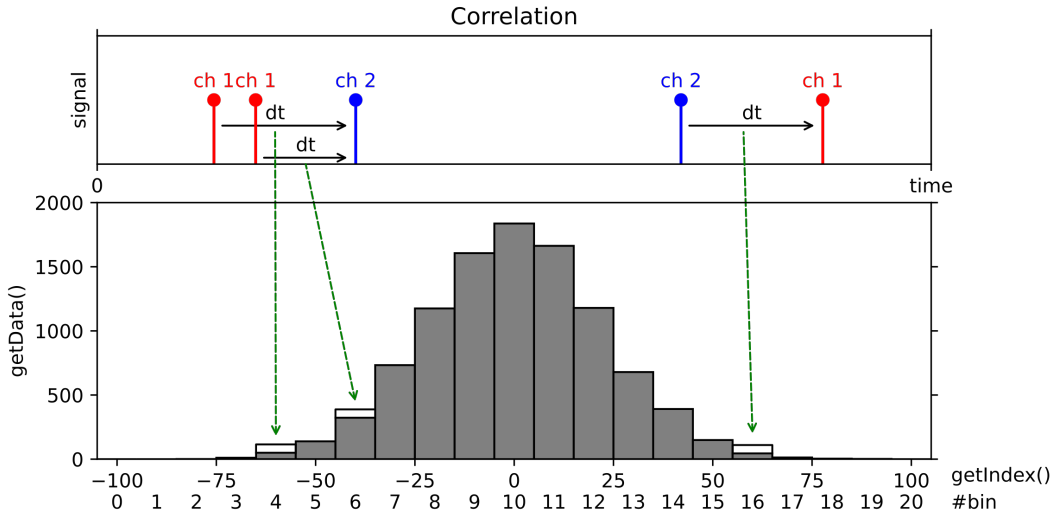


Figure 2.12: Correlation measurement in the Swabian TimeTagger Ultra TCSPC module. Image taken from [15]

Using two spectrometers allows maximum flexibility in terms of the spectral line isolation, as the only lower bound on line filtering is the resolution of the spectrometer at the slit exit and the entrance slit width. For this reason when a higher resolution might be needed (isolating doublet lines), one of the two spectrometers can be set to use a higher density grating ($1800 gr/mm$).

When studying recombination cascades using cross-correlations, a HWP and polarizer can be placed in front of each spectrometer, allowing us to verify the selection rules of said cascades.

Collection time to achieve a given signal-to-noise ratio scales quadratically with the counts at each detector, for this reason splitting all the PL signal into two beams and then isolating separate lines on the spectrometer can be a waste of PL intensity (because only half of the intensity of each transition will go to each APD and the other will be blocked by the slit of the other spectrometer in the case of the correlation of non-degenerate spectral components). Furthermore, the FHR1000 spectrometer uses gratings in a reflection configuration, which have only $\sim 30\%$ efficiency. This greatly increases collection time in the case of weak transitions or, for example, a cluster state characterization using a three-photon correlation.

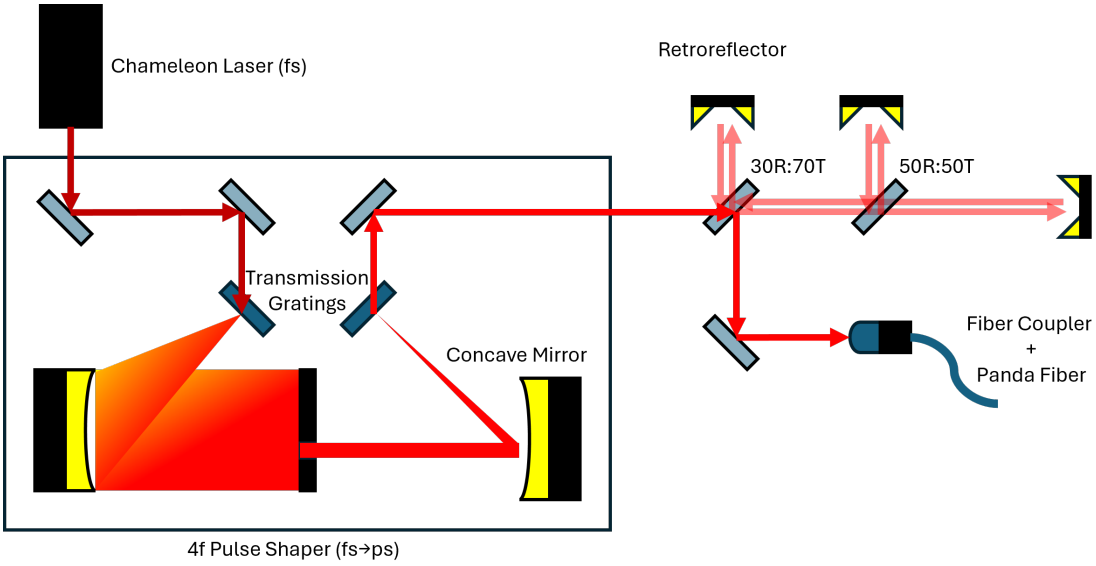


Figure 2.13: Laser multiplexing setup to generate time-tuned pulses.

2.4.4 Cluster State Generation and Characterization Setup

Cluster state generation and characterization has been attempted, most of the procedure is based on the process illustrated in reference [16].

A three arms delay line has been built to attempt a cluster state initialization and measurement, see Fig.2.13. The fs laser had a fixed repetition rate of $80MHz$, which equates pulses with a period of $12.5ps$. The excitation pulses have to be timed to when the QD is in a superposition of spins up and down, due to the controlled precession in a weak magnetic field. The output beam from the pulse shaper was split by a $30R:70T$ beam splitter, the reflection was sent to a fixed retroreflector, the transmission was split by another $50R:50T$ beam splitter and sent to two other retroreflectors. Their position, and thus the relative beam delays, can be set coarsely by using motorized linear stages and a rail system and fine adjustment using manual linear stages. In this way the three pulses can be set to match the hole oscillations at $\pi/2$ and $3\pi/2$ points in a weak magnetic field.

To overcome the poor efficiency of the FHR1000 spectrometer, a transmission grating on a rotator stage can be used, which typically have much better transmission values, around $90-94\%$. A slit filters the transition line that will be used for cluster state generation, in our case the $X^{+}_{\bar{2}0}$ transition, and sends the light to a three-photon correlator, sketched in Fig.2.14. The first detector collapses the $X^{+}_{\bar{2}0}$ to a selected spin configurations and the two other detectors are set to collect curves in the set polarization bases.

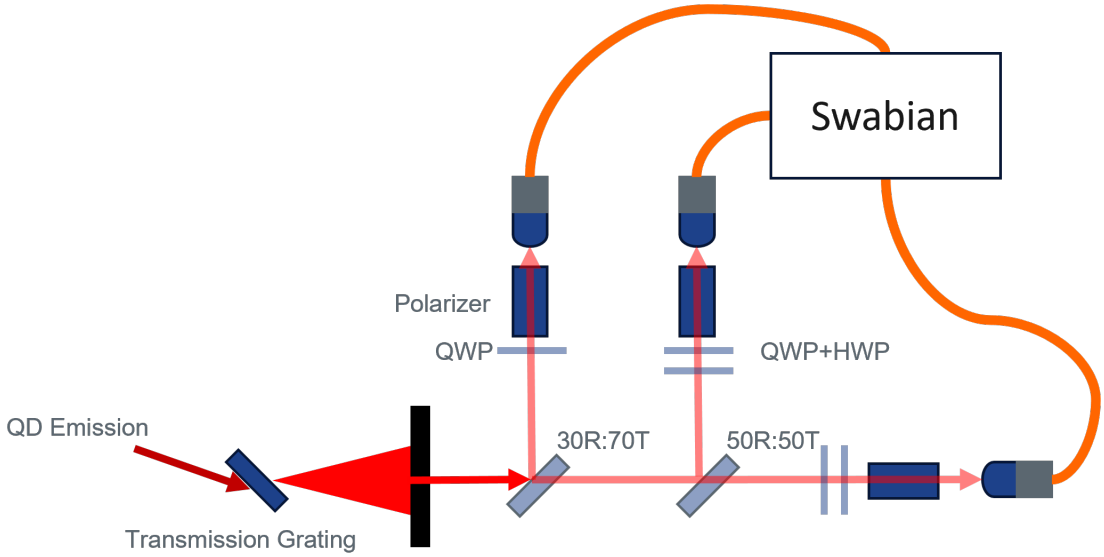


Figure 2.14: Transmission grating spectrometer and three photon correlation setup

2.5 Conclusions

In this chapter we have discussed the steps for fabricating and processing the particular type of QDs that were characterized during the PhD. The pre-patterned substrate allows site controlled growth of the QDs and MOVPE growth process let us engineer the optical properties of the QDs by changing alloys or stack of layers.

We have also discussed sample mapping techniques, involving custom made and commercial setups.

In the last section of the chapter we have described several characterization techniques and relative setup, such as time and polarization resolved spectroscopy.

References

[1] A. Rastelli, S. Kiravittaya, and O. G. Schmidt. "Growth and control of optically active quantum dots". In: *Single Semiconductor Quantum Dots*. Springer Berlin Heidelberg, 2009, pp. 31–69. DOI: 10.1007/978-3-540-87446-1_2.

[2] I. Ranjbar Jahromi et al. "Optical properties and symmetry optimization of spectrally (excitonically) uniform site-controlled GaAs pyramidal quantum dots". In: *Applied Physics Letters* 118.7 (Feb. 2021). DOI: 10.1063/5.0030296.

[3] A. Hartmann et al. "Self-limiting growth of quantum dot heterostructures on nonplanar {111}B substrates". In: *Applied Physics Letters* 71.10 (Sept. 1997). DOI: 10.1063/1.119882.

[4] G. Biasiol and E. Kapon. "Mechanisms of Self-Ordering of Quantum Nanostructures Grown on Nonplanar Surfaces". In: *Phys. Rev. Lett.* 81 (14 Oct. 1998). DOI: 10.1103/PhysRevLett.81.2962.

[5] G. Juska et al. "Complex optical signatures from quantum dot nanostructures and behavior in inverted pyramidal recesses". In: *Phys. Rev. B* 89 (20 May 2014). DOI: 10.1103/PhysRevB.89.205430.

[6] G. Juska. "Pyramidal quantum dots: single and entangled photon sources and correlation studies". 2013.

[7] W.L. Barnes et al. "Solid-state single photon sources: light collection strategies". In: *The Eur. Phys. J. D* 18 (2 Feb. 2002). DOI: 10.1140/epjd/e20020024.

[8] I. Ranjbar Jahromi. "Evaluation and properties of site-controlled pyramidal quantum dots for quantum information processing". 2023.

[9] F. Mattana et al. "GaAs Site-controlled Pyramidal Quantum Dots as Spin Qubit Sources for a Photonic Cluster State Construction: the Role of Light-hole-like Excited States". In: *2023 Conference on Lasers and Electro-Optics (CLEO)*. 2023.

[10] E. Hecht. *Optics*. Pearson Education, Incorporated, 2017. ISBN: 9780133977226. URL: https://books.google.it/books?id=ZarLoQEACAAJ.

[11] J.B. Altepeter, E.R. Jeffrey, and P.G. Kwiat. "Photonic State Tomography". In: vol. 52. Advances In Atomic, Molecular, and Optical Physics. Academic Press, 2005, pp. 105–159. DOI: https://doi.org/10.1016/S1049-250X(05)52003-2.

[12] B. Schaefer et al. "Measuring the Stokes polarization parameters". In: *American Journal of Physics* 75.2 (Feb. 2007). DOI: 10.1119/1.2386162.

[13] M. Fox. "Quantum Optics: An Introduction". In: Oxford University Press, Apr. 2006. ISBN: 9780198566724. DOI: 10.1093/oso/9780198566724.003.0001.

[14] P. Grünwald. "Effective second-order correlation function and single-photon detection". In: *New Journal of Physics* 21.9 (Sept. 2019), p. 093003. DOI: 10.1088/1367-2630/ab3ae0.

[15] Swabian Instruments. *Time Tagger User Manual*. https://www.swabianinstruments.com/static/downloads/TimeTagger_User_Manual.pdf. Accessed: 2025-03.

[16] N. Coste et al. "High-rate entanglement between a semiconductor spin and indistinguishable photons". In: *Nature Photonics* 17 (7 July 2023). DOI: https://doi.org/10.1038/s41566-023-01186-0.

Chapter 3

Quantum Dot Excitation Schemes

In Chap. 1 we gave an overview of quantum computing, its implementation using semiconductor QDs and their electronic and optical properties.

In Chap. 2 we reviewed fabrication and characterization properties of pyramidal site-controlled QDs.

In this chapter, we discuss various excitation schemes for quantum dots, supported by theoretical simulations. The primary purpose of these simulations is to evaluate and define the range of experimental conditions compatible with our lab resources and quantum dots. Where possible, experimental examples are provided to validate the simulations.

The ability to initialize qubits to a known state is one of the requirements for the physical implementation of quantum computation [1]. For this reason the following chapter will describe several quantum dot (QD) excitation schemes. Resonant and quasi-resonant excitation schemes for Two, Three Level systems (2LS, 3LS) will be studied in depth, because they allow selective and high-fidelity state preparation. Simulations and experimental data from $InGaAs$ and $GaAs$ QDs will be compared.

QDs are also coupled with the surrounding environment through the exchange of phonons. These crystal vibrational modes induce decoherence and thus degrade the state fidelity when the system is excited under particular resonant conditions. Despite this, phonons can also be used to prepare a state at high pulse areas and have been shown [2] to be more stable than on-resonance pulses for small wavelength and power variations. They tend to perform better the stronger the coupling is. Phonon-assisted excitation also allows spectral filtering of the laser without suppression of the QD emission if the spectral separation is large enough, unlike fully resonant excitation of a 2LS which requires cross-polarization to suppress the laser, wasting half of the QD emission.

The simulations presented hereafter will involve a single cycle of the excitation

process, either with a monochromatic or dichromatic Gaussian pulse. While Gaussian pulses may not be the optimal solution in certain regimes, [3] and it may be of interest for quantum computation applications to study the effect of different pulse shapes, chirping, additional decoherence mechanisms and of several cycles of the excitation process, this would require additional computational power and the study of several more parameters going beyond the scope of this chapter and thesis overall.

The evolution of the state after the electromagnetic field is switched off will not be simulated as the main focus of this research is state initialization.

A state can be prepared with high fidelity also with Continuos Wave (CW) excitation, but this will not be studied because it does not allow on-demand population inversion.

The systems are simulated with the Quantum Toolbox in Python (QuTiP), an open-source python library for simulating the dynamics of open quantum systems [4], and the Bloch-Redfield formalism, implemented through the *brmesolve* function.

For the experiments, $InGaAs$ and $GaAs$ QDs are excited using a femtosecond Ti:Sapphire laser with a repetition rate of $80MHz$ pulse shaped to have a width of $\sim 10ps$. Without knowing the full brightness of the QD states under pure resonant pumping, though, it is impossible to give an absolute scale of their population under different types of excitation. For this reason the y axis of the power dependence of different measurement will here report the integrated counts in arbitrary units and we will be able to make only relative comparisons, not absolute ones (compared to a full state population inversion).

3.1 Above-band Excitation

A QD can be excited with a laser at higher energy than the bandgap of the barrier layer. Under this type of excitation the charge carriers are created in the bulk, barrier or wires of the sample and then relax to lower energy states through scattering [5]. In a typical sample of $InGaAs$ dots, with a stack of layers described in Fig.2.2 (left), the lowest energy levels are the discrete levels of the InGaAs dots. But for a sample of $GaAs$ dots, see Fig.2.2 (center and right), the lowest energy levels can be the bands of the bulk GaAs. Thus depending on the excitation power, emission from wires and other sample features can be observed together with QD emission.

Fig.3.1 shows (on the left) a typical spectrum of QD of $GaAs$ in $Al_xGa_{1-x}As$ barrier excited with a $635nm$ laser and (on the right) the emission of the $GaAs$ bulk. Due to the incoherent excitation, several charge complexes are created inside the quantum dot and different transitions will be optically active. For this reason

above-band excitation is useful to quickly investigate optical properties of the quantum dot, like fine structure splitting, polarization anisotropy, state lifetime or identifying recombination cascades, but it is not the best tool to selectively address a single QD transitions.

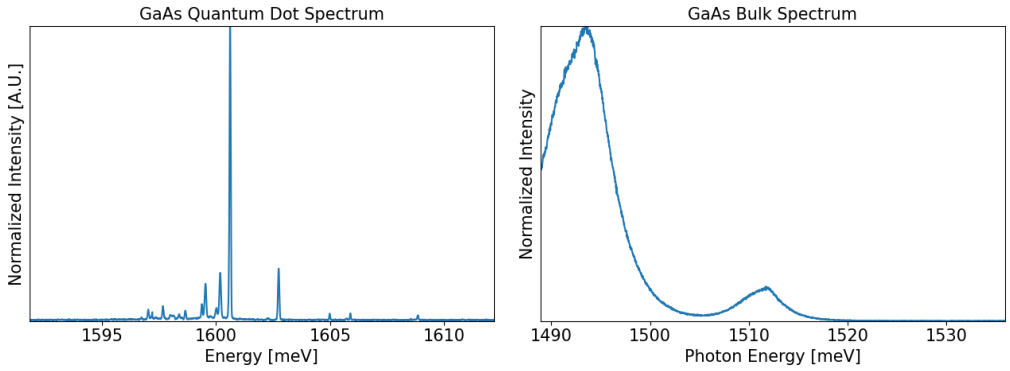


Figure 3.1: (Left) Typical spectrum of a GaAs QD in AlGaAs barrier (Right) Typical spectrum of GaAs bulk left from the backetching process

As a representative example of issues linked to non resonant pumping, Fig.3.2 shows a polarization resolved autocorrelation of the $X^{+}_{\bar{2}0}$ state, excited with a $635nm$ circularly polarized laser. According to selection rules circular polarization should generate e - h couples with opposite spins, but the flatness of the autocorrelation curve indicates that when the QD is populated both spin configurations of the $X^{+}_{\bar{2}0}$ state are equally probable due to spin scattering the charge carries go through while relaxing to the QD states from the more energetic layers. The incoherent nature of the excitation process does not make it a suitable scheme for targeted and on demand initialization of a specific state of the QD and also degrades the single photon emission, due to several recombinations channels and cascades possibly leading to the same state.

Spin injection in QD through trion state excitation will be discussed more in depth in the last chapter of this thesis.

3.2 Resonant and Quasi-Resonant Excitation

The next sections will deal with the theory of resonant and quasi-resonant excitation and the simulations using the QuTiP library.

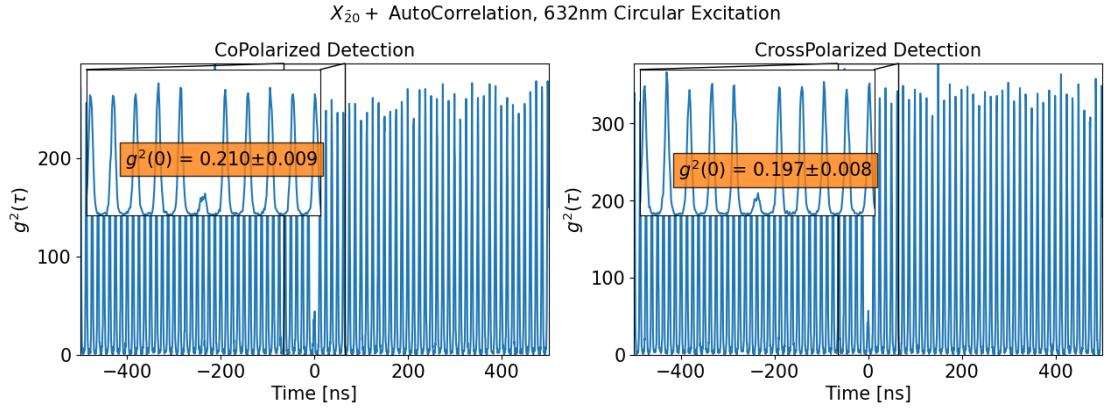


Figure 3.2: Autocorrelation curves of the $X^+_{\bar{2}0}$ peak under above-band circular excitation

3.2.1 Two-Level System

Let's consider a two level system (2LS), which consists of a ground and excited state, interacting with a circularly polarized electromagnetic field (laser). A typical excited state of a 2LS in QDs can be, for example, exciton, X_{10}, or trion, X^+_{20}, states. For ease of notation we will call g and X the eigenstates of the unperturbed Hamiltonian H_0.

$$\begin{gathered} |g\rangle = \begin{pmatrix} 1 \\ 0 \end{pmatrix}; \quad |X\rangle = \begin{pmatrix} 1 \\ 0 \end{pmatrix} \\ H_0 = \hbar\omega_g |g\rangle \langle g| + \hbar\omega_X |X\rangle \langle X| = \begin{pmatrix} 0 & 0 \\ 0 & \hbar\omega_X \end{pmatrix} \end{gathered} \tag{3.1}$$

where $w_{g/X}$ are the frequencies of the ground and excited state transitions, for convenience we will set the energy/frequency of g states to be $0meV = 0THz$.

Fig.3.3 schematically illustrates the relation between the g - X energy separation and laser energy. If the energy of laser is the same as the energy separation of the two levels then the laser is said to be resonant with the transition, if it is more (less) than the energy separation then it is said to be Blue(Red)-detuned from the transition.

In the dipole approximation [6] the interaction part of the Hamiltonian H_I can be written as:

$$\begin{gathered} H_I = -\frac{\hbar}{2} f(t) e^{-i\omega t} |X\rangle \langle g| - \frac{\hbar}{2} f^\dagger(t) e^{i\omega t} |g\rangle \langle X| = \\ = \begin{pmatrix} 0 & -\frac{\hbar}{2} f^\dagger(t) e^{i\omega t} \\ -\frac{\hbar}{2} f(t) e^{-i\omega t} & 0 \end{pmatrix} \end{gathered} \tag{3.2}$$

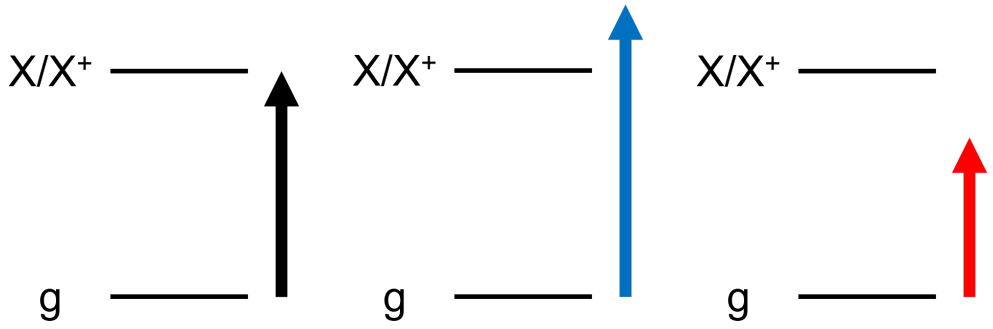


Figure 3.3: Two-Levels System and Laser. (a) Resonant, (b) Blue-Detuned, (c) Red-Detuned

where $f(t)$ is the field (in this case pulse) envelope and ω the laser frequency. For Gaussian pulses:

$$f(t) = f^{\dagger}(t) = \frac{\alpha}{\sigma\sqrt{2\pi}} e^{-\frac{(t-\tau)^2}{2\sigma^2}} \tag{3.3}$$

because the Gaussian is normalized, α is called the pulse area and is equal to the square root of the measured power of a laser:

$$\alpha = \sqrt{P_{laser}} \tag{3.4}$$

The total Hamiltonian H_T is the sum of the two components:

$$\begin{aligned} H_T &= H_0 + H_I = \\ &= \hbar\omega_X \left|X\right\rangle \left\langle X\right| - \frac{\hbar}{2} f(t) e^{-i\omega t} \left|X\right\rangle \left\langle g\right| - \frac{\hbar}{2} f^{\dagger}(t) e^{i\omega t} \left|g\right\rangle \left\langle X\right| = \\ &= \begin{pmatrix} 0 & -\frac{\hbar}{2} f^{\dagger}(t) e^{i\omega t} \\ -\frac{\hbar}{2} f(t) e^{-i\omega t} & \hbar\omega_X \end{pmatrix} \end{aligned} \tag{3.5}$$

H_T, Eq.3.5, depends on the laser frequency, $e^{\pm\omega t}$, this is an oscillating term and can be computationally challenging since it requires to sample the pulse with high resolution. To remove the dependence of the Hamiltonian from the oscillating term and to speed up the calculation we can introduce, as it is custom to do, the Rotating Frame Approximation (RWA) and redefine H_T as the product of a matrix H_{T_U}, which does not depend on the laser frequency, with U and $U^{\dagger}$, two unitary matrices that solely depend on the laser frequency.

$$\begin{aligned} H_T &= U H_{T_U} U^{\dagger} = \\ &= \begin{pmatrix} 1 & 0 \\ 0 & e^{-i\omega t} \end{pmatrix} \begin{pmatrix} 0 & -\frac{\hbar}{2} f(t) \\ -\frac{\hbar}{2} f(t) & \hbar\omega_X \end{pmatrix} \begin{pmatrix} 1 & 0 \\ 0 & e^{i\omega t} \end{pmatrix} \end{aligned} \tag{3.6}$$

We can also redefine the quantum states of the system as:

$$\Phi = U^{\dagger}\Psi = \begin{pmatrix} 1 & 0 \\ 0 & e^{i\omega t} \end{pmatrix} \Psi \longrightarrow \Psi = U\Phi = \begin{pmatrix} 1 & 0 \\ 0 & e^{-i\omega t} \end{pmatrix} \Phi \tag{3.7}$$

We can plug Eq.3.6 and Eq.3.7 in the Schrödinger Equation:

$$\begin{aligned} i\hbar\frac{\partial\Psi}{\partial t} &= H_T\Psi \\ i\hbar\frac{\partial U\Phi}{\partial t} &= UH_{T_U}U^{\dagger}U\Phi \\ i\hbar\left(\frac{dU}{dt}\right)\Phi + i\hbar U\frac{\partial\Phi}{\partial t} &= UH_{T_U}\Phi \\ i\hbar U^{\dagger}\left(\frac{dU}{dt}\right)\Phi + i\hbar U^{\dagger}U\frac{\partial\Phi}{\partial t} &= U^{\dagger}UH_{T_U}\Phi \\ i\hbar U^{\dagger}\left(\frac{dU}{dt}\right)\Phi + i\hbar\frac{\partial\Phi}{\partial t} &= H_{T_U}\Phi \end{aligned} \tag{3.8}$$

with:

$$\begin{aligned} U^{\dagger}\frac{dU}{dt} &= \begin{pmatrix} 1 & 0 \\ 0 & e^{i\omega t} \end{pmatrix} \frac{d}{dt} \begin{pmatrix} 1 & 0 \\ 0 & e^{-i\omega t} \end{pmatrix} = \\ &= \begin{pmatrix} 1 & 0 \\ 0 & e^{i\omega t} \end{pmatrix} \begin{pmatrix} 0 & 0 \\ 0 & -i\omega e^{-i\omega t} \end{pmatrix} = \begin{pmatrix} 0 & 0 \\ 0 & -i\omega \end{pmatrix} \end{aligned} \tag{3.9}$$

replacing in Eq.3.8 we obtain a new Hamiltonian in the RWA that does not have an oscillating term:

$$H_{RWA} = \begin{pmatrix} 0 & -\frac{\hbar}{2}f(t) \\ -\frac{\hbar}{2}f(t) & -\Delta \end{pmatrix} \tag{3.10}$$

with $\Delta = \hbar\omega - \hbar\omega_X$, the detuning of the laser from the exciton transition.

The evolution of a quantum state in 2LS can visualized with the Bloch Sphere, its coordinates are given by the expectation values of the Pauli matrices, $\sigma_{x/y/z}$. Pure states are mapped onto the surface of a Bloch sphere. A resonant excitation, $\hbar\omega = \hbar\omega_X \;\rightarrow\; \Delta = 0meV$, causes the state to move along a meridian, while detuned excitation, $\hbar\omega \neq \hbar\omega_X \;\rightarrow\; \Delta \neq 0meV$, also produces movement along parallels of the sphere. For the rest of the thesis the convention used is:

- $|g\rangle$ ($|X\rangle$) state on the north (south) pole,
- $|\pm i\rangle = \frac{1}{\sqrt{2}}(|g\rangle \pm i\,|X\rangle)$ state in $\pm y$
- $|\pm 1\rangle = \frac{1}{\sqrt{2}}(|g\rangle \pm |X\rangle)$ state in $\pm x$

A figure of merit to quantify the amount of decoherence introduced by phonon is the Bloch vector length, defined as:

$$L = \sqrt{\left(\langle\psi|\,\sigma_X\,|\psi\rangle\right)^2 + \left(\langle\psi|\,\sigma_Y\,|\psi\rangle\right)^2 + \left(\langle\psi|\,\sigma_Z\,|\psi\rangle\right)^2} \tag{3.11}$$

Any pure state, because it is mapped to the surface of the sphere, will have a Bloch vector length of 1 while for mixed states it will be < 1. It will be shown later in the chapter that phonon-assisted excitation despite being an incoherent process can lead to an almost fully coherent state.

3.2.1.1 Phonons

Unlike atoms, QDs are coupled to phonons. For the purpose of this work we will consider only acoustic phonons, because their energy distribution is closer to the dot transition lines and they are the main source of decoherence in QDs [7].

The QD - phonon bath interaction can be described by adding the following contribution to the QD plus electromagnetic field system Hamiltonian:

$$H_{QD-PH} = \sum_{\mathbf{q}} \hbar\omega_{\mathbf{q}} b^\dagger_{\mathbf{q}} b_{\mathbf{q}} + \sum_{\mathbf{q},\nu} \hbar n_\nu \left(g_{\mathbf{q}} b_{\mathbf{q}} + g_{\mathbf{q}} b^\dagger_{\mathbf{q}}\right) |\nu\rangle\langle\nu| \tag{3.12}$$

The first part of Eq.3.12 is the free phonon Hamiltonian, $b^\dagger_{\mathbf{q}}$ ($b_{\mathbf{q}}$) is the operator that creates (annihilates) a phonon of wave-vector $\mathbf{q}$ and frequency $\omega_{\mathbf{q}}$. The second part is the interaction with the dot, n_ν the number of excitons in the state $|\nu\rangle$ and $g_{\mathbf{q}}$ the exciton - phonon coupling constant (which is the difference between the electron - phonon and hole - phonon coupling constants $g_{\mathbf{q}} = g^e_{\mathbf{q}} - g^h_{\mathbf{q}}$ [8]), in the case of a 2LS with a single exciton this becomes:

$$\hbar\,|X\rangle\langle X| \sum_{\mathbf{q}} \left(g_{\mathbf{q}} b_{\mathbf{q}} + g_{\mathbf{q}} b^\dagger_{\mathbf{q}}\right) \tag{3.13}$$

An important quantity is the phonon spectral density, which is related to $g_{\mathbf{q}}$ and the dispersion relation of $\omega_{\mathbf{q}}$; it can be derived [8] that it takes the form:

$$J(\omega) = \frac{\omega^3}{4\pi^2\rho\hbar v_c^5} \left(D_e e^{-\frac{\omega^2 a_e^2}{4v_c^2}} - D_h e^{-\frac{\omega^2 a_h^2}{4v_c^2}}\right)^2 \tag{3.14}$$

assuming that the lattice properties of the QD are not too different from the bulk material, $\rho = 5370 kg/m^3$ and $v_c = 5110 m/s$ are the density and speed of sound of the material, $GaAs$ in the case of this thesis. $D_e = 7eV$ and $D_h = -3.5eV$ are the deformation potentials and $a_{e/h}$ the geometrical confinement length of electron and holes. The ratio between the two has been set to $a_h/a_e = 1.15$ for

the following simulations. In Fig.3.4 the phonon distribution has been plotted for different dot diameters, for increasing dot size the coupling strength decreases and the maximum shifts towards lower frequencies. For most simulation a value of $a_e = 1.5nm$ will be used.

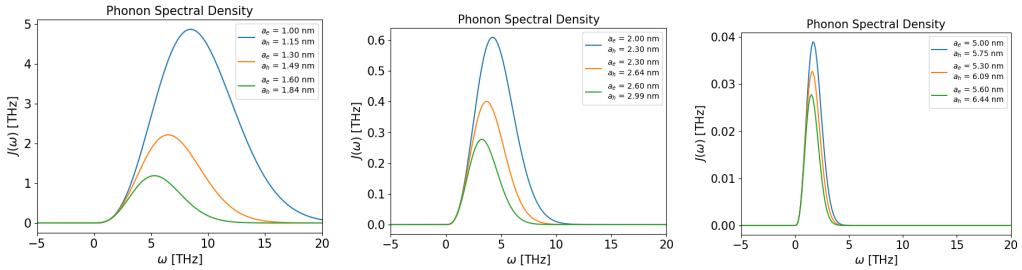


Figure 3.4: Phonon coupling for dots of different size ($a_e = [1, 2, 5]nm$)

The phonon distribution, Eq.3.14, has a maximum for positive frequencies, which means that at 0K only Blue-detuned pulses couple efficiently to the phonon bath.

This can be intuitively explained, at 0K it is more probable that the system releases a phonon after excitation with a more energetic pulse than the bandgap, and it is less probable for the unexcited system to absorb a phonon from the environment during the excitation process with a pulse less energetic than the bandgap. A more in depth study of the temperature dependence of the phonon coupling to the system can be found in [9] and [10], and it can also be seen that at high temperature the phonon coupling becomes symmetrical with respect of the detuning, at the price of not being able to achieve population inversion in the 2LS.

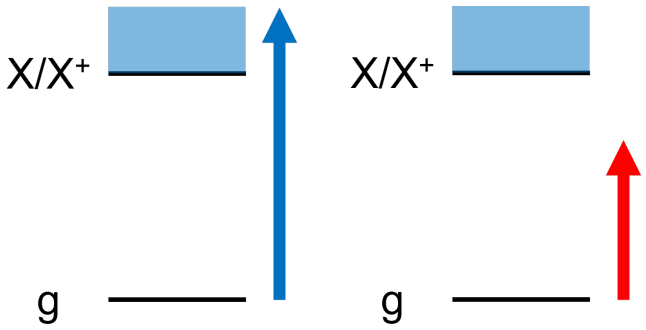


Figure 3.5: Two-Levels System with Phonon Bath and Laser. (a) Blue-Detuned, (b) Red-Detuned

In practical terms, to simulate we will use the function *brmesolve*, from QuTiP library, with the argument a_{ops}, a nested list of a coupling operator and the phonon spectral density.

3.2.1.2 Simulations and Experiment

For simulating the excitation process the time domain was chosen to be $10 \cdot \sigma$ of the pulse (with the pulse centred at $5 \cdot \sigma$). Even though the rotating wave approximation removes high frequency terms and allows a lower sampling of the time domain, to describe accurately the pulse and system dynamics an increase of the sampling may be required. This is also true in the case of pulses with high pulse area (due to the many oscillation between ground and excited state). For these reasons the sampling of the time domain is variable and has been optimized, depending on the simulation parameters, to strike a balance between computation time required and artifacts in the system dynamics.

Tab.3.1 and Fig.3.6 show the time evolution and final state of a 2LS under resonant excitation *without* phonons in the $|g\rangle$ state at $t = 0ps$ interacting with a resonant Gaussian pulse of different pulse areas. It can be seen from Fig.3.6 that even though the final expectation value for $|X\rangle\langle X|$ is 0.5 for both $\Theta = \pi/2$ and $\Theta = 3\pi/2$, the final state differs for a phase. A resonant pulse moves the state only across the meridian line passing through $|g\rangle \pm i\,|X\rangle$. This means that, employing only resonant pulses and a single excitation step, we cannot generate an arbitrary quantum state.

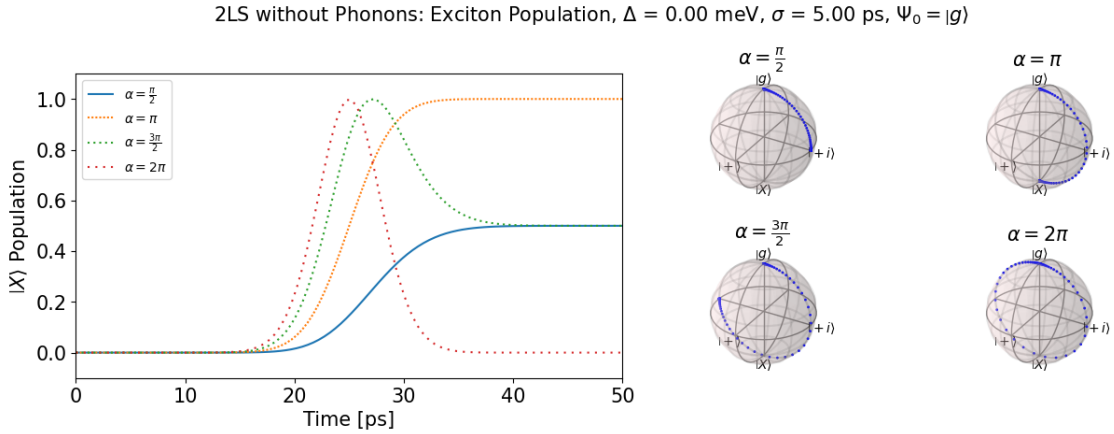


Figure 3.6: 2LS without phonons excited by a resonant Gaussian pulse of different pulse areas: time dynamics and evolution on Bloch Sphere

Detuning the pulse is then necessary to access states outside the meridian line, as it is shown in Fig.3.7 where the pulse has been blue-detuned by $0.1meV$, even

Initial State	Pulse Area	Final State
$\|g\rangle$	$\frac{\pi}{2}$	$\frac{1}{\sqrt{2}}(\|g\rangle + i\|X\rangle) = \|+i\rangle$
	π	$\|X\rangle$
	$\frac{3\pi}{2}$	$\frac{1}{\sqrt{2}}(\|g\rangle - i\|X\rangle) = \|-i\rangle$
	2π	$\|g\rangle$

Table 3.1: Final State of a 2LS excited at different pulse areas

if it will then prevent the system to evolve to the state $|X\rangle$.

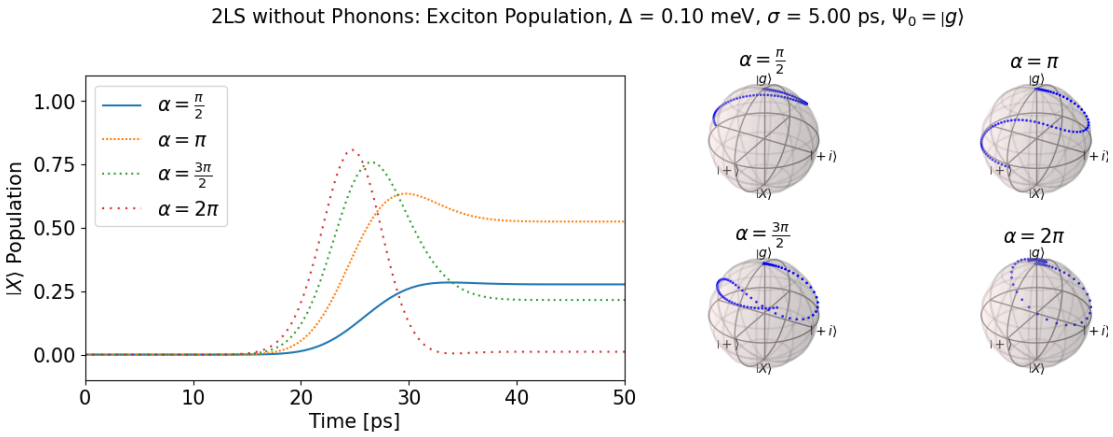


Figure 3.7: 2LS without phonons excited by a detuned Gaussian pulse of different pulse areas: time dynamics and evolution on Bloch Sphere

Another approach is to excite the system with a resonant pulse, with a pulse area less than π, and then let the state evolve, which equals to a precession along a parallel of the Bloch Sphere. This approach will not be simulated, due to the increased complexity and load of simulations after implementing a time evolution operator, but will be experimentally demonstrated with a Ramsey fringes experiment later in the chapter.

Just a note: if the initial state is an equal superposition of the states $\frac{1}{\sqrt{2}}(|g\rangle \pm |X\rangle)$ then there is no evolution in the system because these are the two original eigenstates of the Hamiltonian, see Fig.3.8.

After the pulse finishes the state population distribution does not evolve any further in this model, so a good parameter to monitor is the expectation value for $|X\rangle\langle X|$ at $t_f = 10 * \sigma$.

By changing pulse area the expected pattern of Rabi oscillations emerges, the population of the state $|X\rangle$ at t_f oscillates between 1 at pulse areas around $\Theta = (2n+1)\pi$ and 0 at $\Theta = 2n\pi$. By detuning the laser from the resonance condition,

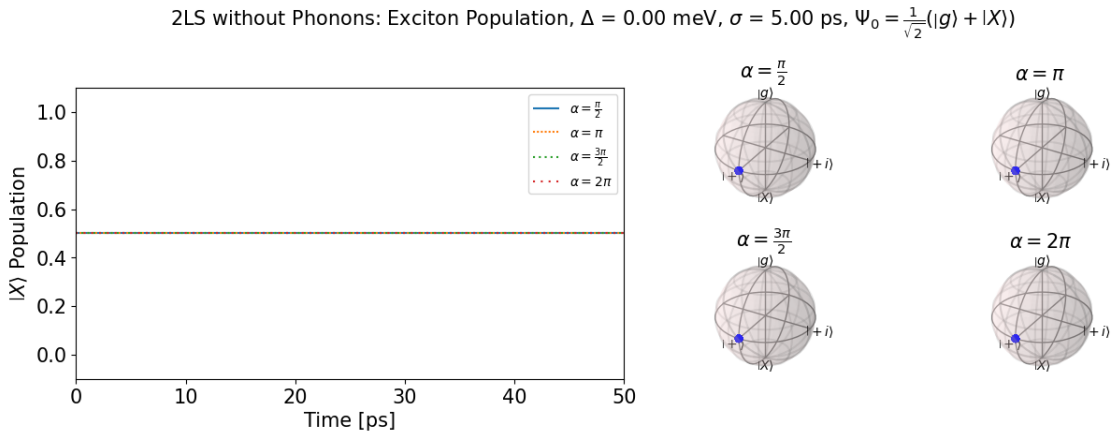


Figure 3.8: 2LS without phonons excited by a Gaussian pulse of different pulse areas ($\Psi_0 = \frac{1}{\sqrt{2}}(|g\rangle + |X\rangle)$): time dynamics and evolution on Bloch Sphere

the oscillating pattern is preserved but the maximum of the population drops for increasing absolute values of the detuning until it drops off to 0 for higher detuning, see Fig.3.9. The red contour highlights the conditions at which the population of the state $|X\rangle$ is more than 0.90.

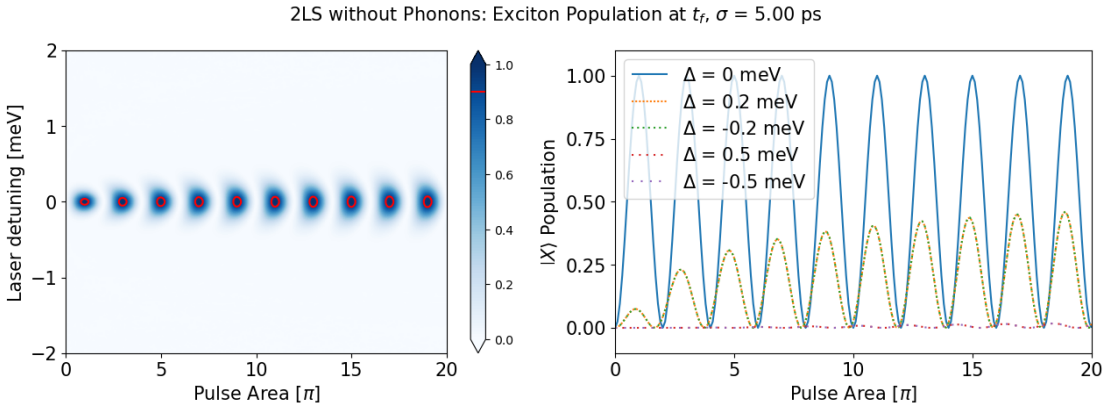


Figure 3.9: Exciton Population after a Gaussian pulse as function of pulse area and detuning for a 2LS *without* Phonon interaction

Simulating the system for different pulse duration (σ) it can be seen that in the absence of phonons the Rabi oscillations are damped faster for longer pulses, because these pulses are energetically narrower and have less overlap with the ground - exciton transition, see Fig.3.10. Shorter pulses though can be harder to suppress when signal is collected (one does not want the pumping pulse to

interfere with the dot signal), especially with a setup that uses notch filters, due to the broader energy width of the pulse.

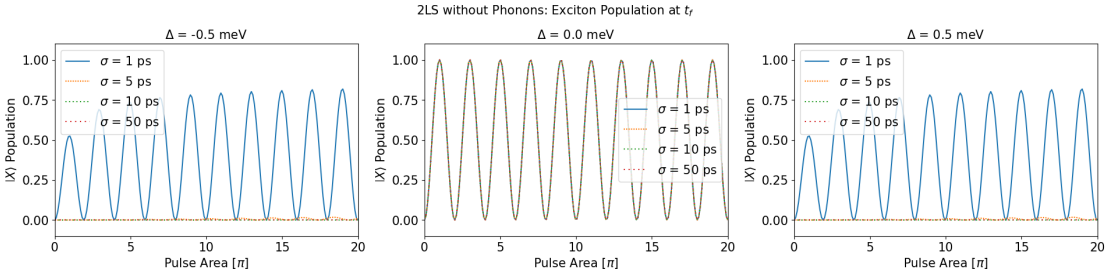


Figure 3.10: Excited State population after a Gaussian Pulse for a 2LS *without* Phonons, at different pulse length and detuning

Adding phonons to the 2LS and scanning again in the simulation pulse area and detuning, see Fig.3.11, the population of the state $|X\rangle$ under resonant condition $\hbar\omega = \hbar\omega_X$ drops below 0.9 for $\alpha > 7\pi$, but a plateau with $|X\rangle\langle X| > 0.9$ emerges at detuned and high area pulses (highlighted again by the red contour). For blue detuned pulses phonons have the effect of increasing the expected population of the excited state, up to an almost total inversion of the population for detuning of $0.5meV$ and pulse area of 15π. For red detuned pulses, instead, a damping of the oscillations takes place due to loss of coherence of the system. This asymmetric behaviour with respect of the detuning is due to the fact that at low temperature phonon absorption is less likely than phonon emission [11].

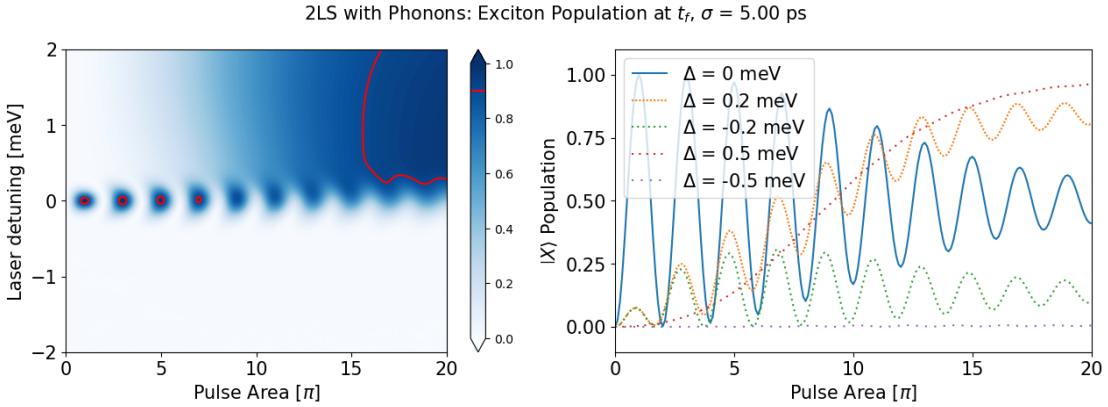


Figure 3.11: Exciton Population after a Gaussian pulse as function of pulse area and detuning for a 2LS with Phonon interaction

When phonons are introduced in the simulation and if the pulse is too short, for a given detuning, the excited state population does not reach a plateau and

is still oscillating. This phenomenon has been studied in terms of dressing and undressing of the states in [3] for rectangular pulses. When a Gaussian pulse is too short (and thus lacks a proper adiabatic switch-off of the electromagnetic field) it prevents the phonons from preparing the excited state with high fidelity and a slower switch off time can increase the gain of exciton occupation after the field intensity goes to zero. This is not fully represented in the plot Fig.3.12 because the longer Gaussian pulses have lower peak intensity, pushing the plateau to higher pulses areas (in [3] rectangular pulses have the same peak intensity and differ only for the speed of the switch-off process). From this analysis, we can take σ to be between $5ps$ and $10ps$ for phonon assisted excitation, because it strikes a good balance between low enough power to reach high fidelity population of the $|X\rangle$ state and stability of peak intensity fluctuations. Smaller σ not only introduce ripples in the $|X\rangle$ population but are also harder to filter with notch filters in a experimental setup, due to the larger frequency range spanned by the pulse.

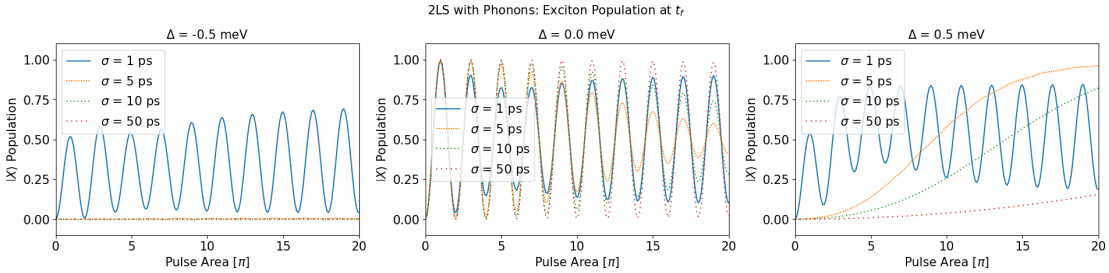


Figure 3.12: Excited State population after a Gaussian Pulse for a 2LS with Phonons, at different pulse length and detuning

The decoherence introduce by phonons can be visualized by exciting a 2LS with a resonant high area pulse. Without phonons the $|X\rangle$ state population would oscillate between 0 and 1 to then stabilize at the end of the pulse, which is equivalent to a rotation on a Bloch Sphere along a meridian passing for the states $|+1\rangle$ and $|-1\rangle$. By adding phonons we can now see that the oscillations are exponentially damped and the state moves not only along the meridian but also precesses along the x axis of the Bloch Sphere slightly going inside as well, see Fig.3.13 solid blue line. In the same figure we can observe that a detuning of $0.5meV$ produces an almost perfect inversion of the population from $|g\rangle$ state to $|X\rangle$ state, the decoherence introduced during the excitation process can reduce the Bloch vector length to almost 0.1, but is then recovered during the adiabatic switch-off of the pulse.

Due to the many sharp transitions of a QDs concentrated in narrow energy range, it may be difficult to approximate a particular state in the QD as a pure 2LS.

Nevertheless, phonon assisted excitation has been achieved with $GaAs$ QDs

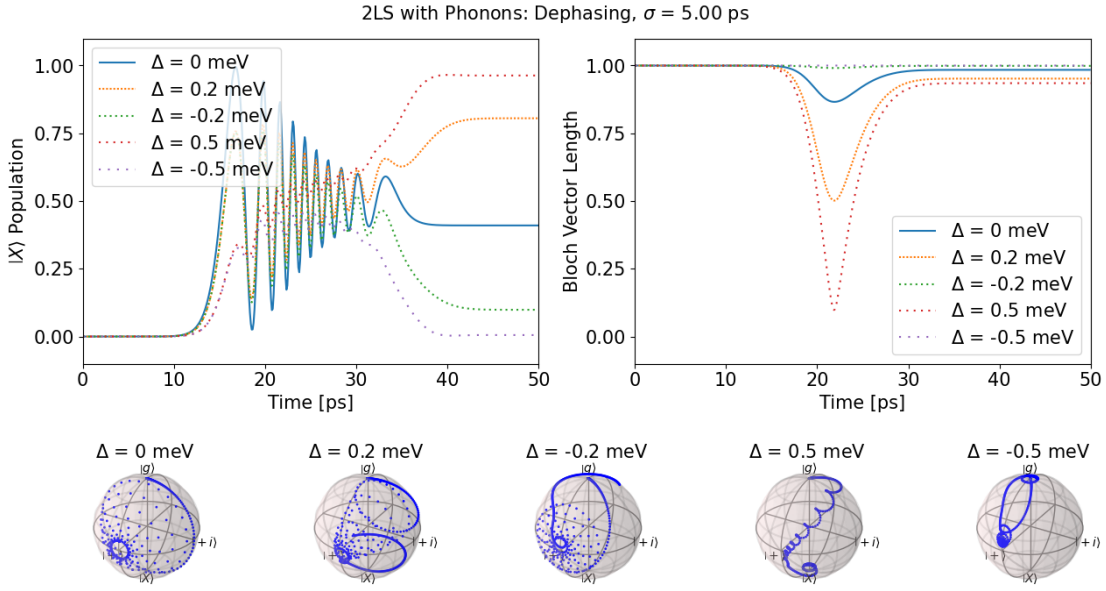


Figure 3.13: 2LS with phonons excited by a Gaussian pulse with $\alpha = 20\pi$ and different detuning. Time evolution of the $|X\rangle$ state population (left), Bloch vector Length (right), state on the Bloch Sphere (under).

by tuning the pulse shaped ps laser a few meV away from the X_{20}^{+} transition, see Fig.3.14. By studying the power dependence of the integrated CCD counts under the transition line, the expected monotonically raising behaviour, with a plateau at high power, emerges.

Despite the laser being resonant with the X_{10} transition, the X_{20}^{+} state is still populated, due to some hole trapping mechanics that happens in the pyramidal QDs which prevents exciton population. The same trapping mechanics probably makes the *GaAs* QDs mostly positively charged, as indicated by the fact the trion is usually brighter than the exciton in above-band excitation for most of the QDs studied.

Despite this trapping mechanism charging the QDs, phonon assisted excitation is still an inefficient process for this type of QDs, as it can be seen by the low value of integrated counts on the CCD. This is valid in general, and not just in this case where the laser has been set resonantly on the X_{10}, since changing the laser wavelength doesn't affect too much the brightness of the trion, unless we tune it to some of its resonances as will be discussed later in the chapter.

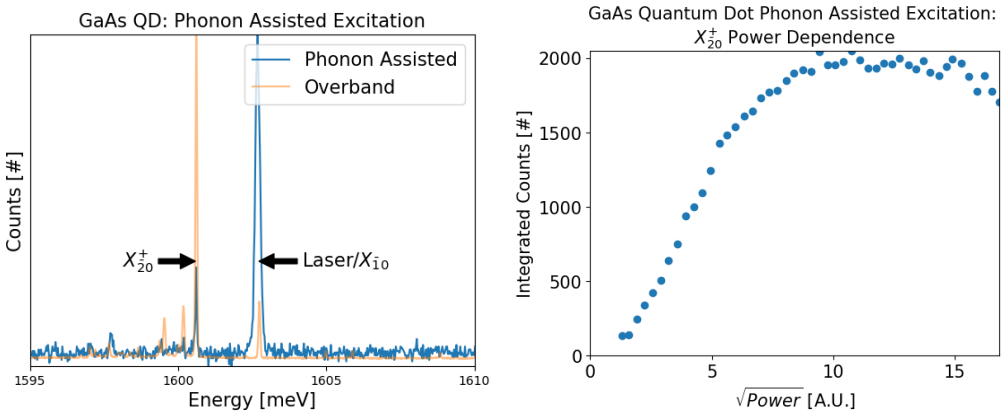


Figure 3.14: Spectrum and power dependence of trion population under phonon assisted excitation.

3.2.2 Three-Level System

The theoretical model of a 2LS can be extended to account for three levels, like in the case of $2X_{\bar{2}0} \rightarrow X_{\bar{1}0}$ cascade or a non-radiative relaxation of a $X^+_{11} \rightarrow X^+_{\bar{2}0}$.

3.2.2.1 XX - X Cascade

To describe a Biexciton - Exciton (XX - X) cascade we need at least three levels in our quantum system model, if we assume that the exciton state is degenerate in energy:

$$|g\rangle = \begin{pmatrix} 1 \\ 0 \\ 0 \end{pmatrix}; \quad |X\rangle = \begin{pmatrix} 0 \\ 1 \\ 0 \end{pmatrix}; \quad |XX\rangle = \begin{pmatrix} 0 \\ 0 \\ 1 \end{pmatrix} \tag{3.15}$$

The energy of the XX can be expressed as $\hbar\omega_{XX} = 2\hbar\omega_X - \Delta_B$, Δ_B is known as binding energy, if it is positive (negative) the $2X_{20}$ is said to be binding (antibinding).

$$\begin{aligned} H_0 &= \hbar\omega_g |g\rangle\langle g| + \hbar\omega_X |X\rangle\langle X| + (2\hbar\omega_X - \Delta_B)|XX\rangle\langle XX| = \\ &= \begin{pmatrix} 0 & 0 & 0 \\ 0 & \hbar\omega X & 0 \\ 0 & 0 & 2\hbar\omega X - \Delta_B \end{pmatrix} \end{aligned} \tag{3.16}$$

Typically $GaAs$ QDs in $Al_xGa_{1-x}As$ barriers have binding $2X_{20}$ with binding energies of $\sim 4meV(2nm)$, while $InGaAs$ QDs in $GaAs$ barriers have antibinding $2X_{20}$ with binding energies of $\sim -2meV$.

The X_{10} state, in absence of FSS, can accommodate two spin configurations of the electron - hole couple ($|\uparrow\Downarrow\rangle$ or $|\downarrow\Uparrow\rangle$) and can still be excited by a circular

polarized photon by addressing only one of the two spin configurations due to selection rules. The $2X_{20}$ state can be excited by a 2 photon process known as two photon excitation (TPE), that is resonant when $2\hbar\omega = 2\hbar\omega_X - \Delta_B$, see Fig.3.15, but the polarization of the photon has to be linear because two photons with the same circular polarization would generate the same spin configuration of the electron and hole and thus be forbidden by the Pauli Exclusion Principle in a $2X_{20}$ state ($|\uparrow\downarrow\Downarrow\Uparrow\rangle$).

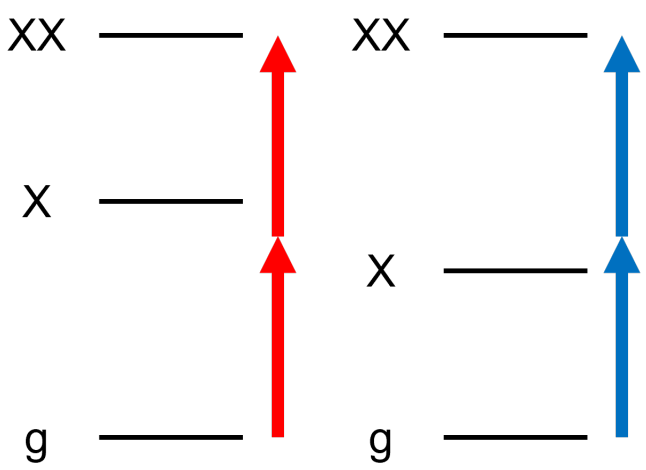


Figure 3.15: Three-Levels System and Laser for (a) Binding and (b) Antibinding QDs

In the binding (antibinding) case the TPE condition implies that the photons are red (blue) shifted from the X transition, the implications of this will be discussed later.

The interaction Hamiltonian for a linearly polarized pulse is:

$$\begin{aligned} H_I &= -\frac{\hbar}{2} f(t) e^{-i\omega t} \left(|X\rangle \langle g| + |XX\rangle \langle X| \right) \\ &\quad - \frac{\hbar}{2} f(t) e^{i\omega t} \left(|g\rangle \langle X| + |X\rangle \langle XX| \right) = \\ &= \begin{pmatrix} 0 & -\frac{\hbar}{2} f(t) e^{i\omega t} & 0 \\ -\frac{\hbar}{2} f(t) e^{-i\omega t} & 0 & -\frac{\hbar}{2} f(t) e^{i\omega t} \\ 0 & -\frac{\hbar}{2} f(t) e^{-i\omega t} & 0 \end{pmatrix} \end{aligned} \tag{3.17}$$

the coupling of the $2X_{20}$ to the ground state can be ignored due to the very high energy separation between the two states.

The total Hamiltonian of the system can be redefined as:

$$H_T = U H_{T_U} U^\dagger = \\ = \begin{pmatrix} 1 & 0 & 0 \\ 0 & e^{-i\omega t} & 0 \\ 0 & & e^{-i2\omega t} \end{pmatrix} \begin{pmatrix} 0 & -\frac{\hbar}{2}f(t) & 0 \\ -\frac{\hbar}{2}f(t) & \hbar\omega_X & -\frac{\hbar}{2}f(t) \\ 0 & -\frac{\hbar}{2}f(t) & 2\hbar\omega_X - \Delta_B \end{pmatrix} \\ \begin{pmatrix} 1 & 0 & 0 \\ 0 & e^{i\omega t} & 0 \\ 0 & & e^{i2\omega t} \end{pmatrix} \tag{3.18}$$

Following the same passages of Eq.3.8 we obtain the Hamiltonian in RWA for a XX - X cascade:

$$H_{RWA} = \begin{pmatrix} 0 & -\frac{\hbar}{2}f(t) & 0 \\ -\frac{\hbar}{2}f(t) & -\Delta & -\frac{\hbar}{2}f(t) \\ 0 & -\frac{\hbar}{2}f(t) & -2\Delta - \Delta_B \end{pmatrix} \tag{3.19}$$

After excitation the $2X_{20}$ state is populated and it decays with a lifetime $\tau_{X_{\bar{2}0}}$ to the X_{10} state.

The phonon coupling operator for a 3LS with a biexciton state is:

$$\hbar \left(|X\rangle \langle X| + 2 |XX\rangle \langle XX| \right) \sum_{\mathbf{q}} \left(g_{\mathbf{q}} b_{\mathbf{q}} + g_{\mathbf{q}} b_{\mathbf{q}}^\dagger \right) \tag{3.20}$$

Simulating the system for varying detuning and pulse area in the absence of phonon interaction, see Fig.3.16, the expected resonances of the X_{10} and $2X_{20}$ states appear at $\Delta = 0meV$ and $\Delta = \Delta_B/2$. Since no decay has been set for the $2X_{20}$ state in the model, the second resonance shows up only on the plot in the right panel, but in an experiment this would be a resonance of the X state as well because ideally all recombinations of the $2X_{20}$ will generate X states.

Adding phonons to the system the plateau for detuned high area pulses shows up as expected for both states, see Fig.3.17.

In the case of the antibinding $2X_{20}$ the TPE condition at $2\hbar\omega = 2\hbar\omega_X - \Delta_B \rightarrow \hbar\omega = 1meV$ is not only a resonance for the $2X_{20}$ but is also overlapping to the energy range in which the X is populated through phonon-assisted excitation. Therefore not all photons from the X states will come from the cascade and be entangled with the $2X_{20}$ photons.

This also fundamentally lowers the efficiency with which the $2X_{20}$ can be maximally populated under TPE, see Fig.3.18. This makes a binding QD intrinsically better for quantum computation when employing a XX - X cascade for generation of polarization entangled photons. It is worth noticing that XX state can be populated with high fidelity for detuned high area pulses in both binding and antibinding configurations.

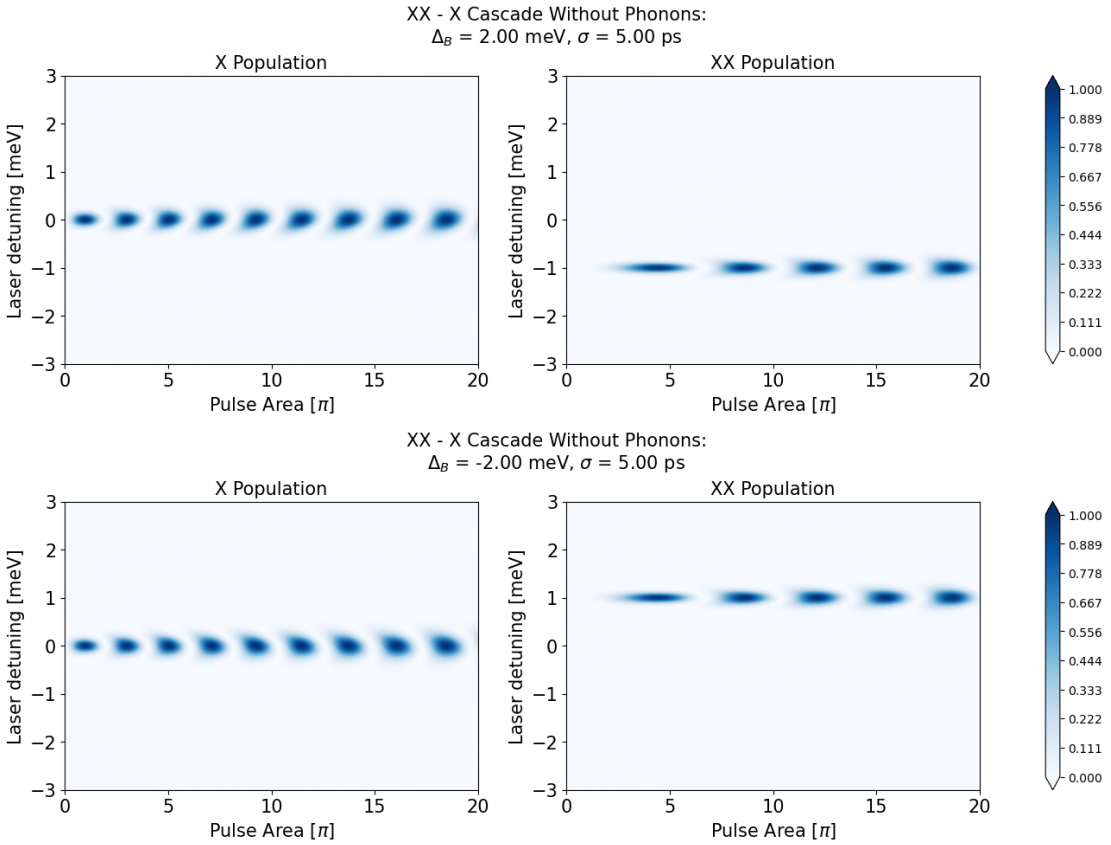


Figure 3.16: $|XX\rangle$ and $|X\rangle$ Population after a Gaussian pulse as function of pulse area and detuning for a cascade, binding (upper half) and antibing (lower half), *without* Phonon interaction. Due to the lack of a decay operator for the $2X_{\bar{2}0} \rightarrow X_{\bar{1}0}$ cascade the X_{10} is populated only when the pulse is on resonance with the transition, $\Delta = 0meV$. If a decay operator was introduced in the simulation the X_{10} population would should a second resonance that maps the $2X_{\bar{2}0}$ population when the pulse detuning is at TPE condition, $\Delta = \pm 1meV$.

TPE has been achieved for both $InGaAs$ and $GaAs$ QDs. For $GaAs$ QDs it can be seen how the spectrum under TPE, see Fig.3.19, is characterized by much fewer transition lines than under above-band excitation, see Fig.3.1 (left) Most of the missing transitions being positive trions states which are not populated under TPE, .

Other than the $X_{\bar{1}0}$ and $2X_{\bar{2}0}$ states, an additional state is present which we speculate is an excited state of the biexciton, $2X\bar{1}1$, as discussed in the next chapter. The aforementioned state can be populated because the laser tuned to the TPE conditions also excites the bulk $GaAs$, including defect levels which create

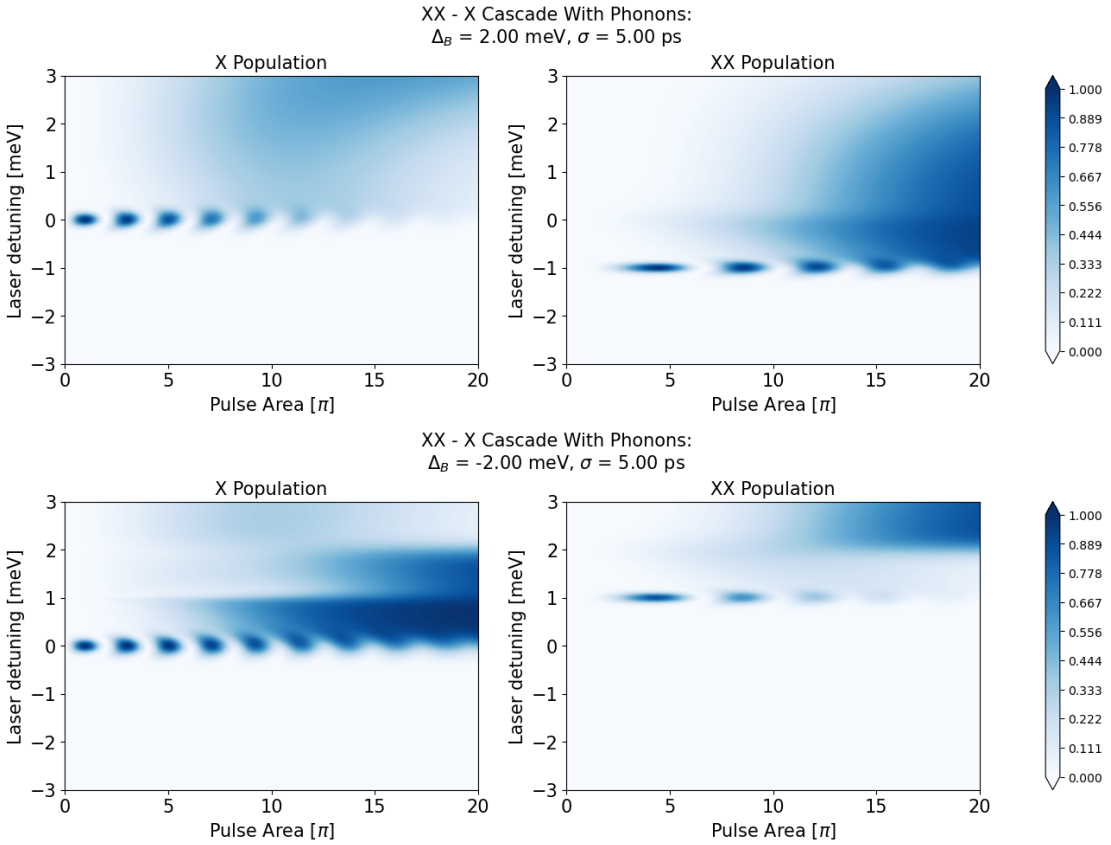


Figure 3.17: $|X_{\bar{2}0}\rangle$ and $|X\rangle$ Population after a Gaussian pulse as function of pulse area and detuning for a cascade, binding (upper row) and antibing (lower row), with Phonon interaction

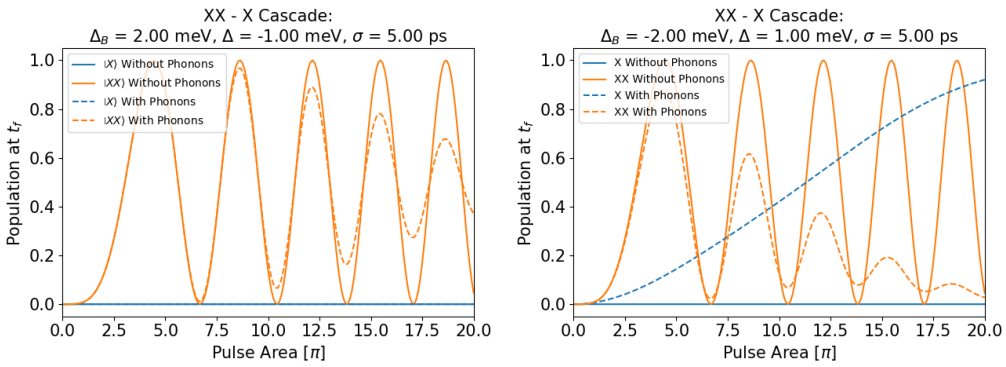


Figure 3.18: $|XX\rangle$ and $|X\rangle$ Populations after a Gaussian pulse as function of pulse area for a cascade at the TPE condition, binding (left) and antibinding (right)

free charges that can then populate the QD states once this is initialized in the $2X_{\bar{2}0}$ state.

Rabi oscillation of the $X_{\bar{1}0}$ and $2X_{\bar{2}0}$ populations are observed up to 7π, see Fig.3.19. Despite the $2X_{\bar{2}0}$ having an higher amplitude than the $X_{\bar{1}0}$ state in the spectrum, the integrated intensity of the $2X_{\bar{2}0}$ is less than the one of $X_{\bar{1}0}$ due to a smaller linewidth, $\sigma_{X_{\bar{2}0}} = 54.2 \pm 1.0\mu eV$, $\sigma_{X_{\bar{1}0}} = 71.9 \pm 1.0\mu eV$. The lower population of the $2X_{\bar{2}0}$ state is not due to phonon assisted excitation of the $X_{\bar{1}0}$ state, but to carrier escape to a higher energy level, marked as excited $2X_{\bar{1}1}$ in Fig.3.19. The $X_{\bar{1}0}$ state is then populated both by the ground and excited $2X_{\bar{1}1}$ cascades.

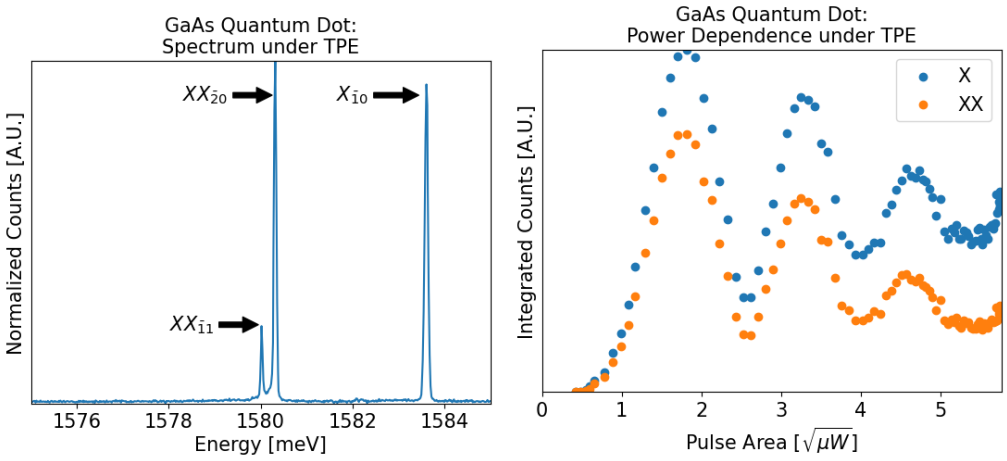


Figure 3.19: (Left) Typical GaAs QD spectrum under Two Photon Excitation (Right) Power dependence of $2X_{\bar{1}1}$ and $X_{\bar{1}0}$ states under Two Photon Excitation, showing Rabi oscillations up to 7π.

An autocorrelation curve of the $X_{\bar{1}0}$ transition gives a $g^2(0) = 0.028 \pm 0.002$ indicating single photon emission, see Fig.3.20.

InGaAs QDs in *GaAs* are typically anti-binding, for this reason the laser has to be tuned with an energy higher than the X_{10} transition for TPE, $E = E_{X_{\bar{1}0}} - E_B/2$. Fig.3.21 shows the spectrum under TPE of a dot with $E_B = -2.5meV$.

A clear asymmetry of the $2X_{20}$ and X_{10} intensities can be observed. This is due to the fact that, as discussed, not all photons of the X_{10} state come from the recombination cascade. By analysing the power dependence of the intensity of the two states, it can be seen how the $2X_{20}$ shows the expected damped oscillations, while X_{10} has a steadily increasing component which we attribute to the phonon-assisted excitation, see Fig.3.21.

An autocorrelation curve of the $2X_{20}$ and X_{10} transitions has been taken, yielding a $g^2_{2X_{20}}(0) = 0.006 \pm 0.001$ and $g^2_{X_{10}}(0) = 0.052 \pm 0.002$ indicating single photon

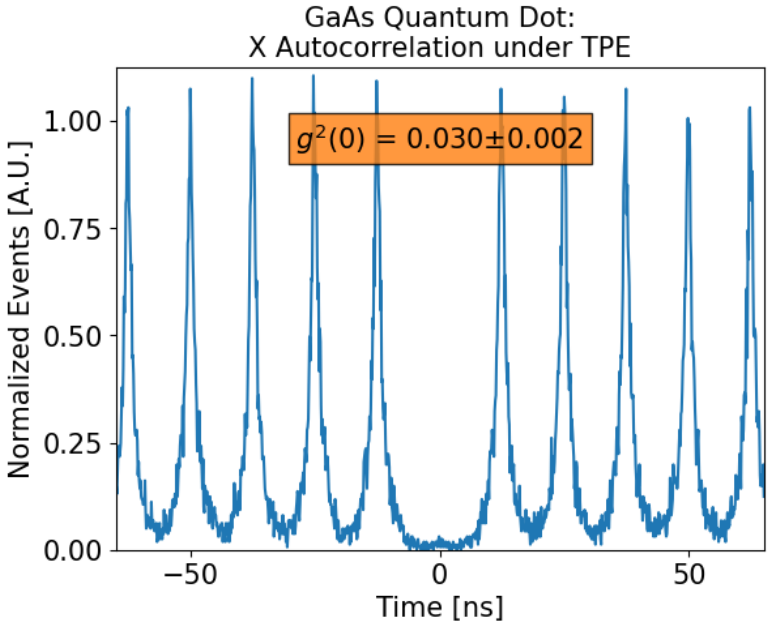


Figure 3.20: Autocorrelation measurement of the $X_{\bar{1}0}$ transition under Two Photon Excitation highlighting single photon emission.

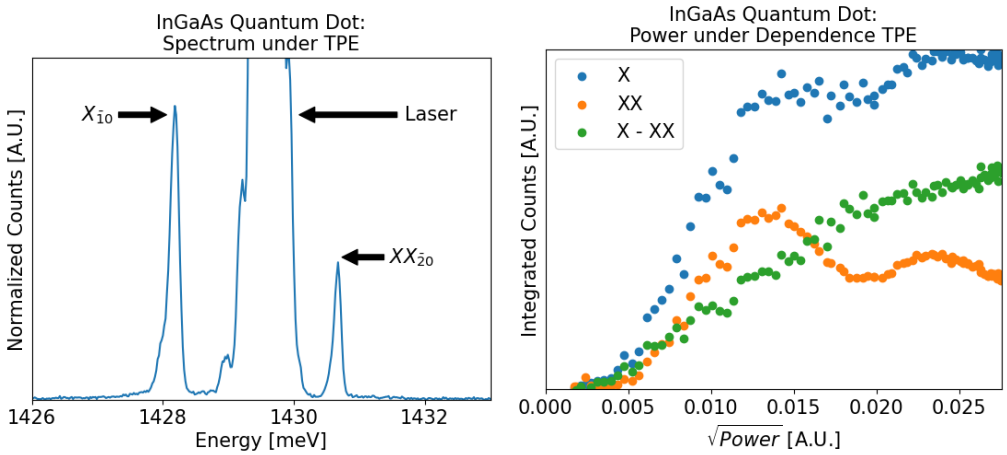


Figure 3.21: (Left) Typical *InGaAs* QD spectrum under Two Photon Excitation (Right) Power dependence of $2X_{20}$ and X_{10} states under Two Photon Excitation, showing the phonon assisted component in the emission of the X.

emission for this type of dots as well, Fig.3.22.

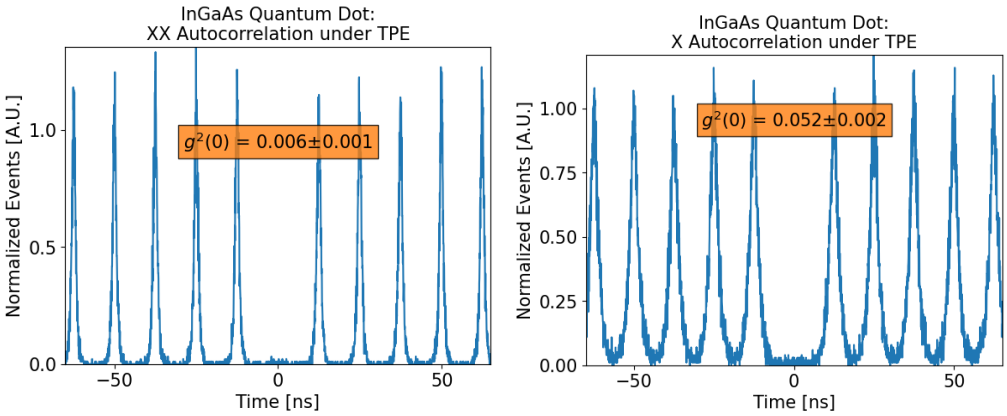


Figure 3.22: Autocorrelation measurement of the $2X_{20}$ and X_{10} transitions under Two Photon Excitation highlighting single photon emission.

3.2.2.2 X_{11}^{+} to X_{20}^{+} relaxation

With a Three-Level System we can also describe the non-radiative decay of an excited trion state to the trion:

$$|g\rangle = \begin{pmatrix} 1 \\ 0 \\ 0 \end{pmatrix}; \quad |X_{20}^{+}\rangle = \begin{pmatrix} 0 \\ 1 \\ 0 \end{pmatrix}; \quad |X_{11}^{+}\rangle = \begin{pmatrix} 0 \\ 0 \\ 1 \end{pmatrix} \tag{3.21}$$

If the excited trion level is energetically well separated from the ground trion and the laser is tuned to the frequency of the excited state, see Fig.3.23, the interaction Hamiltonian of the system can be written as:

$$\begin{aligned} H_I = &-\frac{\hbar}{2} f(t) e^{-i\omega t} \left(|X_{20}^{+}\rangle \langle g| + |X_{11}^{+}\rangle \langle g| \right) \\ &- \frac{\hbar}{2} f(t) e^{i\omega t} \left(|g\rangle \langle X_{20}^{+}| + |g\rangle \langle X_{11}^{+}| \right) = \\ &= \begin{pmatrix} 0 & -\frac{\hbar}{2} f(t) e^{i\omega t} & -\frac{\hbar}{2} f(t) e^{i\omega t} \\ -\frac{\hbar}{2} f(t) e^{-i\omega t} & 0 & 0 \\ -\frac{\hbar}{2} f(t) e^{-i\omega t} & 0 & 0 \end{pmatrix} \end{aligned} \tag{3.22}$$

for this case the field couples the ground level directly to the top level instead of being a two-photon process, and the laser polarization can be linear or circular.

Further details on how this polarization affects the polarization of the X_{20}^{+} will be discussed in a later chapter.

The total Hamiltonian in the RWA is:

$$H_{RWA} = \begin{pmatrix} 0 & -\frac{\hbar}{2} f(t) & -\frac{\hbar}{2} f(t) \\ -\frac{\hbar}{2} f(t) & -\Delta - \Delta_E & 0 \\ -\frac{\hbar}{2} f(t) & 0 & -\Delta \end{pmatrix} \tag{3.23}$$

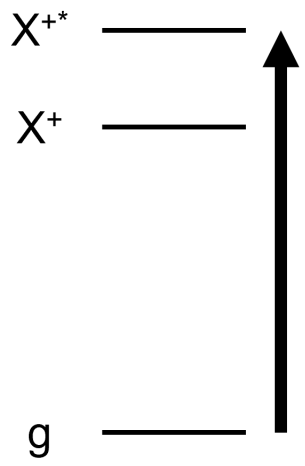


Figure 3.23: Three-Levels System and Laser in a non radiative cascade to X_{20}^{+}

because Δ_E in $GaAs$ QDs is typically $\sim 5meV$ the coupling of the electromagnetic field to the intermediate state is weak.

The excited trion will relax into the ground trion state with a lifetime $\tau_{X_{11}^{+}}$, thus the ground trion photoluminescence will reflect the population of the excited state.

As discussed in [12] using cascades introduces jitter in the emission of the last state and thus degrades the indistinguishability.

To simulate the intermediate state population we added a decay operator that couples the topmost level to the intermediate through a coupling constant $\gamma = \frac{1}{\sqrt{\tau}}$ and feed it to the *brmesolve* function through the c_{ops} argument. The time domain is set to be $10 \cdot \sigma + 10 \cdot \tau$ to account for a full decay of the excited state to the intermediate. Fig.3.24 shows that a very high fidelity population of the intermediate can be achieved through a π pulse of the topmost excited state and damping of the population happens due to phonon induced decoherence.

Oscillation up to a 4π have been observed in $GaAs$ QDs by pumping a resonance of the X_{20}^{+} state, a few meV higher than the ground state, see Fig.3.25. The oscillations are clearly damped, so as stated for phonon assisted excitation the absolute value of the y axis in terms of Trion state population can't be inferred and thus it will be measured in integrated counts.

A Ramsey fringes experiment has been set up to measure the dephasing time of excited trion state.

If we excited the state with a π power pulse we bring the dot from the ground to the excited state along a meridian line of the Bloch sphere, but if we split a π power pulse in 2 $\pi/2$ power pulses and set a delay between them, then the

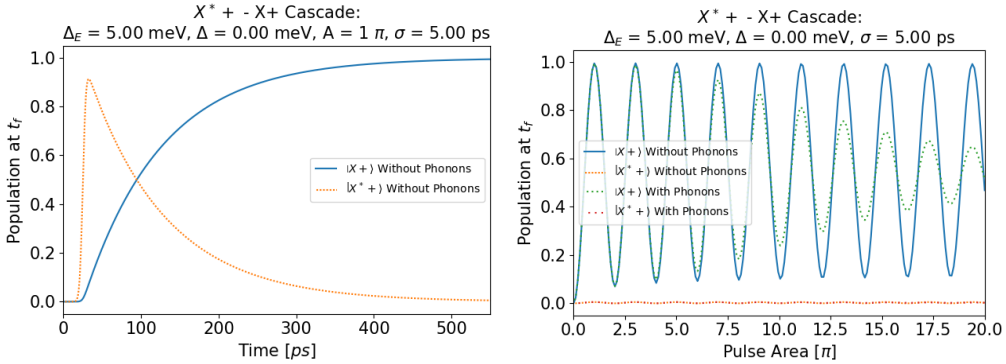


Figure 3.24: Time evolution of the $|X_{11}^+\rangle$ and $|X_{20}^+\rangle$ Populations during a Gaussian pulse and decay, finale states population as function of pulse area for a cascade

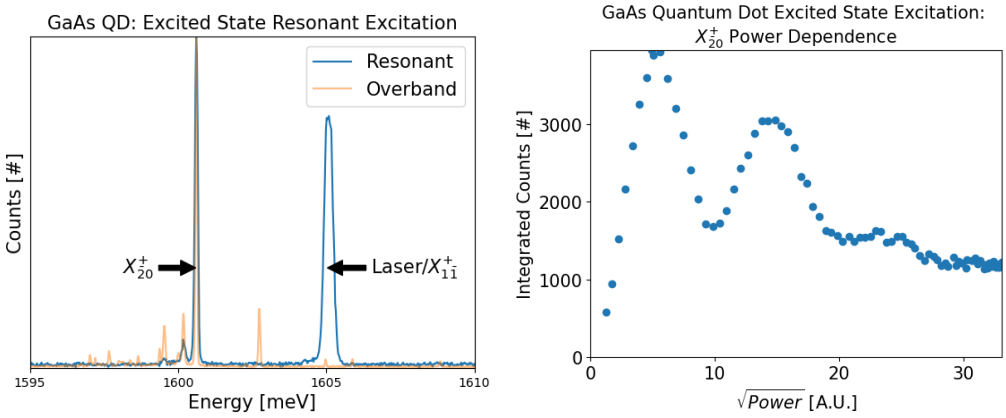


Figure 3.25: Spectrum and power dependence of trion population under resonant excitation of one of its excited states.

dot will be excited from the ground to the superposition state along the equator, see Tab.3.1, and it will start to precess along the equator due to dephasing. By adjusting the delay of the second $\pi/2$ pulse, we can time it so that it matches when the precession causes the state to be again at the $|+1\rangle$ state, reached after the first $\pi/2$ excitation; this delayed and timed $\pi/2$ pulse will then bring the system to the excited state. Plotting the excited state population as function of this delay gives the well known Ramsey fringes.

Of course this is an ideal case in which the dephasing causes precession only along the equator or parallel lines, which means that it keeps constant the ratio of ground and excited state populations, but changes only the relative phase. This is not a realistic scenario in the case of QDs because the dephasing will cause also loss of population, for example through charge escape of non radiative recombination,

so plotting the visibility of the Ramsey fringes, defined by Eq.3.24, as function of the delay will allow us to measure the decoherence time T_2^*.

$$I = \frac{I_{max} - I_{min}}{I_{max} + I_{min}} \tag{3.24}$$

An interferometer has been built by splitting the output of the ps pulse shaper using a $50R : 50T$ beam splitter. On one arm of the interferometer there is a retroreflector mounted a closed loop piezoelectric actuator for fine adjustment of the pulse delay, the other arm has the retroreflector mounted an a linear stage for coarse adjustment. For each step in the coarse delay arm, the fine delay arm scans a range which is roughly double the excitation wavelength with enough resolution to see the interference pattern, after this scan the piezo is sent back to the initial position for the next coarse step. The coarse range is chosen to span a wide range across the coherence time of the reflected and transmitted components of the pulse.

The intensity of the laser is monitored at each step of the coarse and fine delay arms by a power meter, which measures the reflection from a beam splitter placed in the excitation path. The intensity of the $X^+_{\bar{2}0}$ line is instead monitored by an APD after the grating of the spectrometer has been centred at the $X^+_{\bar{2}0}$ line.

By plotting the laser and $X^+_{\bar{2}0}$ line intensity as a function of the fine delay we can observe an oscillating pattern. If the delay of the coarse arm is set to be small enough then the reflected and transmitted component of the laser will interfere and the measurement will not yield useful information on the excitation process dynamics. But if the coarse delay is set to be longer than the coherence time of the two laser components then the oscillating pattern seen from the $X^+_{\bar{2}0}$ line intensity will give a reliable Ramsey fringes measurement.

Plotting the visibility, Eq.3.24, as function of the coarse delay we obtain that the excitation process has a dephasing time $T_2^* = 100ps$, see Fig.3.26

3.3 Dichromatic Excitation

To overcome the issues of time jitter in a state decay and suppression of the laser other excitation, schemes which use two-wavelength pulses have been investigated.

3.3.1 Red-and-Blue Detuned

As described in [13] the dichromatic pulse is composed of two sidebands detuned a certain $\Delta\omega$ from the transition. The pulse has no spectral overlap with the transition that we are interested in exciting and thus allows for easy filter or suppression of the laser.

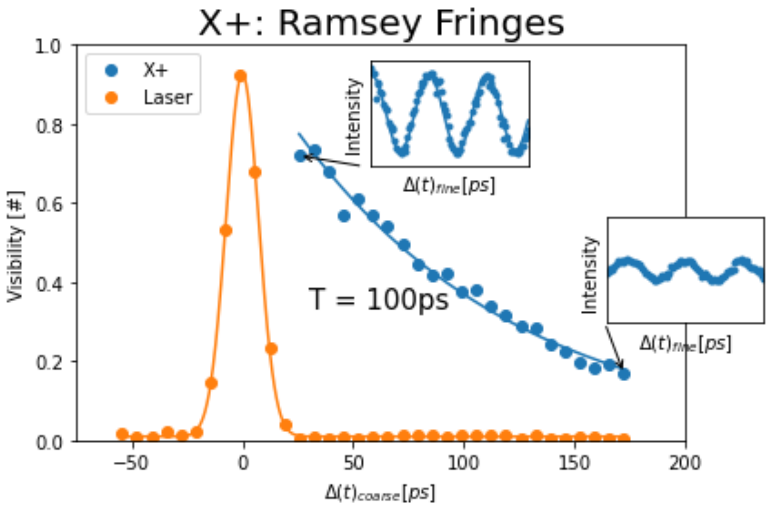


Figure 3.26: Ramsey fringes visibility for laser and X^+_{20} state as function of the coarse delay

To simplify the study we set the pulse envelope to be the same and the phase to be 0, the only parameters that will change is the pulse separation compared to the transition that we want to excite, keeping the two sidebands symmetric, $\Delta\omega_{red} = -\Delta\omega_{blue}$, as well and the pulse area of each sideband, this mean that if $\alpha_{red} = 0\pi$ ($\alpha_{blue} = 0\pi$) the excitation will be with a purely Blue (Red) detuned pulse. As pointed out in [13] the phase could still be engineered to modulate the pulse area over time if we want to sweep different paths along the Bloch sphere.

Due to the two wavelength components the pulse can be written as:

$$\begin{aligned} &\frac{1}{\sigma\sqrt{2\pi}} e^{-\frac{(t-\tau)^2}{2\sigma^2}} \left(\alpha_{red} e^{-i\omega_{red}t} + \alpha_{blue} e^{-i\omega_{blue}t}\right) = \\ =&\frac{1}{\sigma\sqrt{2\pi}} e^{-\frac{(t-\tau)^2}{2\sigma^2}} \left(\alpha_{red} e^{-i(\omega+\Delta\omega)t} + \alpha_{blue} e^{-i(\omega-\Delta\omega)t}\right) = \\ =&\frac{1}{\sigma\sqrt{2\pi}} e^{-\frac{(t-\tau)^2}{2\sigma^2}} e^{i\omega t} \left(\alpha_{red} e^{-i\Delta\omega t} + \alpha_{blue} e^{i\Delta\omega t}\right) = \end{aligned} \tag{3.25}$$

In a RWA of frequency ω the pulse envelope becomes a Gaussian modulated by an oscillating term of frequency equal to the detuning of the two color components.

$$\frac{1}{\sigma\sqrt{2\pi}} e^{-\frac{(t-\tau)^2}{2\sigma^2}} \left(\alpha_{red} e^{-i\Delta\omega t} + \alpha_{blue} e^{i\Delta\omega t}\right) \tag{3.26}$$

According to [14] the final population of the excited state depends on the pulses amplitudes and parameter $\eta = \sigma\Delta\omega$.

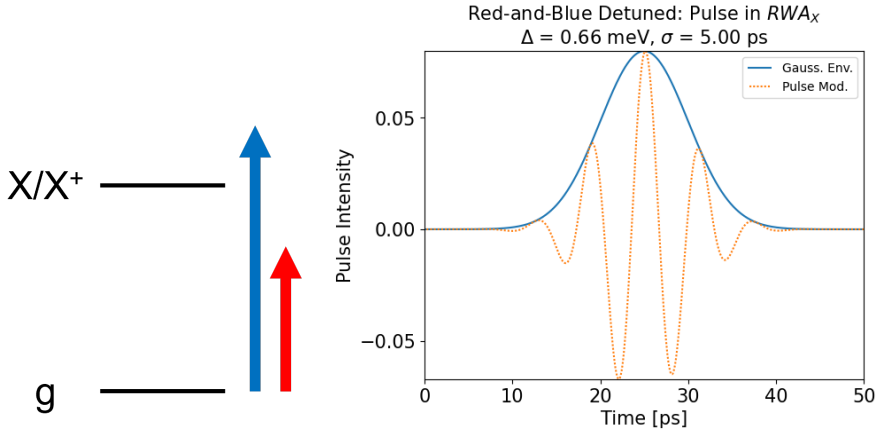


Figure 3.27: (left) Two-Levels System under Red-and-Blue-Detuned Excitation (right) Gaussian envelope of the pulse and its modulation introduced by the two wavelengths

For $\eta = 1$, see Fig.3.28, we can observe that the pattern is symmetric with respect of the pulse area of the two pulses and almost pure Rabi-like oscillations appear along the diagonal.

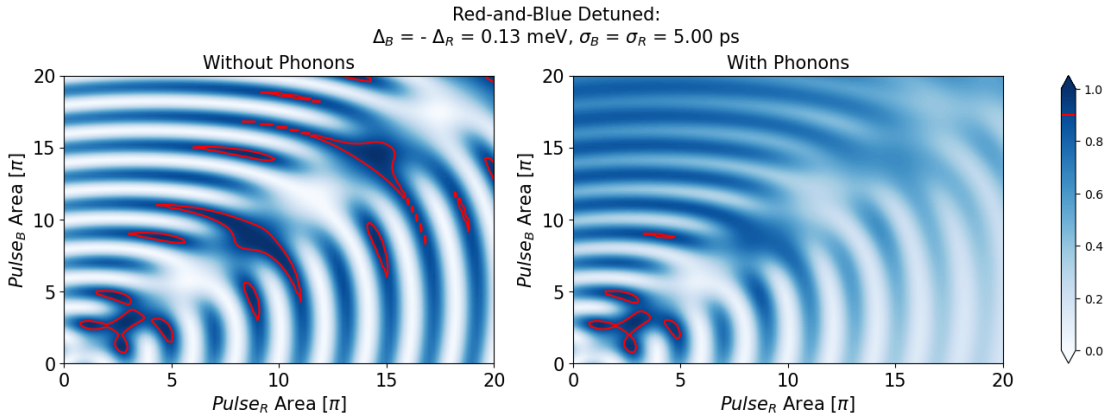


Figure 3.28: Red-and-Blue excitation for $\eta = 1$

For $\eta = 3$, see Fig.3.29, a more complicated pattern can be observed.

By adding phonons to the system we can also observe that the first simulation is affected more or less symmetrically, with a fidelity generally lower than 0.9, while $\eta = 3$ the phonon affect the two sideband in different manners, and as expected a purely red detuned pulse (for $\alpha_{blue} = 0\pi$) does not populate efficiently the state with the help of phonons, while a purely blue detuned pulse ($\alpha_{red} = 0\pi$) has a plateau of the population at high pulse area.

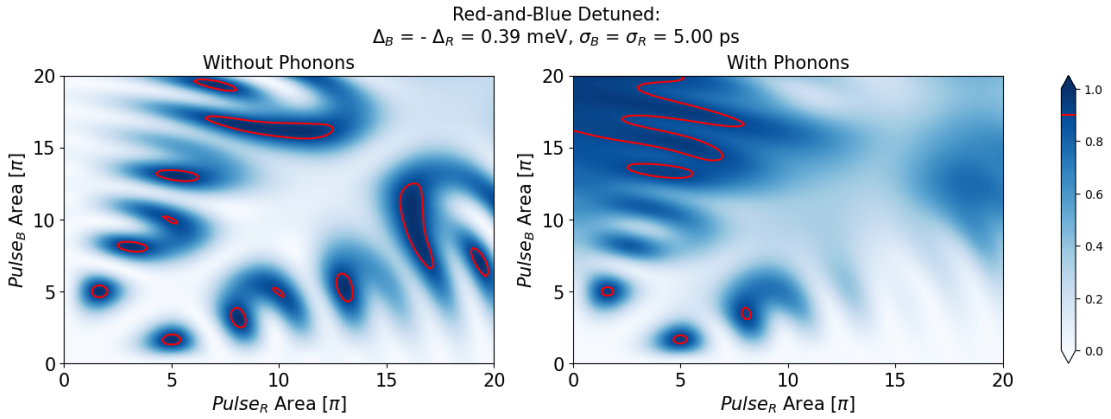


Figure 3.29: Red-and-Blue excitation for $\eta = 3$

We experimentally generate a dichromatic pulse by placing a beam stop, a thin strip of metal or an allen key, in the middle of a slit of a pulse shaper like the one described in the previous chapter. It can be challenging to observe such patterns with a setup like the one described, due to the fact that the power of the two pulses can't be individually controlled, because the two pulses are suppressed by the same amount with the HWP + polarizer at the output of the polarization maintaining fiber.

Also it should be noted that, at the time of experiment, we had no access to the results from [14] and of our later simulations. For this reason we did not take into account the effect of the pulse duration, due to the dependence from the $\eta = \sigma\Delta\omega$ parameter.

Nonetheless, we were able to excite the sample even though the power dependence of the X_{20}^{+} is closer to the behaviour expected from phonon assisted excitation, with the roll off at higher pulse areas, see Fig.3.30.

3.3.2 SUPER

In a two levels system, a single highly detuned laser pulses does not induce significant population of the excited state, especially if the detuning is beyond the phonon spectral density maximum. It has been shown in [15] that population inversion can be achieved by switching between two off-resonant (red-detuned) frequencies. This scheme relies on the periodic change of the Rabi frequency that leads to a swing-up behaviour of the excited state population. By themselves the individual pulses would lead to a negligible population, but the frequency modulation of the excitation pulse allows the population inversion of the system. The scheme is known as Swing-UP of the quantum EmitteR population, SUPER.

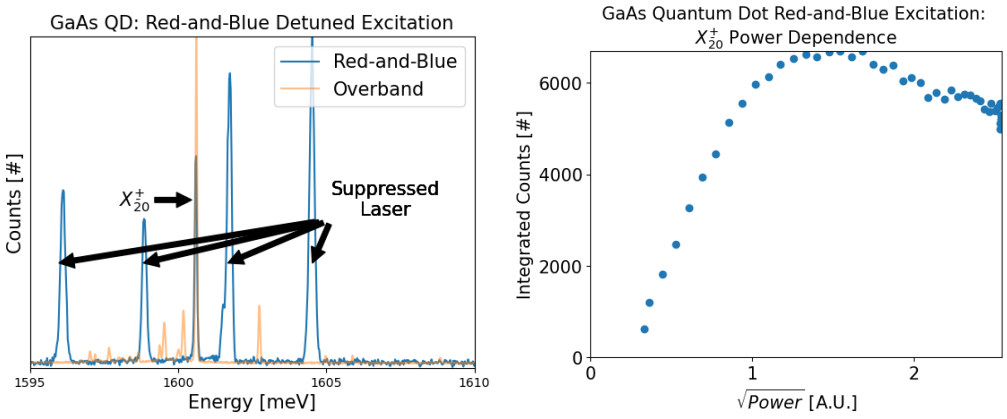


Figure 3.30: (left) Spectrum of GaAs QD under Red-and-Blue-Detuned Excitation (right) Power Dependence of X_{20}^{+}

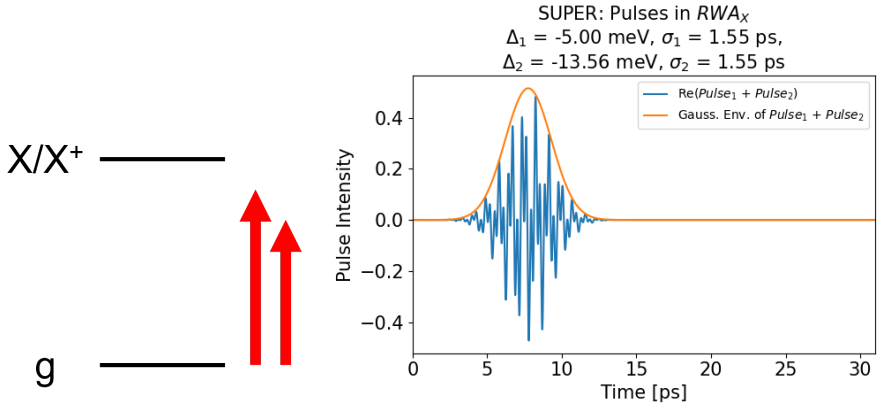


Figure 3.31: (left) Two-Levels System under SUPER Excitation (right) Gaussian envelope of the pulse and its modulation introduced by the two wavelengths

The above-mentioned publication goes over several pulses envelopes, like rectangular wave and gaussian. The first case has not be studied in the following simulations, because, usually, experimental implementation of excitation processes relies on Gaussian pulses.

For this excitation process, the interaction Hamiltonian can be expressed as:

$$\begin{aligned} H_I = &-\frac{\hbar}{2}\left[f_1(t)e^{-i\omega_1 t} + f_2(t-\tau)e^{-i\omega_2 t}\right]|X\rangle\langle g| \\ &-\frac{\hbar}{2}\left[f_1(t)e^{i\omega_1 t} + f_2(t-\tau)e^{i\omega_2 t}\right]|g\rangle\langle X| \end{aligned} \tag{3.27}$$

where $f_1(t)$ and $f_2(t-\tau)$ are the Gaussian envelopes, ω_1 and ω_2 the wavelengths of the two pulses and τ the relative delay between first and second pulse.

In this case, it is convenient to use the frequency ω_X of the $|X\rangle$ state for the RWA. Following the steps from Eq.3.6 to Eq.3.10, we find:

$$H_{RWA} = \begin{pmatrix} 0 & -\frac{\hbar}{2} & \left[f_1(t)e^{i\delta_1 t} + f_2(t-\tau)e^{i\delta_2 t}\right] \\ -\frac{\hbar}{2} & \left[f_1(t)e^{-i\delta_1 t} + f_2(t-\tau)e^{-i\delta_2 t}\right] & 0 \end{pmatrix} \tag{3.28}$$

where $\delta_{1/2} = \omega_{1/2} - \omega_X$. With this RWA the pulses envelopes become a Gaussian modulated by an oscillating term with the frequency of the excited state transition.

Just like the red-and-blue detuned pulses it involves the use of dichromatic excitation but in this case both wavelengths are red detuned from the transition that we want to address, this should in theory decouple the excitation process from the phonons for two reasons: first we are working with red detuned pulses at cryogenic temperatures, second the two wavelengths can be chosen to have a very large detuning from the transition that we want to drive, moving them away from the phonon spectral distribution, see Fig.3.4.

Not all combinations of parameters are suitable to achieve high fidelity occupation of a desired state and the following relations of the detunings holds [15]:

$$\Delta\omega_2 = \Delta\omega_1 - \sqrt{f_1^2(t=0) + \Delta\omega_1^2} \tag{3.29}$$

the second pulse will then be detuned further away from the first and the detuning can be pushed to even tens of meV allowing for a much easier suppression of the laser with the use of long-pass filters.

As the scheme before, the pulses can be produced in the lab by placing a beam stop in the middle of a slit of a pulse shaper, if the separation of the two wavelength components is small enough to fit in a fs pulse spectrum. Otherwise a set of two pulse shapers or sources will be needed.

One challenge of this scheme is the high pulse area required. A 10π pulse area requires 100 times the laser power of a pulse with π pulse area, so this scheme can be realistically used only on samples which require low power to be excited to begin with.

In [15] a table is given with a set of suitable pulse parameters to achieve population inversion of a 2LS, see Tab.3.2. Simulations have been run using all the provided parameters and we were able to reproduce close to unity occupation of the excited state level. For one example of the simulation results, see Fig.3.32 blue curve in the bottom row of plots.

From Fig.3.32, blue curves from first two rows of plots, we can observe that the two individual pulses by themselves can't drive the 2LS from a ground to an excited state, but if we use both wavelengths then an oscillating behaviour of the excited state population drives the system to a full stable inversion once the pulse is switched off, see Fig.3.32 bottom row.

$\hbar\Delta_1$ (meV)	$\hbar\Delta_1$ (meV)	σ_1 (ps)	σ_2 (ps)	α_1 (π)	α_2 (π)	τ (ps)
-5.0	-11.7826	4.50	7.10	25.00	25.00	0.00
-5.0	-13.5624	1.55	1.55	13.06	10.45	0.00
-5.0	-12.5522	2.23	5.00	15.30	28.31	2.40
-8.0	-19.1630	2.40	3.04	22.65	19.29	-0.73
-11.0	-25.7450	2.50	3.60	28.57	27.35	1.50

Table 3.2: Set of example parameters for the SUPER scheme which lead to close to unity occupation of the excited state level, taken from [15]

Apparently phonon do have an effect on the 2LS even under this type of excitation, see orange curves in Fig.3.32. For all set of parameters provided in Tab.3.2, we have found that, if the pulses are simulated individually (first two rows of plots), the occupation of the excited state is higher after introducing phonon in the simulation. On the other hand, combining the two pulses with the SUPER scheme, we have observed a reduction of the excited state population after the phonon are introduced in the simulation.

Results for both cases are unexpected as phonons should have no noticeable effect for red-detuned pulses. This could be an artifact of the simulation due to the choice of frequency for the RWA, as now the hamiltonian is anti-diagonal, see Eq.3.28. The exciton frequency in the bottom right term of the Hamiltonian is removed by the approximation, only the oscillating terms depend on the detuning, which are complex conjugate, probably the way the phonon bath is fed to the simulator is not compatible with the assumptions.

Also the detuning is so far away from the transition that maybe even the RWA is not valid any more. This approximation was supposed to remove high frequency terms from the calculations, but an high frequency parameter itself has been set, therefore it is reasonable to expect that the approximation could diverge and that an expansion which accounts for higher orders is needed.

Further study is required to understand why the simulation results are not in accordance with the theory under these conditions.

3.4 Conclusions

In this chapter we have shown how several excitation models can be simulated using the open source library QuTiP and how these results can be reproduced in the lab. Insight on the phonon distribution of a given dot could be gained in theory by changing the parameters that influence the strength of coupling (like dot size) to match experimental data.

Of all the excitation methods reported above none is perfect and each has some

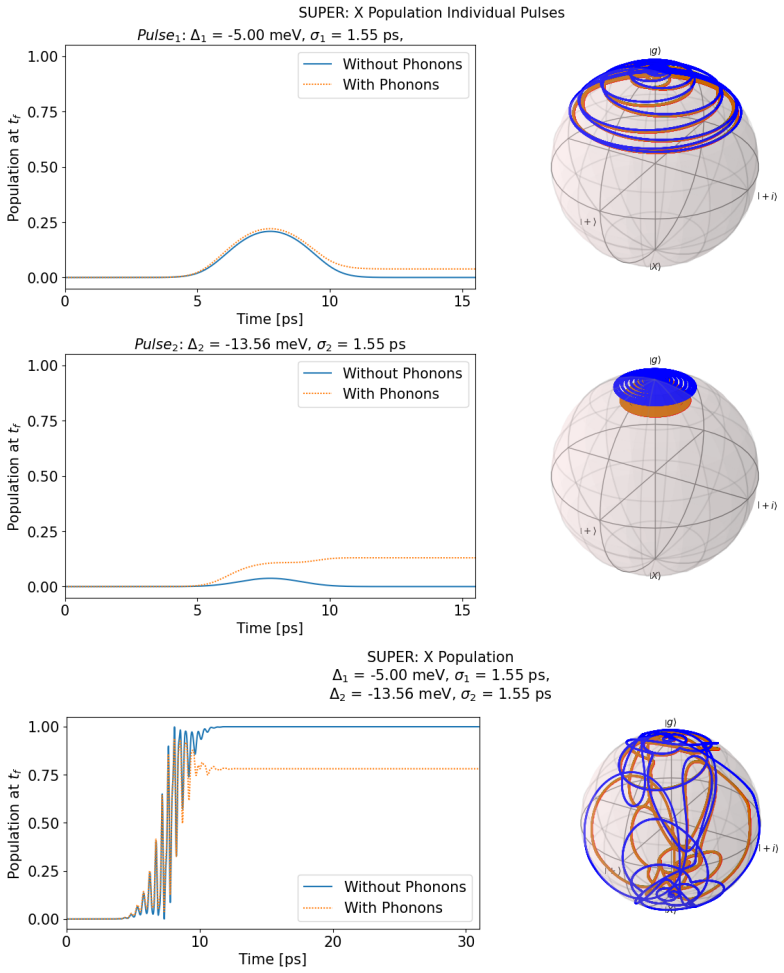


Figure 3.32: Two-Levels System under SUPER Excitation. First two rows of plots are the system excited with single pulses, with and without phonons. Last row is the system excited with the pulses combined according to the SUPER scheme. The images shows the simulation for the second set of parameters from Tab.3.2 [15], similar results have been obtained by the simulations for the other sets as well.

drawback that make it more or less suitable in a laboratory.

A fully resonant excitation is too restrictive, since the pulse and target state have to overlap energetically, the suppression of the laser light can't be achieved by spectral filtering but only by crosspolarizing detection and excitation, for example by pumping a degenerate state, like an X_{20}^{+}, with a linearly polarized laser, this will also suppress half of the population from the state.

Phonon assisted excitation allows for easy spectral, using notch filters, and spa-

tial filtering, using gratings. This type of excitation is also more resilient against laser power and frequency fluctuations due to the plateau of high fidelity initialization. Later in the thesis it will also be shown that a specific spin configuration can be initialized with high fidelity for a X^+ state. The maximum of the phonon distribution can also be tuned by changing the QD geometrical and material properties. The main drawback can be the high power required to reach high brightness, due to the high pulse area which can be sometimes challenging to suppress and can introduce background photons in the detection process. Also, in the case of $GaAs$ QDs, the excitation of bulk states introduce spurious charges and other recombination channels.

Resonant excitation of an excited state that relaxes to a intermediate X^+ state shows higher brightness than phonon-assisted excitation in the case of $GaAs$ QDs. The large separation between the two transitions allows for easier suppression of the laser at detection level. The main drawback is the jitter introduced in the emission of the X^+ photon, due to the relaxation of the excited state and the excitation of few other states, like hot trions and bulk.

Two-Photon Excitation has been a standard excitation scheme in the QD community. Other than allowing easy filtering of the laser, it can generate on-demand entangled photon pairs. Just like the aforementioned excitation of the trion, jitter is introduced in the X photon emission due to the cascade, thus reducing indistinguishability. For antibinding QDs this can also be a non-ideal excitation method due to the phonon-assisted component of the X state.

The Red-and-Blue detuned excitation scheme has the advantage of being a coherent excitation method and because the side bands can be detuned it can be easily suppressed through spectral or spatial filtering, for example picking up the transition signal with the reflection of a notch filter. One main drawback is that the blue detuned pulse will couple to the phonon bath, thus reducing the population of the excited state due to dephasing.

The SUPER scheme allows for even easier filtering of the laser due to the much bigger energy separation. With this scheme it could be possible to filter the laser background with a long pass filter, which is a much cheaper approach than using notch filters. Because the process is coherent it has all the advantages of resonant excitation, and also the pulses can be theoretically decoupled from the phonon bath. One major drawback is the typically higher power required to excite the targeted state, a 20π pulse requires 400 times the power of a pulse of area π, making this approach suitable only for samples which already require very low power to be efficiently excited, like QDs in cavities. Also the pulse shaping process can be more complicated due to the need to tune very well the two wavelength separation.

References

[1] David P. DiVincenzo. "The Physical Implementation of Quantum Computation". In: *Fortschritte der Physik* 48.9-11 (2000). DOI: https://doi.org/10.1002/1521-3978(200009)48:9/11<771::AID-PROP771>3.0.CO;2-E.

[2] Per-Lennart Ardelt et al. "Dissipative preparation of the exciton and biexciton in self-assembled quantum dots on picosecond time scales". In: *Phys. Rev. B* 90 (24 Dec. 2014). DOI: 10.1103/PhysRevB.90.241404.

[3] A. M. Barth et al. "Fast and selective phonon-assisted state preparation of a quantum dot by adiabatic undressing". In: *Phys. Rev. B* 94 (4 July 2016). DOI: 10.1103/PhysRevB.94.045306.

[4] J.R. Johansson, P.D. Nation, and Franco Nori. "QuTiP: An open-source Python framework for the dynamics of open quantum systems". In: *Computer Physics Communications* 183.8 (2012). DOI: https://doi.org/10.1016/j.cpc.2012.02.021.

[5] P. Michler. *Single Semiconductor Quantum Dots*. Springer Berlin, Heidelberg, June 2009. ISBN: 978-3-540-87445-4.

[6] M.O. Scully and M.S. Zubairy. *Quantum Optics*. Cambridge University Press, 1997. ISBN: 9780521435956. URL: https://books.google.it/books?id=20ISsQCKKmQC.

[7] B. Krummheuer, V. M. Axt, and T. Kuhn. "Theory of pure dephasing and the resulting absorption line shape in semiconductor quantum dots". In: *Phys. Rev. B* 65 (19 May 2002). DOI: 10.1103/PhysRevB.65.195313.

[8] A. Vagov et al. "Real-time path integrals for quantum dots: Quantum dissipative dynamics with superohmic environment coupling". In: *Phys. Rev. B* 83 (9 Mar. 2011). DOI: 10.1103/PhysRevB.83.094303.

[9] A. Vagov et al. "Nonmonotonous temperature dependence of the initial decoherence in quantum dots". In: *Phys. Rev. B* 70 (20 Nov. 2004). DOI: 10.1103/PhysRevB.70.201305.

[10] D. E. Reiter et al. "The role of phonons for exciton and biexciton generation in an optically driven quantum dot". In: *Journal of Physics: Condensed Matter* 26.42 (Oct. 2014). DOI: 10.1088/0953-8984/26/42/423203. URL: https://dx.doi.org/10.1088/0953-8984/26/42/423203.

[11] D. E. Reiter et al. "The role of phonons for exciton and biexciton generation in an optically driven quantum dot". In: *Journal of Physics: Condensed Matter* 26.42 (Oct. 2014). DOI: 10.1088/0953-8984/26/42/423203.

[12] E. Schöll et al. "Crux of Using the Cascaded Emission of a Three-Level Quantum Ladder System to Generate Indistinguishable Photons". In: *Phys. Rev. Lett.* 125 (23 Dec. 2020). DOI: 10.1103/PhysRevLett.125.233605.

[13] Y.-M. He et al. "Coherently driving a single quantum two-level system with dichromatic laser pulses". In: *Nature Physics* 15.9 (Sept. 2019). DOI: 10.1038/s41567-019-0585-6.

[14] L. Vannucci and N. Gregersen. "Highly efficient and indistinguishable single-photon sources via phonon-decoupled two-color excitation". In: *Phys. Rev. B* 107 (19 May 2023). DOI: 10.1103/PhysRevB.107.195306.

[15] T. K. Bracht et al. "Swing-Up of Quantum Emitter Population Using Detuned Pulses". In: *PRX Quantum* 2 (4 Dec. 2021). DOI: 10.1103/PRXQuantum.2.040354.

Chapter 4

Energetic Structure of GaAs Quantum Dots

In the previous chapters we have discussed how QDs could be used to implement quantum computing through different protocols, circuit model or one-way quantum computing.

We have also discussed the possibility of using QDs for single and entangled photon emission, through the $2X_{\bar{2}0} \rightarrow X_{\bar{1}0}$ cascade or the linear cluster state protocol using a trion state.

In the following chapter we will focus on the study of the energetic structure of $GaAs$ QDs in $Al_xGa_{1-x}As$. Based on previous studies from the group, [1], these QD have been sandwiched by superlattice structures made of alternating layers of $AlAs$ and $GaAs$ to detach the QD from the vertical wires that form due to material segregation and improve its symmetry-related optical properties.

Investigation of $GaAs$ QD energetic structure is a fundamental step to understand the dynamics involved in the cluster state generation and manipulation and in general to engineer QDs with the desiderated optical properties. Employing a variety of spectroscopic techniques, such as polarization and time resolved microphotoluminescence, and devices, like diode structures and piezoelectric devices, we were able to match most of transition lines with the corresponding excitonic states and characterize their polarization properties to probe the QD symmetry.

We will also show that an approach purely based on calculations of point group selection rules [2] is not enough to explain the typical spectra of our QDs.

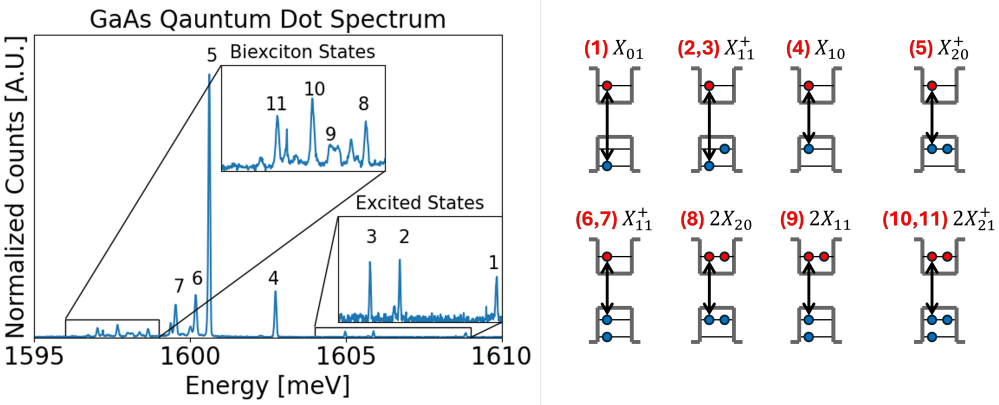


Figure 4.1: A typical spectrum of a $GaAs$ QD with $Al_xGa_{1-x}As$ barrier and superlattice structure with excitonic states matched to the corresponding peak.

4.1 Neutral Excitons

As stated in Chap.1 excitons, X_{10}, are bound electron - hole states, with both charge carriers in their lowest energy level. In a high symmetry QD, with point group symmetry D_{2d}, the bright eigenstates of QD would be the degenerate states $|\uparrow\Downarrow\rangle$ and $|\downarrow\Uparrow\rangle$ and the photons emitted upon recombination of the electron - hole couple would be circularly polarized.

Inhomogeneities, defects, segregation effects, non-uniform potential, piezoelectric effects etc. lower the symmetry of most QDs from D_{2d}. Under these conditions the eigenstates of the system are not the ones of the D_{2d} symmetry, but $\frac{1}{\sqrt{2}}(|\uparrow\Downarrow\rangle \pm |\downarrow\Uparrow\rangle)$. Recombination of bound electron and hole of an exciton is characterized by emission of linearly polarized photons [3] and the degeneracy of the two levels is also lifted by the exchange interaction. The energy separation of the two new eigenstates is known as Fine Structure Splitting, FSS, and it is usually a splitting on the μeV scale.

A biexciton, $2X_{20}$, is composed of two electrons and two holes in their lowest energy level. Due to Pauli exclusion principle, electrons and holes have to be in singlet state (opposing spins) to occupy a single energy level, therefore the biexciton has no FSS and zero angular momentum, $M = 0$. A biexciton state can't optically recombine directly to an empty QD (also characterized by $M = 0$) because photons couple only to $M = \pm 1$ transitions. The recombination to an empty QD happens with an intermediate step where the QD is populated by a single exciton state, $2X_{\bar{2}0} \rightarrow X_{\bar{1}0} \rightarrow 0$. Even though the initial and final states are singlet non-degenerate states without exchange interaction, emission from the biexciton state is characterized by FSS as a consequence of this intermediate step.

FSS can be hard to measure without polarization-resolved photoluminescence,

PL, measurements because it is usually much smaller then the linewidth of the $X_{\bar{1}0}$ transition lines. A rotating HWP and fixed polarizer can be placed in front of the spectrometer and by synchronizing the movement of the HWP and acquisition of spectra from the CCD we can obtain a map of the PL. Due to Malus' Law, the H and V photons contribute differently to the total intensity of the transition line depending on the HWP angle. Fitting the peak with a Guassian curve and plotting the center wavelength/energy of the transition as a function of the HWP angle will return a sinusoidal curve. The peak to peak amplitude of this sinusoidal curve is a measure of the FSS.

The $X_{\bar{1}0}$ peak can be identified by finding a transition line that has central wavelength changing in a sinusoidal pattern as function of the HWP angle θ with respect to the polarizer transmission axis. The $2X_{\bar{2}0}$ peak can be identified by finding a transition line with a sinusoidal pattern which is in antiphase with that of the $X_{\bar{1}0}$. Subtraction of the energies of the two transitions, $E_{X_{\bar{1}0}} - E_{2X_{\bar{2}0}}$, corrects for slow changes in the environment that may happen during the measurement, like a slow global drift of the transitions.

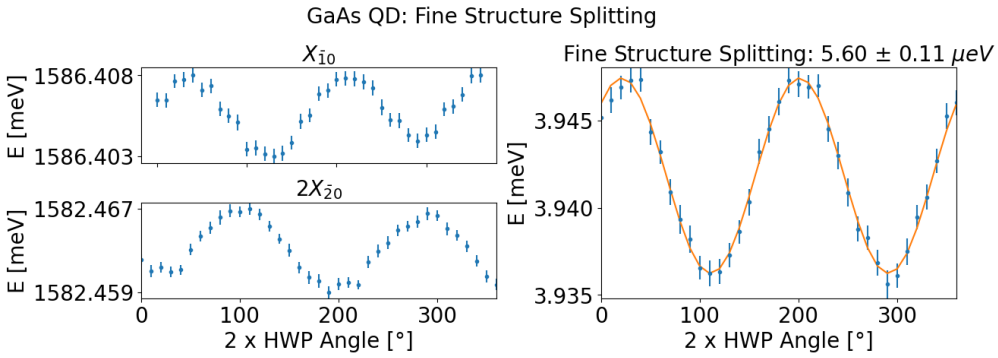


Figure 4.2: Energy of $X_{\bar{1}0}$ (top left) and $2X_{\bar{2}0}$ (bottom left) states as function of HWP angle and Fine Structure Splitting of a *GaAs* QD (right)

In one of our experiments, a set of 60 QDs from the same sample has been analyzed and an average FSS of $12 \pm 10 \mu eV$ has been found. Fig.4.3 shows how most of the QDs analyzed are characterized by a small FSS with few outliers in our sample broadening the mean value spread, thus highlighting the high symmetry of the site controlled growth of QDs.

This is a drastic reduction compared to previous generations of pyramidal QDs in different barriers, Fig.4.4 [1], thus confirming the positive effect of the superlattice on the optical properties of the QDs.

We observed a linear trend for the energy of the $2X_{\bar{2}0}$ as function of the $X_{\bar{1}0}$ energy, see Fig.4.5 (left).

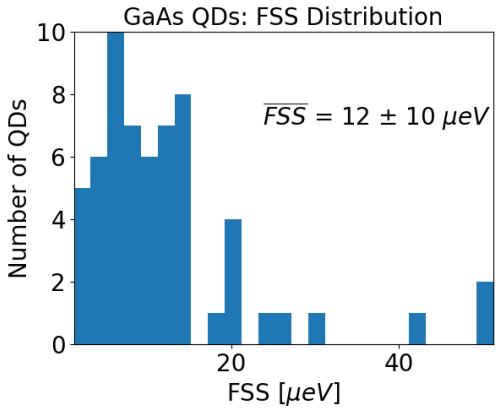


Figure 4.3: Fine Structure Splitting distribution of the the QDs analyzed.

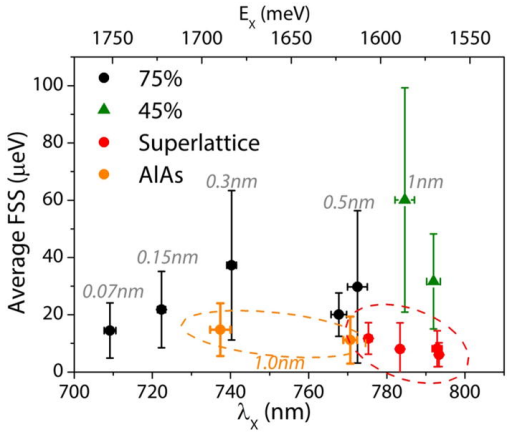


Figure 4.4: Average Fine Structure Splitting for different generations of QDs grown by the EPN group in Tyndall. In black (green) $GaAs$ QDs with $Al_{0.75}Ga_{0.25}As$ ($Al_{0.45}Ga_{0.55}As$) barriers, in orange $GaAs$ QDs in $AlAs$ barriers, and in red $GaAs$ QDs in $Al_{0.45}Ga_{0.55}As$ barriers with superlattice. The sample analysed in this thesis is among the ones of the most blueshifted data point of the superlattice series. Image taken from [1].

Due to Coulomb interaction between the extra charge carriers, in most QD systems [4] [5], the energy of $2X_{\bar{2}0}$ state is not exactly that of $X_{\bar{1}0}$. This energy difference is known as binding energy, $\Delta_B = E_{X_{\bar{1}0}} - E_{2X_{\bar{2}0}}$. In the case of $GaAs$ QD in $Al_xGa_{1-x}As$ barriers this is positive and the $2X_{\bar{2}0}$ is said to be binding.

Analysing the binding energy of the biexciton as function of the exciton energy, we observe that its values is not constant across the sample, but it has a slight dependence on the exciton energy, see Fig.4.5 (right). The binding energy across the sample is distributed over a narrow energy range, making it very easy to

identify the biexciton transition under above-band excitation. This also allows quick tuning of the laser energy for Two Photon Excitation. The strong linear dependence of the binding energy from the exciton energy highlights that this distribution is not random and due to dot-to-dot variations, and is, actually, a strong signature of the structural uniformity of the QDs on the sample.

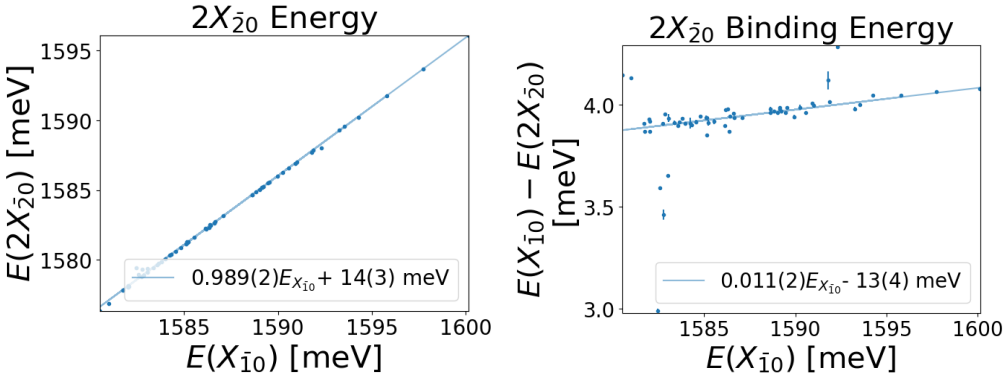


Figure 4.5: Energy of the biexciton (left) and the binding energy (right) of $GaAs$ QDs as function of the $X_{\bar{1}0}$ energy.

On its own, the exciton energy is already a *fingerprint* of the QD radius, r, due to the inverse dependence typical of a particle in a box problem, $E_{X_{\bar{1}0}} \sim \frac{1}{r^2}$ [6]. Combining this information with the linear dependence of binding energy, complex computational models could be developed to further probe the geometrical properties of the QDs.

Further confirmation of the $2X_{\bar{2}0}$ peak can be obtained by observing strong bunching in cross-correlation measurements, typical of recombination cascades as described in Chap.1, see Fig.4.6. As described in Chap.2, cross-correlation, $g^{(2)}(\tau)$, is a measurement of the conditional probability of measuring a *start* photon at time $t = 0$ and a *stop* photon at time $t = \tau$. Therefore, observation of bunching is a marker of recombination cascade between two states.

A dip, antibunching, before (or after, depending on the start stop configuration) the bunching can sometimes be observed in recombination cascades due to the finite lifetime of the final state. If the antibunching is very pronounced this is usually an indication that the final state is populated mostly by the decay of the initial state, with little contribution from other population channels, which would cause the $g^{(2)}(\tau)$ to flatten to unity due to the photons being uncorrelated.

Another neutral excitonic state is the excited exciton, where the hole occupies the first excited level, $X_{0\bar{1}}$. The excited exciton, once electron - hole exchange interaction is taken into account, is characterized by a FSS and isotropic emission in the XY plane (top-view) of linearly polarized photons, just like the ground

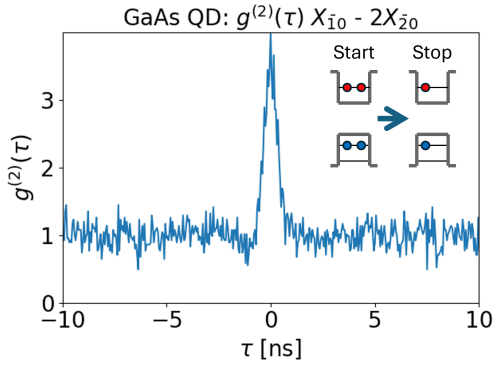


Figure 4.6: $g^{(2)}(\tau)$: recombination cascade $2X_{\bar{2}0} \rightarrow X_{\bar{1}0}$.

exciton [2]. This is indeed consistent with our measurements, as shown in the second plot in Fig.4.7. Interestingly, the FSS of the excited exciton is found to be almost, but not perfectly, antiphasing with an offset of a few degrees with that of the ground exciton, see top and middle panel of Fig.4.7 where a clear offset is present between the two oscillations. A clear theoretical model for this pattern is not available to us at the moment.

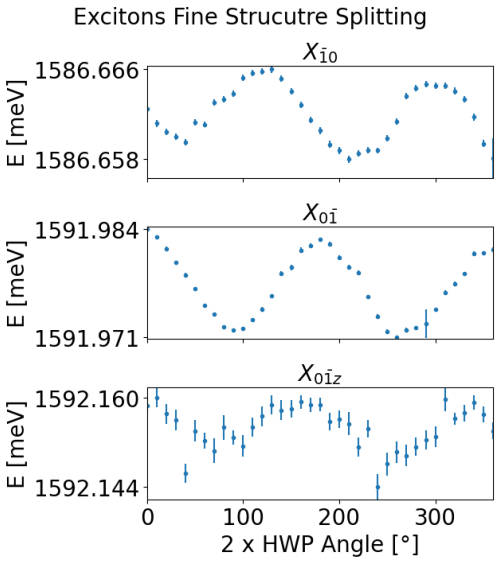


Figure 4.7: Energy of the $X_{\bar{1}0}$ (top), the $X_{0\bar{1}}$ (middle) and the $X_{0\bar{1}z}$ (bottom) states as function of HWP angle.

In Chap.1 we introduced the Luttinger - Kohn notation, with this notation we can mathematically describe electrons, Eq.4.1, heavy, Eq.4.2 and light, Eq.4.3,

holes with the following expressions:

$$\begin{aligned} |\frac{1}{2};+\frac{1}{2}\rangle &= |S\uparrow\rangle \\ |\frac{1}{2};-\frac{1}{2}\rangle &= |S\downarrow\rangle \end{aligned} \tag{4.1}$$

$$\begin{aligned} |\frac{3}{2};+\frac{3}{2}\rangle &= -\frac{1}{\sqrt{2}}\,|(X+iY)\Uparrow\rangle \\ |\frac{3}{2};-\frac{3}{2}\rangle &= \frac{1}{\sqrt{2}}\,|(X-iY)\Downarrow\rangle \end{aligned} \tag{4.2}$$

$$\begin{aligned} |\frac{3}{2};+\frac{1}{2}\rangle &= -\frac{1}{\sqrt{6}}\,[|(X+iY)\Downarrow\rangle + 2\,|Z\Uparrow\rangle] \\ |\frac{3}{2};-\frac{1}{2}\rangle &= \frac{1}{\sqrt{6}}\,[|(X-iY)\Uparrow\rangle - 2\,|Z\Downarrow\rangle] \end{aligned} \tag{4.3}$$

The optical selection rules, dipole transition, for electron - heavy-hole recombination are:

$$\begin{aligned} \langle\frac{1}{2};+\frac{1}{2}|\,\vec{E}\cdot\vec{p}\,|\frac{3}{2};+\frac{3}{2}\rangle &= 0 \\ \langle\frac{1}{2};-\frac{1}{2}|\,\vec{E}\cdot\vec{p}\,|\frac{3}{2};-\frac{3}{2}\rangle &= 0 \\ \langle\frac{1}{2};+\frac{1}{2}|\,\vec{E}\cdot\vec{p}\,|\frac{3}{2};-\frac{3}{2}\rangle &= \frac{\Pi}{\sqrt{2}}\,(E_x\hat{x}-iE_y\hat{y}) = \sigma^- \\ \langle\frac{1}{2};-\frac{1}{2}|\,\vec{E}\cdot\vec{p}\,|\frac{3}{2};+\frac{3}{2}\rangle &= -\frac{\Pi}{\sqrt{2}}\,(E_x\hat{x}+iE_y\hat{y}) = \sigma^+ \end{aligned} \tag{4.4}$$

and for electron - light-hole recombination:

$$\begin{aligned} \langle\frac{1}{2};+\frac{1}{2}|\,\vec{E}\cdot\vec{p}\,|\frac{3}{2};+\frac{1}{2}\rangle &= -\frac{\Pi}{\sqrt{6}}\,(E_x\hat{x}+iE_y\hat{y}) = \sigma^+ \\ \langle\frac{1}{2};-\frac{1}{2}|\,\vec{E}\cdot\vec{p}\,|\frac{3}{2};-\frac{1}{2}\rangle &= \frac{\Pi}{\sqrt{6}}\,(E_x\hat{x}-iE_y\hat{y}) = \sigma^- \\ \langle\frac{1}{2};+\frac{1}{2}|\,\vec{E}\cdot\vec{p}\,|\frac{3}{2};-\frac{1}{2}\rangle &= \frac{2\Pi}{\sqrt{6}}E_z\hat{z} = \pi \\ \langle\frac{1}{2};-\frac{1}{2}|\,\vec{E}\cdot\vec{p}\,|\frac{3}{2};+\frac{1}{2}\rangle &= \frac{2\Pi}{\sqrt{6}}E_z\hat{z} = \pi \end{aligned} \tag{4.5}$$

Therefore, if an exciton state has a p_z orbital component, then an additional non-degenerate transition line linearly polarized along the growth direction, $\hat{z}$, should be visible in cross-section measurements [7].

In this section and in the following chapter, we will demonstrate the light-hole-like nature of the excited states of this family of $GaAs$ QDs employing a variety of spectroscopy methods.

Emission from a non-degenerate and linearly polarized along $\hat{z}$ transition was confirmed by cleaving the sample, see procedure described in Chap.2. In Fig.4.8 we can see the polarization resolved PL from the side-view, instead of the more common top-view configuration.

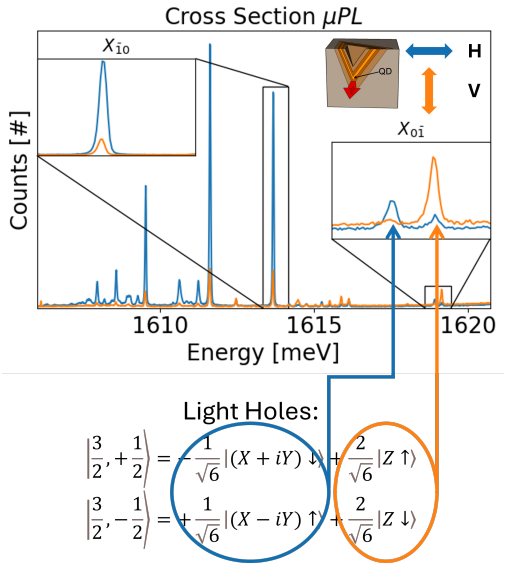


Figure 4.8: PL from the side view, vertical polarization is along the growth direction (top). Highlight of ground and excited exciton showing the non-degenerate $X_{0\bar{1}z}$ transition due to the light-hole-like nature of the excited state (bottom).

The ground exciton, see inset plot on the top left corner from Fig.4.8, is clearly heavily polarized along the horizontal direction, XY plane, and shows no non-degenerate components, thus confirming its heavy-hole-like nature. The emission along the vertical direction could be caused by valance band mixing of heavy and light hole bands, which leads to a lower degree of linear polarization of the transition lines, as we will see later in the chapter.

The excited exciton emission $X_{0\bar{1}}$, see inset plot on the bottom right from Fig.4.8, instead shows a non-degenerate and nearly fully polarized p_z orbital component, $X_{0\bar{1}z}$, thus hinting at the light-hole-like character of the excited states of the QDs. The leftover emission from the p_z component along the XY plane projection could be due to band mixing.

On a small subset of QDs, the $X_{0\bar{1}z}$ was visible from the top-view configuration. Ideally, this component should not be observed in top-view measurements, but

its presence could be explained by sample morphology, such as scattering/light-guiding effect of internal features, the high numerical aperture of the objective, which collects emission from the QDs also at high angles, or fundamental reasons like band mixing which degrades the DOP of the transition. Furthermore, even though $X_{0\bar{1}z}$ should not have any FSS it can be observed in some QDs that, from the top-view, its energy is varying with the HWP angle, see for example the bottom panel in Fig.4.7.

As for the biexciton, we found that the energy of the $X_{0\bar{1}}$ transition is linearly dependent from the ground exciton energy, see Fig.4.9 (left). The energy difference $E_{X_{\bar{1}0}} - E_{X_{0\bar{1}}}$, see Fig.4.9 (right), shows a stronger linear dependence from the ground exciton energy than that shown previously for biexciton state. Furthermore, the linear law has a negative slope indicating that the excited exciton separation increases for excitons with higher energy, which correspond to smaller/more confined QDs. This is again consistent with a simple particle in a box problem where $E_n - E_{n+1} \sim \frac{n^2}{r^2} - \frac{(n+1)^2}{r^2} \sim -\frac{2n+1}{r^2}$. It also shows that the spectra of the QDs and its energy separation among the several transition lines could be used as fingerprint of its geometrical properties.

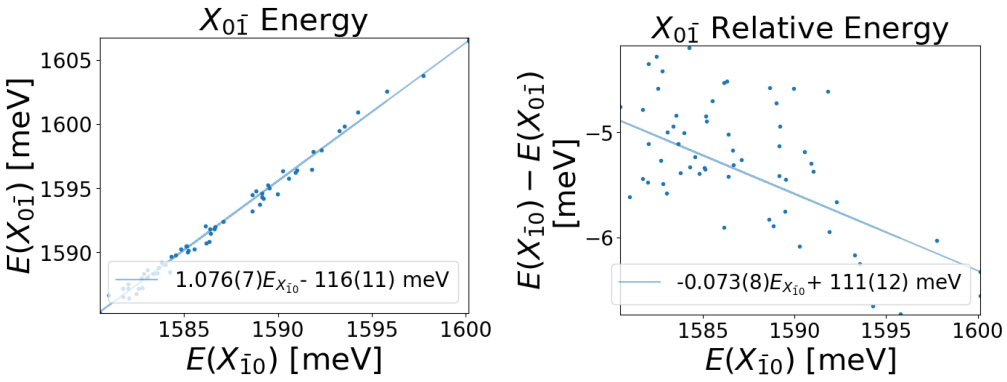


Figure 4.9: Energy of the excited exciton (left) and energy difference with ground exciton (right) of $GaAs$ QDs as function of the $X_{\bar{1}0}$ energy.

Similar conclusion can be drawn for the p_z component and the $X_{0\bar{1}}$ energy, see Fig.4.10.

In plane asymmetry and anisotropic strain can induce valance band mixing between heavy-hole and light-hole states in QDs [7]. Taking these effects into account the eigenstates of the system are now superpositions of the elliptically polarized excitons:

$$|\pm\widetilde{1}\rangle = \sqrt{1-\beta^2}\,|\mp\frac{1}{2};\pm\frac{3}{2}\rangle + \beta e^{\pm 2i\psi}\,|\mp\frac{1}{2};\mp\frac{1}{2}\rangle \tag{4.6}$$

where β and ψ represent amplitude and phase mixing [8].

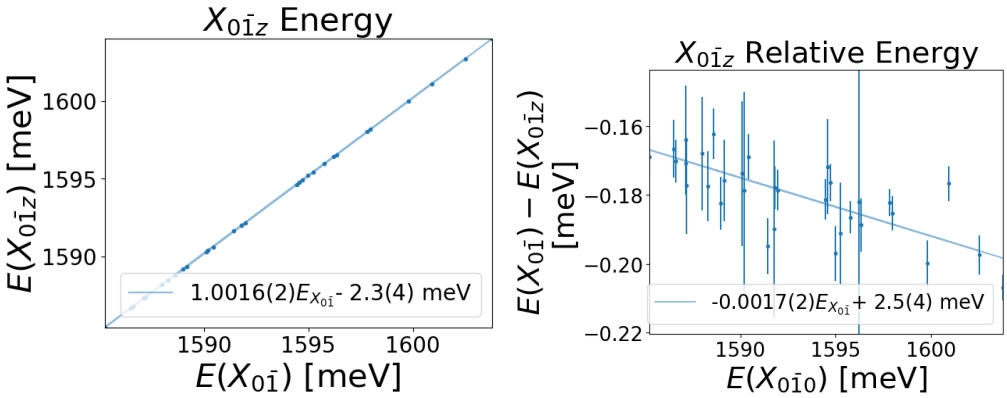


Figure 4.10: Energy of the non-degenerate excited exciton (left) and energy difference with excited exciton (right) of $GaAs$ QDs as function of the $X_{0\bar{1}}$ energy.

If $\beta \neq 0$ then the QD emission is elliptically polarized with an angle ψ with the axis $\hat{y}$. The degree of linear polarization:

$$DOLP = \frac{I_H - I_V}{I_H + I_V} \tag{4.7}$$

can be measured by projecting the QD PL on a linear basis and measuring its intensity. The dependence of the degree of linear polarization from the amplitude band mixing factor β can be expressed as [8]:

$$DOLP = \frac{2\beta\sqrt{3(1-\beta^2)}}{3-2\beta^2} \tag{4.8}$$

Thus given the DOLP of a transition line its light-hole percentage can be estimated by intersection with Eq.4.8, see Fig.4.11.

It was found that in general $GaAs$ QD are characterized by a low degree of polarization, which is indicative of low band mixing. Fig.4.12 plots the DOLP of the excited exciton against that of the ground state, showing that the two values seem to be uncorrelated. It can be seen that the lh - hh ratio is not unambiguously determined because the function Eq.4.8 is not injective, thus a very low degree of polarization implies that a state can be either mostly light-hole like or mostly heavy-hole like. In the case of our QDs due to the lack of z component of the ground exciton we speculate that its very low degree of polarization implies a purely heavy-hole like first energetic level in the valence band. On the other hand the visible non degenerate p_z orbital component of the excited exciton and its very low degree of polarization, seems to imply that the second energetic level in the valence band is mostly light-hole-like.

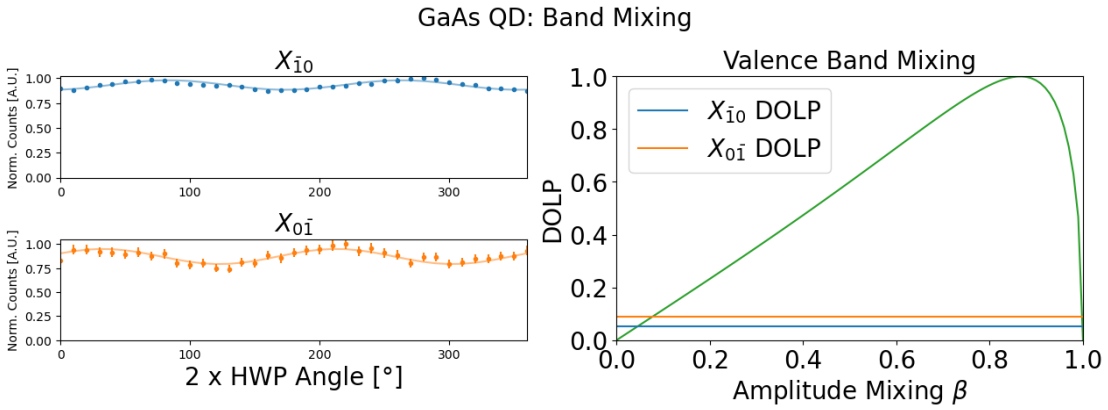


Figure 4.11: Intensity of $X_{\bar{1}0}$ (top left) and $X_{0\bar{1}}$ (bottom left) as function of 2 x HWP angle and corresponding valence band mixing (right).

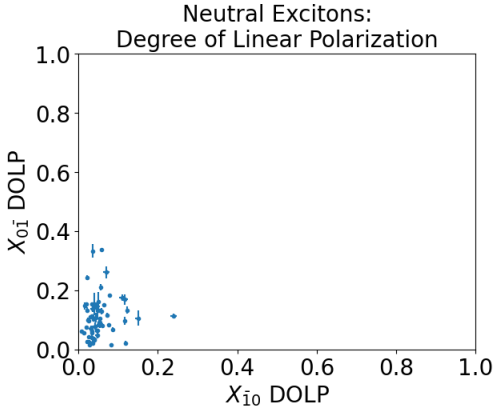


Figure 4.12: Degree of Linear Polarization of $X_{0\bar{1}}$ as function of DOLP of $X_{\bar{1}0}$, the distribution of values is indicative of low band mixing and the two data set seem uncorrelated.

We observed bunching in the $g^{(2)}(\tau)$ of the $X_{0\bar{1}}$ peak and another transition separated $-0.55meV$ from the $2X_{\bar{2}0}$ transition, see Fig.4.13. As stated before, the bunching is an indication of recombination cascade, therefore we identify this line as belonging to the transition $2X_{\bar{1}1}$.

As showed in Fig.1.12 and Fig.1.13, the decay pattern of the $2X_{11}$ state can be very complex depending on the symmetry of the QD. In the *simplest* scenario, corresponding to the D_{3h} symmetry, the $2X_{1\bar{1}}$ has only 3 isotropic transitions visible in the top-view configuration and 1 linearly polarized along the growth direction visible in the cross section, see Fig.4.14. Only one of the isotropic transitions is expected to bunch with the $X_{0\bar{1}}$ state, as we found using the cross-correlation

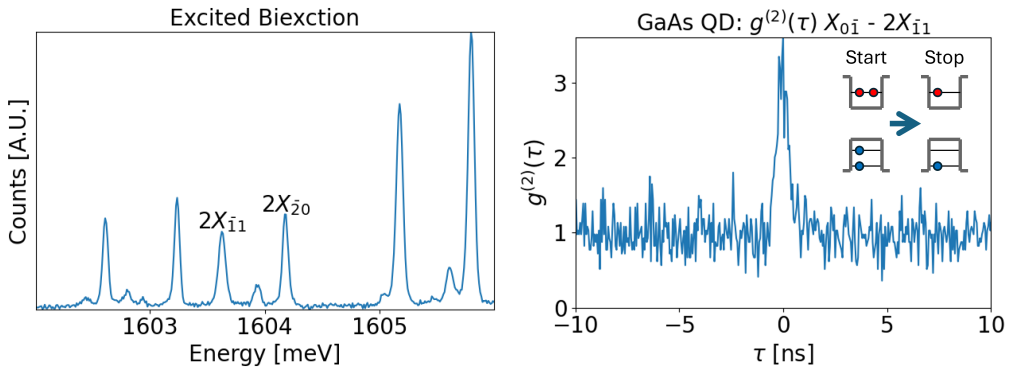


Figure 4.13: (left) Ground and Excited Biexcitons in the *GaAs* QD spectrum, (right) $g^{(2)}(\tau)$: recombination cascade $2X_{\bar{1}1} \rightarrow X_{0\bar{1}}$.

in see Fig.4.13. Observation of this transition is made challenging in most QDs by its close proximity, and maybe sometimes overlap, to a set of heavily linearly polarized doublets, of which we will discuss later in the chapter.

At the time of writing, we were not able to identify the other transition lines of the $2X_{\bar{1}1}$ and $2X_{1\bar{1}}$ states.

It has been shown in literature that FSS can be made arbitrary small by placing a QD on a piezoelectric device. The deformation on the QD induced by the device counterbalances the effect of the QD asymmetry and deforms the barriers until the FSS is compensated [9] [10] [11].

To perfectly counterbalance the QD imperfections it is necessary to have full control of the induced strain in different directions, this can be achieved with a six legged piezoelectric actuator that allows full control of the inplane strain [10]. Nevertheless we have attempted the same procedure, but with a much less sophisticated device.

A sample with similar structure to the one studied in this chapter, Fig.4.15, has been polished according to the procedure described in Chap.2 to reduce the depth of the pyramidal recess. It has then been bonded to a monolithic piezoelectric crystal, with the pyramid bases facing one of the surfaces of the piezoelectric, Fig.4.15.

The yield of QD responsive to the stimulation of the piezoelectric device was found to be very poor. This is probably associated with the loss of strain transfer to the QD once the tip of the pyramid is exposed by the back-etch process. Ideally, pyramids which are almost fully-covered by the substrate should respond better to the strain induced by the piezoelectric device, but that is a very small subset of QDs on the sample due to the inhomogeneous back-etching process.

We were able to prove FSS tuning for a QD in the range of voltages scanned, see Fig.4.16. Even though the FSS never reached $0\mu eV$ we were able to reduce it

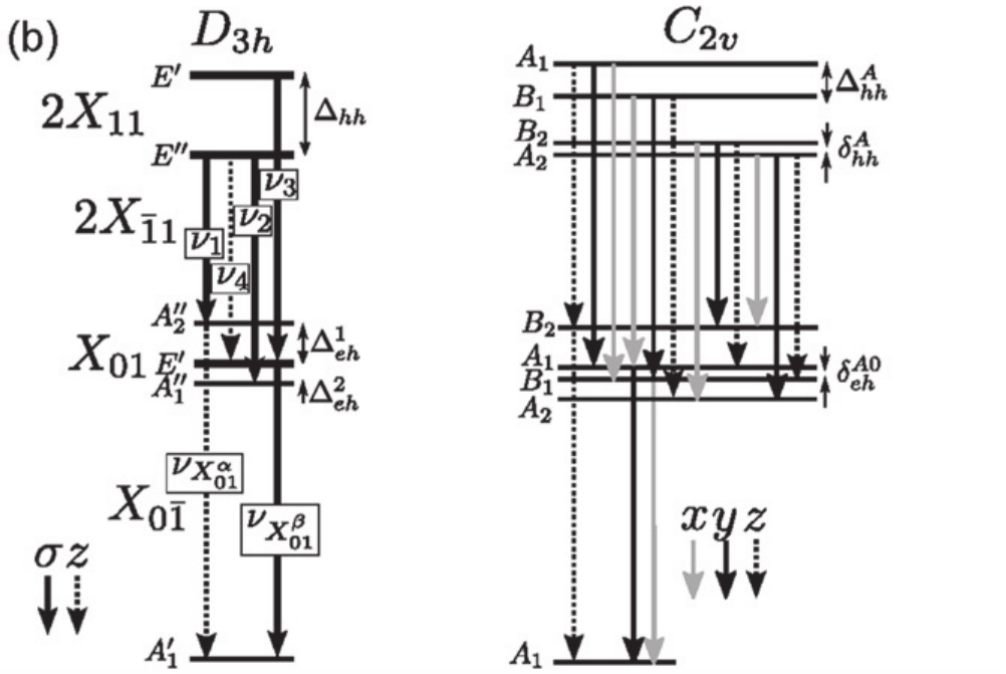


Figure 4.14: Recombination cascade for $2X_{\bar{1}1}$ for D_{3h} symmetries, showing the 3 isotropic transitions visible in the top-view configuration and 1 linearly polarized along the growth direction visible in the cross section. Taken from [2]

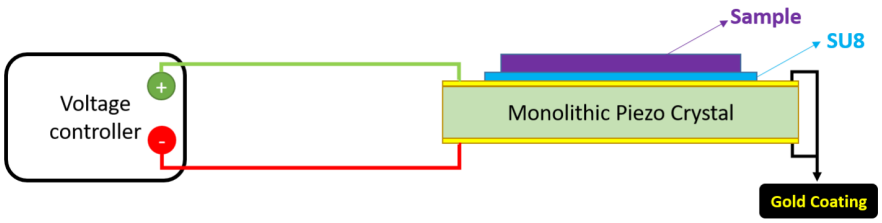


Figure 4.15: Schematic of the $GaAs$ QDs sample mounted on a monolithic piezoelectric device. Image taken from [12].

of a factor 3 with such a crude device and poor yield. The sudden jump in FSS showed at voltages lower than $-300V$ is caused by a breakdown of the device. It can therefore be expected that site controlled pyramidal QD would show better response if more control over the alignment of sample and a specifically engineered substrate is achieved.

Straining the QD induces also changes into the the valence band mixing, this can be observed by plotting the DOLP of the ground and excited exciton states, see Fig.4.16. Initially the DOLP is higher because the substrate has been pre-strained

by the poling operation. We fitted the DOLP data over the working range of the device, from $-300V$ to $100V$, and found that the ground exciton state seems to be barely affected by this induced strain, but the excited shows a response that is almost 5 times stronger. The linear trend of the DOLP as function of the applied voltage is proof that we can engineer nearly pure light- or heavy-like states by applying external strain to the QDs.

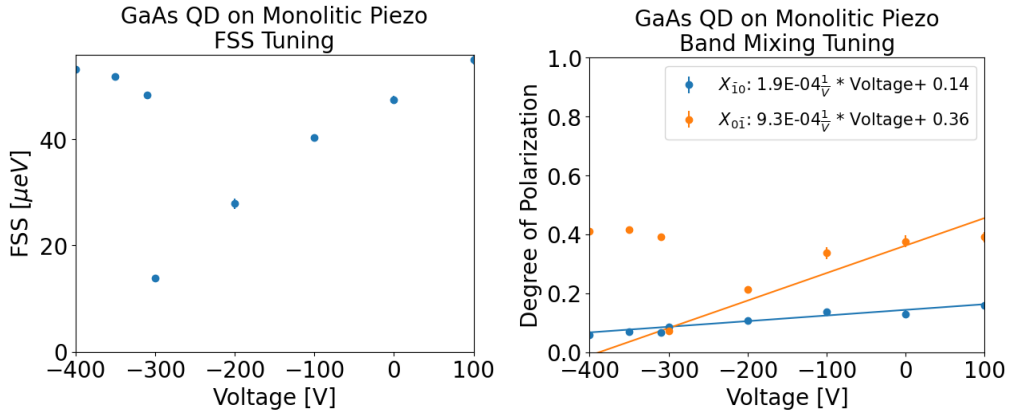


Figure 4.16: Tuning of Fine Structure Splitting (left) and of band mixing (right) as function of the voltage applied to the piezoelectric substrate.

4.2 Positive Trions

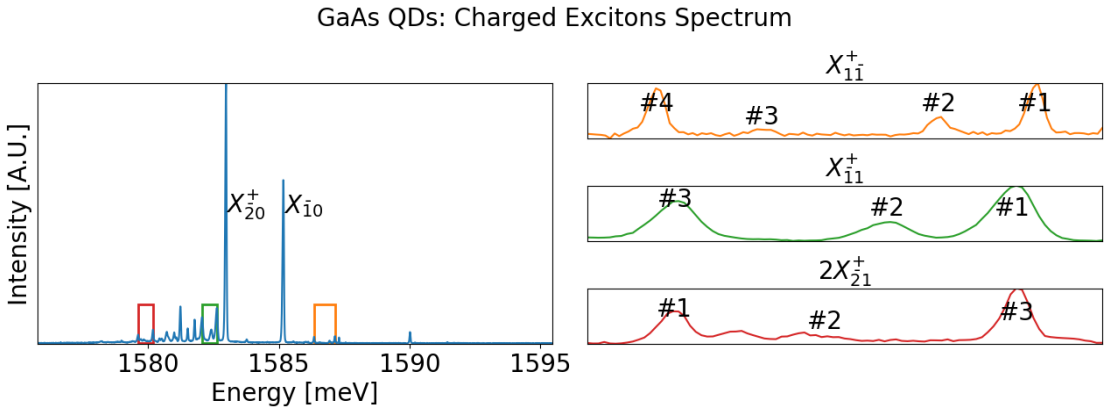


Figure 4.17: (left) Typical spectrum of $GaAs$ QD in superlattice, (right) recombination patterns of (top) $X^+_{1\bar{1}}$ (middle) $X^+_{\bar{1}1}$ (bottom) $2X^+_{\bar{2}1}$.

A positive trion with two holes populating the first level of the valence band in a singlet state, $X^+_{\bar{2}0}$ is characterized by isotropic emission in the XY plane and no FSS. This is valid for D_{2d}, D_{3h}, C_{3v} and lower symmetries [2].

We have found $GaAs$ QDs in superlattice to be usually positively charged and the ground trion to be the dominant peak, making its identification in the spectra quite straightforward, see Fig.4.1. As for biexciton and excited exciton, the energy of the trion is highly linearly correlated to that of the exciton, see Fig.4.18 (left). The relative energy of the ground trion can be estimated by the equation: $-0.003(2)E_{X_{\bar{1}0}} + 8(2)meV$. As for the excited exciton, the slope of the relative energy is negative, see Fig.4.9.

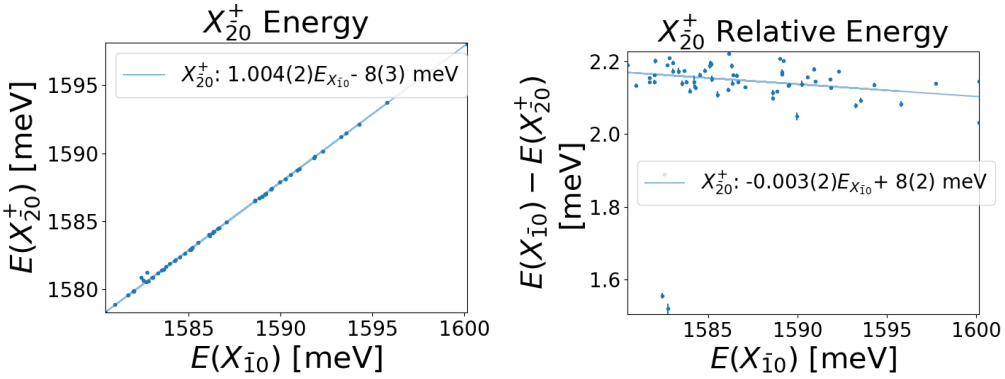


Figure 4.18: Energy (left) and relative energy (right) of the ground trion state as function of the $X_{\bar{1}0}$ energy.

If one of the two holes populates the second level of the valence band, the QD is populated by a so called hot trion state, X^+_{11}. The hole - hole exchange interaction then lifts the degeneracy and splits energetically the levels, further splitting is introduced by electron - hole exchange interaction. The optical activity of hot trions is determined by the symmetry point group of the QD [2] and thus these state could be used to probe the geometry of the QD.

We have found our dots to have 3 optically active hot trion states when the heavy-hole - electron recombine, $X^+_{\bar{1}1}$, see Fig.4.17 (right middle). The energy of these 3 states is always more than the $2X_{\bar{2}0}$ and less than the $X^+_{\bar{2}0}$. Just like the $X^+_{\bar{2}0}$, their energy relative to the $X_{\bar{1}0}$ is also characterized by a sharp distribution, see Fig.4.19.

As usual, the energy of the states exhibits a strong linear dependence from the $X_{\bar{1}0}$ energy, see Fig.4.19 (top). Interestingly, plotting the relative energies of the peaks to the $X_{\bar{1}0}$ as a function of the $X_{\bar{1}0}$ itself, we notice that the least energetic of the $X^+_{\bar{1}1}$ states seems to have a positive slope coefficient, unlike the other trion states, see Fig.4.19 (bottom). A clear theoretical model to explain such behaviour

is not available to us, at the moment of writing, but it could be a pattern of the trion states splitting due to exchange interaction.

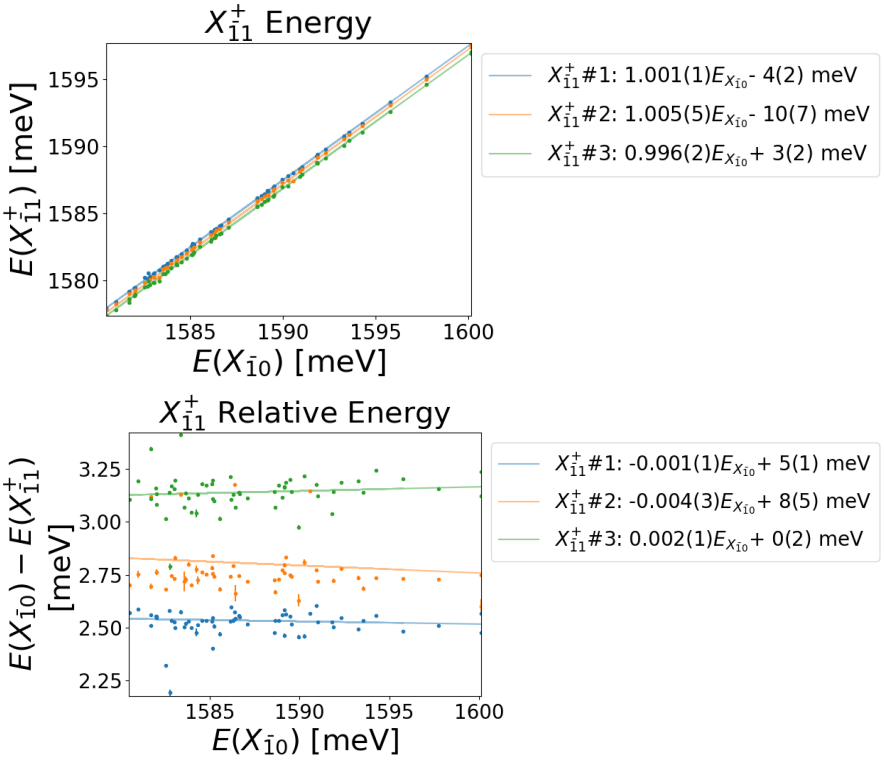


Figure 4.19: Energy (top) and relative energy (bottom) of trions in which the heavy-hole recombines with the electron.

The presence of 4 hot trion states has been also observed in the range of energies between $X_{\bar{1}0}$ and $X_{0\bar{1}}$, typically between $-1meV$ and $-4meV$, see Fig.4.17 (right top). These are the trion states where the hole in the excited level recombines with the electron. In general, 3 of these states are observable in top-view measurements. The presence of a fourth peak is confirmed: in a small number of QDs in top-view measurements, by cross section measurements and by resonantly exciting these states with a tunable laser and observing the presence or lack of resonances for the ground trion states, $X^+_{\bar{2}0}$ and $X^+_{\bar{1}1}$. This topic will be dealt in depth in the following chapter, Chap.5.

A linear dependence from the energy of these states as a function of the $X_{\bar{1}0}$ is again confirmed, see Fig.4.20 (top), although their relative energy as a function of the $X_{\bar{1}0}$ energy shows a much noisier pattern than other peaks, see Fig.4.20 (bottom).

Plotting the relative energy of the $X^+_{1\bar{1}}$ to the excited exciton energy, as a

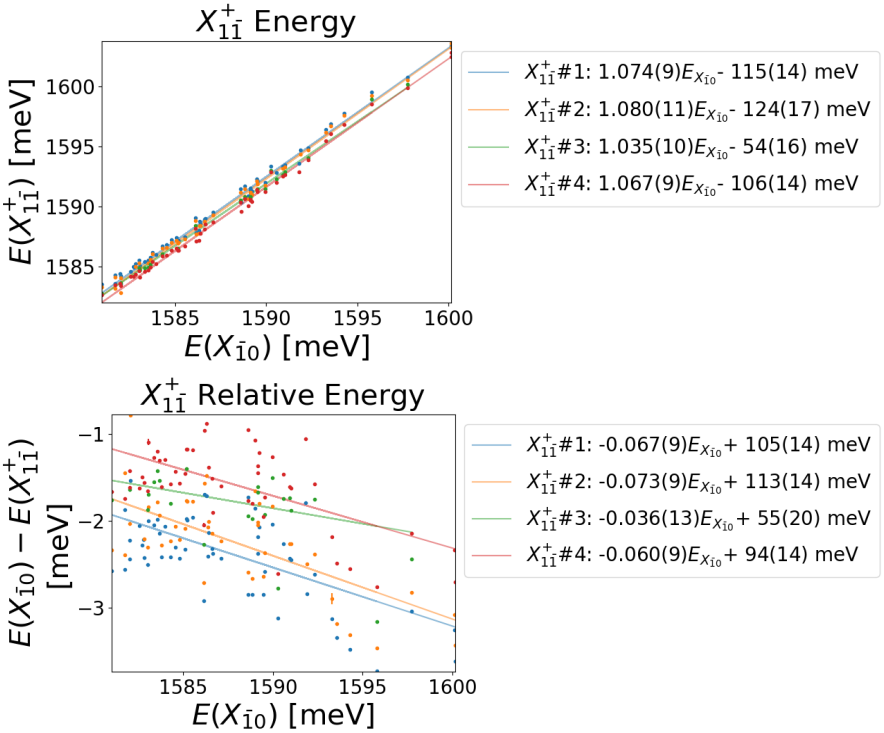


Figure 4.20: Energy (top) and relative energy (bottom) of trions in which the light-hole recombines with the electron.

function of its energy, seems to show a less noisier pattern, see Fig.4.21 (top and bottom). This indicates that the higher spread of the data previously observed is, probably, due to the higher spread of the energy of the first excited level. The splitting introduced by hole - hole exchange interaction on the other hand are less sensitive to dot-to-dot variation, and therefore could be used as a parameter to model the geometric properties of the QD.

The identification of the charged biexciton, $2X^+_{\bar{1}1}$, has been possible with the use of polarization resolved $g^{(2)}(\tau)$ measurements. A QWP at 45° was placed at the transmitted output of the $10R : 90T$ beam-splitter to convert trion emission from circular to linear base, therefore $|R\rangle \rightarrow |H\rangle$ and $|L\rangle \rightarrow |V\rangle$. This has been done, as described in Chap.2, to minimize distortion of circularly polarized light by mirrors and optical elements of the setup. A combination of a polarizer and a rotating HWP allows us then to filter orthogonal states and measure $g^{(2)}(\tau)$ in copolarized or crosspolarized configuration. In the first configuration the events of the $g^{(2)}(\tau)$ are given by photons with the same polarization, in the other by orthogonal ones.

Our study of the two photon radiative cascade $2X^+_{\bar{1}1} \rightarrow X^+_{\bar{1}1}$ was partly based

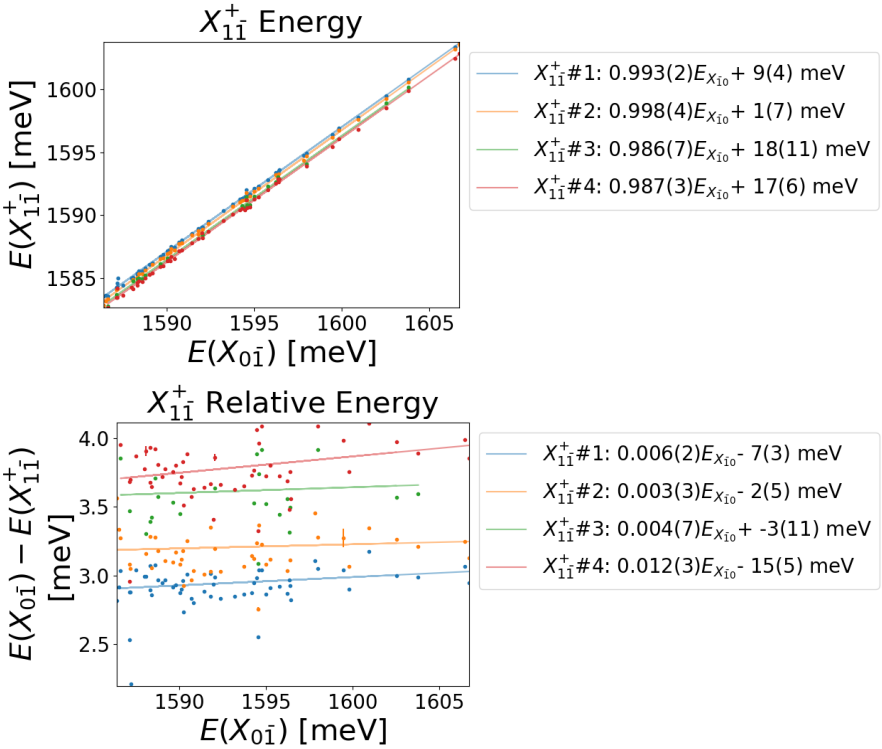


Figure 4.21: Energy (top) and relative energy (bottom) of trions in which the light-hole recombines with the electron. The energy has been calculated in relation to excited exciton to reduce the noise in their energy distribution due to the dot-to-dot variations of the excited state energy.

on the decay diagram shown in Fig.1(a) in [13]. The radiative decay and energy order of the peaks studied in [13] does not fully match our QDs, because their singlet state of the hot trion, $|S^*\rangle = |\uparrow (\Downarrow\Uparrow - \Uparrow\Downarrow)\rangle$, is expected to be a transition at higher energy than the singlet state $X^+_{\bar{2}0}$ and $X_{\bar{1}0}$. In our QDs instead it seems that the hole - hole Coulomb interaction is stronger than the hole - hole exchange interaction.

The recombination of the first electron - hole couple from the $2X^+_{\bar{2}1}$ sets the polarization of the first photon according to the selection rules of heavy holes. Antiparallel spins recombine with emission of circularly polarized photons. Because the electrons in the charged biexciton are in a singlet state, the one left in the QD has opposite spin to the one that just recombined. Therefore, emission from $X^+_{\bar{1}1}$ will be orthogonal to the first photon, see Fig.4.22.

This is consistent with our $g^{(2)}(\tau)$ measurements, see Fig.4.23, in which the least energetic peaks are shown to bunch (antibunch) with the peaks identified as hot trions in crosspolarized (copolarized) detection.

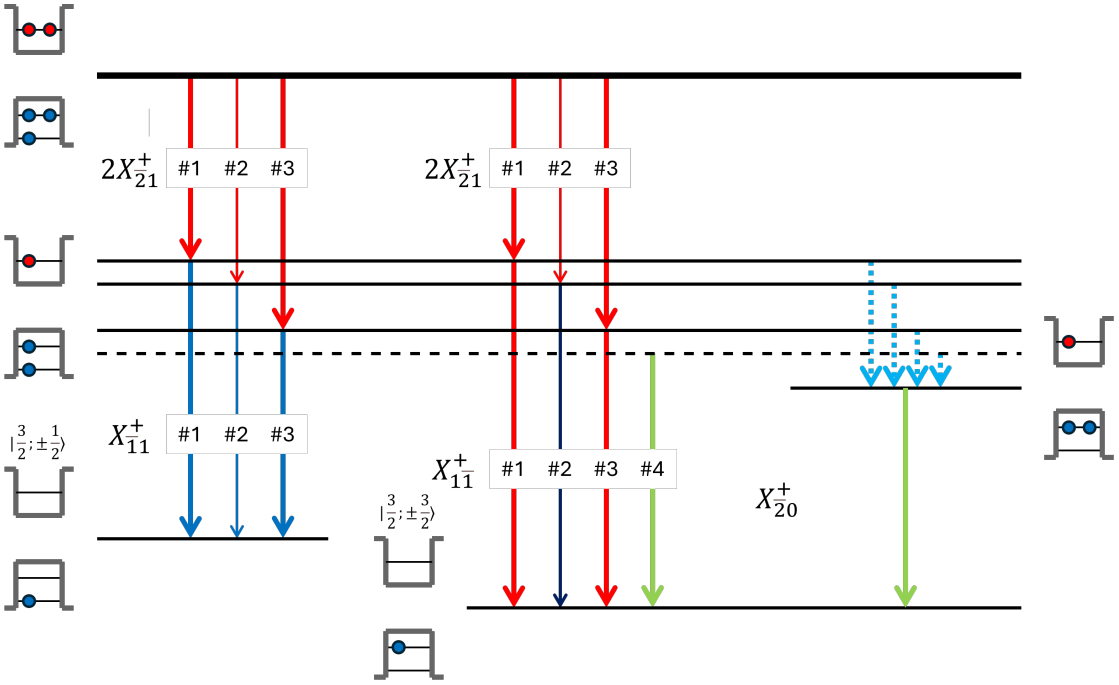


Figure 4.22: Decay of charged biexciton to trion and hot trions. Red/Blue indicate cross-polarized photons in the recombination cascade, red/red photons are co-polarized, green arrows indicate isotropic emission in the XY plane with no clear relation to the $2X^+_{\bar{2}\bar{1}}$ polarization, solid blue arrow indicates a photon linearly polarized along the $\hat{z}$ direction and dashed light blue arrow are associated to non-radiative decays to the trion state.

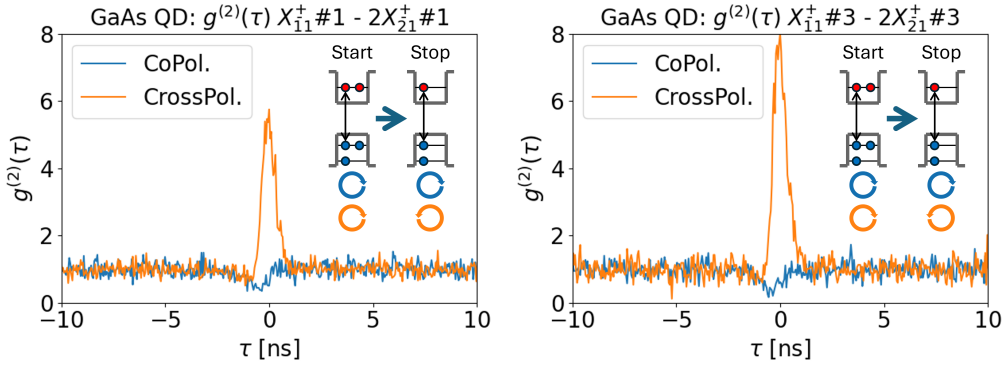


Figure 4.23: $g^{(2)}(\tau)$: recombination cascade $2X^+_{\bar{2}\bar{1}} \rightarrow X^+_{\bar{1}\bar{1}}$.

On the other hand, the recombination from $X^+_{\bar{1}\bar{1}}$ can happen both with parallel and antiparallel spins. Antiparallel spins lead to linearly polarized light along

the $\hat{z}$ direction, which are not easily observed in top-view measurement geometry. Parallel spins recombine with light-hole selection rules, and lead to a $2X^{+}_{\bar{1}1} \rightarrow X^{+}_{1\bar{1}}$ cascade characterized by copolarized photons, see Fig.4.22 (middle recombination). This is also consistent with our $g^{(2)}(\tau)$ measurements, Fig.4.24.

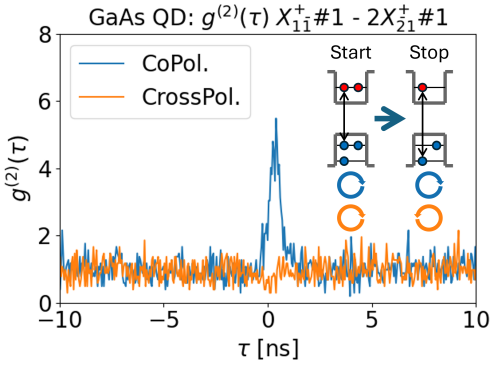


Figure 4.24: $g^{(2)}(\tau)$: recombination cascade $2X^{+}_{\bar{2}1} \rightarrow X^{+}_{1\bar{1}}$.

Some very small bunching is observed for the $2X^{+}_{\bar{2}1} \rightarrow X^{+}_{\bar{2}0}$ cascades, see Fig.4.25, this implies that the hole in the second energy level relaxes via non radiative processes, such as spin flips and phase changes, to the ground level.

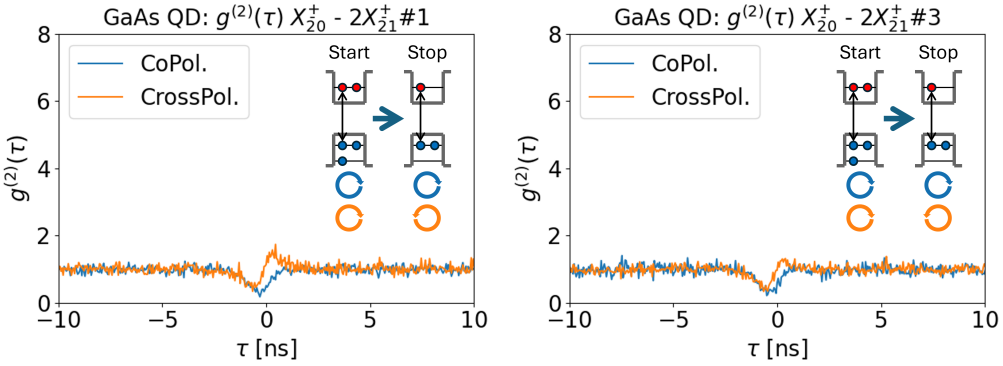


Figure 4.25: $g^{(2)}(\tau)$: recombination cascade $2X^{+}_{\bar{2}1} \rightarrow X^{+}_{\bar{2}0}$.

By analysing the energy separation of the transitions that belong to $2X^{+}_{\bar{2}1}$, $X^{+}_{\bar{1}1}$ and $X^{+}_{1\bar{1}}$ states we can quantify the hole - hole and electron hole exchange interaction. We cleaved a sample and observed a very consistent separation of the optically active transition, see Fig.4.26, according to the decay scheme proposed in Fig.4.22

We have tried to gather the same information, but with measurements from the top-view, see Fig.4.27. While some preliminary analysis shows some promis-

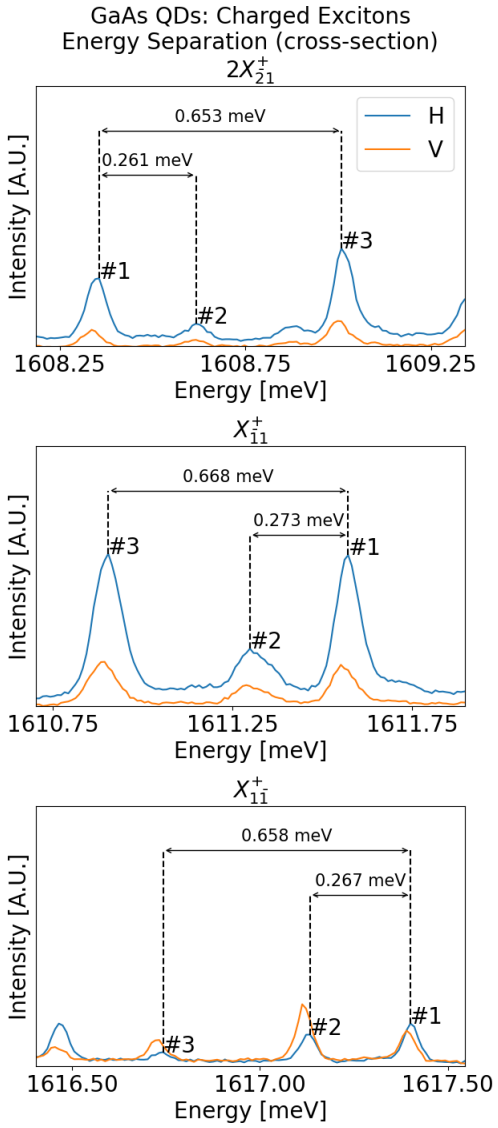


Figure 4.26: Exchange interaction of charged biexciton and trion in cross-section.

ing results, some challenges arise in gathering this data. First of all, the peak $X^+_{1\bar{1}}$#3 is rarely observed in top-view, reducing our available data set for statistic. Second, the observation of peak $2X^+_{2\bar{1}}$#2 seems to be dependent on the excitation power and it is sometimes hard to identify it from other unknown transitions between $2X^+_{2\bar{1}}$#1 and $2X^+_{2\bar{1}}$#3. Third, further theoretical models and simulations will be necessary to understand the higher spread in the data associated with the $X^+_{1\bar{1}}$ states. Nevertheless, the data gathered and analyses so far seems to show a promising trend between the energy separation of the above mentioned state. We

would like to stress that the red dashed line present in the plot below is not a fit of the data, but a line of unitary slope to aid the eye and show the trend of the exchange interaction effects.

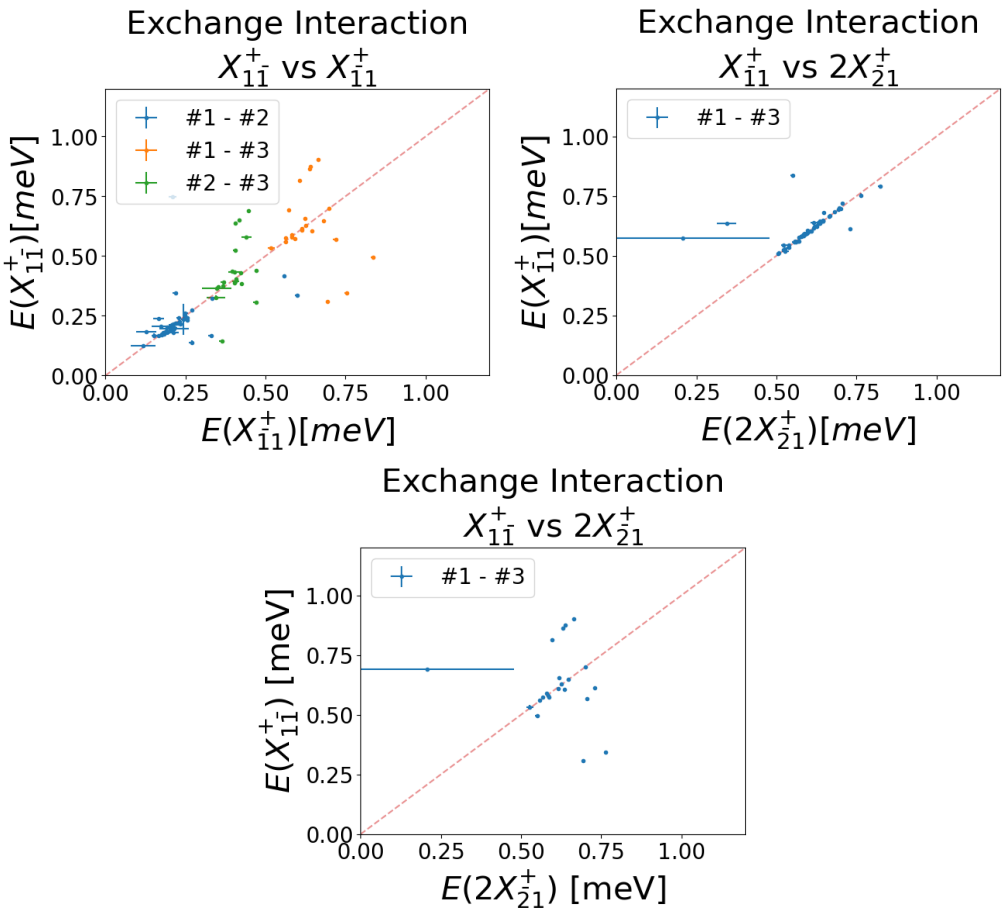


Figure 4.27: Statistics of exchange interaction of charged biexciton and trion in cross-section.

In general we have found trions and charged biexcitons to be isotropic in the XY plane with a low degree of linear polarization.

We have also observed a set of strongly polarized doublets close to the biexciton transition, see Fig.4.28. Further measurements will be necessary to evaluate if they belong to $X^{2+}_{\bar{2}1}$ states.

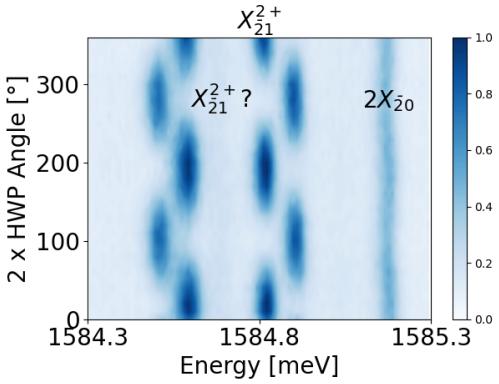


Figure 4.28: Heavily polarized transitions, maybe belonging to the X_{21}^{2+} state.

4.3 Negative Trions

To understand in-depth the energetic structure of $GaAs$ QD, an electric field capability can be instrumental. Also, driving the device with an external voltage allows charge carriers tuning and injection into the active region of the QD, and thus potentially on demand generation of single and entangled photons, in the case of a modulated voltage [14].

Reduction of the FSS can also be achieved by quantum confined Stark Effect by applying an external electric field perpendicular or parallel to the growth direction [15] [16]. A typical approach is to embed the QD in a p-i-n structure which when driven in reverse deforms the electron and hole wavefunction and can potentially reduce the FSS to $0\mu eV$. Furthermore the transition energy of excitonic complexes can be changed via Stark shift in ranges of up to tens of meV [17].

Electroluminescence and entangled photon emission from a p-i-n structure has been proved before by the EPN group for $In_{0.25}Ga_{0.75}As$ in $GaAs$ barriers [18].

To obtain a diode structure for $GaAs$ QD $AlAs$ has been chosen as a barrier and the epitaxial contacts are two $120nm$ and $110n$ thick $Al_{0.65}Ga_{0.35}As$ p and n doped layers. The full sample structure is shown in Fig.4.29 (left).

The non planar structure of the sample does not allow contacting the p and n doped layers in a conventional geometry, for example by etching two opening at different depth, nor is possible to just cover the top surface by metal deposition, as this would cause a short circuit since both p and n doped layers have the top surface in common, Fig.4.29 (right).

To isolate the top surface of the contacts and sidewalls of the pyramidal recess a layer of Si_3N_4 was deposited using Plasma-Enhanced Chemical Vapor Deposition, PECVD.

Gold is then evaporated in three different steps to mask the dielectric material

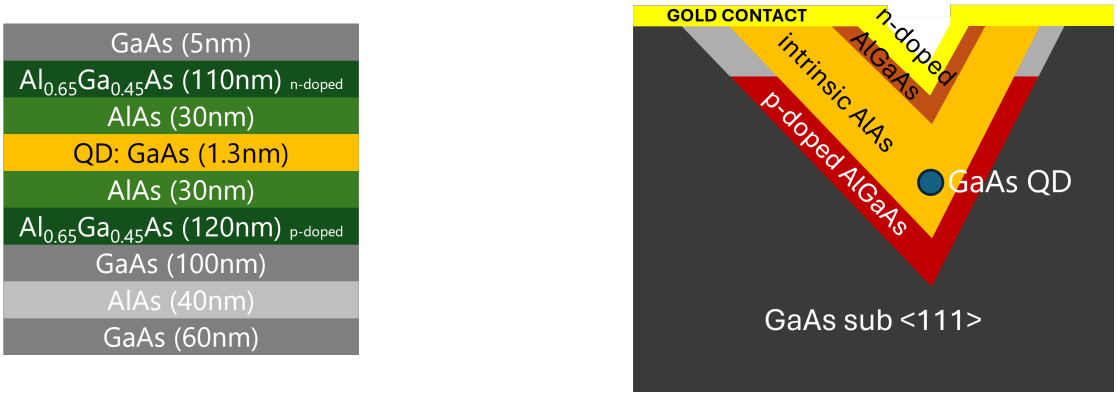


Figure 4.29: p-i-n diode structure for $GaAs$ QDs: epitaxial structure (left) sketch showing the non planar geometry of the sample which would cause the short circuit condition if a gold contact was directly evaporated on top without the trenches (right)

everywhere except in the bottom of the pyramidal recess. The sample is placed inside the evaporator on a 50° inclined stage, due to this inclination the sidewall shadows the bottom of the recess and gold cannot deposit in the bottom of the recess. The step is repeated 3 times rotating the sample by 120° and thus leaving the bottom of the pyramid unprotected at the end of the process, Fig.4.30.

A low power CF_4 dry etching step removed the Si_3N_4 from the bottom of the recess and allows evaporation of the gold contact to the n doped layer.

The sample is then flipped, bonded to a $GaAs$ 100 carrier and processed according to the back-etching process described in Chap.2 in order to access and contact the p doped layer. Aluminium Oxide is produced when the $AlAs$ etch stop layer is exposed to the etching solution. A $2min$ in a HF solution removes the oxide layer, but also etches trenches in the $AlAs$ layer, to avoid an open circuit Si_3N_4 is again deposited to fill these trenches.

A final evaporation of gold on the top surface of the sample produces the contact to the p doped layer.

Analysis of photoluminescence spectra under forward bias of the sample shows very weak Stark shift response in the voltage range scanned, Fig.4.31 (right).

On the other hand the device is very useful to identify excitonic complexes with an unpaired electron or hole. It can be observed that the charging of the QD drastically changes as a function of voltage, moving from dominant positively charged complexes at reverse bias to mostly negatively charged under forward bias. Suppression of neutral excitons and positive trions and their respective excited states is clearly evident in the range $3V$ to $5V$. At $5V$ the emergence of the

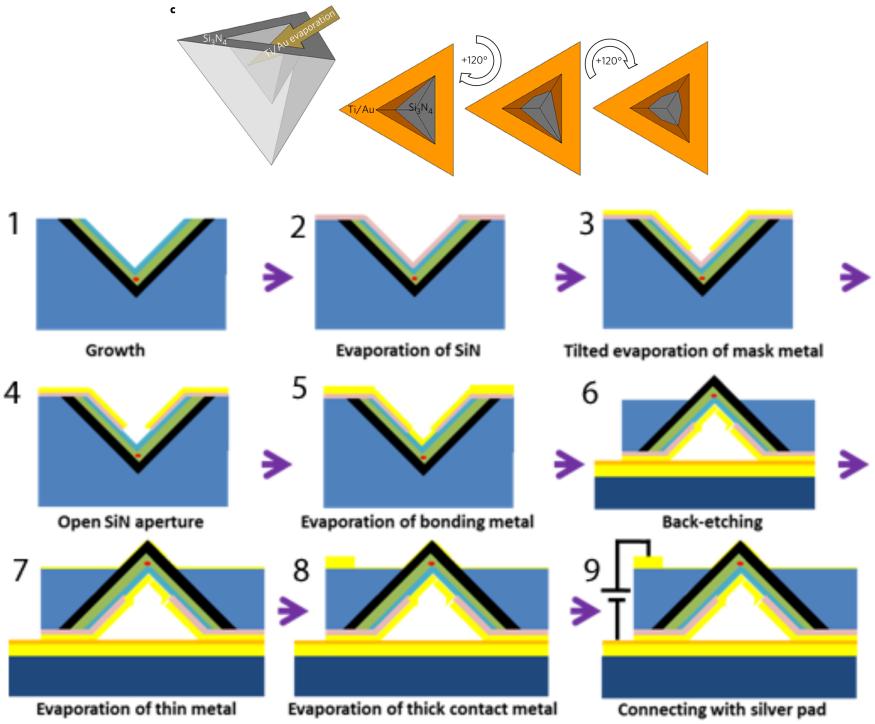


Figure 4.30: p-i-n diode structure for *GaAs* QDs: gold evaporation steps (top) full processing steps (bottom). Images taken from [18]

negative trion and what we speculate to be its excited state can be observed, Fig.4.31 (right).

4.4 Conclusions

In this chapter we have described our findings relative to the energetic structure of GaAs QDs in AlGaAs barriers with superlattice.

We have shown how the superlattice structure greatly improves one of the most important optical properties of the QDs for emission of entangled photons, the FSS, compared to previous generation of GaAs QDs with different barriers, see Fig.4.3.

We have reported the presence in our QDs of an excited state of the exciton state, $X_{0\bar{1}}$, which shows light-hole-like properties, Fig.4.8. This kind of state is not often reported in literature and we have analysed in depth its properties with cross-section, polarization and time resolved spectroscopy. We have shown the possibility of tuning the light-hole component of excited and ground state through band-

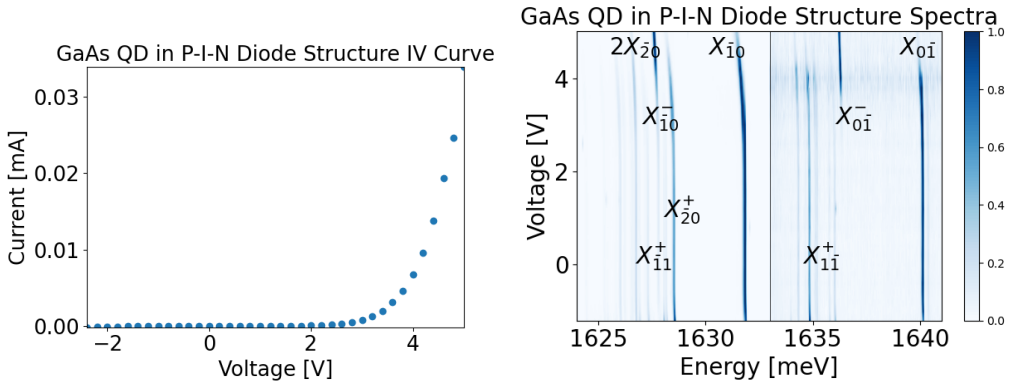


Figure 4.31: p-i-n diode structure for *GaAs* QDs: measured IV curve showing the expected diode behaviour (left) PL spectra as function of the applied voltage showing very weak Stark shift and charge tuning under forward bias, the spectra has been divided in two ranges, ground and excited states, and each range normalized to highlight the relative intensity of the states (right).

mixing induced by strain, applied using a piezoelectric substrate, see Fig.4.16.

Since the main focus of this thesis is to test if our QDs are a suitable candidate for cluster state generation using the Linder and Rudolph protocol [19], we have investigated also the charged complexes present in our QDs, see Fig.4.17. The positively charged biexciton, positive trions and their excited states have been identified by analysis of the charged biexciton cascade, taking into account the light-hole-like nature of the excited state, that changes the selection rules, see Fig.4.22.

The negatively charged trions were identified with the use of custom made a diode device, see Fig.4.31.

The combination of site-controlled and MOVPE growth of the QDs gives us a sample with a very reproducible QD spectrum, therefore after mapping the spectrum to the corresponding excitonic state in a QD we were able to quickly identify the same transitions in other QDs from the sample.

By analysing several QDs in our sample, we found that relative energies of the trions, see Fig.4.18-4.21, and their exchange interaction, see Fig.4.28, are characterized by linear relations, these are a fingerprint of the QD size and shape due the dot-to-dot variation. These informations and data can be used to develop theoretical models or simulations of our QD properties as a function of their size and symmetry.

References

[1] I. Ranjbar Jahromi et al. "Optical properties and symmetry optimization of spectrally (excitonically) uniform site-controlled GaAs pyramidal quantum dots". In: *Applied Physics Letters* 118.7 (Feb. 2021). DOI: 10.1063/5.0030296.

[2] K. F. Karlsson et al. "Spectral signatures of high-symmetry quantum dots and effects of symmetry breaking". In: *New Journal of Physics* 17.10 (Oct. 2015). DOI: 10.1088/1367-2630/17/10/103017.

[3] M. Bayer et al. "Fine structure of neutral and charged excitons in self-assembled In(Ga)As/(Al)GaAs quantum dots". In: *Phys. Rev. B* 65 (19 May 2002). DOI: 10.1103/PhysRevB.65.195315.

[4] T. Heindel et al. "A bright triggered twin-photon source in the solid state". In: *Nature Communications* 8.1 (Apr. 2017). DOI: 10.1038/ncomms14870.

[5] S.T. Moroni et al. "Vanishing biexciton binding energy from stacked, MOVPE grown, site-controlled pyramidal quantum dots for twin photon generation". In: *Journal of Crystal Growth* 506 (2019), pp. 36–39. ISSN: 0022-0248. DOI: 10.1016/j.jcrysgro.2018.10.005.

[6] D. J. Griffiths. *Introduction to Quantum Mechanics*. Pearson Education, 1995. DOI: https://doi.org/10.1017/9781316995433.

[7] Y. H. Huo et al. "A light-hole exciton in a quantum dot". In: *Nature Physics* 10.1 (Jan. 2014). DOI: 10.1038/nphys2799.

[8] C. Tonin et al. "Polarization properties of excitonic qubits in single self-assembled quantum dots". In: *Phys. Rev. B* 85 (15 Apr. 2012). DOI: 10.1103/PhysRevB.85.155303.

[9] T. Lettner et al. "Strain-Controlled Quantum Dot Fine Structure for Entangled Photon Generation at 1550 nm". In: *Nano Letters* 21.24 (2021). DOI: 10.1021/acs.nanolett.1c04024.

[10] M. B. Rota et al. "A source of entangled photons based on a cavity-enhanced and strain-tuned GaAs quantum dot". In: *eLight* 4 (1 July 2024). DOI: 10.1186/s43593-024-00072-8.

[11] D. Huber et al. "Strain-Tunable GaAs Quantum Dot: A Nearly Dephasing-Free Source of Entangled Photon Pairs on Demand". In: *Phys. Rev. Lett.* 121 (3 July 2018). DOI: 10.1103/PhysRevLett.121.033902.

[12] I. Ranjbar Jahromi. "Evaluation and properties of site-controlled pyramidal quantum dots for quantum information processing". 2023.

[13] E. Poem et al. "Radiative cascades from charged semiconductor quantum dots". In: *Phys. Rev. B* 81 (8 Feb. 2010). DOI: 10.1103/PhysRevB.81.085306.

[14] O. Benson et al. "Regulated and Entangled Photons from a Single Quantum Dot". In: *Phys. Rev. Lett.* 84 (11 Mar. 2000). DOI: 10.1103/PhysRevLett.84.2513.

[15] J. D. Plumhof et al. "Experimental methods of post-growth tuning of the excitonic fine structure splitting in semiconductor quantum dots". In: *Nanoscale Research Letters* 7.1 (2012). DOI: https://doi.org/10.1186/1556-276X-7-336.

[16] A. Imamogolu and Y. Yamamoto. "Turnstile device for heralded single photons: Coulomb blockade of electron and hole tunneling in quantum confined p-i-n heterojunctions". In: *Phys. Rev. Lett.* 72 (2 Jan. 1994). DOI: 10.1103/PhysRevLett.72.210.

[17] S. Marcet, Kiyonobu Ohtani, and Hideo Ohno. "Vertical electric field tuning of the exciton fine structure splitting and photon correlation measurements of GaAs quantum dot". In: *Applied Physics Letters* 96 (2010), p. 101117. URL: https://api.semanticscholar.org/CorpusID:121410364.

[18] T. H. Chung et al. "Selective carrier injection into patterned arrays of pyramidal quantum dots for entangled photon light-emitting diodes". In: *Nature Photonics* 10.12 (2016). DOI: https://doi.org/10.1038/nphoton.2016.203.

[19] N. H. Lindner and T. Rudolph. "Proposal for Pulsed On-Demand Sources of Photonic Cluster State Strings". In: *Phys. Rev. Lett.* 103 (11 Sept. 2009). DOI: 10.1103/PhysRevLett.103.113602.

Chapter 5

Hole Spin Initialization and Control

In Chap.1 we have discussed the Lindner and Rudolph protocol [1] for generating cluster states and steps for implementing quantum computing.

In Chap.2 we have described the experimental setups used to characterize the Site - Controlled Pyramidal Quantum Dots and to generate a linear cluster state.

In Chap.3 we have discussed several QDs excitation scheme, highlighting advantages and disadvantages of each scheme. Of particular interest for our application are phonon assisted excitation and excitation of an excited state, that relaxes through a non - radiative process to an intermediate state before emitting a photon.

In Chap.4 we have described our findings on the energy structure of GaAs QDs, discovering 4 excited states of a trion.

In the following chapter we will focus on the analysis of phonon assisted excitation of the trion state and resonant excitation of its 4 excited states.

Since the generation and manipulation of linear cluster states, according to the Lindner and Rudolph protocol [1], requires careful initialization and control of hole or electron spins in a weak magnetic field, we will discuss not only on the excitation process, but also on the dynamics of the spin during the relaxation process to trion state.

In the first section of the following chapter initialization of a specific hole state at $\vec{B} = 0T$ will be demonstrated with phonon-assisted and resonant excitation. In the second section controlled precession in a weak magnetic field, $0.4T \leq \vec{B} \leq 0.6T$, will be demonstrated to enable laser synchronization with the hole spin precession.

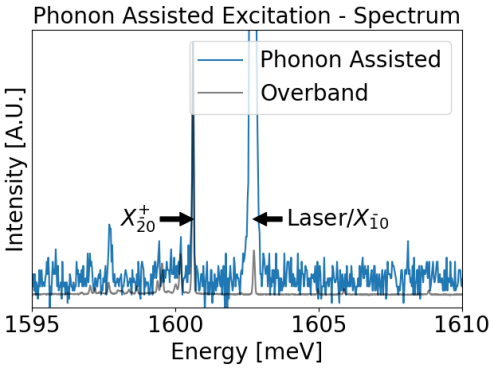


Figure 5.1: Spectrum of GaAs QD under Phonon Assisted Excitation

5.1 Hole Initialization at $\vec{B} = 0T$

5.1.1 Phonon Assisted Excitation

The $X^+_{\bar{2}0}$ state can be excited using phonon assisted excitation by detuning the pulse shaper output a few meV away from the optical transition. Fig.5.1 shows a $GaAs$ QD spectrum when the tunable pulse-shaped Ti:Sapphire laser is set to the energy of the $X_{\bar{1}0}$ state. Emission from $X^+_{\bar{2}0}$ and some weak emission from $2X_{\bar{2}0}$ can be observed in the spectrum. The laser has to be tuned close enough to the $X^+_{\bar{2}0}$, so that the notch filters don't suppress part of the emission and background from the laser tails is rejected by the spectrometer output slit when taking time resolved measurements. In general we have found the excitation process is inefficient for $GaAs$ QDs, resulting in a rate of just a few thousand counts on our APDs,

Polarization resolved photoluminescence shows that, when the QD is excited with right-handed circularly polarized light, the emission of the $X^+_{\bar{2}0}$ has a 0.77 ± 0.01 degree of circular polarization, see Fig.5.2 (left) and is in phase with the tunable laser. This implies that the polarization state of the laser is directly mapped to the polarization state of the emitted photon from the trion state.

The dynamics of the excitation process can be probed by exciting the QD with linearly polarized light and taking a polarization resolved autocorrelation measurement of the $X^+_{\bar{2}0}$ in circular polarization basis.

The $g^{(2)}(\tau)$ shows a pronounced bunching when the detection is co-polarized, see Fig.5.2 (right, blue curve), which means that the correlated photons have the same polarization. The dip at $\tau = 0ns$ is the typical signature of single photon emission from QDs.

In cross-polarized detection, the correlated photons have orthogonal polarization, and strong antibunching is observed, see Fig.5.2 (right, orange curve).

The DOCP and $g^{(2)}(\tau)$ can be explained by the following spin dynamics. Before

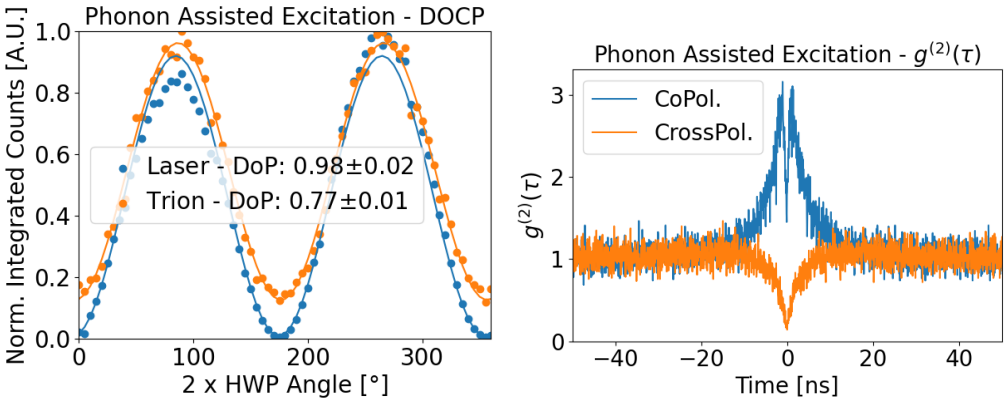


Figure 5.2: Degree of Circular Polarization of laser and X^+_{20} when the QD is under phonon-assisted excitation with circularly polarized light (left). $g^{(2)}(\tau)$ of X^+_{20} in co-polarized and cross-polarized detection when the QD is under phonon-assisted excitation with linearly polarized light (right).

excitation, the QD is populated randomly by either a spin in the up or down configuration, with a 0.50 probability for each spin state. This is a statistical mixture state of $|\Uparrow\rangle$ and $|\Downarrow\rangle$.

If we excite the QD with linearly polarized light, $|H\rangle = \frac{1}{\sqrt{2}}(|R\rangle + |L\rangle)$, only the polarization component that satisfies the selection rule couples to the spin present in the QD at the time. A non radiative relaxation process brings the charges to the ground energy levels of the QD, and the QD is now populated by a X^+_{20} state.

After recombination of an electron - hole couple, we can project the emitted photon to a circular basis to measure its handedness. If we detect a right (left) handed photon, we herald the presence of a $|\Uparrow\rangle$ ($|\Downarrow\rangle$) spin in the QD, because of the selection rules $|\uparrow\Downarrow\Uparrow\rangle \rightarrow |R\rangle$ and $|\downarrow\Uparrow\Downarrow\rangle \rightarrow |L\rangle$.

In the next excitation cycle, the QD will not be populated anymore by a random spin, but by a specific state. Again only the polarization basis satisfying the selection rules will couple to the QD.

Because of the selection rules written above, the single hole $|\Uparrow\rangle$ ($|\Downarrow\rangle$) will only couple to $|R\rangle$ ($|L\rangle$) and the QD will emit again a $|R\rangle$ ($|L\rangle$) photon. At short τ, we are more likely to observe photons with the same polarization than orthogonal ones, and therefore the bunching in co-polarized and antibunching in cross-polarized detection.

Dephasing, spin flips, charge tunnelling and other phenomena can contribute to destroy the coherence of this excitation process and thus both co-polarized and cross-polarized autocorrelation flatten out to $g^{(2)}(\tau) = 1$ at longer τ. Fitting with an exponential function, Ae^{-t/T_1}, where T_1 is the spin lifetime introduced in Chap.1, we measured $T_1 = (4.15\pm0.07)ns$ for co-polarized and $T_1 = (2.61\pm0.15)ns$

for cross-polarized detection.

5.1.2 Excited State Resonant Excitation

A preferred excitation process for cluster state generation would be resonant excitation of a positive trion with the electron in the second energy level of the conduction band, which then relaxes non radiatively to the ground state. These excited states are typically separated a few tens of meV from the ground states. This is the same state that has been used to initialize the QD in [2].

Due to the holes being in a singlet state and the electron being the only charge carrier in the conduction band, there is no exchange interaction and therefore the dynamics of the relaxation process or optical recombination are greatly simplified compared to a positive trion with one hole in the excited energy levels of the valence band.

We have scanned, with the tunable Ti:Sapphire laser, a $\sim 10meV$ range $+5meV$ away from the trion transition. Unfortunately we did not detect any strong resonance of the $X^+_{\bar{2}0}$ state.

Above-band excitation also shows only emission from the superlattice in the $+20meV$ range, and thus any charge that is generated at that energy range would most likely populate the QD after a non-coherent process and its spin state would be randomized. It is also probable the $Al_xGa_{1-x}As$ and superlattice barriers are too shallow to have two energy levels in the conduction band.

For these reasons, resonant excitation has been attempted by scanning only in the range of the excited states of the valence band, where emission from $X^+_{1\bar{1}}$ is observed.

A total of 4 resonances for $X^+_{\bar{2}0}$ and $X^+_{\bar{1}1}$ were found, see Fig.5.3, with the first resonance giving the brightest PL for the $X^+_{\bar{2}0}$ state.

The resonances overlap with the PL pattern of the $X^+_{1\bar{1}}$ states studied in the previous chapter, see Fig.5.4. One of these states is usually not visible in the top view, but is optically active in cross-section.

As discussed in Chap.3, Rabi oscillations for the PL of $X^+_{\bar{2}0}$ were observed when the QD is excited at the first resonance, and with a Ramsey Fringes we measured the coherence time of the excited state, $T_2^* = 100ps$.

Resonantly exciting the QD with circularly polarized light and analysing the polarization of the emission shows that the $X^+_{\bar{2}0}$ is highly polarized with a $DOCP = 0.94\pm0.01$. Unlike phonon assisted excitation the polarization of the $X^+_{\bar{2}0}$ is counter-phasing that of the laser, see Fig.5.5. The high degree of polarization is indicative of the high fidelity of the excitation process in populating the QD with a determined spin.

The $g^{(2)}(\tau)$ of the $X^2_{\bar{2}0}$ is characterized by strong bunching in co-polarized detection and antibunching in cross-polarized, see Fig.5.6 (left). Under CW excitation,

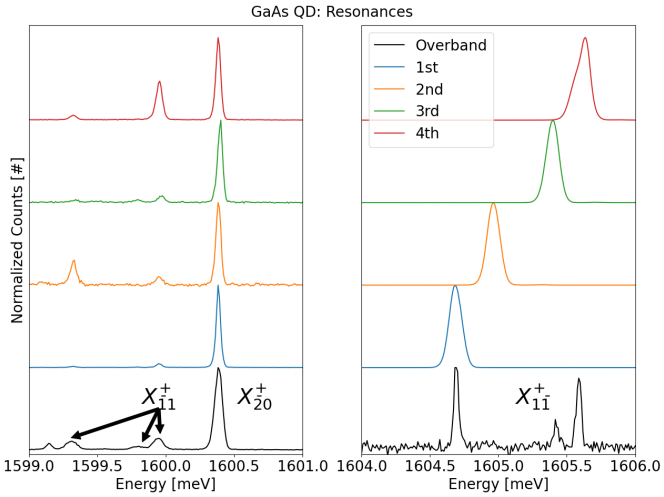


Figure 5.3: Spectrum of a $GaAs$ QD under resonant excitation of the 4 resonances of trion states.

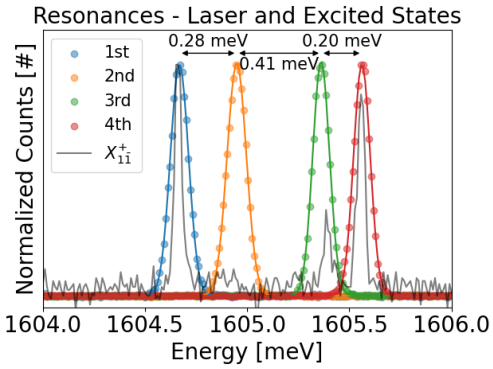


Figure 5.4: Spectrum of the tunable Ti:Sapphire laser at the four resonances of the trion states.

hole spin lifetime has been measured to be $T_1 = 10.04 \pm 0.19ns$ in co-polarized and $T_1 = 6.48 \pm 0.14ns$ in cross-polarized detection. Switching to pulsed excitation at $80MHz$, see Fig.5.6 (right), the exponential envelope of the bunching and antibunching looks drastically improved, indicating that the hole spin may keep its coherence for longer if the QD is not continuously excited.

The antiphasing polarization of excitation and emission can be qualitatively explained using a theoretical framework valid for pure light and heavy hole-related optical selection rules in QDs with the conventional D_{2d} symmetry [3] [4]. As observed in our experiments, in this case, also applicable to the C_{3V} symmetry QDs.

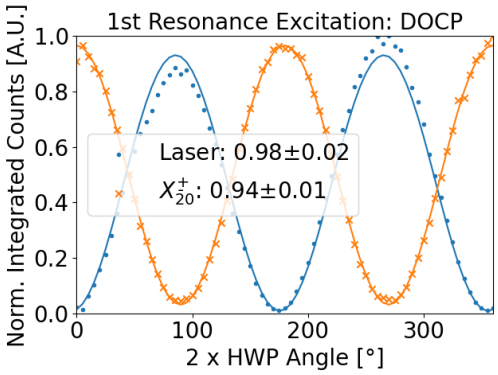


Figure 5.5: Degree of Polarization of laser and X^+_{20} state under resonant excitation with circularly polarized light at the 1st resonance.

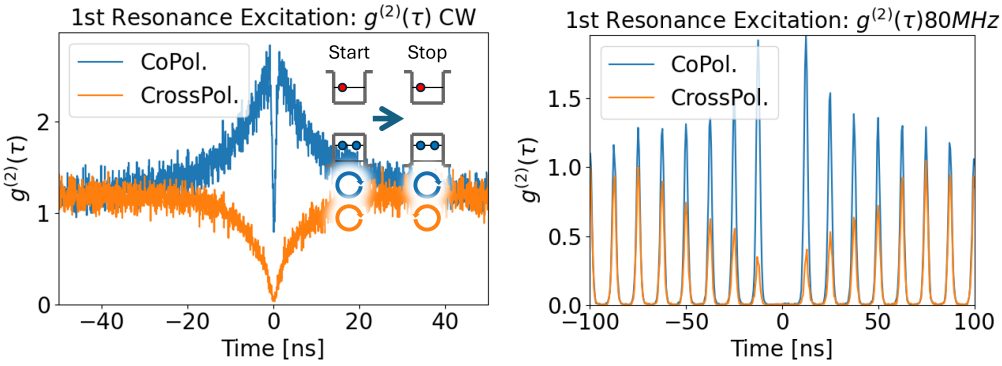


Figure 5.6: $g^{(2)}(\tau)$ of X^+_{20} state under resonant excitation with linearly polarized light, in CW excitation (left) and pulsed at $80MHz$ (right).

We remind the reader that the light-hole state can be expressed in the Luttinger - Kohn notation as:

$$\begin{aligned} |\frac{3}{2};+\frac{1}{2}\rangle &= -\frac{1}{\sqrt{6}}\left[|(X+iY)\Downarrow\rangle + 2\,|Z\Uparrow\rangle\right] \\ |\frac{3}{2};-\frac{1}{2}\rangle &= \frac{1}{\sqrt{6}}\left[|(X-iY)\Uparrow\rangle - 2\,|Z\Downarrow\rangle\right] \end{aligned} \tag{5.1}$$

For light-hole-like states, absorption of a circularly polarized photon happens according the following selection rules:

$$\begin{aligned} |R\rangle = \sigma^+ &= -\frac{\Pi}{\sqrt{6}}\left(E_x\hat{x} + iE_y\hat{y}\right) = \langle\frac{1}{2};+\frac{1}{2}|\,\vec{E}\cdot\vec{p}\,|\frac{3}{2};+\frac{1}{2}\rangle \\ |L\rangle = \sigma^- &= +\frac{\Pi}{\sqrt{6}}\left(E_x\hat{x} - iE_y\hat{y}\right) = \langle\frac{1}{2};-\frac{1}{2}|\,\vec{E}\cdot\vec{p}\,|\frac{3}{2};-\frac{1}{2}\rangle \end{aligned} \tag{5.2}$$

these selection rules still apply even though the excitation process happens in the top-view configuration, XY plane, and the circularly polarized photon does not carry momentum along the $\hat{z}$ axis, $\sigma^{\pm} \sim E_x\hat{x} \pm iE_y\hat{y}$.

Emission of circularly polarized photons from heavy-hole-like states follows the selection rules::

$$\begin{aligned} |L\rangle = \sigma^{-} &= +\frac{\Pi}{\sqrt{2}}\left(E_x\hat{x} - iE_y\hat{y}\right) = \langle \frac{1}{2}; +\frac{1}{2} | \, \vec{E}\cdot\vec{p} \, | \frac{3}{2}; -\frac{3}{2}\rangle \\ |R\rangle = \sigma^{+} &= -\frac{\Pi}{\sqrt{2}}\left(E_x\hat{x} + iE_y\hat{y}\right) = \langle \frac{1}{2}; -\frac{1}{2} | \, \vec{E}\cdot\vec{p} \, | \frac{3}{2}; +\frac{3}{2}\rangle \end{aligned} \tag{5.3}$$

Relaxation of the hole from the excited to the ground state causes emission to be orthogonal to the excitation due to the different selection rules for heavy and light hole bands. If the excited state is also in a singlet state, this relaxation process would also preserve the singlet nature of the state, but at the moment, without a stronger theoretical framework backing these measurements we don't know the value of the phase in the excited state. Because the hole left in QD does not change its spin orientation between excitation cycles, see Fig.5.7, the $g^{(2)}(\tau)$ shows bunching in co-polarized detection.

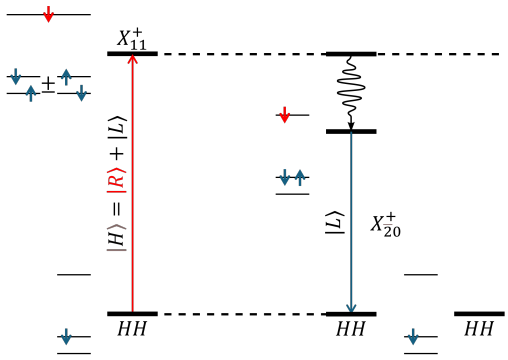


Figure 5.7: Dynamics of the excitation of the X_{11}^{+} state and recombination of the $X_{\bar{2}0}^{+}$ state (at the 1st resonance). The relaxation of the hole from the 2nd to the 1st energy level causes polarization of excitation and recombination to be orthogonal, the spin direction is preserved between excitation cycles, causing bunching in $g^{(2)}(\tau)$ under co-polarized detection. Image adapted from [5].

If the first and second energy levels of the valence band were both purely heavy-hole, then exciting the QD with right(left)-handed circularly polarized would generate right(left)-handed emission, because the polarization of the absorbed and emitted photon will be set by the electron spin, $|\uparrow\Downarrow\rangle \rightarrow |L\rangle$ ($|\downarrow\Uparrow\rangle \rightarrow |R\rangle$). Even under the scenario of the relaxation of the hole happening through a spin-flip process, the emission would not be orthogonal to the excitation, if the electron

spin does not flip as well. This is another demonstration of the light-hole-like nature of the second energy level of the valence band.

The other 3 resonances show a less bright $X^+_{\bar{2}0}$ compared to the first resonance and they also are characterized by emission from the hot trion states. Clear Rabi oscillations have also been observed for the second and fourth resonance, see Fig.5.8.

In the cases of excitation of the X^+_{11} states and recombination from the $X^+_{\bar{1}1}$ states, Rabi oscillations reflect the coherent nature of the whole process, because the hole does not relax through incoherent phenomena, such as spin-flip and phonon exchange, to the ground level.

Relaxation of a X^+_{11} to the $X^+_{\bar{2}0}$ state happens instead always through phonon exchange and spin-flip events, thus the Rabi oscillations of the $X^+_{\bar{2}0}$ intensity reflects only the coherent population of the excited state.

Furthermore under circularly polarized excitation the emission is always in antiphase, see Fig.5.9.

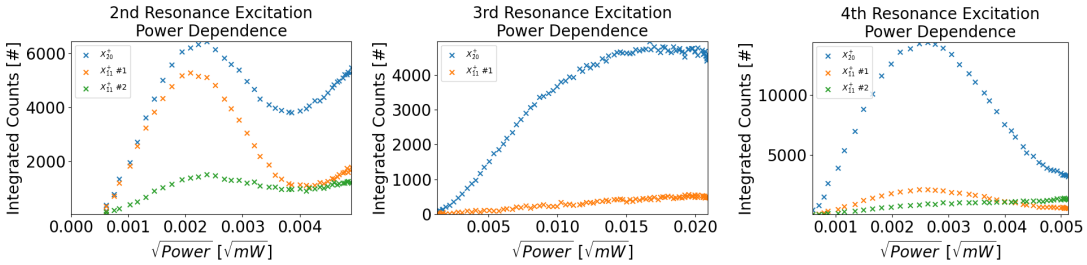


Figure 5.8: Power Dependence the trion states under resonant excitation at the 2nd, 3rd and 4th resonance.

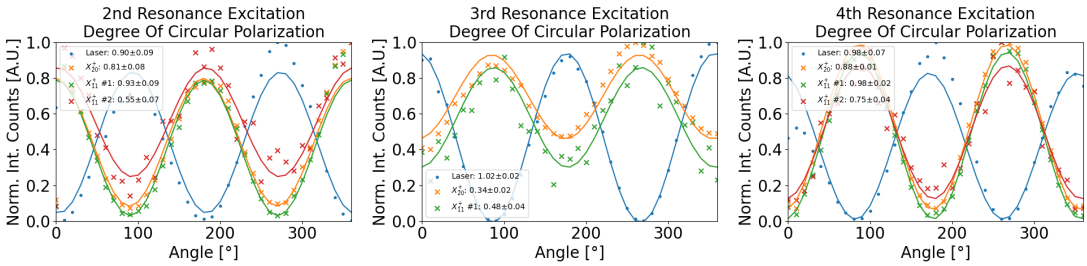


Figure 5.9: Degree of Polarization of laser and trion states under resonant excitation with circularly polarized light at the 2nd, 3rd and 4th resonance.

For the 2nd resonance we observe increased emission from one of the hot trions, taking an autocorrelation measurement show bunching (antibunching) in co-polarized (cross-polarized) detection, see Fig.5.10 (right).

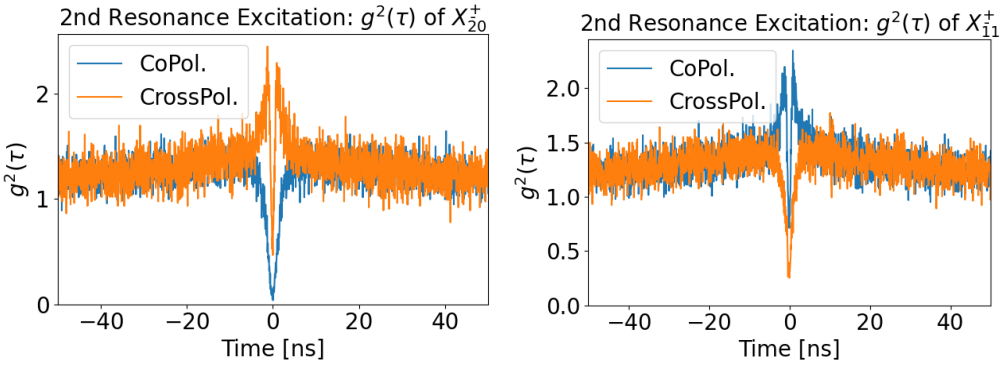


Figure 5.10: $g^{(2)}(\tau)$ of $X^+_{\bar{2}0}$ (left) and $X^+_{\bar{1}1}$ (right) states under resonant excitation with linearly polarized light at the 2nd resonance.

This can be explained by the fact that the hole relaxes after emission of the photon by preserving its spin direction in a manner similar to the first resonance, see Fig.5.11.

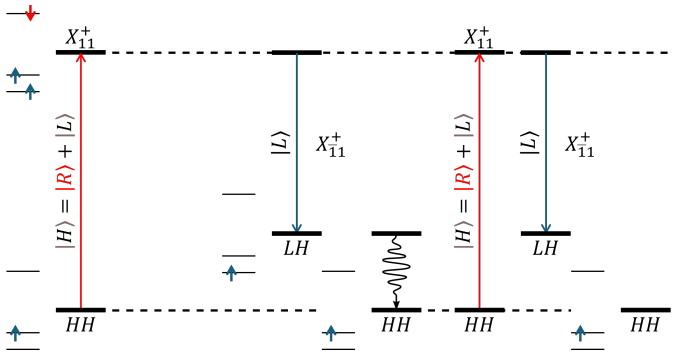


Figure 5.11: Dynamics of the excitation and recombination processes of the $X^+_{\bar{1}1}$ state (at the 2nd resonance of the $X^+_{\bar{2}0}$ state). Excitation and emission are still orthogonal due to recombination from different band, and emission is co-polarized between excitation cycles because the hole relaxation process preserves the spin direction. Image adapted from [5].

Taking autocorrelation of the ground trion at the same resonance shows the opposite behaviour of previous measurements, bunching (antibunching) in cross-polarized (co-polarized) detection, see Fig.5.10 (left). We speculate that this is due to relaxation happening through a spin-flip process, that leaves the QD with a hole spin opposite to the one present before the excitation, Fig.5.12. If the QD is excited with linearly polarized light, then the QD is populated by opposing electron spins every other cycle and will emit left(right)-handed photons in an alternating

cycle, therefore the $g^{(2)}(\tau)$ will show bunching in cross-polarized detection, where the correlated photons are orthogonal.

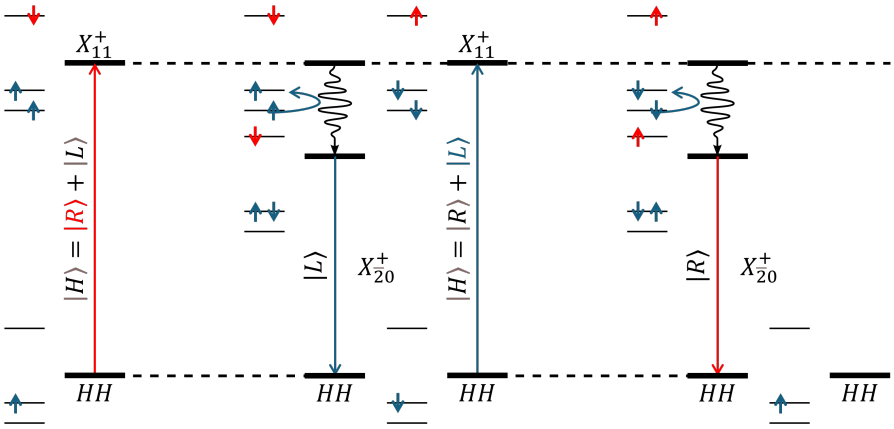


Figure 5.12: Dynamics of the excitation of the X_{11}^{+} state and recombination of the $X_{\bar{2}0}^{+}$ state (at the 2$^{\text{nd}}$ resonance). The holes relaxes to the 1$^{\text{st}}$ energy level through a spin-flip process, excitation and emission are still orthogonal but so is the emitted photons between two consecutive cycles, due to the hole flipping direction. Image adapted from [5]

The ones presented above are of course simplified pictures of the relaxation processes. A stronger theoretical framework which takes into accounts the exchange interaction of the two holes in different levels is needed to fully explain the dynamics of the relaxation processes. But the results shown above prove that a combination of analysis of degree of polarization and polarization resolved $g^{(2)}(\tau)$ are essential tools to probe the spin state dynamics.

5.2 Hole Precession in Weak Magnetic Field

Due to the lack of a tunable electro-magnet at Tyndall National Institute laboratories at the time of writing, the measurements at high magnetic fields were taken at the laboratories of La Sapienza University in Rome.

There are two conventional configurations for measurements of QD in a magnetic field, Faraday and Voigt.

In the Faraday configuration the magnetic field is parallel to the growth direction, and thus perpendicular to the growth plane $\vec{B} = B\hat{z}$. Polarization resolved PL shows that the $X_{\bar{2}0}^{+}$ splits into two sets of doublets in Faraday configuration, Fig.5.13. This spin-splitting scenario has been reported in literature for QDs grown by droplet epitaxy on (111) surface [6] [7] and for $InGaAs$ QDs in $GaAs$ barriers

grown in pyramidal recess on (111) plane [8]. The splitting into four lines was explained by the mixing of hole states $|\pm\frac{3}{2}\rangle$.

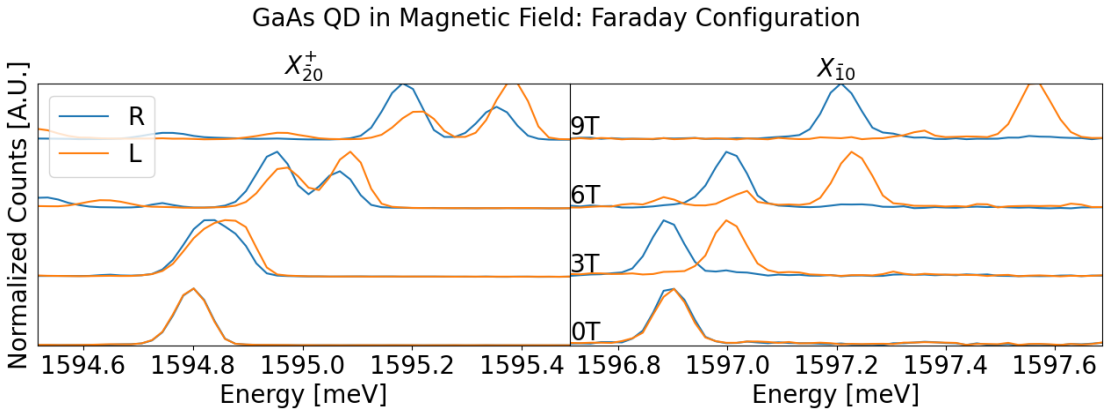


Figure 5.13: Splitting in GaAs QD of Trion and Exciton lines into two doublets in a magnetic field (Faraday Configuration).

In the Voigt configuration the magnetic field is perpendicular to the growth direction, and thus in-plane with the growth plane $\vec{B} = B\hat{x}$. At high magnetic field values, Zeeman effect splits the trion line into four non degenerate transitions [9]. Diagonal recombination through the emission of linearly polarized photons is allowed, see Fig.5.14 (right).

For quantum computing applications, one could theoretically populate the QD through the transition $|\Uparrow\rangle \rightarrow |\uparrow\Uparrow\Downarrow\rangle$ or $|\Downarrow\rangle \rightarrow |\downarrow\Uparrow\Downarrow\rangle$ and observe the recombination $|\uparrow\Uparrow\Downarrow\rangle \rightarrow |\Downarrow\rangle$ or $|\downarrow\Uparrow\Downarrow\rangle \rightarrow |\Uparrow\rangle$ that heralds the spin state of the QD [9].

But this is not a suitable configuration for cluster state initialization and generation, because we need the ground and excited trion states to still be degenerate, within the transition linewidth, to be able to populate the QD with their superposition. Furthermore only the hole spin needs to precess and selection rules need to be preserved.

Selection rules in Voigt geometry for SK QDs and the QDs studied in this thesis should be the same. From measurements taken in the laboratories of La Sapienza University in Rome, we could not observe any splitting of the $X^+_{\bar{2}0}$ beyond the direct resolution of the spectrometers ($\sim 10\mu eV$). Only a diamagnetic shift is observed.

By plotting the DOCP of the trion's lifetime decay trace, $DOCP = \frac{I_H(t)-I_V(t)}{I_H(t)+I_V(t)}$, precession of the trion state is observed, see Fig.5.15. This is an indication that a field $> 0.5T$ is too strong, because, ideally, in a cluster state only the hole spin should precess while the trion spin state evolves as little as possible to preserve the selection rules and superposition state.

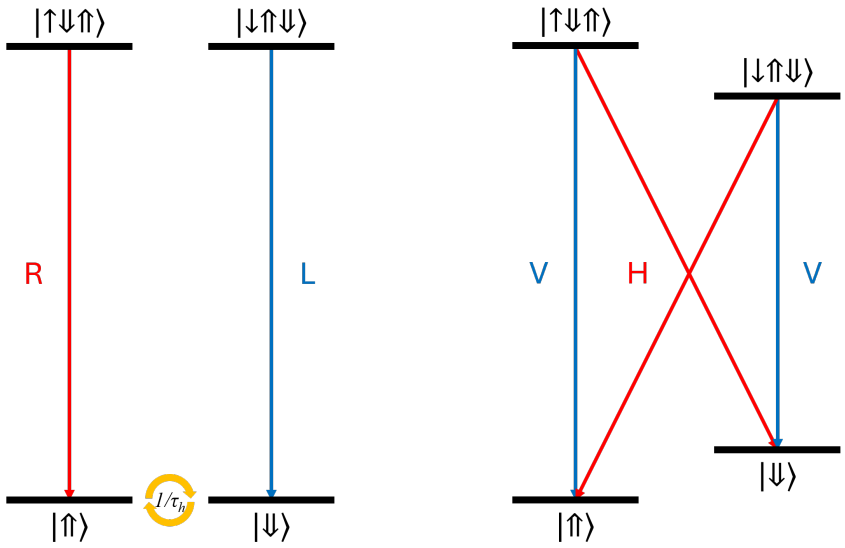


Figure 5.14: Selection rules in weak (left) and strong (right) magnetic field in Voigt geometry. The trion oscillation term becomes relevant when the lifetime of the state is longer than the precession period.

To compensate the lack of tunable electro-magnet in the Tyndall National Institute laboratory, we have decided to use permanent magnets to generate the weak magnetic field needed for hole precession. The samples has been diced into a $1.8mm$ wide strip. Two cylindrical N35 magnets are placed $2mm$ apart in a custom designed magnet holder across the sample, the field generated is $0.4T < B < 0.6T$ in a Voigt configuration.

Scanning the 1^{st} resonance with a tunable CW laser, we have verified that the splitting induced by the magnetic field is lower than the linewidth of the transition of the ground and excited trions. No appreciable difference in the energy of the transition is observed when exciting the QD with different polarization, see Fig.5.16, this implies that selection rules, Fig.5.14 (left), still apply.

Furthermore, by pumping the QD in a weak magnetic field with a pulsed and circularly polarized laser, no excessive degradation of the $X^{+}_{\bar{2}0}$ degree of circular polarization has ever been observed. This implies that the trion is not precessing between $|\uparrow\Downarrow\Uparrow\rangle$ and $|\downarrow\Uparrow\Downarrow\rangle$ states and only the hole is precessing.

In a weak magnetic field the hole will precess with a Larmor period $T_h = 2\pi/\omega_h = 2\pi\hbar/g_h\mu_B B$, where g_h is the gyromagnetic factor of the hole and μ_B the Bohr magneton constant.

To observe the hole precession, $g^{(2)}(\tau)$ of the $X^{+}_{\bar{2}0}$ in co and cross-polarized detection is taken under phonon assisted, see Fig.5.17 (left), and resonant excitation of the first excited state, see Fig.5.17 (right), with the polarization of the laser

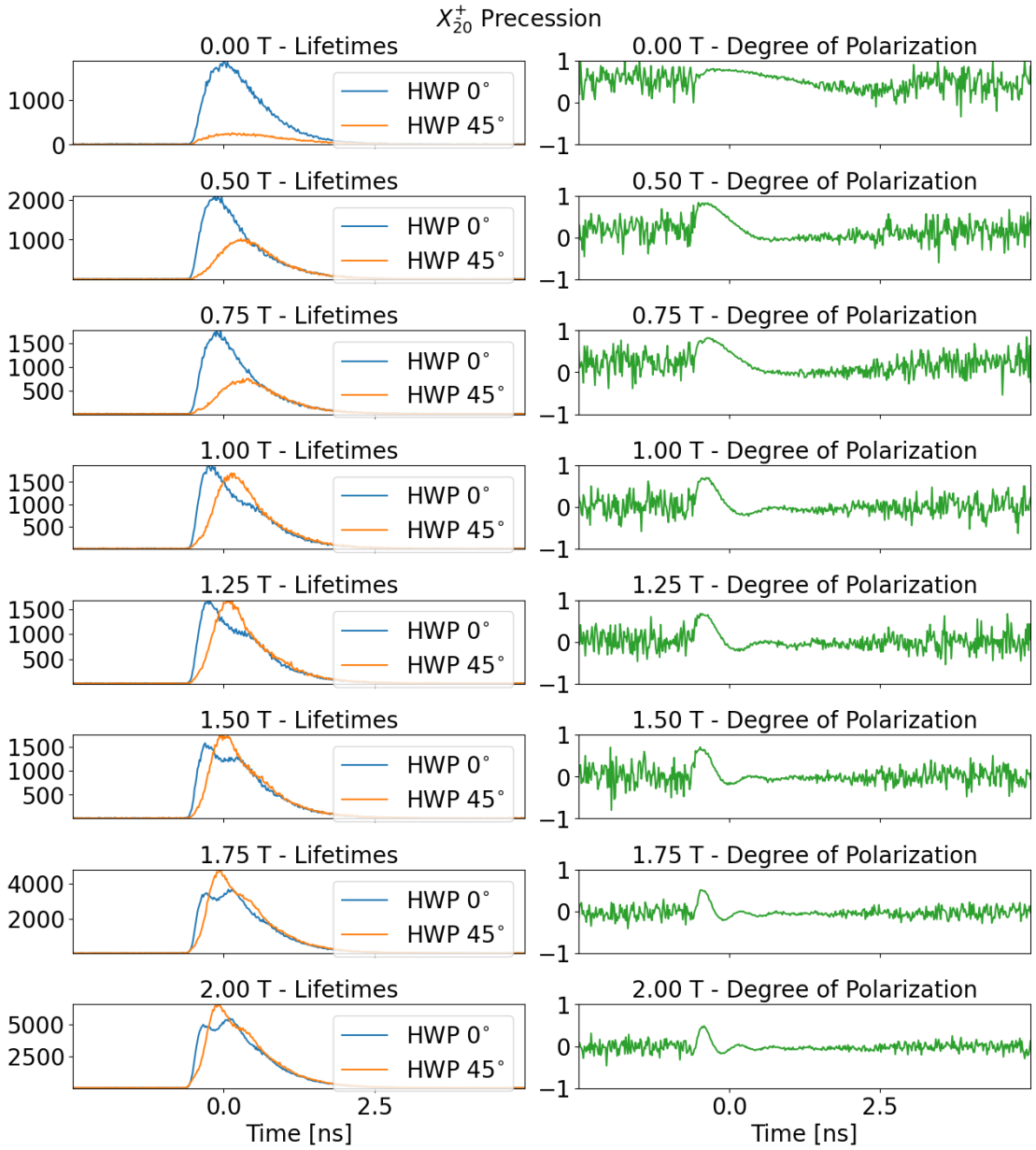


Figure 5.15: Precession of Trion in a strong magnetic field.

set to linear. Because the hole is now oscillating between the $|\Uparrow\rangle$ and $|\Downarrow\rangle$, linearly polarized light can couple to both spin states.

Co-polarized and cross-polarized detection show in both cases damped oscillations of the $g^{(2)}(\tau)$. The intersecting points of the two $g^{(2)}(\tau)$ happen when the hole is in the $\frac{1}{2}(|\Uparrow\rangle \pm |\Downarrow\rangle)$ state.

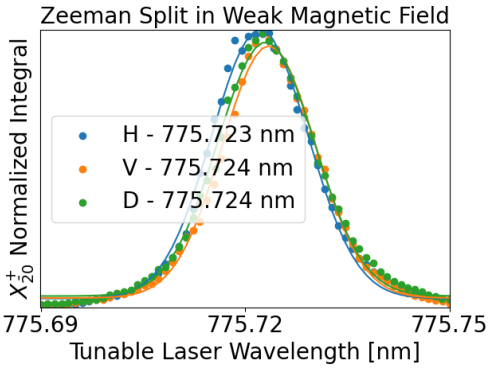


Figure 5.16: Scan of the trion resonance with a tunable CW laser, highlighting no split of the state within the linewidth of the transition.

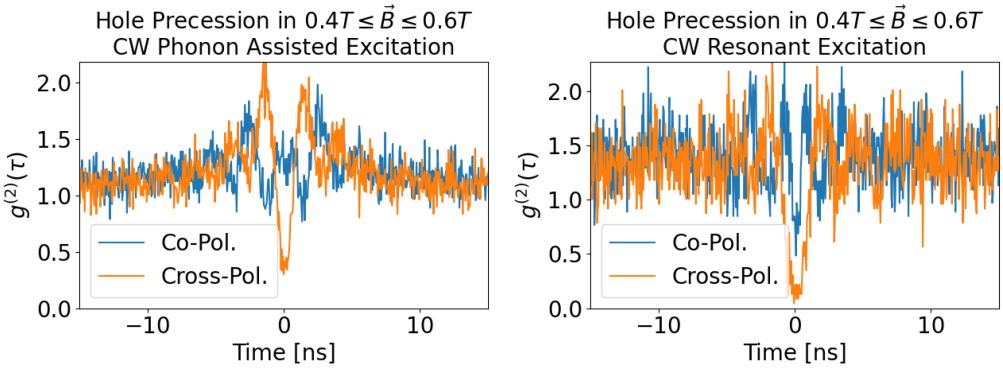


Figure 5.17: Hole precession in phonon-assisted (left) and resonant (right) excitation.

The hole oscillations are better visualized by plotting the degree of circular polarization of the $g^{(2)}(\tau)$, defined as:

$$DOCP_{g^{(2)}} = \frac{g^{(2)}(\tau)_{Cross} - g^{(2)}(\tau)_{Co}}{g^{(2)}(\tau)_{Cross} + g^{(2)}(\tau)_{Co}} \tag{5.4}$$

The zero crossing points of the curve, see Fig.5.18, are the superposition states necessary for cluster state generation [10].

By fitting the DOCP with a damped sinusoid, $y0 + Ae^{-|t|/T_2^*} cos\,(t/T)$, from the phonon assisted excitation data we extracted a pure dephasing time $T_2^* = 2.46 \pm 0.13ns$ precession period of $T = 2.69 \pm 0.02ns$ for the hole. A satisfying fit could not be achieved for the resonant excitation data, although we can clearly *assess by eye* that the data is much noiser than the phonon assisted excitation.

The spin oscillations are, in both cases, strongly damped, already at $\tau = 5ns$

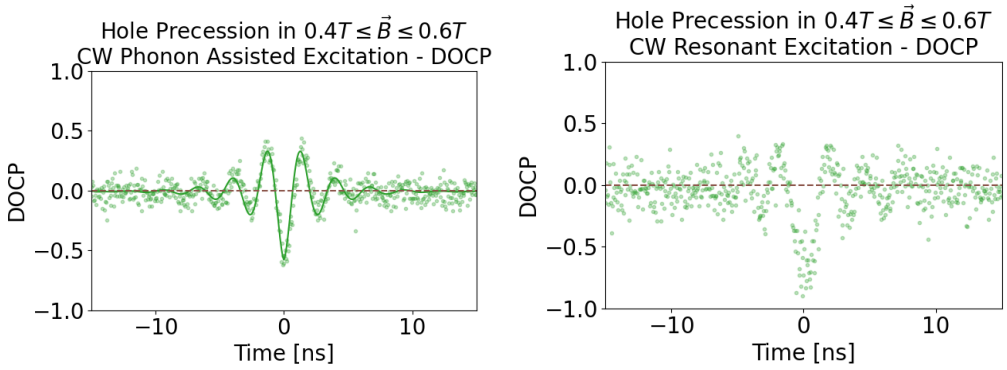


Figure 5.18: Hole precession in phonon-assisted (left) and resonant (right) excitation.

the hole precession is washed away by decoherence. Compared to the spin lifetime at $\vec{B} = 0T$, see Fig.5.6, the decoherence in a magnetic field happens much faster.

It seems that phonon assisted excitation is characterized by less damping and the oscillations are preserved for a bit longer. Unfortunately what is gained in coherence time is lost in reduced brightness of sample, thus making it unsuitable for three photon correlations, which is needed to characterize the cluster state.

It is interesting to note that the zero-photon dip of the $g^{(2)}(\tau)$ is wider in resonant excitation than in phonon assisted, the difference in timing is around $350ps$ and corresponds to the rise time of the trion lifetimes in resonant excitation. This timing difference is due to the different relaxation processes happening in the QD.

Under CW excitation the QD is available for excitation immediately after the recombination of electron - hole couple has happened, the process is thus not on-demand and the excitation can't be timed according to the proposal by Lindner and Rudolph [1]. For this reason the measurement of hole oscillations has been repeated in pulsed mode with the pulse shaped Ti:Sapphire laser. Due to the decreased brightness in phonon assisted excitation, only resonant excitation has been studied.

The original fs pulse has a repetition rate of $f = 80MHz$ and a period of $T = 12.5ns$, which is too big compared to hole precession period and coherence time. To increase the rate of excitation and have an adjustable delay between two pulses, the output of the pulse shaper has been split by a beam splitter and one of the two pulses sent to a variable delay line. By setting the delay to be less $\Delta T < T = 12.5ns$ the spin state can now be probed.

The correlated events of the $g^{(2)}(\tau)$ can now come from either the delayed pulse or the fixed one, Fig.5.19.

The correlation peaks that would be observed without delay at integer multiples

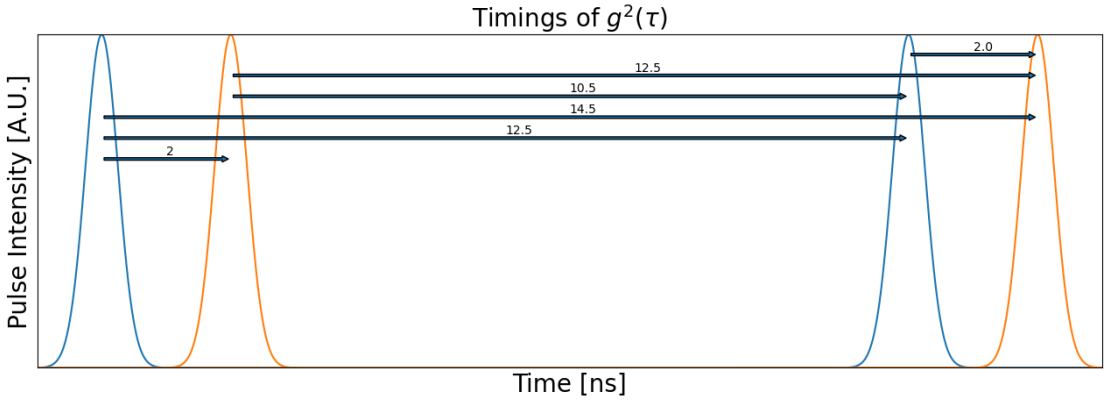


Figure 5.19: Possible combinations in the $g^{(2)}(\tau)$ when the laser pulsed is delayed.

of laser period $T = 12.5ns$, now split into three pronged peaks which spread away with increasing delay, Fig.5.20. The two peaks around the antibunching at $\tau = 0ns$ are the only ones with useful events because they are generated by the fixed and first delayed pulse. After a certain delay ΔT_{max} the side peaks from the ones around the multiples $\tau = \pm 12.5ns$ start to merge with the ones coming from the first delayed pulse and the measurement does not become reliable anymore. The maximum delay that we were able to measure is less than $\Delta T = 4ns$.

Integrating the counts of the two correlation peaks around $t = 0ns$ in co-polarized and cross-polarized detection we can again measure the degree of polarization of $g^{(2)}(\tau)$. The results in pulsed mode overlap with the ones in CW, Fig.5.21, thus confirming the precession period already obtained.

5.3 Cluster State Generation

Due to the the very short spin coherence, $T_2^* = 2.46 \pm 0.13ns$, we can't generate an arbitrary long linear cluster state by synching the hole precession with the laser repetition rate by decreasing the magnetic field and thus increasing the precession period. A workaround is to split a single laser pulse into a 3-arms delays line, described in Chap.2, to generate a 3-qubit cluster state. The processes is then repeated every $12.5ns$.

To generate a three-qubit cluster state, photon - photon - charge carrier entanglement, three excitation pulses are necessary.

The 1st pulse at $t = 0$ populates the QD with a statistical mixture of $|\uparrow\Downarrow\Uparrow\rangle$ and $|\downarrow\Uparrow\Downarrow\rangle$, detection of $|R_1\rangle$ photon will herald the hole spin $|\Uparrow\rangle$.

The 2nd pulse has to be timed to when the $DoP = 0$ for the first time, because after precession of the hole will be in the state $\frac{1}{\sqrt{2}}(|\Uparrow\rangle + |\Downarrow\rangle)$. Excitation will bring

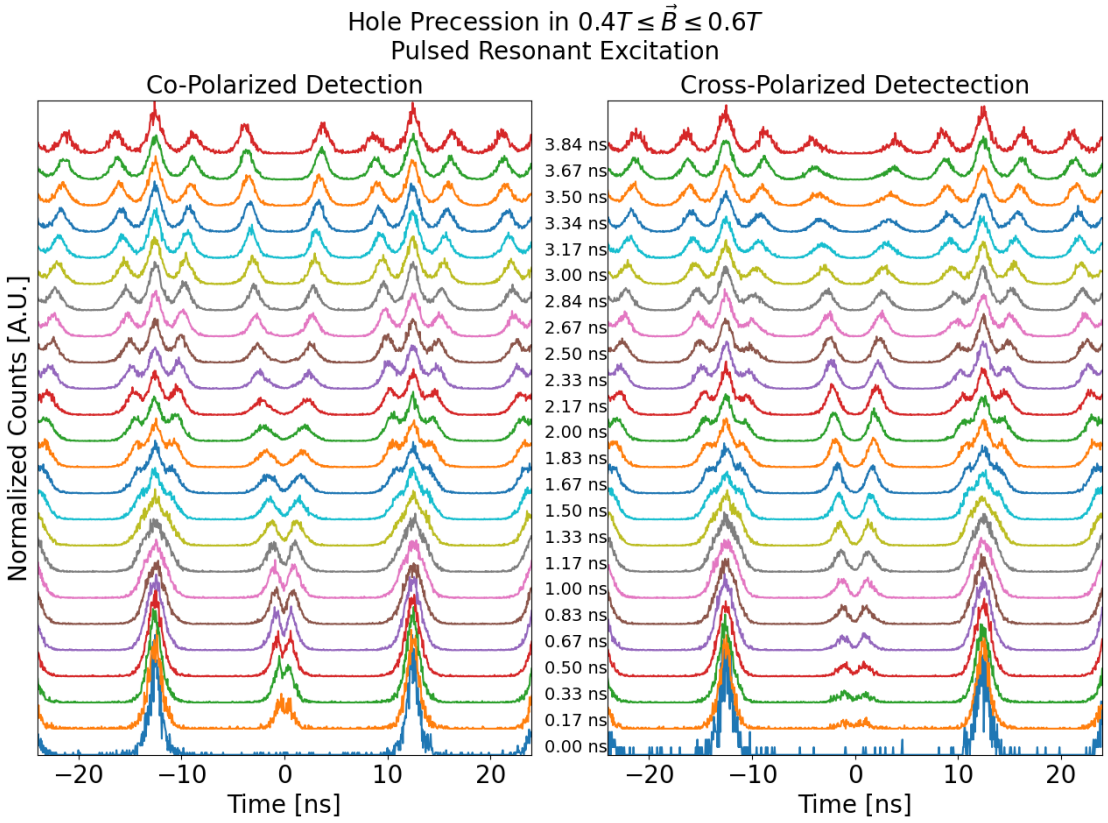


Figure 5.20: Hole precession in phonon-assisted (left) and resonant (right) excitation for variable delays.

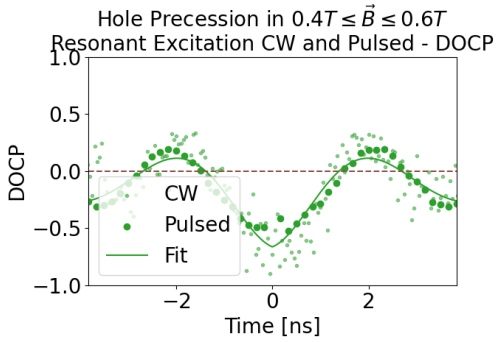


Figure 5.21: Hole precession in resonant excitation with CW and pulsed laser at variable delay.

the QD to $\frac{1}{\sqrt{2}}(|\uparrow\Downarrow\Uparrow\rangle + |\downarrow\Uparrow\Downarrow\rangle)$ state, after recombination the photon - hole system will be in an entangled state $\frac{1}{\sqrt{2}}(|R_2\Uparrow\rangle + |L_2\Downarrow\rangle)$

The 3rd pulse is timed to when the $DoP = 0$ the second time. The hole will keep precessing until the system is in the state $\frac{1}{2}(|R_2 \Uparrow\rangle + |R_2 \Downarrow\rangle + |L_2 \Downarrow\rangle - |L_2 \Uparrow\rangle)$. Excitation and emission will generate the 3-qubit cluster state

$$\frac{1}{2}(|R_2R_3 \Uparrow\rangle + |R_2L_3 \Downarrow\rangle + |L_2L_3 \Downarrow\rangle - |L_2R_3 \Uparrow\rangle) \tag{5.5}$$

By detecting the second photon on a linear base and using the definitions $|H\rangle = \frac{1}{\sqrt{2}}(|R\rangle + |L\rangle)$ and $|V\rangle = \frac{i}{\sqrt{2}}(|R\rangle - |L\rangle)$, the cluster state mathematical form can be simplified to:

$$\frac{1}{\sqrt{2}}(|\Downarrow H_2R_3\rangle - i\,|\Uparrow V_2L_3\rangle) \tag{5.6}$$

disentangling the charge carrier would leave us with a two-photon entangled state equivalent to a Bell pair.

We have tuned the delay line with the required delays, Fig.5.22.

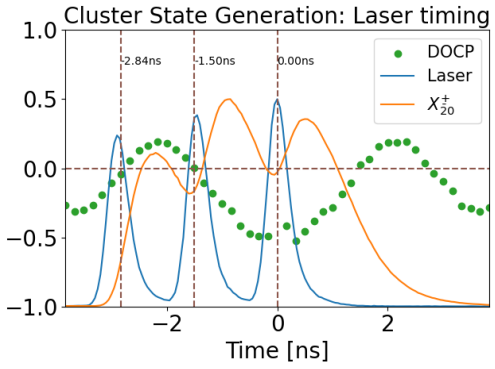


Figure 5.22: Timing of the laser to generate a 3-qubit cluster state.

A Three-photon correlation, which executes initialization, entanglement and spin readout, with setup described in Chap.2, will give us conditional probabilities of detecting the second photon in $|H\rangle$ or $|V\rangle$ state and spin in $|\Downarrow\rangle$ or $|\Uparrow\rangle$ state.

With our sample, extraction efficiency is too low and switching from a reflection to transmission grating based setup did not compensate enough for the losses, so it was not possible to verify the presence of entanglement due to the very low rate of events.

5.4 Conclusions

In the first section of this chapter we have proved our capability of initializing the QDs in a desired hole spin state, we have achieved this both with phonon-assisted

excitation and resonant excitation of one of the trion excited states, see Fig.5.2 and Fig.5.5. Analysing the polarization and time resolved photoluminescence of the QD under resonant excitation we are able to describe the spin dynamics of the process, Fig.5.7.

Spin initialization in a QD is the first step of the cluster state generation according to the protocol proposed by Lindner and Rudolph [1]. We also further proved the light-hole-like character of the first excited state of the hole.

We have also studied the behaviour of the QD photoluminescence under resonant excitation of the other three trion resonances. Even though these resonances show Rabi oscillations, see Fig.5.8, they are not suitable for cluster state applications due to the reduced brightness of the trion state and reduced fidelity of the spin initialization process (reflected in a reduced DOCP of the trion transition). Nevertheless, we have investigated them with time and polarization resolved spectroscopy to gain insight on the hole spin dynamics. While this is not fundamental for cluster state generation, we have proven that spin dynamics can be studied without magnetic field and with regular spectroscopy techniques.

In the second section of the chapter, we have proved the second step required for cluster state generation: controlled spin precession in a weak magnetic field. By analysis of the time resolved DOCP, we were able to extract a hole precession period of $T = 2.69 \pm 0.02ns$ and hole dephasing time $T_2^* = 2.46 \pm 0.13ns$ for a $0.4T \leq \vec{B} \leq 0.6T$ in Voigt configuration. The result was consistent both in pulsed and CW excitation, see Fig.5.21.

We have achieved this by using a custom made copper holder for two cylindrical static magnets, see Fig.2.7. While fixed magnets, unlike a dedicated electromagnet, may lack in field uniformity and ease of tuning of the precession period to match the repetition rate of a laser, we can compensate such limitations by building a custom delay line as described in Chap.2, see Fig.2.13. This proves that such complicated measurement could be achieved on a single QD with very simple and cheap tools, thus lowering the cost of entry for cluster state generation.

In the last section of the chapter we have attempted a 3-qubit, two photon and a charge, cluster state generation, in a manner similar to the measurements done in [10]. We correctly timed the laser pulses thanks to the custom made delay line, but we were unable to prove entaglement of the state due the low extraction efficiency from the QD and fast dephasing time of the hole.

References

[1] N. H. Lindner and T. Rudolph. "Proposal for Pulsed On-Demand Sources of Photonic Cluster State Strings". In: *Phys. Rev. Lett.* 103 (11 Sept. 2009). DOI: 10.1103/PhysRevLett.103.113602.

[2] D. Cogan et al. "Deterministic generation of indistinguishable photons in a cluster state". In: *Nature Photonics* 17 (4 Apr. 2023). DOI: 10.1038/s41566-022-01152-2.

[3] Y. H. Huo et al. "A light-hole exciton in a quantum dot". In: *Nature Physics* 10.1 (Jan. 2014). DOI: 10.1038/nphys2799.

[4] T. Belhadj et al. "Impact of heavy hole-light hole coupling on optical selection rules in GaAs quantum dots". In: *Applied Physics Letters* 97.5 (Aug. 2010). DOI: 10.1063/1.3473824.

[5] F. Mattana et al. "GaAs Site-controlled Pyramidal Quantum Dots as Spin Qubit Sources for a Photonic Cluster State Construction: the Role of Light-hole-like Excited States". In: *CLEO 2023*. Optica Publishing Group, 2023, FF3G.2. DOI: 10.1364/CLEO_FS.2023.FF3G.2.

[6] G. Sallen et al. "Dark-Bright Mixing of Interband Transitions in Symmetric Semiconductor Quantum Dots". In: *Phys. Rev. Lett.* 107 (16 Oct. 2011). DOI: 10.1103/PhysRevLett.107.166604.

[7] M. V. Durnev et al. "Magnetic field induced valence band mixing in [111] grown semiconductor quantum dots". In: *Phys. Rev. B* 87 (8 Feb. 2013). DOI: 10.1103/PhysRevB.87.085315.

[8] G. Juska. "Pyramidal quantum dots: single and entangled photon sources and correlation studies". 2013.

[9] R. J. Warburton. "A Self-assembled Quantum Dot as Single Photon Source and Spin Qubit: Charge Noise and Spin Noise". In: Springer International Publishing, 2017. DOI: 10.1007/978-3-319-56378-7_9.

[10] N. Coste et al. "High-rate entanglement between a semiconductor spin and indistinguishable photons". In: *Nature Photonics* 17 (7 July 2023). DOI: https://doi.org/10.1038/s41566-023-01186-0.

Chapter 6

Summary and Perspectives

6.1 Summary

In Chap.1 we gave an overview of the basic principles of quantum computing and information processing, giving special attention to entanglement, a particular class of entangled states, the cluster state, and loss of coherence of quantum systems. Semiconductor QDs have been chosen as a platform to study and reviewed their properties regarding charge complexes and photon emission.

In Chap.2 we described a particular class of QDs, site controlled pyramidal QDs, sample growth and post-process techniques and the setups used to optically characterize the QDs.

In Chap.3 we reviewed the theory of several excitation schemes, simulated them using the open source QuTiP library for Python, and for some of them compared the results of the simulations with experimental data from pyramidal site-controlled QDs.

In Chap.4 the energetic structure of $GaAs$ QDs in $Al_xGa_{1-x}As$ barriers has been studied in depth, matching transition lines to their respective charge complexes.

In Chap.5 hole spin initialization and controlled precession have been proven, a key step for cluster state generation and manipulation.

6.2 Perspectives

Semiconductor QDs are a promising platform for implementation of quantum information. Although at the moment in the field, there is not a platform that offers a practical implementation of quantum computing, the community is always developing new solutions and devices to overcome the issues arising.

QDs extraction efficiency has been boosted by embedding the emitters in photonic structures, such as circular Bragg resonators [1], allowing for high photon throughput. In the same publication, the authors show the capability of compensating the QD defect by application of strain with an external piezoelectric device, and thus improving the quality of the entangled photons emitted from the sample.

Hahn Echo techniques have recently increased spin coherence times to the ms regime [2] and QD have been proven as reliable emitters for QKD applications [3].

Of particular interest for the purpose of this thesis has been the generation of linear cluster states, already proven with different types of QDs [4] [5].

Pyramidal Site-Controlled Quantum Dots are promising and advantageous due to their flexibility in material composition and high uniformity of optical properties. Nonetheless there is need to further improve their quality when it comes to spin coherence and extraction efficiency. In the last chapter of this thesis we have shown how these two factors are severely limiting their use in cluster state generation and quantum computing application.

The sources of this quick loss of spin coherence have to be investigated more. From literature [6], it is known that there can be many sources of spin noise and decoherence in QDs, such as nuclear spin and charge noise. To overcome the nuclei noise, spin-echo techniques can be used to refocus the spin. Surface/interface defects can be a source of charge noise in QDs, broadening the linewidth of the transition, for this reason encapsulation and surface passivation could reduce the defects introduced by sample post-processing and further improve the spin coherence. Another source of noise are charge fluctuations in the environment, and since the $GaAs$ QDs are embedded in a bulk $GaAs$ carrier with a lower bandgap, emission from the bulk is always present whenever exciting resonantly the QD. This constant background of charge recombination from the bulk could be removed by finding further processing to etch away the carrier or by engineering the QDs to have a longer wavelength than the bulk material, even though the last approach would require a change of QD material, a procedure that would probably come with a set of issue on its own. Spin echo technique can also increase the coherence of the spin.

The second limiting factor, extraction efficiency, could be addressed by integrating these QDs in photonic structures, as already proven by the community. The complex geometry of the pyramidal recesses and the [111] growth direction make this a complex task, since the vertical growth of DBRs layers or etching of bullseye cavity can be an option only after significant epitaxial growth and fabrication modifications allowing for thin membrane release from the substrate. Pillar-like resonators are also an option.

Even with these limitations still to be addressed, pyramidal site-controlled QDs can still be a platform for further studies. For example the ability to vertically

stack QDs with extreme precision has been already proven by the EPN group [7]. The vertical alignment of several QDs will play a crucial role in proposals of generation of bidimensional cluster states which involved coupled QDs and shared energy levels and at the moment other epitaxial growth processes can't ensure high yield of perfect alignment of the QDs.

References

[1] M. B. Rota et al. "A source of entangled photons based on a cavity-enhanced and strain-tuned GaAs quantum dot". In: *eLight* 4 (1 July 2024). DOI: 10.1186/s43593-024-00072-8.

[2] L. Zaporski et al. "Ideal refocusing of an optically active spin qubit under strong hyperfine interactions". In: *Nature Nanotechnology* 18.3 (Jan. 2023). DOI: 10.1038/s41565-022-01282-2.

[3] F. Basso Basset et al. "Quantum key distribution with entangled photons generated on demand by a quantum dot". In: *Science Advances* 7.12 (2021), eabe6379. DOI: 10.1126/sciadv.abe6379. eprint: https://www.science.org/doi/pdf/10.1126/sciadv.abe6379. URL: https://www.science.org/doi/abs/10.1126/sciadv.abe6379.

[4] D. Cogan et al. "Deterministic generation of indistinguishable photons in a cluster state". In: *Nature Photonics* 17 (4 Apr. 2023). DOI: 10.1038/s41566-022-01152-2.

[5] N. Coste et al. "High-rate entanglement between a semiconductor spin and indistinguishable photons". In: *Nature Photonics* 17 (7 July 2023). DOI: https://doi.org/10.1038/s41566-023-01186-0.

[6] A. Ludwig et al. "Ultra-low charge and spin noise in self-assembled quantum dots". In: *Journal of Crystal Growth* 477 (2017). Proceeding of the 19th International Conference on Molecular Beam Epitaxy, pp. 193–196. ISSN: 0022-0248. DOI: https://doi.org/10.1016/j.jcrysgro.2017.05.008.

[7] S. T. Moroni et al. "Statistical study of stacked/coupled site-controlled pyramidal quantum dots and their excitonic properties". In: *Applied Physics Letters* 111.8 (Aug. 2017). DOI: 10.1063/1.4985259.

List of Figures

1.1 Bloch Sphere with a $|+\rangle$ state on it 4

1.2 Graphical representation of quantum gate operating on qubits. . . . 5

1.3 A 1-dimensional 4 qubit cluster state 8

1.4 Realization of Hadamard and CNOT gates with cluster states. . . . 10

1.5 (Left) Type-I and Type-II fusion gates (Right) fusion operations between two 1-dimensional cluster states. Taken from [24] 10

1.6 Decoherence processes visualized on a Bloch Sphere. Left, a longitudinal relaxation process. Right, a pure dephasing process. Picture adapted from [8] 11

1.7 Confinement and density of states for different semiconductor structures. Taken from [31] 13

1.8 Possible charge configuration in a QD described by one electron level in the conduction band and two hole levels in the valance band. 15

1.9 Selection rules for electron - hole recombination from different bands. 17

1.10 Decay of $X_{\bar{1}0}$ and $X_{0\bar{1}}$ with symmetries C_{3v} and D_{3h}. Taken from [36] 20

1.11 Recombination cascade for $2X_{\bar{2}0}$ for D_{3h} and C_{2v} symmetries. Linearly polarized along the $\hat{z}$ direction emission from $X_{\bar{1}0}$ recombination is predicted in C_{2v} symmetry. Taken from [36] 21

1.12 Decay of $2X_{\bar{1}1}$ and $2X_{1\bar{1}}$ with symmetries C_{3v} and D_{3h}. Taken from [36] 22

1.13 Decay of $2X_{\bar{1}1}$ (left side) and $2X_{1\bar{1}}$ (right side) with symmetries D_{3h} and C_{2h}. Taken from [36] 22

1.14 Recombination cascade of $2X^{+}_{\bar{2}1}$ (left side) and $2X^{+}_{11}$ (right side) with symmetries C_{3v}, D_{3h} and C_{2h}. Taken from [36] 23

2.1 Features formed in a pyramidal recess during the QD growth process. VQW/LQW are the Vertical/Lateral Quantum Wells and VQWr/LQWr are the Vertical/Lateral Quantum Wires, these features are formed by Ga segregation in the ternary compound $Al_xGa_{1-x}As$. Image taken from [6] 40

2.2 Stacks of material used for the different types of QDs studied in this thesis. In light grey the etch stop layers, in dark green the barriers, in light green superlattice ($GaAs$ QDs) and additional barriers ($InGaAs$ QDs), in yellow the QDs. 41

2.3 Backetch process, image taken from [8]. Steps: 1) Recesses are patterned on a (111)B $GaAs$ substrate, 2) the QDs are grown inside the recesses in the MOVPE reactor, 3) as-grown sample is flipped and attached with SU8 to a (100) $GaAs$ carrier, 4) excess substrate material is mechanically removed, down to a thickness of $\sim 30\mu m$, 5) the leftover substrate is removed using a chemical back-etching process until the pyramid's tips are exposed. 43

2.4 Schematic of a cross section of a pyramidal QD. (Left) angle α between the pyramid orientation and cleaving plane (110), highlighting the different distances of the QD from the exposed plane. Image taken from [3] (Right) Emission from the p_z component will be vertically polarized at the spectrometer due to the configuration in which the sample is mounted. Image taken from [9] 44

2.5 Test patterns written with the scratch built lithography setup. The scale bars for reference are (left) $500\mu m$, (right) $50\mu m$. 45

2.6 Sample mapping with squares identified by a number, each square contains a few hundred dots that can be identified by their distance from the edges. 46

2.7 3D model of the custom built magnet holder. The cylindrical magnets, of $3mm$ radius, are inserted in the two round holes at the center of the left and right pieces. The magnets holder are $10mm$ tall, $5mm$ wide and $20mm$ long. The sample, up to $2mm$ in length, is attached in the central part. The whole unit is kept together by M3 bolts. 47

2.8 4f Pulse Shaper to convert a fs pulse to ps 49

2.9 Measured intensity as function of the QWP angle for the polarization basis states. 55

2.10 Characterization of four beam splitters available in the laboratory, 2 $50R:50T$, $30R:70T$ and $10R:90T$ using circular polarized light as input and a rotating HWP and fixed polarizer as analyser. 56

2.11 Beam path of lasers and imagining system. If the QWP for excitation is inserted, the QWP for detection is removed. 57
2.12 Correlation measurement in the Swabian TimeTagger Ultra TCSPC module. Image taken from [15] 59
2.13 Laser multiplexing setup to generate time-tuned pulses. 60
2.14 Transmission grating spectrometer and three photon correlation setup 61

3.1 (Left) Typical spectrum of a GaAs QD in AlGaAs barrier (Right) Typical spectrum of GaAs bulk left from the backetching process . 67
3.2 Autocorrelation curves of the $X^{+}_{\bar{2}0}$ peak under above-band circular excitation 68
3.3 Two-Levels System and Laser. (a) Resonant, (b) Blue-Detuned, (c) Red-Detuned 69
3.4 Phonon coupling for dots of different size ($a_e = [1, 2, 5]nm$) 72
3.5 Two-Levels System with Phonon Bath and Laser. (a) Blue-Detuned, (b) Red-Detuned 72
3.6 2LS without phonons excited by a resonant Gaussian pulse of different pulse areas: time dynamics and evolution on Bloch Sphere . . 73
3.7 2LS without phonons excited by a detuned Gaussian pulse of different pulse areas: time dynamics and evolution on Bloch Sphere . . 74
3.8 2LS without phonons excited by a Gaussian pulse of different pulse areas ($\Psi_0 = \frac{1}{\sqrt{2}}(|g\rangle + |X\rangle)$): time dynamics and evolution on Bloch Sphere 75
3.9 Exciton Population after a Gaussian pulse as function of pulse area and detuning for a 2LS *without* Phonon interaction 75
3.10 Excited State population after a Gaussian Pulse for a 2LS *without* Phonons, at different pulse length and detuning 76
3.11 Exciton Population after a Gaussian pulse as function of pulse area and detuning for a 2LS with Phonon interaction 76
3.12 Excited State population after a Gaussian Pulse for a 2LS with Phonons, at different pulse length and detuning 77
3.13 2LS with phonons excited by a Gaussian pulse with $\alpha = 20\pi$ and different detuning. Time evolution of the $|X\rangle$ state population (left), Bloch vector Length (right), state on the Bloch Sphere (under). . . 78
3.14 Spectrum and power dependence of trion population under phonon assisted excitation. 79
3.15 Three-Levels System and Laser for (a) Binding and (b) Antibinding QDs 80

3.16 $|XX\rangle$ and $|X\rangle$ Population after a Gaussian pulse as function of pulse area and detuning for a cascade, binding (upper half) and antibing (lower half), *without* Phonon interaction. Due to the lack of a decay operator for the $2X_{\bar{2}0} \rightarrow X_{\bar{1}0}$ cascade the X_{10} is populated only when the pulse is on resonance with the transition, $\Delta = 0meV$. If a decay operator was introduced in the simulation the X_{10} population would should a second resonance that maps the $2X_{\bar{2}0}$ population when the pulse detuning is at TPE condition, $\Delta = \pm 1meV$. 82
3.17 $|X_{\bar{2}0}\rangle$ and $|X\rangle$ Population after a Gaussian pulse as function of pulse area and detuning for a cascade, binding (upper row) and antibing (lower row), with Phonon interaction 83
3.18 $|XX\rangle$ and $|X\rangle$ Populations after a Gaussian pulse as function of pulse area for a cascade at the TPE condition, binding (left) and antibinding (right) 83
3.19 (Left) Typical GaAs QD spectrum under Two Photon Excitation (Right) Power dependence of $2X_{\bar{1}1}$ and $X_{\bar{1}0}$ states under Two Photon Excitation, showing Rabi oscillations up to 7π. 84
3.20 Autocorrelation measurement of the $X_{\bar{1}0}$ transition under Two Photon Excitation highlighting single photon emission. 85
3.21 (Left) Typical $InGaAs$ QD spectrum under Two Photon Excitation (Right) Power dependence of $2X_{20}$ and X_{10} states under Two Photon Excitation, showing the phonon assisted component in the emission of the X. 85
3.22 Autocorrelation measurement of the $2X_{20}$ and X_{10} transitions under Two Photon Excitation highlighting single photon emission. 86
3.23 Three-Levels System and Laser in a non radiative cascade to X^+_{20} . 87
3.24 Time evolution of the $|X^+_{11}\rangle$ and $|X^+_{20}\rangle$ Populations during a Gaussian pulse and decay, finale states population as function of pulse area for a cascade 88
3.25 Spectrum and power dependence of trion population under resonant excitation of one of its excited states. 88
3.26 Ramsey fringes visibility for laser and $X^+_{\bar{2}0}$ state as function of the coarse delay 90
3.27 (left) Two-Levels System under Red-and-Blue-Detuned Excitation (right) Gaussian envelope of the pulse and its modulation introduced by the two wavelengths 91
3.28 Red-and-Blue excitation for $\eta = 1$ 91
3.29 Red-and-Blue excitation for $\eta = 3$ 92
3.30 (left) Spectrum of GaAs QD under Red-and-Blue-Detuned Excitation (right) Power Dependence of X^+_{20} 93

3.31 (left) Two-Levels System under SUPER Excitation (right) Gaussian envelope of the pulse and its modulation introduced by the two wavelengths 93

3.32 Two-Levels System under SUPER Excitation. First two rows of plots are the system excited with single pulses, with and without phonons. Last row is the system excited with the pulses combined according to the SUPER scheme. The images shows the simulation for the second set of parameters from Tab.3.2 [15], similar results have been obtained by the simulations for the other sets as well. . . 96

4.1 A typical spectrum of a $GaAs$ QD with $Al_xGa_{1-x}As$ barrier and superlattice structure with excitonic states matched to the corresponding peak. 102

4.2 Energy of $X_{\bar{1}0}$ (top left) and $2X_{\bar{2}0}$ (bottom left) states as function of HWP angle and Fine Structure Splitting of a $GaAs$ QD (right) . 103

4.3 Fine Structure Splitting distribution of the the QDs analyzed. . . . 104

4.4 Average Fine Structure Splitting for different generations of QDs grown by the EPN group in Tyndall. In black (green) $GaAs$ QDs with $Al_{0.75}Ga_{0.25}As$ ($Al_{0.45}Ga_{0.55}As$) barriers, in orange $GaAs$ QDs in $AlAs$ barriers, and in red $GaAs$ QDs in $Al_{0.45}Ga_{0.55}As$ barriers with superlattice. The sample analysed in this thesis is among the ones of the most blueshifted data point of the superlattice series. Image taken from [1]. 104

4.5 Energy of the biexciton (left) and the binding energy (right) of $GaAs$ QDs as function of the $X_{\bar{1}0}$ energy. 105

4.6 $g^{(2)}(\tau)$: recombination cascade $2X_{\bar{2}0} \rightarrow X_{\bar{1}0}$. 106

4.7 Energy of the $X_{\bar{1}0}$ (top), the $X_{0\bar{1}}$ (middle) and the $X_{0\bar{1}_z}$ (bottom) states as function of HWP angle. 106

4.8 PL from the side view, vertical polarization is along the growth direction (top). Highlight of ground and excited exciton showing the non-degenerate $X_{0\bar{1}_z}$ transition due to the light-hole-like nature of the excited state (bottom). 108

4.9 Energy of the excited exciton (left) and energy difference with ground exciton (right) of $GaAs$ QDs as function of the $X_{\bar{1}0}$ energy. 109

4.10 Energy of the non-degenerate excited exciton (left) and energy difference with excited exciton (right) of $GaAs$ QDs as function of the $X_{0\bar{1}}$ energy. 110

4.11 Intensity of $X_{\bar{1}0}$ (top left) and $X_{0\bar{1}}$ (bottom left) as function of 2 x HWP angle and corresponding valence band mixing (right). 111

4.12 Degree of Linear Polarization of $X_{0\bar{1}}$ as function of DOLP of $X_{\bar{1}0}$, the distribution of values is indicative of low band mixing and the two data set seem uncorrelated. 111
4.13 (left) Ground and Excited Biexcitons in the $GaAs$ QD spectrum, (right) $g^{(2)}(\tau)$: recombination cascade $2X_{\bar{1}1} \rightarrow X_{0\bar{1}}$. 112
4.14 Recombination cascade for $2X_{\bar{1}1}$ for D_{3h} symmetries, showing the 3 isotropic transitions visible in the top-view configuration and 1 linearly polarized along the growth direction visible in the cross section. Taken from [2] 113
4.15 Schematic of the $GaAs$ QDs sample mounted on a monolithic piezoelectric device. Image taken from [12]. 113
4.16 Tuning of Fine Structure Splitting (left) and of band mixing (right) as function of the voltage applied to the piezoelectric substrate. . . 114
4.17 (left) Typical spectrum of $GaAs$ QD in superlattice, (right) recombination patterns of (top) $X^{+}_{1\bar{1}}$ (middle) $X^{+}_{\bar{1}1}$ (bottom) $2X^{+}_{\bar{2}1}$. 114
4.18 Energy (left) and relative energy (right) of the ground trion state as function of the $X_{\bar{1}0}$ energy. 115
4.19 Energy (top) and relative energy (bottom) of trions in which the heavy-hole recombines with the electron. 116
4.20 Energy (top) and relative energy (bottom) of trions in which the light-hole recombines with the electron. 117
4.21 Energy (top) and relative energy (bottom) of trions in which the light-hole recombines with the electron. The energy has been calculated in relation to excited exciton to reduce the noise in their energy distribution due to the dot-to-dot variations of the excited state energy. 118
4.22 Decay of charged biexciton to trion and hot trions. Red/Blue indicate cross-polarized photons in the recombination cascade, red/red photons are co-polarized, green arrows indicate isotropic emission in the XY plane with no clear relation to the $2X^{+}_{\bar{2}1}$ polarization, solid blue arrow indicates a photon linearly polarized along the $\hat{z}$ direction and dashed light blue arrow are associated to non-radiative decays to the trion state. 119
4.23 $g^{(2)}(\tau)$: recombination cascade $2X^{+}_{\bar{2}1} \rightarrow X^{+}_{\bar{1}1}$. 119
4.24 $g^{(2)}(\tau)$: recombination cascade $2X^{+}_{\bar{2}1} \rightarrow X^{+}_{1\bar{1}}$. 120
4.25 $g^{(2)}(\tau)$: recombination cascade $2X^{+}_{\bar{2}1} \rightarrow X^{+}_{\bar{2}0}$. 120
4.26 Exchange interaction of charged biexciton and trion in cross-section. 121
4.27 Statistics of exchange interaction of charged biexciton and trion in cross-section. 122
4.28 Heavily polarized transitions, maybe belonging to the $X^{2+}_{\bar{2}1}$ state. . . 123

4.29 p-i-n diode structure for $GaAs$ QDs: epitaxial structure (left) sketch showing the non planar geometry of the sample which would cause the short circuit condition if a gold contact was directly evaporated on top without the trenches (right) 124

4.30 p-i-n diode structure for $GaAs$ QDs: gold evaporation steps (top) full processing steps (bottom). Images taken from [18] 125

4.31 p-i-n diode structure for $GaAs$ QDs: measured IV curve showing the expected diode behaviour (left) PL spectra as function of the applied voltage showing very weak Stark shift and charge tuning under forward bias, the spectra has been divided in two ranges, ground and excited states, and each range normalized to highlight the relative intensity of the states (right). 126

5.1 Spectrum of GaAs QD under Phonon Assisted Excitation 130

5.2 Degree of Circular Polarization of laser and $X^{+}_{\bar{2}0}$ when the QD is under phonon-assisted excitation with circularly polarized light (left). $g^{(2)}(\tau)$ of $X^{+}_{\bar{2}0}$ in co-polarized and cross-polarized detection when the QD is under phonon-assisted excitation with linearly polarized light (right). 131

5.3 Spectrum of a $GaAs$ QD under resonant excitation of the 4 resonances of trion states. 133

5.4 Spectrum of the tunable Ti:Sapphire laser at the four resonances of the trion states. 133

5.5 Degree of Polarization of laser and $X^{+}_{\bar{2}0}$ state under resonant excitation with circularly polarized light at the 1^{st} resonance. 134

5.6 $g^{(2)}(\tau)$ of $X^{+}_{\bar{2}0}$ state under resonant excitation with linearly polarized light, in CW excitation (left) and pulsed at $80MHz$ (right). 134

5.7 Dynamics of the excitation of the X^{+}_{11} state and recombination of the $X^{+}_{\bar{2}0}$ state (at the 1^{st} resonance). The relaxation of the hole from the 2^{nd} to the 1^{st} energy level causes polarization of excitation and recombination to be orthogonal, the spin direction is preserved between excitation cycles, causing bunching in $g^{(2)}(\tau)$ under co-polarized detection. Image adapted from [5]. 135

5.8 Power Dependence the trion states under resonant excitation at the 2^{nd}, 3^{rd} and 4^{th} resonance. 136

5.9 Degree of Polarization of laser and trion states under resonant excitation with circularly polarized light at the 2^{nd}, 3^{rd} and 4^{th} resonance. 136

5.10 $g^{(2)}(\tau)$ of $X^{+}_{\bar{2}0}$ (left) and $X^{+}_{\bar{1}1}$ (right) states under resonant excitation with linearly polarized light at the 2^{nd} resonance. 137

5.11 Dynamics of the excitation and recombination processes of the $X^{+}_{\bar{1}1}$ state (at the 2nd resonance of the $X^{+}_{\bar{2}0}$ state). Excitation and emission are still orthogonal due to recombination from different band, and emission is co-polarized between excitation cycles because the hole relaxation process preserves the spin direction. Image adapted from [5]. 137
5.12 Dynamics of the excitation of the X^{+}_{11} state and recombination of the $X^{+}_{\bar{2}0}$ state (at the 2nd resonance). The holes relaxes to the 1st energy level through a spin-flip process, excitation and emission are still orthogonal but so is the emitted photons between two consecutive cycles, due to the hole flipping direction. Image adapted from [5] . . 138
5.13 Splitting in GaAs QD of Trion and Exciton lines into two doublets in a magnetic field (Faraday Configuration). 139
5.14 Selection rules in weak (left) and strong (right) magnetic field in Voigt geometry. The trion oscillation term becomes relevant when the lifetime of the state is longer than the precession period. 140
5.15 Precession of Trion in a strong magnetic field. 141
5.16 Scan of the trion resonance with a tunable CW laser, highlighting no split of the state within the linewidth of the transition. 142
5.17 Hole precession in phonon-assisted (left) and resonant (right) excitation. 142
5.18 Hole precession in phonon-assisted (left) and resonant (right) excitation. 143
5.19 Possible combinations in the $g^{(2)}(\tau)$ when the laser pulsed is delayed. 144
5.20 Hole precession in phonon-assisted (left) and resonant (right) excitation for variable delays. 145
5.21 Hole precession in resonant excitation with CW and pulsed laser at variable delay. 145
5.22 Timing of the laser to generate a 3-qubit cluster state. 146

List of Tables

1.1 Proposed quantum systems to realize qubits. Taken from [8] 4

2.1 Combination of angles used to measure the Stokes vector. 53
2.2 Normalized Stokes vector of the polarization basis states, measured with the rotating QWP method. 54

3.1 Final State of a 2LS excited at different pulse areas 74
3.2 Set of example parameters for the SUPER scheme which lead to close to unity occupation of the excited state level, taken from [15] . 95